Cell Expansion and Delivery Methods for Heart Regeneration

Acott, Samuel

Award date:
2017

Awarding institution:
University of Bath

CELL EXPANSION AND DELIVERY METHODS FOR HEART REGENERATION

Samuel Max Acott

A thesis submitted for the degree of

Doctor of Philosophy

University of Bath

Department of Chemical Engineering

September 2016

[Page intentionally left blank]

ABSTRACT

The aim of this work was to improve the utility of hollow fibre bioreactors (HFB) for the growth of clinically applicable cell populations by improving initial rates of cell attachment using a novel dynamic seeding methods, and to investigate their use as a novel cell encapsulation device for the delivery of cell therapies to infarcted heart tissue.

Cardiac cell therapies starting are traditionally administered by direct injection or intravenous infusion to a target area in the heart. Mesenchymal stem cells (MSCs) have shown promise as a cell therapy and can be isolated from a patient's adipose tissue surrounding the heart, allowing 812,800 ± 318,400 cells to be harvested; however this population requires expansion to a minimum of 50 million cells to be an effective traditionally administered dose in humans. Hollow fibre bioreactors have shown to offer the highest rates of MSC growth compared to other bioreactor designs, owing to their large surface area to volume ratio and their ability to provide the cells with a low shear environment that can emulate *in vivo* conditions. However, a concern with using HFBs is the relatively low rates of initial cell attachment, with authors observing rates around 20%. At this rate of attachment and with an initial population of 812,800 ± 318,400 cells, it would take 12.6 ± 5.2 days to grow 50 million MSCs in a HFB. For use as a medical intervention the MSCs must be grown as soon as possible, and to ensure this the efficiency of cell seeding on the external hollow fibre surface must be as high as possible. In an attempt to improve rates of initial cell attachment Chapter 4 illustrated how dynamic seeding can allow additional opportunities for a given cell to make contact with hollow fibres contained in a bioreactor. MG63 human osteosarcoma cells were used as an alternative cell type due to their lower cost and increased resilience over a greater number of passages. Static horizontal seeding of MG63 cells on single fibre bioreactors provided 18% ± 16% cell attachment confirming values found in literature, however dynamic attachment on horizontally orientated multi fibre bioreactors rotating at 6 RPM offered improved attachment of 39% ± 12%, double the rate of static attachment. At this improved rate of cell attachment, it would now take 11.2 ± 4.7 days to grow 50 million cells, 1.4 days quicker than before. This novel approach to HFB seeding will lead to quicker administration of medical treatments for patients.

While traditional delivery methods have shown to improve heart function, the active dose retained at the wound site is around 2%, much lower than that actually administered. Cells can be ejected from the insertion site due to heart contractions, and doses contained in the bloodstream become highly diluted. Engineered alternatives include cellular sheets, cell-loaded sutures, and cell encapsulation within hydrogels. However, each of these have their own inherent limitations, with cellular sheets demonstrating poor rates of migration into infarct site, cells on suture surfaces shearing away when sown into a wound site, and cells in hydrogels suffering from poor initial rates of engraftment.

Hollow fibres made from poly(lactic-co-glycolic acid) (PLGA) were further investigated for use as an engineered cell delivery vector, with cells seeded within the hollow fibre lumen, allowing cells to be protected during implantation, biodegrade, and provide a concentrated cell dose at a wound site. Hollow fibre scaffolds have been used as a delivery device for encapsulation of pharmaceuticals, but never for encapsulation of cells in this manner. Chapter 5 investigates the development of a hollow fibre with internal and external surface porosity, which allowed passive permeation of liquid through its structure from one side to the other. Manufacturing a hollow fibre using NaCl porogen at 60% the weight of PLGA resulted in pores 4 – 6 µm in diameter, which provided the desired liquid permeation characteristics and a flux of 6.6 $m^3m^{-2}h^{-1}bar^{-1}$ (± 77%). Chapter 6 sought to encapsulate a population of MG63 cells within the lumen of the hollow fibre, fed by permeation of media flowing in the extracapillary space (ECS), and investigate the viability of cells over a 6 day time course. Studies revealed that the cells became non-viable after 24 hours as a result of poor rates of dissolved oxygen permeation. Subsequent modelling of the system showed that an increased ECS flow rate of a 1.49 mL/min should provide sufficient dissolved oxygen to sustain a population of 100,000 cells in this system. This work demonstrates a vital first step in exploring a potential evolution in cell delivery, with further investigation required to fully explore the viability of hollow fibre devices for cell encapsulation.

[Page intentionally left blank]

ACKNOWLEDGEMENTS

I would like to thank my supervisor Dr. Marianne Ellis, whose relentless enthusiasm and amazing patience somehow kept me on the straight and narrow all this time, despite a few hiccups from me along the way. Also my gratitude to the University of Bath for funding my research.

Thanks to my friends in the research group, Nelly and Jas, for keeping me sane in the lab and helping to fill in the gaps in my biology knowledge; the technicians Dan and Alex for their help with the lab equipment and generally keeping me entertained with the latest gossip from around the department; the post docs Ian, Mike and Kim for their expertise and guidance; and my board gaming and pub buddies Will, Ben, Alex and Alf.

Thanks to the IChemE for funding my trip to Worcester Polytechnic Institute in Boston; Katrina who assisted me during my visit; her supervisor Prof. Glenn Gaudette, who kindly had me over for thanksgiving dinner with his family; my friends Sean, Remy, Lydia, Chuck, Megan, Spencer and Patrick for making me the official Brit of the GDC.

My Mum, Uncle and Nan for always believing in me and encouraging me to always do my best and strive to achieve something great. I am so thankful to my mum in so many ways that I cannot adequately describe, but let's just say that you are an inspiration to me. I regret that my Nan wasn't here to see me finish my academic career. I know that she'd have been so proud of me for what I have achieved.

Finally I would like to thank my wonderful girlfriend Corinne, for all of the love, care and advice she has given me throughout this PhD, and over the last 9 years. Without you I absolutely could not have gotten through this part of my life and would not be the person I am today.

Onto the future!

"Sometimes science is more art than science...a lot of people don't get that."

Rick

[Page intentionally left blank]

TABLE OF CONTENTS

LIST OF FIGURES

[Page intentionally left blank]

LIST OF TABLES

[Page intentionally left blank]

LIST OF EQUATIONS

NOMENCLATURE

ABBREVIATIONS

Abbr.	Full Name	Abbr.	Full Name
2D	Two dimensional	MSC	Mesenchymal stem cells
3D	Three dimensional	N2	Nitrogen
A/A	Antibiotic-Antimycotic	NaCl	Sodium chloride
ANOVA	Analysis of variance	NADH	nicotinamide adenine dinucleotide
ATP	Adenosine triphosphate	NaPy	Sodium Pyruvate
ATP	adenosine triphosphate	NEAA	Non-essential amino acid
BM	Bone marrow	NHS	National Health Service
CO2	Carbon dioxide	NMP	1-methyl-2-pyrrolidinone
d	Distilled	O2	Oxygen
dd	Double distilled	OD	Outer Diameter
DMEM	Dulbecco's modified eagle medium	P/S	Penicillin-streptomycin
DNA	Deoxyribonucleic acid	PBS	Phosphate buffered saline
ECM	Extracellular matrix	PCL	Poly(ε-caprolactone)
ECS	Extracapillary space	PEG	Polyethylene glycol
EDTA	Ethylenediaminetetraacetic acid	PES	Poly(ether sulphone)
EPC	Endothelial progenitor cells	PETP	Poly(ethylene terephthalate)
ESC	Embryonic stem cells	PGA	Poly(glycolic acid)
EtOH	Ethanol	PLA	Poly(lactic acid)
EVR	Endocardial viability ratio	PLCL	Poly(L-lactide-co-caprolactone)
FBS	Foetal bovine serum	PLGA	Poly(lactic-co-glycolic acid)
FDA	Food and Drug Administration	PS	Poly (styrine)
GMP	Good manufacturing practice	PU	Poly(urethane)
HFB	Hollow fibre bioreactor	PVA	Poly (vinyl alcohol)
HFZ	Hollow fibre zone	RPM	Rotations per minute
HSC	Hematopoietic stem cells	SD	Standard deviation
ID	Internal Diameter	SEM	Scanning electron microscope
IV	Intravenous	STLV	Slow turning lateral vessel
K'NEX	K'NEX	TE	Tris-EDTA
LVEDP	Left ventricular end-diastolic pressure	VEGF-A	Vascular endothelial growth factor A
LVEF	Left ventricular ejection fraction	WPI	Worcester Polytechnic Institute
MB	Methylene blue		

SYMBOLS

Symbol	Description	SI Units	Symbol	Description	SI Units
A	Surface area	[m^2]	r	Radius	[m]
C	Concentration	[kg/m^3]	R	Radius of rotation	[m]
c	Chord	[m]	R_G	Gas constant	[kJ/mol.K]
D	Diffusivity	[m^2/s]	Re	Reynolds number	[-]
d	Diameter	[m]	S	Surface area per unit volume	[m^2/m^3]
F	Force	[$kg.m/s^2$]	t	Time	[s]
f	Volume fraction	[-]	u	Velocity	[m/s]
f_D	Darcy friction factor	[-]	u_s	Superficial velocity	[m/s]
G	Mass consumption	[kg/s]	V	Volume	[m^3]
g	Gravity	[m/s^2]	x	Thickness	[m]
H_{sol}	Heat of solution	kJ/mol	y	Hindering exponent	[-]
J	Flux	[$m^3/m^2.s$]	Δ	Change in parameter	[-]
K	Carman constant	[-]	δ	Change in value	[-]
K_a	Acid dissociation const	[mol/L]	ϵ_S	Surface porosity	[-]
k_B	Boltzmann constant	[$m^2.kg/s^2.K$]	ε_b	Bed Voidage	[-]
k_H	Henry's constant	[mol/atm.L]	Θ	Standard conditions	[-]
k_{se}	Sechenov constant	[-]	θ	Angle	[°]
L	Length	[m]	κ	Permeability	[m^2]
M	Mass	[kg]	λ	Mean free path	[m]
N	Number of replicates	[-]	μ	Viscosity	[kg/m.s]
N	Molar consumption	[mol/s]	ν	Linear velocity	[m/s]
n	number of trials	[-]	π	Pi	[-]
P	Pressure	[$kg/m.s^2$]	ρ	Density	[kg/m^3]
P_A	atmospheric	[$kg/m.s^2$]	τ	Tortuosity	[-]
P_G	gauge	[$kg/m.s^2$]	Ω	Resistance	m^{-1}
Q	Volumetric Flow Rate	[m^3/s]	ω	Angular velocity	[1/s]
			*	Significant difference	[-]

SUBSCRIPTS

Symbol	Description	Symbol	Description
b	buoyancy	L	Liquid
C	Cell	LA	Lactic acud
c	Centrifugal	OB	Outer bioreactor
d	drag	OF	Outer fibre
F	Hollow fibre	O2	Oxygen
G	Gas	p	Pore
g	Gravity	r	Radial position
H	Hindered cell	S	Superficial
IB	Inner bioreactor	X	distance from rotation
IF	Inner fibre		

CHAPTER ONE: INTRODUCTION

1.1 THE NEED FOR HEART TISSUE ENGINEERING

All organs have potential for infection or injury, and the heart is no exception, however the impact of heart disorders on patients and the associated costs are comparatively greater than any other organ disease. The National Health Service (NHS) in the United Kingdom spent approximately £6.8 billion on treating cardiovascular disease with in the tax year 2012/2013 (BHF, 2014) making up 7.2% of the total NHS budget that year (NHS-England, 2013), with costs set to rise greatly before the end of the decade (Cebr, 2014). This is second only to mental health spending, but greater than the funds allocated to treat the respiratory system, gastrointestinal system, musculoskeletal system and sensory organs. Including private institutions, the direct healthcare cost of cardiovascular disease in the UK is approximately £8.7 billion, with an additional economic bill of over £10.3 billion for loss of patient productivity and the costs of informal care by spouses, family members, friends etc. This is displayed in Table 1.1 (Nichols, 2012).

Table 1.1 – Total Costs of Cardiovascular Disease in the UK in 2009 (Nichols, 2012).

Healthcare Parameter	Cost (£1,000's)	% of Total
Primary care	1,123,675	5.9%
Outpatient care	1,027,352	5.4%
A&E	154,784	0.8%
Inpatient care	4,363,721	23.0%
Medications	2,011,360	10.6%
Productivity loss due to mortality	4,023,834	21.2%
Productivity loss due to morbidity	2,446,575	12.9%
Informal care costs	3,797,564	20.0%
Total	**18,948,865**	**100.0%**

Cardiovascular disease, an umbrella term for any disease that affects the cardiovascular system, is the second largest cause of death in the UK (second only to dementia), causing 27% of all deaths in 2014 (BHF, 2015). The number of deaths has been in decline since the 1960's, due to a combination of improved treatment and mitigation of risk factors. An increased survival rate from heart attacks is the main reason, which can be characterised by an upward trend in the number of prescriptions being written to prevent and treat cardiovascular disease and an increase in the number of heart surgeries. In 2014 approximately 313 million prescriptions were written, with 92,000 instances of percutaneous coronary interventions and 180 whole heart transplant surgeries performed (BHF, 2015). Reduction in behavioural risk factors such as an overall decline in smoking and the consumption of fats have also helped to

mitigate heart disease, but a decrease in the prevalence for individuals to perform physical activity and an increase in childhood obesity is countering this effect (BHF, 2015).

Given the remarkably high cost of treating cardiovascular disease and the general unavailability of replacement hearts from donors, the field of tissue engineering has been investigating how to treat heart problems using cell therapies. In this report the work is continued.

1.2 AIM OF THE RESEARCH

The research contained in this report aims to assist the field of heart tissue engineering by applying the principles of engineering, biology and material science to address the current limitations of heart tissue engineering. Specifically, this report aims to improve the initial rate of cell attachment on poly (lactic-co-glycolic) acid (PLGA) hollow fibre membranes within hollow fibre bioreactors (HFB), to facilitate an acceleration in the acquisition of a clinically applicable number of cells for use as a cell therapy for the heart. In parallel with this, hollow fibres made from PLGA will be modified with sodium chloride (NaCl) in order to impart a surface porosity to its external structure, which will allow the prolonged culture of cells within a perfused flow HFB system. PLGA hollow fibres will also be investigated for use as a device to encapsulate cells, which could be used to deliver cell therapies into the heart, while overcoming the limitations of current methods.

1.3 OUTLINE OF THESIS

This report is presented in six chapters. Chapter One is an introduction to the report which shows a basic financial assessment and the moral costs of heart disease in the UK, and the important trends and statistics in heart health. The research to be conducted in this report is presented.

Chapter Two reviews the available literature on the subject of heart tissue engineering. Initially tissue engineering is defined, including a brief history of major historical events in the field. Next, major breakthroughs in heart surgery are discussed, including the introduction of cell therapies as treatment option, and the fundamentals of heart anatomy and histology are explored. Cell types with clinical applications in heart tissue engineering are investigated, as well as the technologies used to grow these cells. Methods of cell delivery into the heart are reviewed, and their limitations discussed; followed by outlining the available methods used to manufacture hollow fibres, and the ways surface porosity can be imparted onto this scaffold. It concludes with outlining the aims and objectives of Chapter Four, Chapter Five and Chapter Six.

Chapter Three describes the various materials and methods used in the experiments shown in Chapter Four, Chapter Five and Chapter Six. Materials used for this work are subcategorised into those used for cell culture, cell analysis, membrane production and bioreactor construction; including a list of lab consumables and equipment. Experimental procedures for manufacture of flat sheet and hollow fibre membranes are described, as well as cell attachment on or within these scaffolds, including production of the NaCl porogen. Analytical methods used to investigate scaffold properties such as porosity and permeability are shown; including assays investigating cell viability and media composition. Chapter Three concludes with a statistical methods section, documenting the statistical analyses undertaken in this report.

Chapter Four analyses cell attachment onto flat sheets of PLGA to determine the time needed for different levels of cell attachment. Following this, both static and dynamic seeding experiments are conducted on single module hollow fibre bioreactors, and then subsequently on larger bundles of hollow fibres using static and dynamic seeding methods. Cell attachment efficiency is determined through a combination of mass balances and picogreen assay. This chapter includes discussion of the feasibility of the hollow fibre bioreactor system in light of the conclusions drawn from the experiments within Chapter Four and a thorough error analysis of the available data.

Chapter Five investigates how the surface porosity of PLGA hollow fibres can be changed by supplementing the polymer dope with different quantities of NaCl porogen. Four different proportions of NaCl will be added, with the resulting scaffolds imaged and analysed to determine the resulting degree of porosity and if any trends emerge. The porous scaffolds will then be tested for their gas and liquid permeability to determine the optimum degree of porosity to allow sufficient media flow when used in a hollow fibre bioreactor.

Chapter Six studies the feasibility of using a porous hollow fibre to maintain an internally seeded cell population, specifically investigating if cells are affected by media flow rate in a continuously recycling hollow fibre bioreactor system. Cell viability is analysed by picogreen assay, and concentrations of D-glucose and L-lactic acid in the media are monitored over a six day time course. This is a vital first step to determine the feasibility for hollow fibres to be used as devices for cell encapsulation.

Chapter Seven concludes the studies undertaken in this report and proposes avenues for future work in the areas of dynamic cell attachment, porous hollow fibre manufacture and internally encapsulated cell viability.

[Page intentionally left blank]

CHAPTER TWO: IDENTIFYING THE LIMITATIONS OF CELL THERAPIES FOR HEART TISSUE REPAIR

2.1 INTRODUCTION

Tissue engineering is a branch of engineering which pools knowledge from cell biology, material science and engineering methodology to improve or replace biological functions in the human body (Culme-Seymour, 2012). It encompasses areas of medicine such as surgical implants, organ transplants and targeted drug delivery. Typically cells are seeded onto a three dimensional (3D) biological scaffold specially manufactured to ensure good biocompatibility with the attached cells and host's extracellular matrix (ECM) within the target tissue.

A branch of tissue engineering is regenerative medicine, which investigates how the human body's own cells can be applied as 'cell therapies' to treat diseases and injuries. Cells can be removed from a patient, grown or modified in the laboratory, and reintroduced to a wound area within that patient. This method is used to aid in the healing of damaged organs without the risk of rejection by the host tissue (Mason and Dunnill, 2007). These cells may be one of many differentiated cell types in the body known as somatic cells, or undifferentiated adult or embryo derived stem cells.

The advancement of medical science and development of new technologies in the last century has led to improved outcomes for patients suffering from heart conditions. The design of the heart-lung machine to maintain oxygenated blood flow around the body led to the first successful heart operation in 1953 (Cohn, 2003). This technology is still used today for operations such as valve replacement and coronary bypass surgeries. The first tissue grafts to treat damaged regions of the heart were utilised in a surgical procedure called cardiomyoplasty in 1985, which sourced an autograft of skeletal muscle from the patient that was sewn into the wound site of the heart and activated by electrical stimulation to aid heart contraction (Carpentier and Chachques, 1985).

It wasn't until the 1990's that cell therapies were investigated as a method for regenerating scarred heart tissue. A successful study on transplanting functional skeletal myoblasts onto diseased myocardium was published in 1993 (Koh *et al.*, 1993), quickly followed by transplanting foetal cardiomyocytes (Soonpaa *et al.*, 1994). Later studies on rat models investigated injecting skeletal myoblasts suspended in culture media and phosphate buffered saline into heart tissue, however this study also showed limited retention and survival of the transplanted cells (Reinecke and Murry, 2000). From this a number of different cell sources

began to be utilised including skeletal myoblasts and cardiomyocytes derived from mesenchymal stem cells (MSCs), embryonic stem cells (ESCs) and hematopoietic stem cells (HSCs). Today cell therapies are still being investigated for their efficacy in treating heart conditions, incorporating patient derived cells with engineered scaffolds to improve the targeting of wound sites.

This chapter will provide a brief overview of the heart and its histology, and an in-depth look at cells that can provide therapeutic benefits to heart, the bioreactors used to expand them, the methods used to deliver them, and identify limitations in current technologies and potential solutions.

2.2 THE HEART

The heart is a vital organ present in any organism which uses a circulatory system for the transfer of oxygen, carbon dioxide, nutrients and waste materials around its body. The heart is the core organ of the circulatory system, which acts as a peristaltic pump rhythmically pulsating to facilitate blood flow to other organs and to the extremities of the body.

All cells within the human body require oxygen for aerobic respiration (Jafri *et al.*, 2001), so the performance of the heart directly effects the operation of every organ, tissue and cell in the human body. A highly distributed circulatory system facilitates this, comprising of larger arteries (diameter ~30 mm) (Litalien *et al.*, 1979) to narrow capillaries (diameter < 10 μm) (Wiedeman, 1963) where the majority of mass transfer to and from cells takes place.

The circulatory system can be said to be analogous to a chemical engineering processes. A peristaltic pump forcing liquid into a pipe which flows into a series of smaller pipes and undergoes mass transfer exchanges and separation processes through semi-permeable walls, before being recycled back to the pump. However this comparison is complicated by additional human factors such as health, diet, mood and sex; all of which could lead to variations in heart flow rate, pressure drop through blood vessels, and mass transfer of dissolved gases, chemicals and hormones.

The following section will provide a general overview of the anatomy, physiology, histology and pathology of the heart. It will aid in improving the understanding of how the heart functions on a cellular level, and what intrinsic and extrinsic factors affect its performance.

2.2.1 Heart Structure and Anatomy

The structure of the heart is comprised of several layers as shown in Figure 2.1. The outer layer is a fibrous membrane named the pericardium, and the inner layer is the heart wall. A narrow layer of pericardial fluid resides in the pericardial cavity in between these two layers that provides lubrication for the heart as it pumps (Carola *et al.*, 1992).

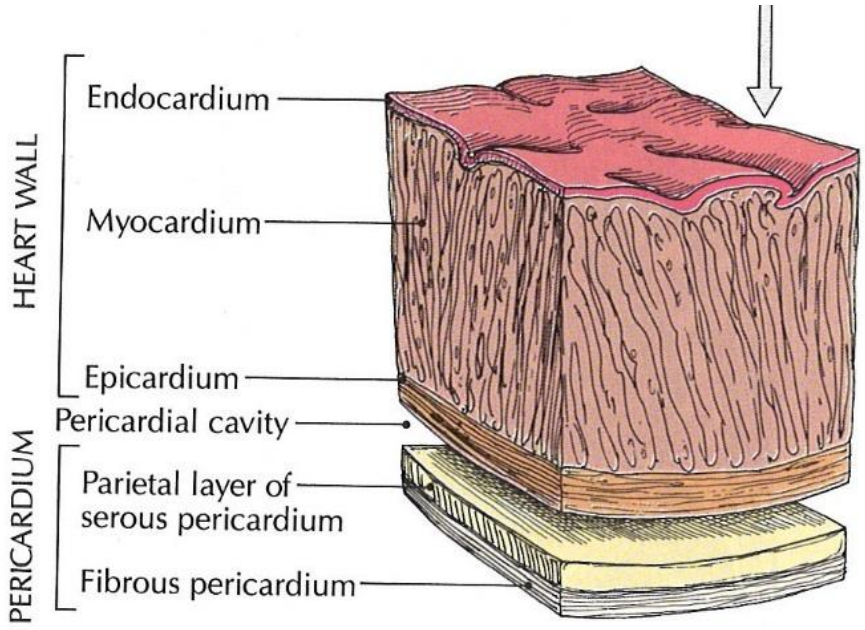

Figure 2.1 – Layers of the heart wall (Carola *et al.*, 1992).

The thick inner wall of the heart is the myocardium which is mostly comprised of cardiac muscle cells known as cardiomyocytes (NCBI, 2009). The myocardium contracts and provides the necessary pressure to pump blood from the heart. It is lined with a thin layer of squamous endothelial cells called the endocardium, which regulates myocardium contraction (Hsieh *et al.*, 2006). Blood that is pumped through the heart does not exchange material through the walls of the heart to the myocardial cells, instead blood is supplied through coronary arteries in the epicardium which branch off from the aorta (Iskandrian and Segal, 1979). Approximately 5% of the blood pumped by the heart is used for its own muscle tissue (Carola *et al.*, 1992).

2.2.2 Heart Histology

Cardiac Skeleton

At its core the heart is comprised of fibrous connective tissue providing sites of attachment for the valves and cardiac muscles, and gives overall structure to the heart (Zhu, 2015). A decellularised rat heart is shown in Figure 2.2 (Tandon and Joachim, 2014). The connected muscle tissue is arranged such that a wringing motion is induced when the ventricles contract, allowing a more efficient expulsion of blood (Seeley *et al.*, 2000).

Figure 2.2 – Decellularised human heart (Tandon and Joachim, 2014).

The Myocardium

The myocardium (cardiac muscle) comprises of cardiomyocytes, smooth muscle cells, fibroblasts and cardiac pacemaker cells (Xin *et al.*, 2013). It is responsible for the synchronised beating of the heart that facilitates blood flow. Cardiac, skeletal and smooth muscle cells are the three main type of muscle in the human body (NCBI, 2011). The myocardium is comprised of basic muscle units (sarcomeres) which contain thick myosin and thin actin filaments, and are joined end to end by intercalated discs with adjacent gap junctions (Widmaier *et al.*, 2006). Intercalated discs allow the connected cells to function as one tissue, allowing the synchronised contraction of the myocardium (Hill, 2016). The myosin and actin filaments are contractile proteins organised into an array which enables muscle contraction (Leger *et al.*, 1975). Gap junctions provide a connection between the cytoplasm of two adjacent cells, and allow the efficient transfer of signalling between cells for muscle contraction (Kanno and Saffitz, 2001).

Cardiomyocytes

Cardiomyocytes (also known as myocardiocytes or cardiac muscle cells) comprise the majority (56%) of the heart myocardium (Banerjee *et al.*, 2007), and are built from several muscle fibres (myofibrils) joined by a network of sarcoplasmic reticulum, encompassed in a plasma membrane (sarcolemma) (Tomanek and Runyan, 2012) and contain high quantities of mitochondria, as shown Figure 2.3 (Blausen, 2014).

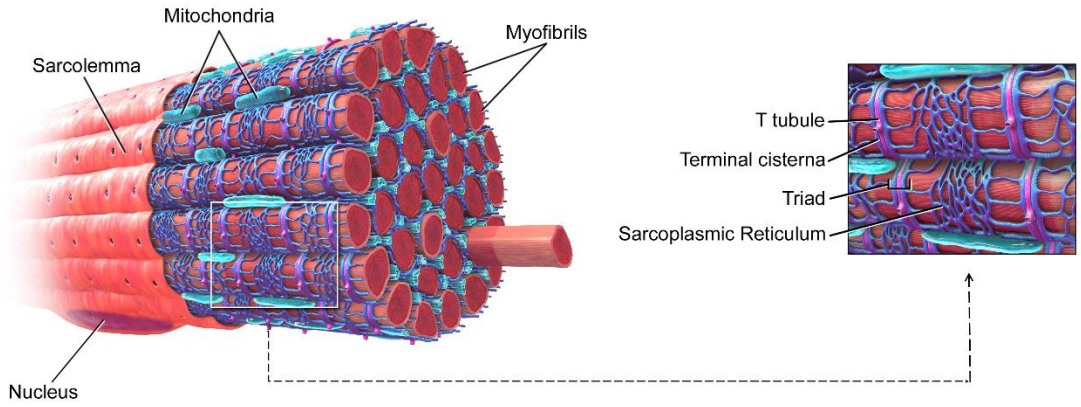

Figure 2.3 – The structure of a cardiomyocyte (Blausen, 2014).

The sarcolemma controls diffusion between the ECM and the cell, and contains proteins to aid electrical signalling between cells (Walker and Spinale, 1999). The sarcoplasmic reticulum is used as a storage area for calcium ions and pumps these ions around the cell to facilitate electrical signalling (Diaz *et al.*, 2005). Mitochondria are organelles that participate in the chemical production of energy by making adenosine triphosphate (ATP) molecules via cellular respiration (Lemieux and Hoppel, 2009). Mitochondria comprise 36% of cardiomyocyte volume due to the increased energy demand required for muscle contraction, compared to 2% in skeletal muscle cells (Carola *et al.*, 1992).

2.2.3 Quantifying Heart Disease

Heart disease usually results from lifestyle choices such as poor diet, smoking or lack of exercise; with subsequent angina or heart attack a result of insufficient oxygen reaching the cardiomyocytes in the heart. Data collected by physicians can provide insight into the performance of the heart, and indicate if enough oxygen is being provided to heart tissue (Libonati *et al.*, 1999).

Blood pressure is typically expressed as systolic pressure (ventricles contracting) over diastolic pressure (ventricles filling), for example 180 over 110, each with units of mmHg. An individual with these blood pressure readings is categorised as having a ‘hypertensive crisis’ and is in need of immediate medical attention (AHA, 2016). Other negative factors are a high pulse and high left ventricular end-diastolic pressure (LVEDP), which can lead to undesirably

low diastolic time (Salem *et al.*, 2006). The pressure of blood entering the coronary arteries is calculated as the difference between diastolic pressure and LVEDP.

Utilising these parameters, a value called the endocardial viability ratio (EVR) can be calculated, the value of which illustrates if the heart tissue is receiving enough oxygen as a result of the blood flow through the coronary arteries, which is dependent on overall heart health. It is the ratio of the diastolic pressure time index (the product of coronary pressure and diastolic time), and the tension time index (the product of systolic pressure and systolic time). A value of 1 or more characterises a 'normal' healthy value, and a value less than 0.8 associated with subendocardial ischemia (Ramanathan and Skinner, 2005). Typical values for a healthy and unhealthy individuals are shown in Table 2.1.

Table 2.1 – Parameters used by clinicians to characterise heart health.

Parameter	Serious Heart Disease	Healthy Heart
Systolic Pressure (mmHg)	180	105
Diastolic Pressure (mmHg)	110	70
Heart Rate (beats per min)	120	80
Left Ventricular End Diastolic Pressure (mmHg)	15	8
Coronary Perfusion Pressure (mmHg)	95	62
Heart Beat Duration (s)	0.50	0.75
Systolic Time (s)	0.20	0.20
Diastolic Time (s)	0.30	0.55
Diastolic Pressure Time Index (mmHg.s)	28.5	34.1
Tension time index (mmHg.s)	36.0	21.0
Endocardial Viability Ratio (-)	**0.79**	**1.62**

These values are useful to clinicians for characterising a patient's condition, but do not provide quantifiable values for a required blood oxygen content for normal heart function. However, by knowing the quantity of oxygen in blood, as well as blood flow rate through the coronary arteries, the quantity of oxygen the heart requires can be calculated.

An average healthy heart beats at 80 bpm, pumping 95 mL of blood per beat for a total of 7.6 L per minute (Maceira *et al.*, 2006). Approximately 5% of this is required by the heart itself to maintain its functionality (Carola *et al.*, 1992), therefore a healthy heart will utilise 380 mL/min of blood. In patients with a partial blockage of the coronary arteries this is reduced to 290 ± 60 mL/min, and in those with a significant blockage blood flow rate can be further inhibited to 165 ± 30 mL/min (Zafar *et al.*, 2014). At these flow rates the amount of oxygen provided can be calculated by taking into account the density of the blood, the amount of haemoglobin in the blood and the number of oxygen molecules bound to the haemoglobin. As

the left ventricle is fed newly oxygenated blood directly from the lungs, and the coronary arteries are served first after expulsion into the aorta, the oxygen content of blood passing through coronary arteries is assumed to be fully oxygenated at 20.4% (AnaesthesiaUK, 2005) or 9.87 µmol/mL assuming a total of 4.7 L of blood in an average human body. The rate of oxygen consumption has been identified as 5.3 µmol/min.g_{heart} in some studies (Beard, 2006) and total oxygen consumption is dependent on the mass of the heart, which is 300 g on average (Shier *et al.*, 1996). A mass balance on oxygen in heart tissue is shown in Table 2.2

Table 2.2 – Mass balance of oxygen within heart tissue.

Property		Healthy Heart	Partial Block-age(s)	Major Block-age(s)	Source(s)
O_2 In	Coronary arteries flow rate (mL/min)	380	290	165	Calculated
	Density of Blood (g/mL)	1.06			Cutnell *et al.* (1995)
	Coronary arteries flow rate (g/min)	403	307	175	Calculated
	Haemoglobin proportion in blood (%)	15%			Klabunde (2014)
	Haemoglobin molecular mass (g/mol)	64,450			Van Beekvelt *et al.* (2001)
	Haemoglobin flow rate (mol/min)	9.37E-04	7.15E-04	4.07E-04	Calculated
	Number of O_2 per Haemoglobin (-)	4			Costanzo (2007)
	O_2 flow rate (mol/min)	3.75E-03	2.86E-03	1.63E-03	Calculated
	O_2 flow rate (µmol/min)	3,750	2,862	1,628	Calculated
	Entering O_2 content in blood (%)	20.4%			AnaesthesiaUK (2005)
O_2 Used	Consumption rate (µmol/min.g_{heart})	5.3			Beard (2006)
	Average mass of human heart (g)	300	300	300	Shier *et al.* (1996)
	Consumption rate (µmol/min)	1,590	1,590	1,590	Calculated
O_2 Out	O_2 flow rate (µmol/min)	2,160	1,272	38	Calculated
	Extraction rate (%)	42%	56%	98%	Calculated
	Exiting O_2 content in blood (%)	12%	9%	1%	Calculated

From Table 2.2 it can be seen that a normal heart with no blockages will extract 42% of the available oxygen for normal resting function. This is larger in hearts with blockages in their coronary arteries as the available flow rate of oxygenated blood coming in has been reduced. Table 2.2 is a simplification of oxygen consumption. In reality diseased hearts will compensate by developing new heart muscle to increase the stroke volume, but this increases the heart's mass and thus again increases its oxygen requirements, which is not sustainable (Pai, 2016). However, this analysis has shown the required rate of oxygen required for normal heart operation (3,751 µmol/min), which is important when emulating *in vivo* conditions *ex vivo*.

2.3 HEART TISSUE ENGINEERING

2.3.1 Cells with Clinical Applications

One of the main symptoms of heart disease is a heart attack, which occurs when blood flow is limited to the heart tissue, which in turn limits the amount of oxygen available to cardiomyocytes, which subsequently die. This is a myocardial infarction, which damages the tissue in the left ventricle, reducing its ability to pump blood. The size of the infarct is dependent on the duration of low oxygen (ischemic) conditions and is typically quantified as a percentage of the available left ventricle area, increasing from 21% ± 13% at less than 3 hours of ischemic conditions to 77% ± 10% at greater than 9 hours (Hasche *et al.*, 1995). Clinicians typically quantify the severity of the infarction by stating the percentage of available surface that has been damaged. Presumably this is because of the heart's contractive nature causing the actual value of internal surface area to change as the heart beats.

The health of the left ventricle is primarily characterised by its ejection fraction (LVEF), which is 67% ± 5% in a healthy human heart (Maceira *et al.*, 2006). Studies have shown that patients who have suffered acute myocardial infarction have a lower LVEF ranging from 31% ± 6% (Sjoblom *et al.*, 2014), 48% ± 7% (Nijland *et al.*, 2002) or 52% ± 12% (Ndrepepa *et al.*, 2007)) depending on the severity.

Native cardiomyocytes have a remarkably low rate of turnover, with an annual renewal of only 1% in a healthy 20 year old human, decreasing with age to 0.3% at age 75 (Bergmann *et al.*, 2009). Cell therapies seek to facilitate accelerated tissue renewal by introducing a new population of cells to repair the infarcted tissue and improve heart LVEF. Human clinical trials traditionally administer somatic muscle cells, angiogenic cells and stem cell derived myocytes at doses ranging between 50-800 million cells (Sanganalmath and Bolli, 2013). These studies do not quantify cell dose for a specific 'infarct area', with many focusing on the improvement of heart functionality such as stroke volume and LVEF, and not directly characterising the reduction in the infarct area (Sanganalmath and Bolli, 2013).

The introduction of cell therapies to infarcted regions of the heart promotes myocardial repair by releasing signals to the surrounding tissue, which then initiate a number of mechanisms that regenerate the damaged areas. These include activation and proliferation of endogenous cardiac stem cells (Tang *et al.*, 2010), the formation of microvascular networks to enable blood flow (Jujo *et al.*, 2008), the inhibition of native cardiomyocyte apoptosis (Bonaros *et al.*, 2006), the inhibition of heart hypertrophy (Farahmand *et al.*, 2008) and the remodelling of the ECM (Rota *et al.*, 2008). Essentially, the administration and engraftment of living cells can kick-start a chain of events that can lead to improved heart function, with higher cell doses showing improved effectiveness (Menasché *et al.*, 2008), (Schuleri *et al.*, 2009).

Somatic Muscle Cells

Somatic cells are a classification for cells that make up the internal organs, muscle, bone and skin in the body. Somatic muscle cells are a subcategory which focuses on the cells that make up muscles and connective tissue in the body (Chen *et al.*, 2008).

Foetal Cardiomyocytes

Foetal cardiomyocytes share similar properties with adult cardiomyocytes whilst maintaining a greater degree of proliferation and *in vivo* survival. Studies in rat models show foetal and adult cardiomyocytes grafted into normal and damaged myocardium behave differently, with adult cells not surviving the grafting procedure and foetal cells proliferating in the host tissue (Reinecke *et al.*, 1999). Foetal cells formed gap junctions and intercalated disks to the host myocardium, and grew in volume over an 8 week period (Reinecke *et al.*, 1999). Other studies suggest that nearly half of the implanted foetal cells die off one hour after implantation, with 15% remaining after 12 weeks. These cells were shown to be 25% smaller than the host myocardium, which is indicative of arrested development (Muller-Ehmsen *et al.*, 2002). In another study, less than 2% of the initial inoculum of neonatal cardiomyocytes survived past 30 minutes in the host tissue, with authors citing that cells died from irreversible ischemic injury and apoptosis (Zhang *et al.*, 2001). While the concept of foetal cardiomyocyte replacement cell therapy was initially promising, an insufficient quantity of viable replacement tissue is formed to heal a sufficient area of infarcted heart tissue; and as the cells were from a donor, an immunosuppressant was also required (Chen *et al.*, 2008).

Skeletal Myoblasts

Skeletal myoblasts are progenitor cells that give rise to skeletal muscle fibres (Seeley *et al.*, 2000) and originate from myosatellite cells found in healthy, mature muscle tissue. Myosatellite cells activate when muscle damage is detected, triggering their differentiation into myoblasts. These can then attach to the damaged muscle fibres or form new fibres (Kadi *et al.*, 2004). Skeletal myoblasts possess many of the same properties as cardiomyocytes and can be harvested from the patient to allow an autologous transplant of cells. This eliminates the problem of tissue rejection from the patient's immune response. They are also able to withstand ischemic conditions better than other types of cells, and pose no risk of tumorigenicity when expanded in high concentrations (Menasche, 2005). Unfortunately in most cases skeletal myoblasts do not change into a cardiomyocyte phenotype when placed into heart tissue. Gap junctions do not form in myoblasts, thus electromechanical connections cannot be formed between the host tissue and the implanted cells (Rubart *et al.*, 2004). Despite this, in animal models the pumping efficiency of the left ventricle was improved after treatment of infarcted host tissue with skeletal myoblasts (Scorsin *et al.*, 2000), and soon after the method was accepted for phase I clinical trials. A four year follow up study on one of these

trials heralded it as a success (Dib *et al.*, 2005), however fundamental flaws with the experimental method of the trial such as not being randomised, inconsistent cell transplantation methodology, and the procedure occurring alongside a standard coronary bypass surgery cast doubt onto the effectiveness of this cell therapy alone (Caspi and Gepstein, 2006). Another trial also displayed a high incidence of patients displaying arrhythmia after treatment (Menasche *et al.*, 2003).

Angiogenic Cells

Angiogenic cells contribute to the formation of new blood vessels from pre-existing vessels (angiogenesis). Angiogenesis is dependent on the presence of vascular endothelial growth factor A (VEGF-A) released from tissues in hypoxic conditions and the metabolic activity of the patient (Adair, 2010). Angiogenesis usually occurs at the proliferative phase of the wound healing process where 'sprouts' of endothelial cells grow towards tissue expressing VEGF-A. In the context of tissue engineering, it is important that after a cell therapy has been administered to a patient the new graft has an adequate blood supply so that the implanted cells can successfully assimilate into the existing heart structure.

Fibroblasts

Fibroblasts are a vital component of the ECM, helping to form collagens, glycoproteins and elastins. They are used in the wound healing process to make new connective tissue (granulation tissue). Fibroblasts enter the wound site during the proliferative phase of wound healing at the same time as angiogenesis is initiated in the wound area (Falanga, 2005). Whole 3D scaffolds with fibroblast culture have shown to stimulate angiogenesis and improve heart wall blood flow in an infarct region of the heart in animal models (Kellar *et al.*, 2001). However, subsequent studies have shown that this does not improve left ventricle pump ejection efficiency or help in left ventricle remodelling (Lancaster *et al.*, 2010). Remodelling has been seen to reverse in one case (Thai *et al.*, 2009)

Endothelial Progenitor Cells

Endothelial Progenitor Cells (EPCs) are precursor cells that can differentiate into endothelial cells. They aid vascular regeneration by forming the lining of blood vessels and by secreting other angiogenic factors (Kawamoto *et al.*, 2011). They are sourced from bone marrow and peripheral blood (Urbich and Dimmeler, 2004), and make up less than 1% and 0.01% of these sources respectively (Smadja *et al.*, 2007). EPCs in peripheral blood are in such low abundance in the blood stream that over 10 L is required to produce a sufficient quantity of EPCs to achieve angiogenesis in one patient (Iwaguro and Asahara, 2005). EPCs are identified by their expression of a combination of CD133, CD34 and KDR markers, however there is some dispute over this (Smadja *et al.*, 2007). Studies have indicated that the inoculation of

EPCs into the bloodstream improve myocardial performance in animal models suffering from induced infarcted heart tissue (Werner *et al.*, 2005). EPCs have been attached to a collagen matrix and were shown to improve cardiac function when used to treat myocardial infarction in rodent hearts (Ahmadi *et al.*, 2010); however there is concern that sufficient numbers of cells cannot be cultured for human treatments, and that long term culture may cause modifications to the cell's phenotype (Eggermann *et al.*, 2003).

Stem Cell Derived Myocytes

Stem cells have the ability to differentiate into many different types of cell, including cardiomyocytes. This process can be controlled, allowing a stem cell to selectively differentiate into whatever cell type is desired simply by modifying the conditions the stem cell is subjected to (Thomson *et al.*, 1998). They can be sourced from several different places, including the patient's own tissue. All cells have surface molecules which can act as ligands that allow attachment, or can play a role in cell signalling. Cell populations can be defined by determining if they possess or lack these markers using a '+' or '-' symbol respectively. Stem cells can be quantified from other cells in this way by looking for these characteristic protein molecules on their surfaces. For example the researchers at Bristol Royal Infirmary consider MSCs to be positive for CD90, CD73, and CD105 and negative for CD45, CD34, CD14 or CD11b, CD79α or CD19 and HLA-DR surface markers; however in many published articles there is not a consensus as to what combinations of markers guarantee a certain cell type.

Stem cells are classified by the differentiation potential of the stem cell in question (potency), of which there are five subcategories shown in Table 2.3 (Ilic and Polak, 2011); or by their origin - divided into embryonic, foetal, perinatal and adult stem cells, shown in Table 2.4. Ethical and religious arguments are unavoidable when discussing the sourcing of embryonic and foetal stem cells, and have affected scientific policy in some countries (Mazzaschi, 2015). However, the recovery and storage of perinatal stem cells after pregnancy as an insurance for the future health of a child is increasing in popularity (Searcey, 2014).

Table 2.3 – Classification of stem cells based on their differentiation potential.

Potency	Differentiation Potential	Cell Example
Totipotent	Embryonic and extra-embryonic tissue	Fertilised ovum
Pluripotent	All tissues and organs	Embryonic stem cell
Multipotent	Restricted to the associated cell family	Mesenchymal stem cell
Oligopotent	Restricted to a few cell families	Hematopoietic stem cell
Unipotent	Restricted to one cell type	Muscle stem cell

Table 2.4 – Classification of stem cells based on their origin.

Stem Cell Type	Source	Potency
Embryonic	Blastocyst stage of embryo (5-6 days)	Pluripotent
Foetal	Terminated pregnancies	Pluripotent
Perinatal	Amniotic fluid, placenta and umbilical cord	Multipotent
Adult	Bone Marrow, peripheral blood and adipose	Oligopotent or Unipotent

Adult stem cells are present in all organs of the body and are used for tissue regeneration and cell renewal in normal bodily operations. They can be isolated from some areas of the body such as the bone marrow, blood and adipose (fat) tissue; however it is much more difficult and intrusive to obtain cells from an internal organ. Because of this, research is being undertaken to see how to encourage adult stem cells sourced from one tissue to be used in repairing a different tissue (Ilic and Polak, 2011). Some of the stem cells mentioned in this section will be expanded upon in regards to their use in cardiac tissue engineering.

Hematopoietic Stem Cells

Hematopoietic stem cells are progenitor cells that give rise to all blood cells, and are sourced from bone marrow, umbilical cord blood and peripheral blood. They are also part of the revascularisation process in wound healing. In conjunction with EPCs they have been shown to improve heart function in ischemic heart disease patients (Caspi and Gepstein, 2006), however HSCs cannot directly differentiate into cardiomyocytes (Murry *et al.*, 2004).

Native Cardiac Progenitor Cells

As previously stated, cardiomyocytes have a small degree of self-renewal *in vivo* (Bergmann *et al., 2009)* but this occurs at too low a rate to be useful in regenerating badly damaged heart tissue. Recent clinical studies in humans have shown improvements in cardiac regeneration using autologous cardiac progenitor cells isolated from heart biopsies, expanded *in vitro*, then injected into the target tissue during surgery (Chugh *et al.*, 2012). Cells sourced in a similar way, but suspended on spherical beads, showed reduction in cardiac scarring after administration in human heart tissue (Makkar *et al.*, 2012). However there is some debate as to whether or not these cells were actually cardiomyocytes, despite the author's claims (Mummery and Lee, 2013).

Bone Marrow Derived Mesenchymal Stem Cells

Mesenchymal stem cells are multipotent, and as such are restricted to differentiating within specific cell families. In this case MSCs differentiate into connective tissue such as bone, cartilage and adipose. MSCs from bone marrow has been observed differentiating into cardiomyocytes both *in vitro* and *in vivo*, with human MSCs transplanted into infarcted mouse and pig heart tissue showing spontaneous improvement in heart function (Behfar *et al.*, 2010;

Williams *et al.*, 2013). Their ability to not stimulate an immune response indicates a potential for the cells to be autotransplanted or allotransplanted in patients. Some experiments have shown that their presence delays immune responses by inhibiting the formation of T-lymphocytes, indicating that MSCs possess an intrinsic immunosuppressive property (Le Blanc, 2003). A meta-analysis of bone marrow stem cell transplants in 999 patients over 18 studies concluded with 95% confidence that only an average increase of 3.66% in left ventricular ejection fraction (LVEF) was established (Abdel-Latif *et al.*, 2007).

Adipose Derived Mesenchymal Stem Cells

MSCs can also be found within human adipose tissue. They are contained within the stromal vascular fraction of adipose tissue, and can be isolated using various separation processes. Depending on its location in the body, adipose tissue can be removed via liposuction, a low cost and low risk procedure. It has been proposed that adipose MSCs are superior to bone marrow MSCs in regards to their angiogenic ability when responding to ischemia in mouse leg muscle (Kim *et al.*, 2007). There are mixed results from studies using these cells, with MSCs derived from rat epididymis adipose tissue aiding treatment of cardiomyopathy (Lin *et al.*, 2010) and those derived from rat skin promoting angiogenesis in heart tissue (Schenke-Layland *et al.*, 2009); but in other instances have shown no disposition to take to the host heart tissue (van der Bogt *et al.*, 2009). Some data suggests that adipose tissue can spontaneously differentiate into functional cardiomyocyte cells without the need for chemical intervention (Choi *et al.*, 2010). A majority of studies derive adipose derived MSCs from rat groin tissue (Lin *et al.*, 2010; Diaz-Herraez *et al.*, 2013), rat subcutaneous skin tissue (Schenke-Layland *et al.*, 2009), or human abdomen fat (Kim *et al.*, 2013; Yang *et al.*, 2013a) for use in animal heart models.

Studies into isolation of adipose derived MSCs from around the heart itself is a new avenue of investigation which has not yet been fully explored, primarily because of the invasive methods of obtaining the tissue and the requirement for cell expansion to clinically applicable quantities. No studies have investigated a human autographed transplant; however an allograft transplant is currently being set up for human clinical trials (Bayes-Genis *et al.*, 2013). Stem cells derived from adipose tissue provide higher yields compared with those derived from bone marrow and amniotic fluid (Kim and Heo, 2014). It is believed that stem cells isolated from adipose tissue surrounding the heart will be more likely to differentiate into cardiomyocytes (Ascione, 2013) making this cell type unique out of those described in this section, and suitable for further investigation.

MSCs extracted from abdomen adipose tissue yield around 2,000,000 cells per 250 mL of lipoaspirate using a standard isolation technique (Francis *et al.*, 2010), however the volume of

epicardial adipose tissue around the heart is only 101.6 ± 39.8 mL in patients suffering from heart disease (Wu *et al.*, 2016). This equates to a total extraction of approximately 812,800 ± 318,400 cells from a patient. As doses of traditional cell therapies into the human heart myocardium typically start at 50 million cells (Sanganalmath and Bolli, 2013), it is clear that the quantity of cells extracted from a patient's heart must be expanded in order to be used as a cell therapy.

2.3.2 Cell Expansion

Once a suitable cell type has been identified to be therapeutically relevant it must be expanded to a clinically applicable quantity for use as a successful cell therapy. As mentioned in the previous section a starting population of 812,800 ± 318,400 MSCs must be expanded to a dose of 50 million cells. This represents 5.9 ± 0.5 population doublings or an increase in initial cell number by 61 ± 17 times. There are many different technologies that can be used to culture cells, from simple flat flasks to engineered perfused bioreactors. The advantages and drawbacks of these devices are described in this section.

Traditional Bioreactors for Cell Culture

Microbiologists would rarely describe their cell culture flasks as bioreactors, but from a chemical engineering perspective T-flasks and tissue culture well plates would be static semi-batch bioreactor systems. Examples of such flasks are shown in Figure 2.4. This is defined as a system that operates with either batch or continuous inputs of reactants and/or outputs of undesired products. Taking the T-flask as an example, it is initially seeded with a batch of cells in a solution of cell media, and as the cells grow they utilise oxygen as a reactant and provide carbon dioxide as a waste product, which can be defined as a continuous input and output respectively. The cells consume the nutrients in the media over time, after which the cells must be moved into a new T-flask as a batch and given fresh media.

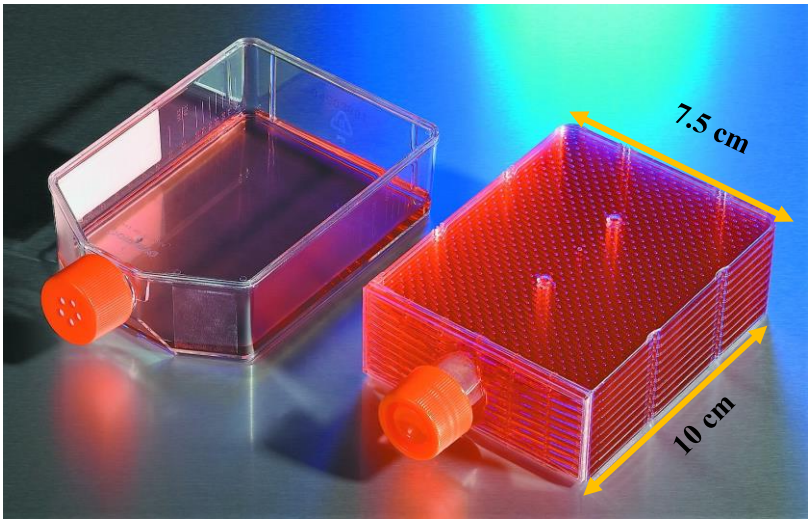

Figure 2.4 – A typical T-75 flask and a stackable T-75 flask manufactured by Corning.

The available specific area for cells that can be cultured on a traditional T-75 tissue culture flask is approximately 300 cm^2/L. This can be improved with multi-layered flasks which increases the overall surface area by a factor of ten, for the same available flask volume. One model shown in Figure 2.4 has a specific area of 3,000 cm^2/L, however these stacked designs still have the same limitations as single flask models. These flasks only encourage 2D monolayer cell growth, whereas 3D cell culture offered by alternative bioreactors allow improved cell-cell interactions that lead to cells which resemble *in vivo* architecture (Edmondson *et al.*, 2014). Flat flasks do have a use in the initial expansion of cells to sufficient quantities before their passage into other systems that encourage 3D cell culture.

Stirred Tank Bioreactors

This bioreactor type can be operated as batch, semi batch or continuous configuration, and is usually characterised by the dynamic mixing from a mechanical force. This includes using a rotating impeller or magnetic stirrer to mix the bioreactor contents from within; or placing the reactor onto rollers to provide an external source for the mixing. The dynamic agitation of the bioreactor contents mitigates the presence of concentration gradients, allowing a well-mixed homogeneous system. Any mechanical force applied to the bioreactor must be strong enough so that the contents become well mixed, however excessive forces could cause cells to detach from their solid support. For this reason impellers are not generally used for cell culture as their edges could contact the cells. External forces typically provide a more uniform flow.

Spinning Flask

A spinning flask bioreactor is a static flask with an internal stirring metal bar and ports on its lid for the addition and removal of cells, media and gases. An image of this bioreactor design is shown in Figure 2.5 (Techne, 2012). MSCs can be seeded onto micro-carriers that remain in suspension within the media. Spinning flasks have been used for MSC growth and differentiation in several studies showing improved rates of cell growth and increases in final cell number over monolayer culturing in T-flasks (Wang *et al.*, 2009; Boo *et al.*, 2011; Elseberg *et al.*, 2012; Rafiq *et al.*, 2013). Metabolism of porcine bone marrow (BM) derived MSCs has been shown to be unaffected when grown in a spinning flask, showing comparable energy usage to BM-MSCs grown in T-flasks, but with a 40% increase in growth rate (Ferrari *et al.*, 2014). Initial rates of cell attachment onto micro-carriers can be as high at 63% with improved rates occurring at a high stirring speed delivered intermittently (100 rotations per minute (RPM) for 3 minutes, 0 RPM for 27 mins) for shorter durations (4 hours) and lower bovine serum concentrations (0%) (Yuan *et al.*, 2014). Spinning flask bioreactors are more complex than monolayer cultures because of the added factor of micro-carrier properties. Micro-carriers with a greater surface area per gram (Ferrari *et al.*, 2014) and larger pore sizes (Mygind *et al.*, 2007) yield larger growth rates and increased cell number after 14 days.

Figure 2.5 – Spinning flask culture system, 125 mL – 5 L, manufactured by Techne.

One of the drawbacks of the spinning flask bioreactor is cell aggregation which can lead to sub-populations of MSCs with unwanted heterogeneity. This can be reduced by adding additional carriers free of cells to the bioreactor for the excess cells to migrate to (Ferrari *et al.*, 2012). In one study variation of stirring rates in the bioreactor (25 RPM and 75 RPM) had no effect on growth kinetics of porcine BM-MSCs over 14 days, showing the same growth curve trends and identical growth rates (Ferrari *et al.*, 2012).

Rotating Wall Bioreactor

A rotating-wall bioreactor, shown in Figure 2.6 (Synthecon, 2015), also known as a slow turning lateral vessel (STLV), is a cylindrical flask that rotates about its central radial point at a radial velocity that keeps the cells or cell carriers suspended in a state of free fall within the bioreactor. The bioreactor is completely filled with media, with no gas–liquid surface interface available; however in some designs oxygen can be applied to the system via the rotating central cylinder. The radial velocity of the bioreactor can be set to provide a radial velocity to the cell media that is equal and opposite to the sedimentation rate of the cells/cell carriers, essentially fixing them in the same space. This flow regime around the particles reduces the thickness of the boundary layer surrounding the micro-carriers leading to a shorter diffusion distance for gas or nutrients to travel (Godara *et al.*, 2008). Some studies have shown that rotating wall bioreactors have improved MSC growth rates over static culture (Chen *et al.*, 2006; Song *et al.*, 2011), but others show worse performance in comparison to spinner flasks (Sikavitsas *et al.*, 2002; Wang *et al.*, 2009). These studies also show that spinner flasks are better for encouraging osteogenic and chondrogenic differentiation due to the mechanically active environment. One study has shown no appreciable difference in turnover rate between the static, stirring and rotating bioreactors (Frith *et al.*, 2010).

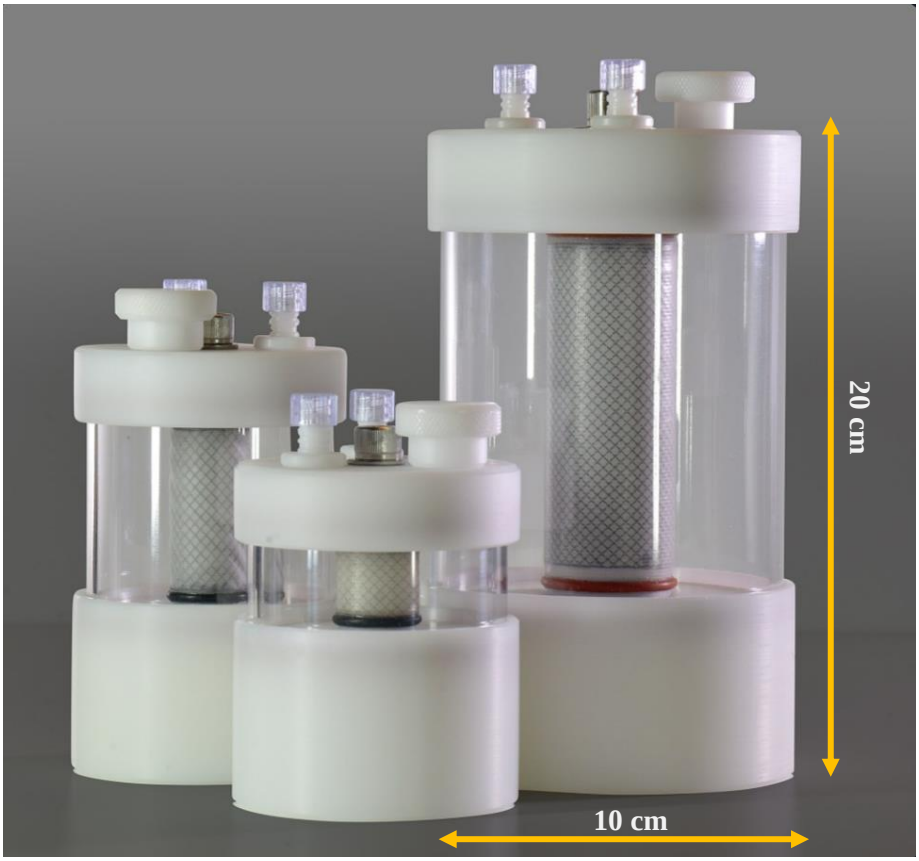

Figure 2.6 – Rotating wall bioreactors, 110 mL, 250 mL and 1 L, manufactured by Synthecon.

Differentiation of human ESCs into the cardiac phenotype using a STLV and a spinning flask has been achieved by applying hypoxic conditions as evidenced by expression of a number of cardiac genes (Niebruegge *et al.*, 2009). A STLV has been optimised to culture high levels of embryoid bodies, the intermediate between ESCs and specialised cell types, which then spontaneously differentiated into cardiomyocytes (Rungarunlert *et al.*, 2011).

Whilst the gentle shear conditions have led to the cultivation and differentiation of various cell types, rotating wall bioreactors are not well suited for culture within scaffolds as the low shear environment inhibits sufficient nutrient transport to cells seeded internally (Rauh *et al.*, 2011). This can be addressed by not operating the bioreactor as a STLV and simply rotating the bioreactor at a faster rate, however this can lead to collisions between scaffolds, causing damage and disruption of cell functions. Other disadvantages include poor scalability to larger volumes, and an increased complexity compared to other configurations (Schaffer *et al.*, 2012).

Wave Bioreactor

A sterile disposable bag is inoculated with cells and media and inflated with air. The bag is placed on a moving platform that induces waves at the gas-liquid interface, as shown in Figure 2.7 (GE-Healthcare, 2015). These waves facilitate a higher oxygen transfer than spinner flasks

(Godara *et al.*, 2008), is easily scalable up to 500 L (Schaffer *et al.*, 2012), and is compliable with good manufacturing practice (GMP) guidelines due to its low likelihood of contamination (Somerville *et al.*, 2012); however the bags are expensive, only have a single use, and monitoring and sampling the cells within the bag is difficult (Rodrigues *et al.*, 2011). Only a single instance of MSC expansion using a wave bioreactor was found, but did not offer empirical comparisons to other bioreactor types (Timmins *et al.*, 2012), however studies on HSCs show improvements in cell yield using this system (Hami *et al.*, 2004; Timmins *et al.*, 2009).

Figure 2.7 – A wave bioreactor manufactured by GE Healthcare.

Stirred tank bioreactor configurations have proven to be useful when attempting to grow a large quantity of cells in solution, but the final cell number when harvesting is still not enough for a one step cell expansion system for to reach a clinically applicable number of cells (Rafiq *et al.*, 2013). These bioreactors are sufficient for mixing bulk media in a system, however they have additional disadvantages such as the inability to regulate shear stress or manage oxygen, carbon dioxide and nutrient concentrations within the structure of the scaffolds, creating non homogeneous regions (Yeatts *et al.*, 2013).

Perfusion Bioreactors

These bioreactors are typically characterised by a recirculating media over cells attached to a firm surface. This flow ensures a continuous concentration gradient that encourages nutrient and waste exchange between the cells and bulk media. It also more closely emulates blood flow in an *in vivo* environment, leading to improved rates of cell growth compared to static systems.

Packed Bed Bioreactor

A packed bed (also known as fixed bed) reactor is a tubular shape, orientated vertically, and filled with macro-structured, reactive packing material, as shown in Figure 2.8 (Medorex, 2014). Packed beds facilitate excellent contact between a fluid and solid, typically catalysing reactions or removing impurities from fluid streams depending on the packing material and application. Packing is fixed in position with supporting plates so the bed does not move with the fluid flow. For use as a bioreactor, immobilised cells or enzymes are attached to the packing material, which can be made from glass, ceramic, plastic (Meuwly *et al.*, 2007), all of which vary in porosity and available internal surface area. Cultured cells are seeded within the packing material, to provide protection from the shear forces of the flowing liquid.

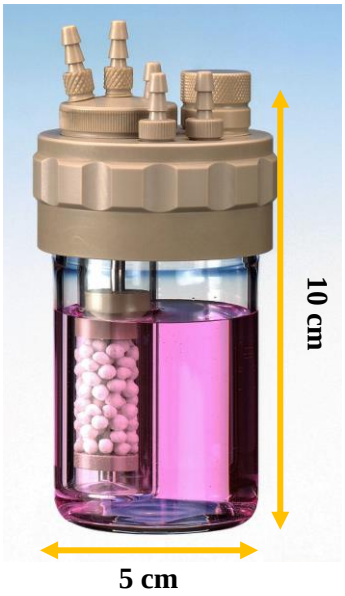

Figure 2.8 – A packed bed bioreactor manufactured by Medorex.

MSCs have been successfully grown in packed bed bioreactors, with a Fibra-Cel disks (Eppendorf) (Mizukami *et al.*, 2013; Tsai *et al.*, 2016), polystyrene pellets (Osiecki *et al.*, 2015) and glass beads (Weber *et al.*, 2010), as packing material. Single-use packed bed bioreactors are increasingly being used in lab scale mammalian cell production including for culturing MSCs (Kaiser *et al.*, 2015).

Problems inherent with packed bed bioreactors typically arise due to poor homogeneity of the bioreactor contents, with localised concentration gradients of nutrients and dissolved oxygen, however this issue is limited at bench-scales. They are also difficult to scale up due to the increasing pressure drop, require proper liquid distribution to avoid channelling, and direct sampling of cells is usually impossible without removal of the packing (Warnock *et al.*, 2005).

Fluidised Bed Bioreactor

Advantages of a fluidised bed are similar to those found in a packed bed. Good mixing ensures good mass transfer of nutrients and waste, and seeding within particles protects them from the shear forces that arise from the mixing. A fluidised bed has several improvements over a packed bed. Fluidisation removes the risk of channelling between particles, provides a lower risk of particle abrasion and subsequent cell damage, and the low gravity environment encourages proliferation as opposed to differentiation (Ellis *et al.*, 2005). Fluidised beds also require complex computational fluid dynamics modelling to determine optimum conditions for cell expansion (Benzeval *et al.*, 2012).

Comparisons with static controls show fluidised beds to be superior, with greater cell proliferation and distribution of murine MSCs on coral scaffolds for use as bone constructs (David *et al.*, 2011). Placental-derived human MSCs co-cultured with hepatoma-derived C3A cells seeded onto alginate microspheres have been grown in a fluidised bed system and showed increased urea secretion compared to a static control (Yang *et al.*, 2013b). However, in a direct comparison with a packed bed bioreactor, a fluidised bed performed worse at cultivating a co-culture of peripheral blood derived human hematopoietic stem cells and bone marrow derived stromal cells over a 2 week time course (Meissner *et al.*, 1999), with the author determining that the weak adherence between the two cell types causes detachment of the hematopoietic stem cells in the fluidised conditions.

Hollow Fibre Bioreactor

A hollow fibre bioreactor (HFB) consists of a bundle of hollow fibres enclosed in a cylindrical housing with openings at either end for tube side media flow and side ports for shell side media flow (Figure 2.9). Cells are typically attached to the external fibre surface, or within a hydrogel in the extra-capillary space between the fibres and the reactor housing. The fibres themselves are porous, allowing the bioreactor to act as a membrane for size exclusion of certain molecules or cellular products. Like all membranes HFBs can foul, but this is mitigated through good flow control and occasional back-flushing. HFBs allow for a much increased surface area to volume ratio over stirred bioreactors and other perfusion bioreactors, allowing for a greater number of cells to be cultured per unit reactor capacity. Good shear and mixing conditions are provided in a HFB, with convection through the fibres and diffusion within the porous matrix of the fibres available to provide good rates of oxygenation and nutrient uptake in seeded cells.

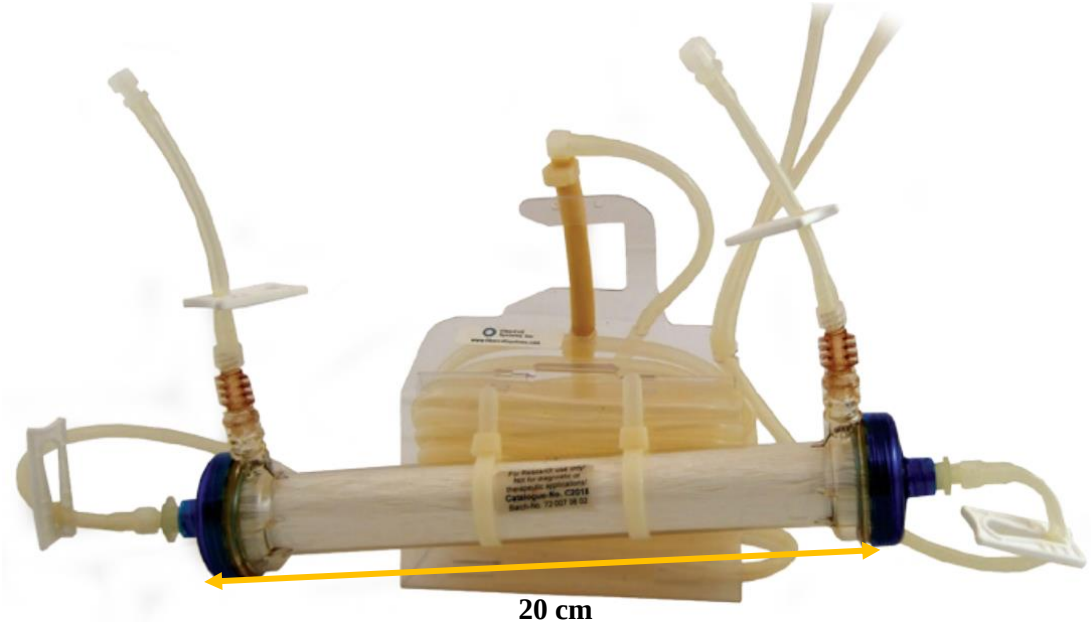

Figure 2.9 – A hollow fibre bioreactor system from Fibercell Systems.

HFBs have been utilised in commercial products for renal dialysis treatments as membranes to filter out proteins from blood. Other commercial products have been developed for the specific task of cell expansion (Spectrum-Labs, 2012; Terumo-BCT, 2012; FiberCell, 2014), with researchers using these systems yielding cells in greater number than other reactor types. In one study using the Quantum cell expansion system from Terumo, 5 million MSCs were seeded and expanded 20 fold over 13 days to 98 million MSCs (Nold *et al*. 2013). In a different study using the same HFB (2100 cm^2 surface area) but comparing it to equivalent static seeding in a T-flask (25 cm^2 surface area), data suggests that at identical seeding densities of MSCs (775 ± 251 cells/cm^2) after 6 days 122 million ± 49 million MSCs were harvested from the HFB and 748,000 ± 419,000 MSCs from a T-25 flask (Rojewski *et al.*, 2013). Whilst this is expected due to the increased available surface area, the harvesting density was 5,800 ± 2,300 MSCs/cm^2 in the HFB and 29,900 ± 16,700 MSCs/cm^2 in the flask, which, may indicate that an increase in culture time in the HFB may allow for further population doublings due to the additional availability of surface area within the HFB. The material the hollow fibres are made from is not indicated in this product.

A phenomenon known as Starling flow is also present in HFB. Higher upstream pressure can force media flowing within the fibre lumen out of the upstream section of the fibre into the ECS and then back through the fibre into the lumen downstream where the pressure is lower. This drives cells to the end of the hollow fibre and causes an inhomogeneous cell density on the hollow fibres (Godara *et al.*, 2008). Investigations on a bundle of 46 polypropylene hollow fibres of 330 μm inner diameter, 150 μm wall thickness and 0.1 μm maximal pore size with sheep BM-MSCs seeded in Matrigel in the ECS showed lower Starling flows in HFBs

(0.3 mL/min intraluminal flow) led to increased cell viability and improve rates of sheep BM-MSC attachment throughout the hollow fibre surface, but do not provide favourable conditions for MSC proliferation or differentiation; whereas high Starling flows (11 mL/min intraluminal flow) promote MSC proliferation, accelerate differentiation but yield dense 3D cell aggregates in the downstream section of the fibre (De Napoli *et al.*, 2011). However this effect is not as apparent in hollow fibres with lower permeability (Godara *et al.*, 2008).

Hollow fibres provide a great deal of flexibility for cell proliferation, with adjustable fibre permeability and bioreactor flow rates. Cells are most commonly attached to the external surface to take advantage of the increased surface area to volume ratio, low shear environment, and simple operation. While direct sampling of cells during operation is not achievable, and uniform seeding is often difficult, hollow fibre bioreactors provide the highest quantity of cells of all bioreactor types, which is imperative in order to produce a highly concentrated cell dose for cell therapies.

One major drawback of HFBs is the poor initial rates of cell attachment (Wung *et al.*, 2014). Seeding efficiencies of around 15% (Storm *et al.*, 2016), and 20% (Morgan *et al.*, 2007) have been reported, with authors requiring higher initial seeding densities compared to flat tissue culture plastic in order to obtain equivalent cell densities (Storm *et al.*, 2016). This is likely due to the curvature of hollow fibres providing a sub-optimal geometry for cells to easily attach to, instead rolling off the fibre or potentially 'missing' it entirely. This can also lead to poor distribution of the initial dose across the length of the hollow fibre (Ellis and Chaudhuri, 2007). No authors have sought to improve initial cell attachment rates of hollow fibres, despite the potential time saving benefits when growing a dose of cells for clinical purposes. A dynamic seeding regime which would offer cells several opportunities to attach, might offer improved rates of cell attachment, and should be investigated.

Comparing Bioreactors

A collection of data showing the growth of MSCs over 7 days in each bioreactor type is shown in Table 2.5, with average values for cell doubling, fold increase, growth rate and doubling time for each bioreactor type summarised in Table 2.6. These tables show that MSCs grown in hollow fibre bioreactors offer the quickest rate of growth, the shortest doubling times, and the greatest increase in cell number over 7 days. Hollow fibre bioreactors are typically seeded at much higher concentrations in part due to their increased available surface area for cell attachment, resulting in larger batches of MSCs compared to other systems. As speed of treatment may be critical in a medical environment, the hollow fibre bioreactor was chosen as the cell expansion device for this work.

Table 2.5 – MSC expansion data in various bioreactor types.

Bioreactor Type	Cell	Species	Concentration (cells/mL)		Cell Expansion Properties				Source
			Day 0	Day 7	Doublings	Fold Increase	Growth Rate ($days^{-1}$)	Doubling Time (days)	
Monolayer	MSC	Human	500,000	1,500,000	1.6	2.0	0.2	4.4	(Wang *et al.*, 2009)
	MSC	Human	20,000	380,000	4.2	18.0	0.4	1.6	(Elseberg *et al.*, 2012)
	MSC	Human	19,375	748,000	5.3	37.6	0.5	1.3	(Nold *et al.*, 2013)
Spinner Flask	MSC	Human	500,000	3,200,000	2.7	5.4	0.3	2.6	(Wang *et al.*, 2009)
	MSC	Lapine	121,000	221,000	0.9	0.8	0.1	8.1	(Boo *et al.*, 2011)
	MSC	Human	20,000	620,000	5.0	30.0	0.5	1.4	(Elseberg *et al.*, 2012)
Rotating Wall	MSC	Human	160,000	192,000	0.3	0.2	0.0	26.6	(Zhang *et al.*, 2010)
	MSC	Human	500,000	4,400,000	3.1	7.8	0.3	2.2	(Wang *et al.*, 2009)
Packed Bed	MSC	Human	160,000	1,600,000	3.3	9.0	0.3	2.1	(Osiecki *et al.*, 2015)
	MSC	Human	10,000,000	54,000,000	2.4	4.4	0.2	2.9	(Tsai *et al.*, 2016)
Fluidised Bed	C3H/10T1/2	Murine	300,000	1,100,000	1.9	2.7	0.2	3.7	(David *et al.*, 2011)
Hollow Fibre Bioreactor	PDC	Human	20,000,000	440,000,000	4.5	21.0	0.4	1.6	(Lambrechts *et al.*, 2016)
	MSC	Lapine	500,000	8,500,000	4.1	16.0	0.4	1.7	(Li *et al.*, 2016)
	MSC	Human	2,000,000	18,700,000	3.2	8.4	0.3	2.2	(Nold *et al.*, 2013)
	MSC	Human	1,627,500	122,000,000	6.2	74.0	0.6	1.1	(Rojewski *et al.*, 2013)
	MSC	Human	200,000	16,000,000	6.3	79.0	0.6	1.1	(Morgan *et al.*, 2007)

Table 2.6 - Average MSC expansion data for each bioreactor type.

Bioreactor Type	Cell Expansion Properties							
	Doublings		Fold Increase		Growth Rate ($days^{-1}$)		Doubling Time (days)	
	Av.	*SD*	Av.	*SD*	Av.	*SD*	Av.	*SD*
Monolayer	3.7	*1.9*	19.2	*17.8*	0.4	*0.2*	2.5	*1.7*
Spinner Flask	2.8	*2.0*	12.1	*15.7*	0.3	*0.2*	4.0	*3.5*
Rotating Wall	1.7	*2.0*	4.0	*5.4*	0.2	*0.2*	14.4	*17.2*
Packed Bed	2.9	*0.6*	6.7	*3.3*	0.3	*0.1*	2.5	*0.5*
Fluidised Bed	1.9	*0.0*	2.7	*0.0*	0.2	*0.0*	3.7	*0.0*
Hollow Fibre Bioreactor	**5.0**	***1.6***	**44.3**	***37.3***	**0.5**	***0.2***	**1.5**	***0.5***

Taking into account the maximum number of MSCs that can be extracted from around the human heart (812,800 ± 318,400), the expected rate of cell attachment within HFBs (20%) the quantity typically required for a therapeutic dose in a damaged human heart (50 million), and the average doubling time of MSCs in hollow fibre bioreactors from literature (1.5 ± 0.5 days); a hollow fibre bioreactor could grow the necessary number of cells in 12.6 ± 5.2 days. If 100% cell attachment can be obtained, this is reduced to 9.1 ± 4.0 days. Clearly, if rates of cell attachment on hollow fibres can be improved, this would reduce the amount of time taken to acquire the necessary cell dose, and would accelerate a patients treatment timetable.

2.3.3 Cell Delivery

Many of the research trials mentioned in Section 2.3.1 were utilising isolated cell suspensions which were directly injected into the damaged areas of the heart. This method of delivery has an advantage because it avoids an intrusive open heart surgery; however it can be difficult to be accurate when administering this treatment and a large number of the injected cells are often not retained at the wound site. To combat these issues, alternative delivery vectors have been investigated such as using a scaffold seeded with cells for grafting onto a specific area of damaged tissue. This section outlines traditional and engineered methods of cell delivery.

Traditional Cell Delivery Vectors

Traditional delivery vectors administer cells to a wound site using a syringe, a catheter or intravenously. It is a common theory among authors that MSCs will migrate to either their organ of origin, or to a site of damage in a tissue (Lee *et al.,* 2016). Traditional cell delivery methods take advantage of this homing behaviour by administering free floating cells into the patient. Studies utilising stem cells have consistently shown low rates of cell retention in the target tissue, independent of cell type, cell dose, and method of delivery. Typically over 90% of injected cells disappear from the wound site in the first few days, with less than 2% retained after 4 weeks, with high doses of cells required (starting from 50 million) in order to facilitate improvements in heart function (Sanganalmath and Bolli, 2013).

Intravenous Infusion

Intravenous (IV) infusion takes advantage of cell homing mechanisms to treat myocardial infarction. The cells are directly injected into a vein and are transported to the heart as shown in Figure 2.10. It is a simple and non-invasive procedure. A Phase I study (NCT00114452) dosing patients (n=53) with 0.5 – 5.0 million MSCs/kg within 10 days after a myocardial infarction showed improvement in pulmonary function, LVEF and reduced instances of tachycardia (Hare *et al.*, 2009).

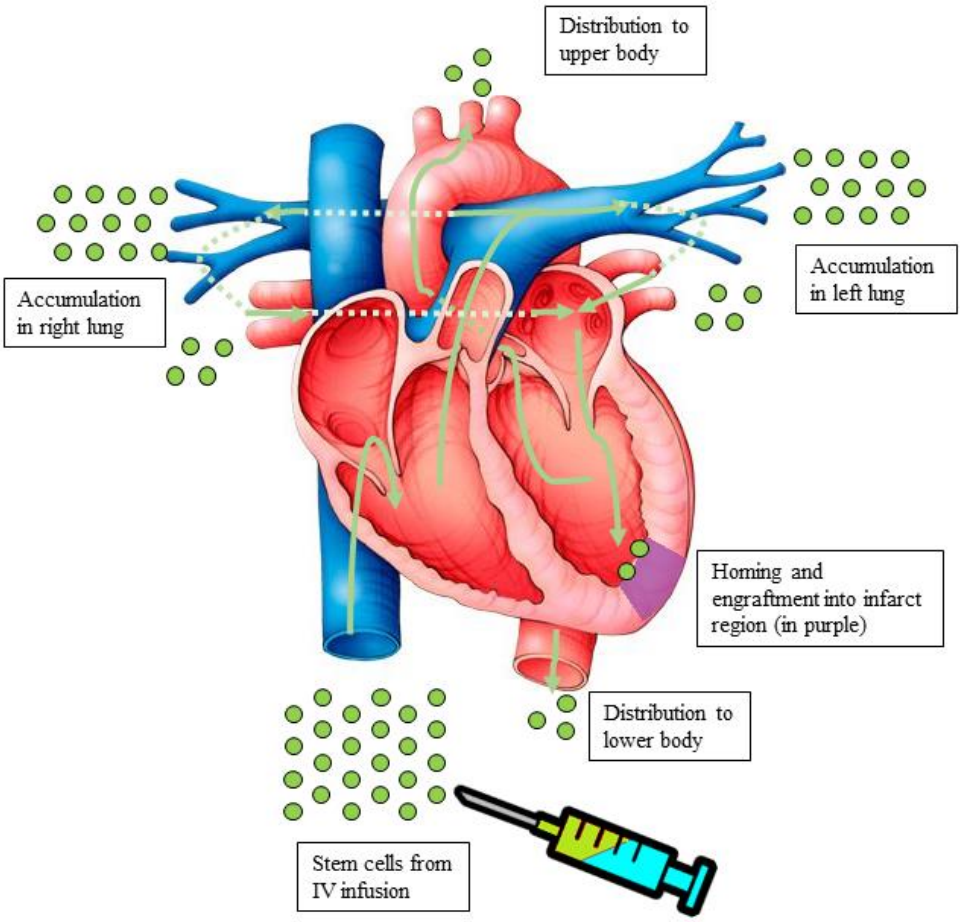

Figure 2.10 – Intravenous infusion of cells to treat myocardial infarction (Shim *et al.*, 2013).

This method is heavily hindered by the first pass effect, with the cell dose becoming greatly diluted by the time it reaches the target area. In one study, MSCs administered to treat myocardial infarction initially became highly localised in the lungs with slower accumulations in the liver, spleen and bone marrow (Chin *et al.*, 2003). There is also evidence that MSCs administered intravenously are also eliminated by monocytes and macrophages by the immune system (Barbash *et al.*, 2003). Other studies with smaller patient cohorts report no clinical effectiveness (Chin *et al.*, 2003; Hofmann *et al.*, 2005; Nogueira *et al.*, 2009), and a Phase II trial (NCT00877903), evaluating the efficacy of this treatment using MSCs to improve left ventricular end-systolic volume, is currently ongoing (n=220).

Intra-coronary infusion

Cells are administered directly to the infarct site using a catheter fed through the coronary artery as shown in Figure 2.11. A balloon catheter inflates to block the blood vessel preventing the backflow of cells and increasing exposure times to the affected area. This method is cost effective and non-invasive (Shim *et al.*, 2013) and is the standard cell therapy for patients suffering from a myocardial infarction (Mozid *et al.*, 2011; Wu *et al.*, 2012).

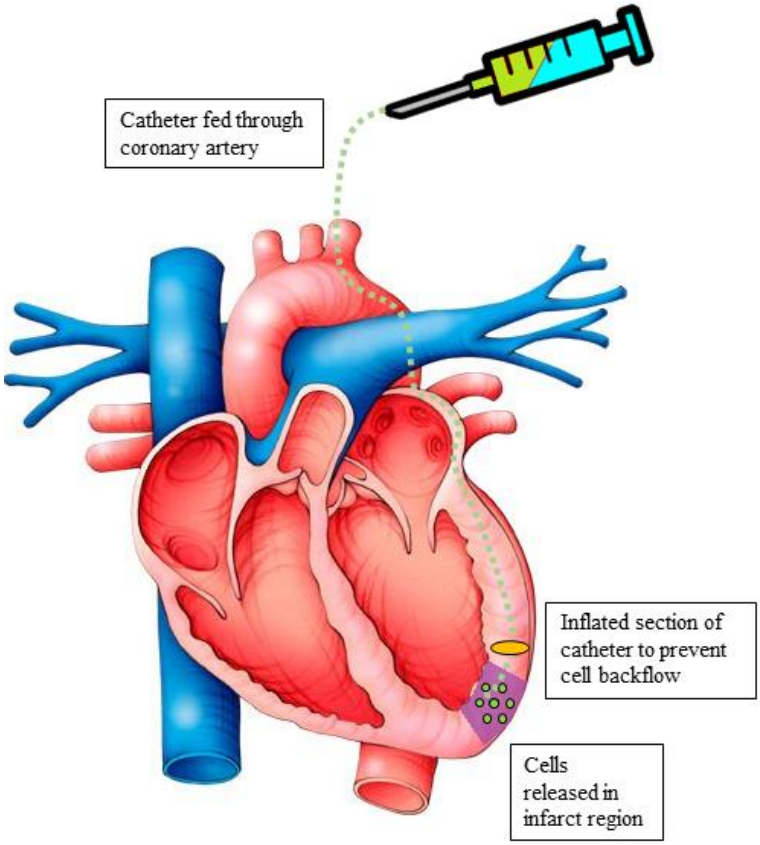

Figure 2.11 – Intra-coronary infusion of cells to treat myocardial infarction (Shim *et al.*, 2013).

The main disadvantage of this method is navigating the tortuous circulatory network of the heart to get to the damaged tissue. This network also varies between patients, making the procedure highly challenging, however it is possible to reach the distant areas of cardiac tissue located in the apex of the heart using this method (Siminiak *et al.*, 2005). Cells administered in this way have similar drawbacks to IV infusion in that the first pass effect is still present, and cells usually escape into the circulatory system and reappear in other organs. Studies have shown a retention rate less than 10% within the damaged myocardium after 2 hours, decreasing to 2-3% by 24 hours (Schots *et al.*, 2007), indicating that a large cell dose would be required to facilitate myocardial repair. Despite this, several controlled trials using bone marrow cells have shown improvements in patient left ventricle function, fitness and infarct size (Akar *et al.*, 2009; Miettinen *et al.*, 2010; Bolli *et al.*, 2011; Quyyumi *et al.*, 2011; Roncalli *et al.*, 2011), and at least five Phase III trials are currently ongoing (Wu *et al.*, 2012).

Trans-Epicardial Route

This method is much more invasive, but is normally used in situations where surgical intervention needs to be undertaken already. Cells are directly injected into the infarct region as shown in Figure 2.12. This eliminates the first pass effect found using IV infusion, improving dosage accuracy, and removing the additional complications of cell mobilisation and homing (Sheng *et al.*, 2013). From studies that utilise direct injection of bone marrow mononuclear cells (14), bone marrow stem cells (7), granulocyte colony-stimulating factor activated CD34+ cells (3), myoblasts (2) and MSCs (1), 20 showed improved LVEF (Wu *et al.*, 2012; Shim *et al.*, 2013).

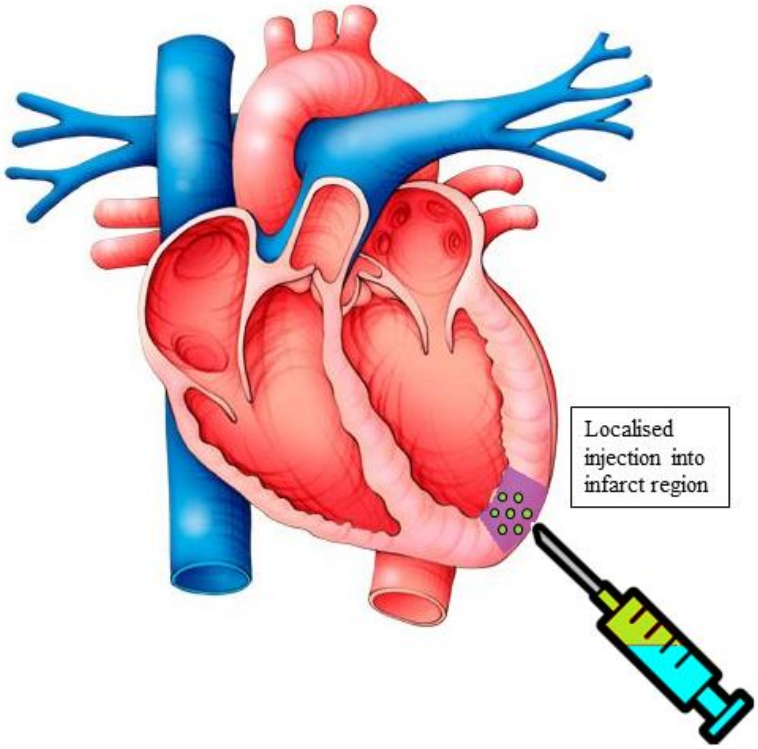

Figure 2.12 – Direct external injection of cells to treat myocardial infarction (Shim *et al.*, 2013).

Direct injection results in longer recovery times due to the required surgery, as well as potential complications resulting from accidental perforation of the ventricular wall, embolisation of coronary blood vessels, and cardiac arrhythmias (Hagege *et al.*, 2006). The main drawback of this method is the low retention of the cell dose due to leakage from the site of injection. An ischemic swine model injected with peripheral blood mononuclear cells had a maximum retention of 11% ± 3%, with 26% ± 3% of those cells found within the lungs (Hou *et al.*, 2005). Another swine model using MSCs observed only 5.8% of the initial cell dose in the heart after 10 days (Gyongyosi *et al.*, 2008). A Phase III clinical trial (NCT00950274) involving the injection of CD133+ bone marrow stem cells into infarcted heart tissue during routine coronary artery bypass graft surgery is in progress (n=142).

Trans-endocardial route

This method is features a catheter fitted with a needle that pierces the myocardial wall when expanded allowing a targeted release of cells into the inside of the ventricle as shown in Figure 2.13. Cells are administered in this way when the arteries in the infarct region have become blocked (Wu *et al.*, 2012). Electromechanical mapping techniques are employed to facilitate this avenue of treatment, allowing a contrast between viable, infarcted and scarred heart tissue (Kornowski *et al.*, 1998).

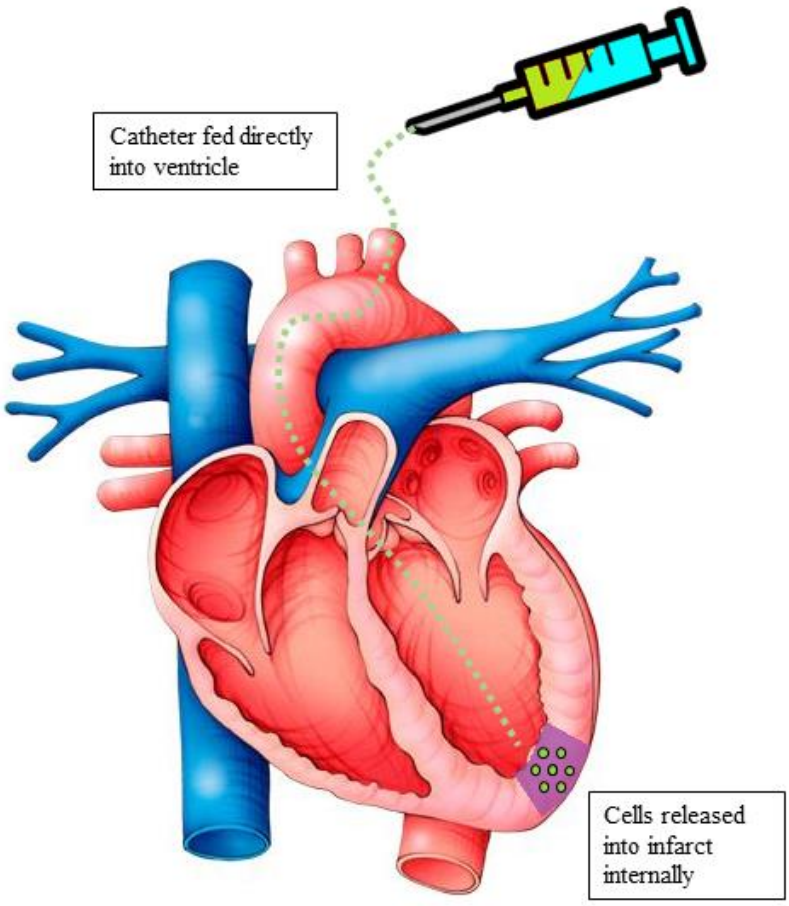

Figure 2.13 - Direct internal injection of cells to treat myocardial infarction (Shim et al., 2013).

It has similar risks to the trans-epicardial route but with lower likelihoods of wall perforation or arrhythmia occurring (Sheng *et al.*, 2013). Very few trials have reported on the efficacy of this method (Shim *et al.*, 2013), but those that have been positive showing improvements in myocardial perfusion and LV function (Wu *et al.*, 2012). Current research is focussing on optimal catheter design to improve the efficiency of this treatment (Sheng *et al.*, 2013). No studies at present give details on cell retention after injection.

Engineered Cell Delivery Vectors

Engineered delivery vectors involve direct application of the cells to the damaged area through the use of an artificial scaffold to provide a targeted treatment that can also provide additional structural support to the infarct region. A scaffold (also referred to as a substrate or matrix) is a construct that the desired cells are seeded onto or within in order to form a 2D or 3D tissue. Typically these scaffolds are biodegradable, and their degradation products biocompatible with the host, and can be constructed from natural ECM materials such as collagen, fibrin or chitosan, or synthetic polymers such as poly (lactic-co-glycolic acid) (PLGA), poly (glycerol sebacate) (PGS) or poly (ε-caprolactone) (PCL). There are several scaffold designs that have been used in cardiac treatment as engineered cell delivery vectors, which are outlined in this section.

Cell Patch

Patches can be placed over a damaged area of heart tissue or used to block openings caused by congenital problems. Patches typically comprise of a scaffold supporting a population of seeded cells on its surface, however recently cell sheets without scaffolds have been investigated as treatment avenues (Narita *et al.*, 2013; Domenech *et al.*, 2016; Moschouris *et al.*, 2016). This involves growing a 2D monolayer of cells, and removing them from their growth scaffold while retaining their cell surface proteins and ECM connections. These sheets can be layered, and can be applied to the wound site without sutures.

Despite the promising treatment outcomes of patches loaded with MSCs, few of these studies quantify the actual number of implanted cells that are retained in the wound site. Heart patches seeded with MSCs have shown improved rates of retention within the scaffold over traditional cell therapies, however exhibit poor migration into the infarct tissue itself. Freeman *et al.* (2015) showed that on collagen patches seeded with 100,000 hMSCs transplanted into mice 22 ± 17% were retained within the patch but only 1% penetrated into the damaged tissue after 2 days, with hMSCs detected in greater concentrations in the stomach and intestine. Poor transfer of hMSCs into mice hearts has also been shown using patches comprised of cardiac fibroblasts, with imaged sections of the heart showing minimal transfer after 2 days (Schmuck *et al.*, 2014). Longer term studies in rats have shown rates of engraftment reduce to 40 ± 15% after 2 weeks and to less than 5% after 4 weeks (Ishikane *et al.*, 2013). As with traditional methods, the limited, albeit improved, cell retention of patches are leading to treatments that are not meeting their full potential.

Injectable Hydrogels

Hydrogels are water swollen cross-linked polymer networks made from natural or synthetic materials (Radisic and Christman, 2013). Hydrogels have been used in a wide range of tissue

types such as bone, cartilage, adipose, neural and cardiac (Munarin *et al.*, 2012). For cardiac applications hydrogels can be made from components that already exist in the ECS of the myocardium such as collagen or fibrin, or from other natural materials such as gelatin or alginate (Lee and Mooney, 2001). Hydrogels can be loaded into syringes and injected into the infarct, or perfused onto the infarct using a catheter. The material is a viscous liquid at the time of injection, but can be made to gelate with the addition of an activating material or a change in environmental conditions (Shuman *et al.*, 2013). This gelation must be achieved quickly, because the liquid hydrogel/cell solution can be ejected from the injection site similar to traditional cell delivery methods (Li and Guan, 2011).

The mechanical properties of interest are gelation times, stiffness and degradation profile; and once implanted the degradation of the hydrogel can be triggered by hydrolysis, enzyme action, pH, temperature or electrical fields (Munarin *et al.*, 2012). Synthetic materials such as polymers are easier to configure for a specific organ and/or degradation rate than natural materials; however synthetic hydrogels are comparatively much softer than heart tissue and do not provide sufficient mechanical support to a heart at all points in systole and diastole in human subjects (Prabhakaran *et al.*, 2011). In clinical studies wall thickness of the infarct region typically increases and dilation of the left ventricle typically decreases, sometimes leading to an increase in pumping efficiency (Fujimoto *et al.*, 2009; Tous *et al.*, 2011; Wu *et al.*, 2011; Shuman *et al.*, 2013). However in these cases the hydrogel acts like a bulking agent, offering no regenerative therapy to the infarcted tissues.

Cells, drugs, growth factors or gene therapies can be suspended within hydrogel microspheres. This has been attempted *in vitro* using polylactic acid (PLA) microspheres to contain MSCs, where in one study the cells maintained their phenotype but the cells grew in inhomogeneous clumps within the microspheres (Forte *et al.*, 2009). Another study conducted experiments on rat models to investigate encapsulated MSCs in microspheres of RGD modified alginate, which led to a significant reduction in infarct size and improved angiogenesis over a phosphate-buffered saline (PBS) control (Yu *et al.*, 2010). However, initial cell retention rates using microspheres (0.650%) were comparable to traditional MSC injection (0.613%). Despite this, after two weeks cells in microspheres were retained in the myocardium (0.576%) whereas no injected cells could be detected. The low rates of cell retention may be due to cell death during the encapsulation process or caused by an immediate ejection from the point of injection in the heart. Using collegen hydrogel loaded with cardiomyoblasts has similarly shown improved cell engraftment over 4 weeks compared to injections, however once again, initial cell retention at the wound site after 24 hours was no different compared to traditionally injected control hearts (Kutschka *et al.*, 2006). If initial cell retention rates could be improved, cell therapies delivered this way are likely to have a greater clinical impact.

Tubular Thread

Threads are typically woven from several micro fibres and can offer a three dimensional, highly interconnected porous structure to facilitate cell growth and migration into the scaffold, leading to the development of ECM components while allowing for diffusion of nutrients, oxygen and waste. Cells which are allowed to spread through a scaffold in this way provide increased vascularisation to the wound site (Hasan *et al.*, 2016).

Threads can be attached to needles to act as sutures to assist in wound healing, with several FDA approved devices such as Vicryl (Ethicon, 2014), Surgicryl (SMI, 2010), Dexon (Covidien, 2016) and Polysorb (Medtronic, 2016) made from PLA, poly(glycolic acid) (PGA), or poly(lactic-co-glycolic acid) (PLGA) tailored to a necessary degradation time. Advanced versions of these products such as Vicryl Plus (Ethicon, 2014) are coated with an antibacterial agent, with future development of sutures to provide anaesthetic or antineoplastic functionality (Azimi *et al.*, 2014).

Polymeric sutures have also been investigated for their drug loading ability within tubular scaffolds (Catanzano *et al.*, 2014; Wei *et al.*, 2014; Kang *et al.*, 2015), and are currently being investigated as a delivery device for cells seeded on the external surface of the hollow fibre as shown in Table 2.8. Higher rates of initial cell retention have been shown using these sutures (20% - 45%), however as they are sewn in, shear forces cause the cells to detach from the scaffold (Guyette *et al.*, 2013), limiting the therapeutic potential of this treatment.

Hollow Fibre Encapsulation

The limitations of the previously discussed engineered cell delivery methods are outlined in Table 2.7 which indicates a common limitation - the number of cells that are initially retained at the wound site after implantation are limited. In cellular sheets, attached cells are detected in significant quantities in other organs and have poor rates of migration into the damaged tissue itself. Injectable hydrogels offer much promise with many tailorable properties and improved long term retention, however can suffer from immediate expulsion from the injection site if gelation is not achieved quickly – limiting the initial dose. Cells loaded onto the surfaces of tubular threads allow cell migration throughout the scaffold, however cells on its surface can be stripped off due to shear forces while being sewn into the wound site.

Table 2.7 – Advantages and concerns of current engineered cell delivery systems.

Construct	Advantages	Concerns	Ref.
Cell sheet	Invasive, but easy to apply; Increased vascularisation; Long term survival on infarct surface.	Poor integration with host tissue; Low initial cell retention after grafting; Difficult to handle.	Freeman *et al.* (2015) Schmuck *et al.* (2014) Ishikane *et al.* (2013) Ishikane *et al.* (2013)
Injectable hydrogel	Minimally invasive; Improved long term retention of cells.	Expulsion of cells after implantation, prior to gelation.	Rufaihah and Seliktar (2016) Li and Guan (2011) Yu *et al.* (2010) Kutschka *et al.* (2006)
Tubular thread	Increased vascularisation.	Invasive, Requires suturing; Cells stripped off suture during grafting.	Hasan *et al.* (2016) Guyette *et al.* (2013)

Hollow fibres may offer a solution to this problem. Hollow fibres have been previously been investigated for their use as devices to encapsulate drug therapies (Ceci-Ginistrelli *et al.*, 2017; Chilukuri *et al.*, 2015; Zhu *et al.*, 2007), and if constructed from a biodegradable material a timed dosage profile can be customised for the desired treatment schedule (Stubbe *et al.*, 2004); (Qiu and Zhu, 2001).

So far, no authors have furthered this line of investigation to determine if hollow fibres can be utilised as a device to encapsulate cells for delivery into a wound site. Such a device would protect cells from mechanical shear during handling and implantation, and potentially overcome the poor initial retention rates that characterise traditionally administered therapies. The cells can also be grown prior to implantation within the hollow fibre itself by utilising a hollow fibre bioreactor configuration.

As discussed in Section 2.3.2, hollow fibre bioreactors are typically used to grow a cells on its external surface, and have been shown to offer increased rates of MSC growth over other bioreactor types due to their larger surface area to volume ratio, favourable shear conditions, and high availability of nutrients and oxygen through the porous hollow fibre scaffold. A common HFB configuration allows media flowing through the lumen to permeate through the hollow fibre into the ECS where the cells are seeded. Instead, this proposed system would reverse this, with cells seeded on the inner surface of the hollow fibre, fed by media permeation from the ECS.

Once implanted *in vivo* such a device would need to be sufficiently porous to allow permeation of nutrients and oxygen from diffusion alone. The device would also need to biodegrade so that the encapsulated cells could fully assimilate into the host tissue. However, the first step in this endeavour is to determine if a HFB can be operated in this configuration and if viable cells can be retained in the lumen long term.

[Page intentionally left blank]

Table 2.8 – A summary of studies showing external cell seeding on tubular scaffolds

Material (Product)	Cell Type	Seeding Location	Model	Cell Attachment on Scaffold	Cell Retention in Host	Clinical Outcome	Source
Fibrin and collegen micro-threads (VitaSutures)	Bone marrow derived human MSC	External	Murine heart (*in vivo*)	11.8% ± 3.9% (24h)	30% ± 11% (1h)	Greater cell retention then direct injection	Guyette et al, 2013
Commercial polymeric fibre (FiberWire)	Murine embryo fibroblast	External	N/A	17% (12h)	N/A	Coating fibres in poly-L-lysine improves cell attachment on suture.	Yao et al, 2008
Commercial polymeric fibre (FiberWire)	Murine embryo fibroblast	External	Leporine Achilles tendon (*ex vivo*)	Unknown	44.5% (48h)	Cells successfully implanted and proliferate over 8 days	Yao et al, 2011
Commercial polyester suture (Ethicon Inc.)	Bone marrow derived murine MSC	External	Murine Achilles tendon (*ex vivo*)	Unknown	Unknown	Cell seeded sutures increased tendon strength over 28 days	Yao et al, 2012
PLGA (Vicryl)	Adipose derived murine MSC	External	Murine trachea (*ex vivo*)	80% (72h)	Unknown	Suppression of local inflammatory infection	Gergiev-Hristov et al, 2012

Cellulose nano-fibres	Adipose derived human MSC	External	Porcine skin (*ex vivo*)	Unknown	Unknown	Cells were retained on fibres after suturing while maintaining their phenotype	Mertaniemi et al, 2015
PLGA (Vicryl)	Adipose derived human MSC	External	Murine cecum (*in vivo*)	Unknown	Unknown	Sutures with attached MSCs promoted better recovery and wound healing of induced cecal fistula	Volpe et al, 2014
PGA with polycaprolate coating (Dexon-II)	Bone marrow derived porcine and murine MSC	External	None	Unknown	Unknown	Vicryl fibre had greater cell attachment than other commercial sutures	Casado et al, 2014
PGA with PCL coating (Assufil)							
PETP with silicone coating (Ticron)							
PGA with magnesium stearate coating (Safil Quick)							
PGA with glyconate coating (Safil)							
PLGA (Vicryl)			Porcine 'gut' *(in vivo)*	Unknown, however 'best' of those tested	50% ± 10%		

PGA – Poly (glycolic acid), *PLA – Poly (lactic acid),* *PLGA – Poly (lactic-co-glycolic acid),*
PCL – Poly (ε-caprolactone) *PETP – Poly (ethylene terephthalate)*

2.3.4 Scaffold Materials

It is of vital importance that a suitable scaffold material be selected to ensure biocompatibility with the seeded cells and host tissue, and so that the desired cell delivery device can be manufactured reliably and safely. Such a material must also be able to allow cell attachment, growth and migration throughout its structure, deliver cells to a target area after implantation, allow cell nutrients and products to diffuse freely, and be able to break down after being implanted in the body. This indicates a dependence on the porosity, tortuosity, pore size, biocompatibility, mechanical strength and rate of degradation. Some of these properties are dependent on the material the scaffold is made from, as well as the shape and design of the scaffold itself. The desired properties may also be inferred depending on medical requirements. In this section different biomaterials will be investigated for their application as a hollow fibre medical device.

Natural Biomaterials

Utilising materials which are similar to those found in the extracellular matrix is a logical starting point when attempting to encourage cell attachment. By emulating the host tissue as closely as possible, natural tissue engineered grafts provide excellent biocompatibility and are biodegradable. However these materials tend to have poor and inconsistent mechanical properties, and will sometimes cause an immune response (Lakshmanan *et al.*, 2012). They are typically more expensive than synthetic polymers, have greater batch to batch variation and are more susceptible to cross-contamination (Garg *et al.*, 2012). Natural biomaterials with applications in heart tissue engineering include proteins such as collagen, fibrin, elastin and gelatin, and polysaccharides such as hyaluronic acid, chondroitin sulphate, alginate and cellulose (Garg *et al.*, 2012).

Synthetic Polymers

Synthetic polymers provide an alternative to naturally derived materials. They are easily processed and manufactured on a large scale, allowing for consistent mechanical and chemical properties. They are readily available, have good biocompatibility, can be biodegradable, and have much better mechanical properties than natural polymers. One disadvantage is that unwanted products can be released during the *in vivo* biodegradation, leading to inflammation of the local tissue if the products are acidic. Another problem is the potential for erosion from external flows or movements, and the negative impact that can have on a scaffold with a previously understood degradation profile. Biodegradable polymers include PLA, PGA, its co-polymer PLGA, PEG, PCL, PGS, poly (L-lactide-co-caprolactone) (PLCL) and poly (urethane) (PU); their key properties are listed in Table 2.9

Table 2.9 – List of synthetic polymers used in heart tissue engineering.

Material	Key Properties	Source(s)
PLA	FDA approved Good biocompatibility Wide range of degradation rates Good bioresorption Slow degradation (30-50 weeks) Strong mechanical properties Hydrophobic	(Xu *et al.*, 2004) (Kaiser and Coulombe, 2015)
PGA	FDA approved Good biocompatibility Good bioresorption Rapid degradation (2-4 weeks) Brittle Hydrophobic	(Brugmans *et al.*, 2015) (Kaiser and Coulombe, 2015)
PLGA	FDA approved Tuneable degradation rate Good biocompatibility Good bioresorption Hydrophobic Poor cell seeding surface distribution Inflammation caused by acidic by-products	(Makadia and Siegel, 2011) (Garg *et al.*, 2012) (Chen *et al.*, 2015) (He *et al.*, 2016)
PGS	FDA approved Good biocompatibility Good degradation Lower stability Good elasticity Tuneable tensile strength	(Garg *et al.*, 2012) (Kaiser and Coulombe, 2015)
PEG	Good biocompatibility Good surface wetting (hydrophilic) Uniform cell seeding Offers protection from immune system Poor cell adhesion Poor stiffness	(Naderi *et al.*, 2011) (Simon-Yarza *et al.*, 2013) (Pascual-Gil *et al.*, 2015)
PCL	Slow degradation Good mechanical properties Good biocompatibility	(Baheiraei *et al.*, 2015) (Brugmans *et al.*, 2015)
PLCL	Tuneable degradation rate Good biocompatibility	(Inthanon *et al.*, 2016)
PU	Biodegradable Good biocompatibility Good reproducibility Good physical and mechanical properties Small pores formed only	(Gretzer *et al.*, 2003) (Siepe *et al.*, 2007) (Garg *et al.*, 2012)

PLGA

PLGA is a lactide-glycolide copolymer that possesses excellent biocompatibility, tuneable biodegradability and good processability; and can be engineered to construct clinically applicable microarchitectures such as flat sheets, microspheres, thin films and fibres. PLGA has been approved for use in humans by the Food and Drug Administration (FDA) in the United States, and has permitted the manufacture of many commercial devices for medical use. PLGA is also soluble in many solvents, unlike PLA and PGA, allowing it to be manufactured into a desired scaffold design. PLGA is amorphous in its structure, with a glass transition temperatures above human body temperature (37°C), allowing its structure to retain significant mechanical strength once fashioned into a scaffold (Azimi *et al.*, 2014).

The ratio of lactide to glycolide within the PLGA copolymer can be altered during formation to create a specific form of PLGA which has the desired mechanical and degradation properties. PLA and PGA alone both take a greater amount of time to degrade then their copolymer, which degrades at its fastest rate at a 50:50 ratio as first discovered by Miller *et al.* (1977), with a longer degradation provided by an increase in glycolide content (Makadia and Siegel, 2011). Table 2.10 shows data from a model for how *in vivo* drug release profiles are affected by the lactide:glycolide ratio. Note that degradation characteristics of PLGA are also affected by molecular weight, the properties of the encapsulated treatment, and the design of the scaffold; as well as the environment of the host tissue such as temperature, pH and enzyme activity (Makadia and Siegel, 2011).The data in Table 2.10 will vary depending on those parameters.

Table 2.10 – Data showing how PLGA composition changes a drug release profile.

Lactide to Glycolide Ratio	50% Drug Release (days)
50:50	22
65:35	40
75:25	54
85:15	64

PLGA degrades by hydrolysis, producing molecules of lactic acid and glycolic acid. *In vivo* the former enters the tricarboxylic acid cycle to be metabolised resulting in carbon dioxide and water as its products (Crotts and Park, 1998), and the latter is excreted in the kidney (Makadia and Siegel, 2011). Toxicological studies show that PLGA can cause inflammation of local tissue (Dailey *et al.*, 2006), however these reactions are mild and have not impacted its FDA approval.

Different PLGA ratios have also been tested for their cell attachment and proliferation ability on flat sheet scaffolds. Ellis and Chaudhuri (2008) showed a 75:25 lactide to glycolide ratio allowed a greater rate of both when compared to a 50:50 ratio. This data is presented to the nearest thousand cells in Table 2.11.

Table 2.11 – Data showing cell attachment of 560pZIPv.neo osteobgenic cells on PLGA flat sheets.

Lactide to Glycolide Ratio	Cell Number (Cells/cm^2)		Cell Attachment Percentage	
	Average	*SD*	Average	*SD*
50:50	12,000	*5,000*	60%	*25%*
75:25	15,000	*5,000*	75%	*25%*
TCP	18,000	*5,000*	90%	*25%*

The desired rate of PLGA degradation would be selected by the clinician to fit the patient's needs. In this work a 75:25 ratio is chosen because of its improved rate of initial cell attachment over the 50:50 variant, which is an important factor in acquisition of a higher eventual cell number, and because of its longer degradation time. As this work will also analyse internal cell encapsulation over a number of days, degradation is undesirable at this early stage while still evaluating hollow fibre cell encapsulation as a concept.

2.3.5 Hollow Fibre Manufacture

Hollow fibres are typically made by extrusion of melted or dissolved polymer through a spinneret that shapes the fibres and determines fibre thickness and lumen size. Production of hollow fibres can be achieved through three different methods: melt-spinning, electro-spinning and solution-spinning; each of which greatly influence fibre properties and scaffold applications (Postema *et al.*, 1990; Ellis and Chaudhuri, 2007).

Melt-spinning

Polymer is heated to its melting point, extruded through a spinneret, cooled with air as the fibres emerge, with the resulting fibre wound on a spooler (Fambri *et al.*, 1997; Pivsa-Art *et al.*, 2015). With the correct equipment a high throughput is achievable, allowing the production of thousands of metres per minute if raw material cost is not an issue. It also does not require the use of solvents. PLGA fibres have been successfully spun using this method (Xie *et al.*, 2010; Wang *et al.*, 2011b; Cui *et al.*, 2015), however there was no suitable equipment to produce PLGA in this way at the University of Bath.

Electro-spinning

In this process a strong electric field is applied to the extruded polymer melt or polymer solution. A droplet of polymer emerging from the spinneret has its surface tension

counteracted by the electric field, and becomes elongated leading to a charged polymer fibre that is attracted to a collecting spool. Electrospun PLGA have been manufactured (Bini *et al.*, 2004; You *et al.*, 2006; Kwak *et al.*, 2016), however the dimensions of the lumen are typically only large enough to house therapeutic molecules and not whole cells (Kang *et al.*, 2015; Ranjbar-Mohammadi *et al.*, 2016).

Solution-spinning

Solution spinning involves dissolving a polymer into a solvent (also known as a dope) and extrusion through a spinneret into a non-solvent environment. Wet-spinning uses a liquid non-solvent such as water, and dry-spinning is simply at ambient conditions in air. The polymer and solvent de-mix when the mixture contacts the non-solvent, leaving behind the desired scaffold structure (Azimi *et al.*, 2014). De-mixing can occur instantly or very slowly depending on the affinity between the solvent and non-solvent. Dry-formed scaffolds typically take longer to form due to the low affinity between solvents and air. While formation of flat sheets in this way is achievable, hollow fibres will lose their shape before de-mixing completes, so wet-spinning is preferable.

Typical solvents include 1-methyl-2-pyrrolidinone (NMP), 1,4-dioxane, dichloromethane, chloroform and methyl chloride; and typical non-solvents include water, methanol, ethanol and propanol. Mixtures with higher affinities de-mix quickly and result in the formation of porous networks within the scaffold (Mulder, 2003). Of the listed materials, NMP and water have high affinity for each other and are safest (Ellis and Chaudhuri, 2007). Wet-mixing is the slowest of the methods listed because spun fibres must be soaked in water for several days to ensure full de-mixing, fibre output is also much slower at 1 – 2 m/min, and large quantities of non-solvent are required. However this allows fibres with large lumens and thin walls to be made, which is necessary for a device suited to encapsulate cells and biodegrade quickly.

2.3.6 Surface porosity

Internal porous networks are formed as part of the polymer/solvent de-mixing process during wet-spinning; however during this process the outer and inner surfaces of the hollow fibre form a non-permeable ‘skin’ layer. To manufacture a hollow fibre for cell encapsulation it must be permeable enough to allow nutrient and waste exchange. Surface porosity is a property that can be added utilising a specialised manufacturing technique, or by modifying an existing mixture using pore forming additives, the most common of which are described in this section.

Sintering

Sintering involves compacting polymer particles into a desired shape heating to just below melting point. This method is traditionally used to provide porosity to ceramic scaffolds, however sintering has been used to manufacture cylindrically moulded PLGA composite scaffolds for drug delivery (Kim and Jung, 2015; Sidney *et al.*, 2015), and particles used for cell delivery (Liang *et al.*, 2014; Rutledge *et al.*, 2014), without the need for solvents. While this method allows for the production of a scaffold with tuneable thermal, mechanical and surface porosities, it is the most complex of those considered, the most energy intensive, and has not been shown to produce hollow fibres of small enough dimensions.

Surface Removal

The impermeable skin layer on some polymer scaffolds can be etched away using plasma treatment, which also has the added benefit of improving cell adhesion by modifying the surface wetting properties of the scaffold (Hegemann *et al.*, 2003). Treatment of both internal and external surfaces of whole hollow fibre modules (6 x 20 cm) has been achieved (Li *et al.*, 2013a), with improved gas permeation through hollow fibres in some studies, however this only occurred in fibres which already had some initial degree of surface porosity (Huang *et al.*, 2016). By assuming a uniform reduction in the skin layer using this method, the resultant underlying porosity would not be accurately predictable or controllable, and instead would be a function of the polymer/solvent de-mixing thermodynamics. There is also a concern that plasma treatment can be damaging to the bulk structure of the scaffold (Li *et al.*, 2013b).

The non-porous skin layer could also be removed by physically dissolving the polymer using a solvent. Preliminary experiments were conducted by re-exposing a flat sheet PLGA scaffolds to NMP briefly, however bulk scaffold structure broke down quickly. De-mixing in a weak solvent solution led to an increased de-mixing time and localised surface regions where the skin was removed, however this was not replicable during hollow fibre spinning (Acott, 2014).

Particle Leaching

Particles of salt (Zhang *et al.*, 2013), sugar (Qu and Ding, 2013), gelatin (Wang *et al.*, 2013) PEG (Xu *et al.*, 2016) and poly (vinyl alcohol) (PVA) (Meneghello *et al.*, 2009) can be used as porogens. These particles are mixed with a polymer dope prior to scaffold manufacture remaining undissolved in suspension, and leach out of the dope during wet-spinning when exposed to a non-solvent that the particle will readily dissolve into. This provides greater interconnection between pores within the scaffold, and imparts porosity to the external surfaces. The selected porogen can be sized to provide pores of the required diameter.

Typically, sodium chloride (NaCl) particles are used in tissue engineering due to their quick leaching, customisable sizing, and availability; however traditional grinding and sieving methods lead to NaCl particles with wide size distributions (Xin *et al.*, 2016). NaCl particles can be grown to a required size by a simple crystallisation procedure, as first achieved by Marshall (1940) and further characterised by Tran *et al.* (2011). Addition of NaCl particles to PLGA dopes has been investigated and is shown to be an adequate porogen for use in tissue engineering. PLGA scaffolds supplemented with large NaCl particles (300 – 500 µm) have shown reduced mechanical integrity, whereas smaller particles (150 – 180 µm) provide a faster degradation rate (Kuo and Leou, 2006). Recently, pores in the range of 30 – 60 nm have been imparted onto PLGA microspheres used for drug delivery applications (Ilyas *et al.*, 2013).

Utilising porous PLGA hollow fibres as a biodegradable cell carrier is undocumented in literature, and as such some assumptions must be made to determine the required surface pore size. As cardiomyocytes are approximately 30 µm in diameter (Calvillo *et al.*, 2003), a surface pore size much greater than that would lead to cell spread within the hollow fibre scaffold itself, causing potential blocking of internal pores and prevention of media permeation to areas of the lumen where the bulk of cells are located. Conversely, a pore size too small could lead to jetting of permeating cell media into the cells on the lumen surface, potentially puncturing the cell membrane and reduction in overall cell viability. A target pore size of 5 µm has been selected to balance these concerns, and because a procedure for the manufacture of 5 µm NaCl crystals is available (Marshal, 1940).

2.4 CONCLUSIONS

In this literature review a basic overview of the heart, its structure, histology and function was described in Section 2.2. The effects of heart disease on heart function was defined, with differences between healthy and unhealthy heart behaviour quantified in terms of available blood flow rate and oxygen concentration.

Section 2.3.1 catalogued a number of cell types which have application in cardiac tissue engineering, concluding with mesenchymal stem cells sourced from the adipose tissue surrounding the heart as a novel area of investigation, with authors claiming that MSCs sourced from this region were more likely to differentiate into cardiomyocytes than MSCs sourced from other areas. Additionally, MSCs from this source have not yet been investigated for their ability to be autographed in human subjects. MSC extraction rates from this source were quantified to be approximately 812,800 ± 318,400 cells, requiring expansion to a minimum of 50 million cells for traditional cell therapies.

Section 2.3.2 investigates several bioreactor types, concluding that hollow fibre bioreactors provide a quickest MSC growth rate, shortest doubling times, and greatest quantities of cell growth, which would allow 50 million MSCs to be grown in the shortest amount of time for use in traditional cell therapies. The main drawback of HFBs is their poor initial rates of cell attachment compared to other bioreactors (~20%), mainly due to their curved geometry. No investigations have been conducted in literature to seek to improve the initial rates of cell attachment on hollow fibre bioreactors. Currently 20% cell attachment will yield 50 million cells in 12.6 ± 5.2 days, whereas 100% attachment would take 9.1 ± 4.0 days. If higher rates of attachment could be obtained it would reduce the time required to grow a traditionally administered cell dose. This would be a novel contribution to the field if a new cell seeding procedure could be discovered.

As stated in Section 2.3.3, traditional cell therapies require large doses because of the high degree of cell loss, with 90% disappearing in the first few days and less than 2% found at the injection site after 4 weeks. This indicates that of the original dose of 50 million cells, only 1 million cells are retained, a quantity similar to the initial MSC extraction rate of 812,800 ± 318,400 cells. Despite this, studies have shown improvements in LVEF, reduction in infarct size and increased angiogenesis in animal models. Therefore it can be concluded that a much smaller initial dose is required so long as it can be retained at the wound site. To that end, Section 2.3.3 continues to suggest alternative engineered methods, suggesting an encapsulation within a tubular scaffold to be a novel alternative which protects the entire cell population, and can receive nutrients from the host tissue and allow gas exchange via diffusion through a porous membrane. This engineered device would aim to encapsulate and retain a minimum of 1 million cells to retain parity with traditional therapies, however there is scope to encapsulate a larger cell dose expanded separately on externally seeded HFBs which could lead to even greater improvements in heart function. The first step in this process is to see if a population of cells can survive within the lumen of a hollow fibre over the long term.

Section 2.3.4 investigates suitable materials for such a device, concluding with PLGA due to its FDA approval for use in medical devices, its tuneable biodegradability, and because its degradation products can be processed by normal body functions. Section 2.3.5 outlines how hollow fibres can be manufactured, choosing a wet spinning method via extrusion through a custom designed spinneret to provide fibres with a consistent internal porosity, and because of availability of equipment and previous experience in its operation. Section 2.3.6 summarises how an external surface porosity can be provided to wet-spun PLGA hollow fibres, determining that addition of NaCl particles is a simple, well-used and easily controllable method to achieve this.

Exact requirements to sustain a population of cells within a hollow fibre will be dependent on the permeability of the produced fibres, with the appropriate external flow rate in the ECS selected to ensure sufficient permeation of liquid nutrients and dissolved oxygen. These metabolic considerations will be quantified in detail in the appropriate chapter.

2.5 AIMS AND OBJECTIVES

The aim of this thesis is to improve the utility of hollow fibre bioreactors. Specifically, to decrease the required time to grow appropriate doses of cells on their external surface, and to investigate their application as engineered delivery devices encapsulating cells within their lumen as a cell therapy to treat damaged heart tissue. To this end, the following objectives have been set:

OBJECTIVE 1: Improve external cell seeding efficiency on hollow fibres.

OBJECTIVE 2: Manufacture hollow fibre scaffolds with suitable surface porosity and liquid permeability.

OBJECTIVE 3: Sustain a population of cells within the lumen of a hollow fibre.

A scale schematic of the proposed system is shown in Figure 2.14, displaying the operation of a HFB in external cell seeding mode (A), and internal cell encapsulation mode (B). The bioreactor is 100 mm long, with an inner diameter of 2.5 mm and an outer diameter of 3.5 mm. The hollow fibre itself has the same length and approximate inner diameter of 0.8 mm and outer diameter of 1.0 mm.

Objective 1 will utilise standard PLGA hollow fibres in a bioreactor operating in Mode A to determine if external cell seeding efficiency can be improved using a series of dynamic seeding regimes. MG63 human osteosarcoma cells will be used as an alternative to MSCs. No previous studies aiming to improve cell attachment on hollow fibres in this way have been conducted by others, making this a novel endeavour. This is outlined in Chapter 4.

Objective 2 will augment PLGA hollow fibres with various concentrations of custom made NaCl particles in order to obtain fibres with porous internal and external surfaces. This is to enable the permeation of liquid media for an encapsulated population of cells. No previous studies have characterised the addition of NaCl manufactured using this method to wet-spun hollow fibres of PLGA, making this a novel endeavour. This is outlined in Chapter 5.

Objective 3 will utilise porous PLGA hollow fibres in a bioreactor operating in Mode B to encapsulate cells and attempt to sustain them for six days. MG63 human osteosarcoma cells will be used as an alternative to MSCs. Media will be pumped through the ECS to enable permeation through the fibre and into the lumen. No previous studies attempting to sustain an encapsulated population of MG63 cells within a hollow fibre lumen have been conducted by others, making this a novel endeavour. This is outlined in Chapter 6.

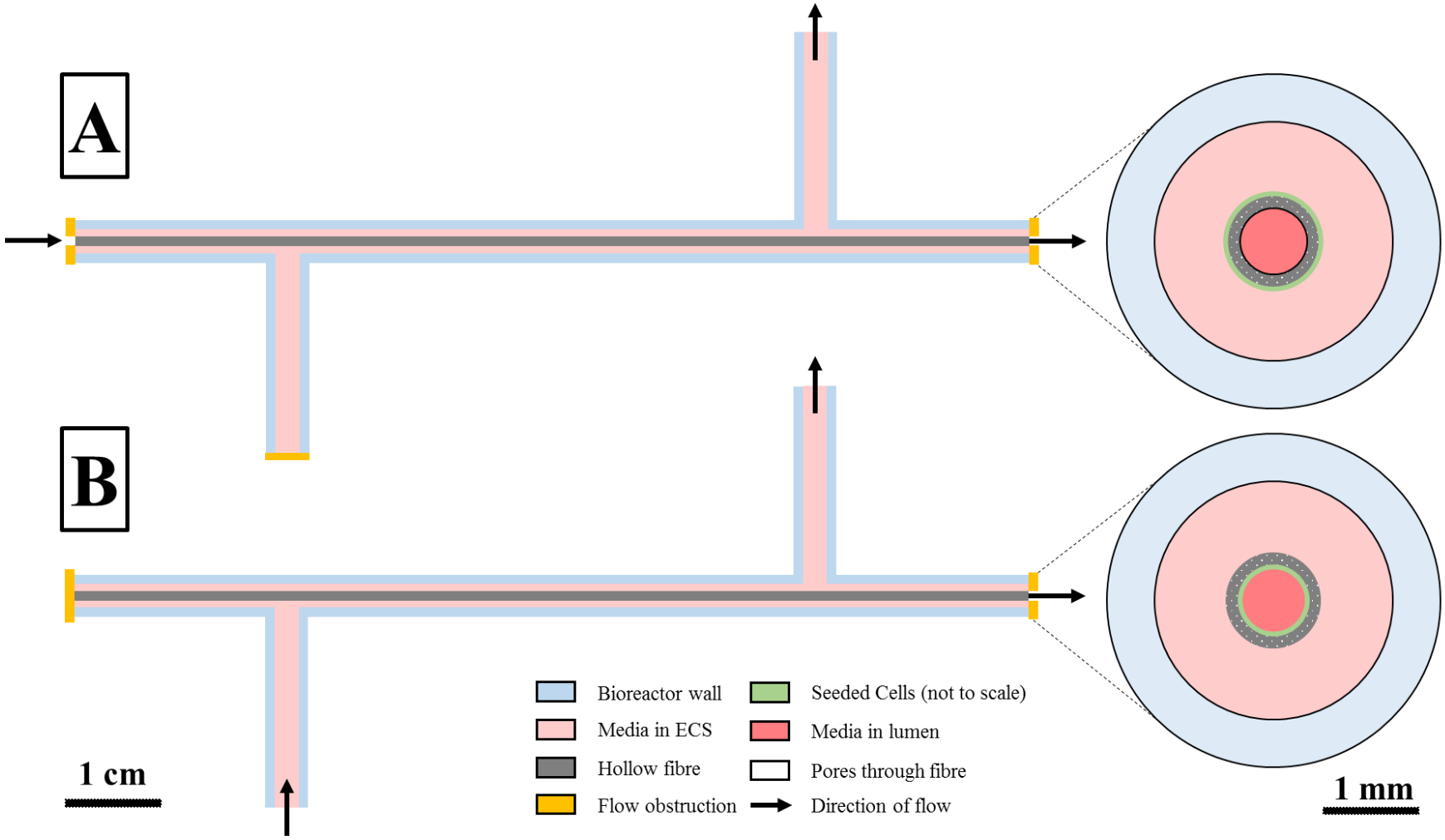

Figure 2.14 – A side view and cross section of a HFB operating in external cell seeding mode (A) and internal cell encapsulation mode (B). Flow in mode A is representative of the expected configuration for cell growth. Flow is not initiated during static or dynamic seeding.

[Page intentionally left blank]

CHAPTER THREE: MATERIALS AND METHODS

3.1 INTRODUCTION

This chapter contains a list of all the materials and an outline of all the methods used for the experiments in this thesis, subdivided into experimental, analytical and statistical methods. Additional specific variations in experimental methods are explained in relevant chapters.

3.2 MATERIALS

All materials are sub-divided into appropriate lists depending on their application: materials used for cell culture (Table 3.1), materials used for cell culture analysis (Table 3.2), materials used to manufacture scaffolds (Table 3.3), materials used during bioreactor construction (Table 3.4), lab consumables (Table 3.5) and lab equipment (Table 3.6).

Table 3.1 – Materials used for cell culture.

Item	Supplier	Ref. No
Antibiotic-Antimycotic (A/A)	Gibco Life Technologies	15240-062
Dulbecco's modified eagle medium (GlutaMAX-l) (DMEM)	Gibco Life Technologies	32430-027
Ethanol (EtOH)	Sigma Aldrich	F203233
Foetal bovine serum (FBS)	Sigma	F7524
MG63 human osteosarcoma	Sigma Aldrich	86051601
Non-essential amino acid solution 100x (NEAA)	Sigma Life Science	M7145
Penicillin-streptomycin (P/S)	Sigma Life Science	P4333
Phosphate buffered saline (PBS)	Sigma Life Science	D8537
Sodium Pyruvate (NaPy)	Sigma Life Science	S8636

Table 3.2 – Materials used for cell culture analysis.

Item	Supplier	Ref. No
λ DNA standard	Gibco Life Technologies	P7589
D-glucose assay kit (GOPOD format)	Megazyme	K-GLUC
Formaldehyde solution	Sigma Aldrich	F1635
L-lactic acid assay kit	Megazyme	K-LATE
Methylene blue (MB)	Sigma	M4159
MTT cell growth determination kit	Sigma Aldrich	CGD1-1KT
Pico fluorescence Quant-iT Picogreen ds DNA reagent	Gibco Life Technologies	P7589
TE buffer (20X)	Invitrogen	T11493
Trypan blue stain	Gibco Life Technologies	15250-061
Trypsin-EDTA solution (10x)	Sigma Life Science	T4174

Table 3.3 – Materials used for scaffold manufacture.

Item	Supplier	Ref. No
1,4-Dioxane	Sigma Aldrich	154822
Ethanol (EtOH)	Sigma Aldrich	F203233
1-Methyl-2-pyrrolidone (NMP)	Acros Organics	127630025
Poly(lactic-co-glycolic acid) (PLGA)	Evonik Industries	99024545
Poly(styrene) (PS)	Aldrich	182427
Sodium chloride (NaCl)	Sigma Aldrich	31434.500G.R
Tetrahydrofuran	Fisher Scientific	10174150

Table 3.4 – Materials used for bioreactor construction.

Item	Supplier	Ref. No
1/16” straight connector	Cole-Parmer	WZ-30506-00
1/4" flat bottom to 1/16" barbed to thread adaptor	Kinesis	P-668
3-Stop Pharmed 1.52 mm ID BPT pump tubing	Cole-Parmer	WZ-95714-36
4 mm ID barbed Y-connector	Cole-Parmer	EW-06295-10
8 mm ID Marprene tubing	Watson-Marlow	902.0080.I4
Araldite rapid 2k part A/B	Huntsman	2542708
Ethanol (EtOH)	Sigma Aldrich	F203233
Glass bioreactor	University of Bath	N/A
Helixmark 1.98 mm ID silicone tubing	Helix Medical	45630109
Male luer lock plug	Cole-Parmer	WZ-45503-56
Masterflex 0.8 mm ID platinum L/S 13 silicone tubing	Cole-Parmer	WZ-96410-13
Masterflex 1.6 mm ID platinum L/S 14 silicone tubing	Cole-Parmer	HV-96410-14
Masterflex 3.1 mm ID platinum L/S 16 silicone tubing	Cole-Parmer	WZ-96410-16
Masterflex barbed 1.8” ID to L/S 13/14 reducer	Cole-Parmer	EW-30616-04
Omnifit Q-series bottle cap	Kinesis	00932Q-3V
Savona D1 Washing up liquid	Premier Products	12006
Sigmacote	Sigma-Aldrich	SL2
Silcoset 151	ACC Silicones	151
Silicone elastomer sheet	Goodfellow	SI303200/1
Slide clamps	Qosina	12065
T-piece 3/32"	Cole-Parmer	EW-06365-86
Vircon	Antec International	P550
Watson Marlow 1.42 mm ID PVC manifold tubing	Watson-Marlow	980.0142.000
Whatman Hepa-vent filtration unit	Sigma-Aldrich	WHA67235000

Table 3.5 – Lab consumables.

Item	Supplier	Ref. No.
Aspirator tip (2 mL)	VWR	734-0456
Autoclave tape	Fisher	12370489
Cell culture flask (150 cm^2)	Appleton Woods	BC302
Cell culture flask (25 cm^2)	Appleton Woods	BC300
Cell culture flask (75 cm^2)	Appleton Woods	BC301
Cell culture plate (12 well)	Fisher	10136810
Cell culture plate (24 well)	Fisher	10380932
Cell culture plate (48 well)	Fisher	10065370
Cell culture plate (6 well)	Fisher	10578911
Cell culture plate (96 well flat bottom)	Fisher	10687551
Cell culture plate lid	Greiner Bio One	656161
Cell Strainer (70 um)	Fisher	11597522
Centrifuge tube (15 mL)	Fisher	11849650
Centrifuge tube (50 mL)	Fisher	11819650
Conductive carbon tape	Agar Scientific	AGG3939
Filter paper (0.2 µm)	Sigma-Aldrich	WHA10411411
Forceps	Fisher	11562113
Gloves (Nitrile)	Starlab	US-INT-L
Haemocytometer Slides	Una Health	87144
Micro centrifuge tube (0.5 mL)	Fisher	11508232
Micro centrifuge tube (1.5 mL)	Fisher	11558232
Needle (16 G)	Appleton Woods	BD401
Needle (18 G)	VWR	613-3495
Needle (21 G)	VWR	913-4970
Needle (27 G)	Appleton Woods	BD419
Parafilm	VWR	291-1212
Pipette Tip (1000 µL)	Fisher	11592813
Pipette Tip (20 µL)	Greinier	774288
Pipette Tip (200 µL)	Greinier	739288
Plastic pot (150 mL)	Fisher	11399143
Plastic pot (7 mL)	Fisher	12799985
Scalpel blade	Appleton Woods	GC683
Stripette (10 mL)	Fisher	10084450
Stripette (2 mL)	Fisher	10288370
Stripette (25 mL)	Fisher	10606151
Stripette (50 mL)	Fisher	10041591
Syringe (1 mL)	Fisher	10142104
Syringe (5 mL)	Fisher	10080264
Tissue paper	Fisher	12704296

Table 3.6 – Lab equipment.

Item	Full Name	Manufacturer
Angled extractor vent	Plymovent	Plymovent
Aspirator pump	VP series aspirator pump	KNF Neuberger
Autoclave (1)	Priorclave Tactrol 2	Grant
Autoclave (2)	Boxer 200/40 LR	Boxer
Biohood (1)	Heraeus HeraSafe Biohood	Heraeus
Biohood (2)	Microflow Advanced Biosafety Cabinet	Astec Microflow
Biohood (3)	Safe 2020	Thermo-Scientific
Bioreactor rotator	STR4 rotator drive	Stuart
Bubble column	Soap film flowmeter 1-10-100 mL	Hewlett-Packard
Camera	Nikon CoolPix 995	Nikon
Cell Counter	Handheld counter tally	Fisher
Cell culture plate (6 well, custom)	Cell culture plate (6 well, custom)	University of Bath
Cell culture plate (24 well, custom)	Cell culture plate (24 well, custom)	University of Bath
Cell culture plate (96 well, custom)	Cell culture plate (96 well, custom)	University of Bath
Cell freezing container	Mr Frosty Freezing Container	Thermo-Scientific
Centrifuge (up to 1.5 mL)	MSE Micro Centaur (micro-centrifuge)	Sanyo
Centrifuge (up to 50 mL)	ALC Centrifuge PK20	DJB Labcare
Centrifuge tube mixer	Whirli Mixer	Fisons
Carbon dioxide cylinder	CO_2 vapour withdrawal cylinder	BOC gases
Carbon dioxide regulator	Multistage Carbon Dioxide Regulator	GCE Group
Dissolved oxygen probe	Orion 083005MD	Thermo-Scientific
Electrochemistry meter	Orion Versastar electrochemistry meter	Thermo-Scientific
Freezer (-20°C) (1)	Hotpoint Future RZFM 751	Hotpoint
Freezer (-20°C) (2)	Sparkfree Labfeezer	Labcold
Freezer (-80°C)	Scientific -80°C Freezer	New Brunswick
Freeze-dry bottle	750 mL Fast Freeze Flask	Labconco
Fridge (1)	Bosch Exxcel freestanding fridge	Bosch
Fridge (2)	Laboratory Fridge Freezer	Lec Medical
Fume cupboard	Fume cupboard	S+B, UK
Gearbox (spinning)	Spaggiari Helical Gearboxes	Spaggiari
Glass bottle (50 mL)	Pyrex bottle reagent screw neck 50 mL	Fisher
Glass bottle (100 mL)	Pyrex bottle reagent screw neck 100 mL	Fisher
Glass bottle (1 L)	Flask 1 L glass polypropylene cap	Fisher
Glass rod	Stirring rod button end glass	Fisher
Goniometer	Dataphysics Contact Angle System OCA	Dataphysics
Hot block	Hot block QBT2	Grant

Item	Full Name	Manufacturer
Incubator (1)	Reach-In CO2 Incubator	Thermo-Scientific
Incubator (2)	Galaxy S Incubator	Wolf Labs.
K'NEX	K'NEX	K'NEX Ltd
Liquid nitrogen cell storage	Statebourne bio 20	Statebourne
Magnetic stirrer	Magnetic Stirrer SM5	Stuart
Metal wire	Stainless steel wire (30 G)	Miltex
Motor (spinning)	RS 440-571	RS Components
Microscope	Nikon Eclipse TS100 Light Microscope	Nikon
Multi-pipette	300 µL multichannel pipette	Rainin
Needle Valve (permeation)	SS Integral Bonnet Needle Valve 1/4"	Swagelok
Needle valve (spinning)	5,000 PSI Needle Valve - V Series	Parker
Nitrogen cylinder	Nitrogen vapour withdrawal cylinder	BOC gases
Nitrogen regulator	Multistage Nitrogen Regulator	GCE Group
pH probe	pH Electrode (General Plastic)	Eutech Instruments
Plate reader	Fluorospectrometer BioTek Synergy HT	NorthStar Sci.
Pressure gauge (gas permeation)	0-1 bar pressure gauge	Swagelok
Pressure gauge (liquid permeation)	0-15 psi pressure gauge	Omegadyne
Pressure gauge (spinning)	0-7 bar pressure gauge	BOSS
Pressure vessel	0.15L 250-18 MPT	Parker
Pump (cell proliferation)	Ismatech Reglo IIC	Ismatech
Pump (spinning)	Masterflex L/S multichannel pump	Cole-Parmer
Rheometer	Bohlin C-VOR rheometer	Bohlin
Rocker	Stuart Scientific 3D Rocking Platform	Stuart
Roller mixer	Roller Mixer SRT9D	Stuart
Rotameter (1)	MOB 12000	MPB
Rotameter (2)	Platon NGXV	Platon
Scales	Denver Instrument SI04002	Denver Inst.
Scanning electron microscope (SEM)	Joel JSM 648OLV SEM.	Joel
Spinneret	Spinneret	University of Bath
Spinning rig	Spinning rig	University of Bath
Sputter coater	Edwards Sputter Coater S150B	Edwards
Tube Rotator	MACSmix Tube Rotator	Miltenyi Biotec
Vacuum Desiccator	MicroModulyo Freeze Dryer	Savabt Modulyo
Water bath (1)	Grant Waterbath	Grant
Water bath (2)	Sub Aqua 2S Plus	Grant
Water treater (~0.05 µS/cm)	DirectQ UV3	Millipore
Water treater (~15 µS/cm)	Midi RO	Veolia Water

3.3 EXPERIMENTAL METHODS

3.3.1 Scaffold Preparation

PLGA polymer (75% lactide, 25% glycolide) was dissolved in NMP solvent at a weight ratio of 20:80 in a glass bottle. The bottle was placed onto rollers at 37°C for 24 hours to facilitate the dissolution of the polymer, and to ensure a homogeneous polymer dope.

Flat Sheet Membranes

Flat sheet membranes were prepared using a wet-spinning phase inversion casting method. The flat sheets were made by pouring 5 ml of polymer dope solution onto a flat sheet of glass and spreading it using a glass rod (Fisher) (Figure 3.1A). The sheet was kept to a uniform thickness by wrapping a strand of 200 µm diameter metal wire (Miltex) around the glass rod at each end, raising it 200 µm from the glass. The glass sheet was then immersed into ultrapure water from a DirectQ UV3 water purification system (Millipore) at a conductivity of 0.05 µS/cm (also known as 'double distilled' or ddH_2O) at 20°C. The water acted as a non-solvent, causing the NMP to de-mix from the PLGA, leaving behind a flat sheet scaffold (Figure 3.1B). This water was replaced twice daily to facilitate the removal of the NMP from the flat sheet structure. After three days the flat sheet membrane was removed from the water and hung to air dry (Figure 3.1C).

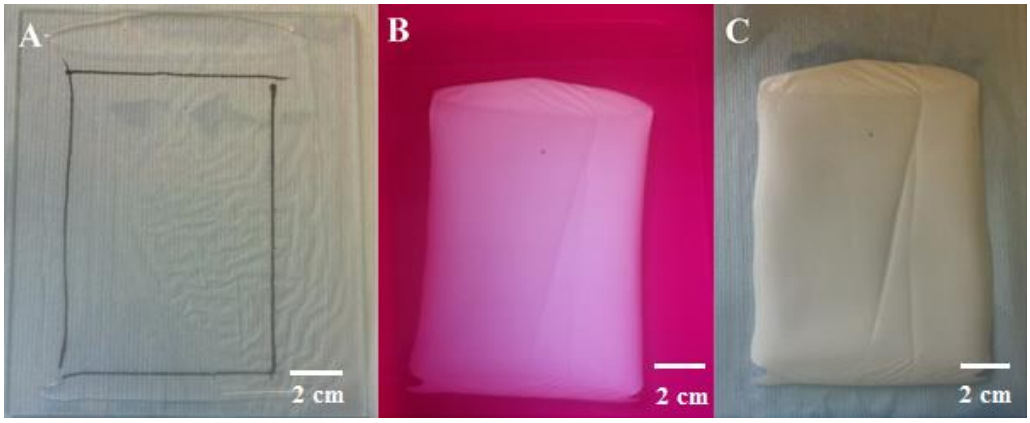

Figure 3.1 – Flat sheet fabrication. (A) prior to immersion, (B) during immersion, (C) after immersion.

Hollow Fibres

Hollow fibres were spun using a spinneret into a water trough (coagulation bath), both custom built at the University of Bath. A 150 ml pressure vessel (Parker) containing the polymer dope was mounted beside it, with a nitrogen gas inlet supplied to the top, and a polymer exit line fitted to the bottom (Figure 3.2). Needle valves were placed at both ends of the pressure vessel. The exit line fed polymer into the lower chamber of a spinneret, which had a 1.5 mm diameter bore hole at its base. A second line entering the upper chamber of the spinneret provided water to a 22 gauge needle (ID = 0.41 mm, OD = 0.72 mm) at its base, which passed through the lower chamber, emerging at the bottom of the spinneret, exposed to air.

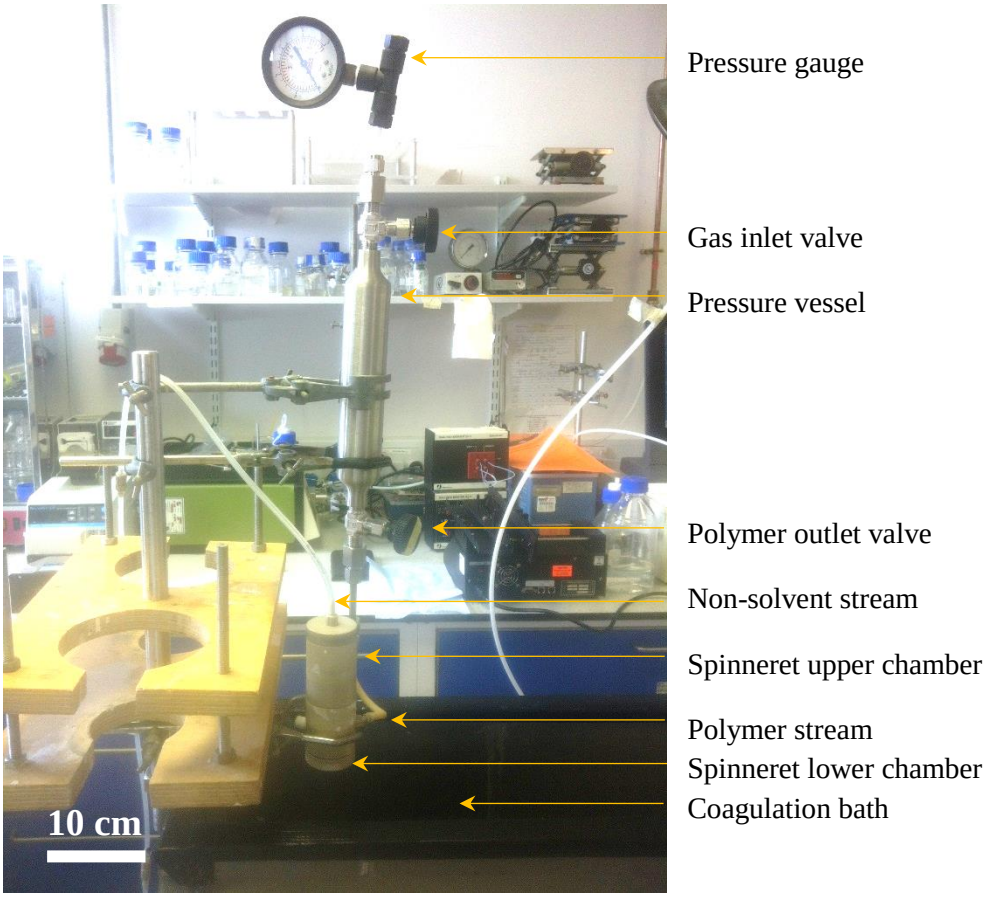

Figure 3.2 – Pressure vessel and spinneret configuration.

Water was flowed through the needle at a flow rate that provided an unbroken vertical stream of liquid, typically at 8 – 12 ml/min. A pressure was applied to the polymer inside the pressure vessel to initiate a polymer flow into the lower chamber of the spinneret, typically anywhere between 0.5 barg and 4.0 barg depending on the viscosity of the polymer and the type of spinneret used. Polymer emerged from the bottom of the spinneret through an annulus between the needle and the bore hole, which undergoes internal coagulation from the flow of water though the needle. The resulting semi coagulated polymer was fed into the primary coagulation bath (Figure 3.3). The gap between the exposed needle and the water bath is referred to as the 'air gap'. Spinning was performed with no air gap.

The hollow fibre was fed through the primary and secondary baths before being picked up on a rotor directing the hollow fibre into a collection bucket of non-solvent. Manufactured fibres were typically 75 – 150 µm thick, with ID of 700 – 1,100 µm and OD of 900 – 1,300 µm, with these dimensions dependent on the size of the needle, the subsequent size of the exit annulus, and the polymer flow rate. This non-solvent was replaced twice daily for three days before the batch of fibre was removed to dry. A more detailed operating procedure and schematic is included in Appendix A.

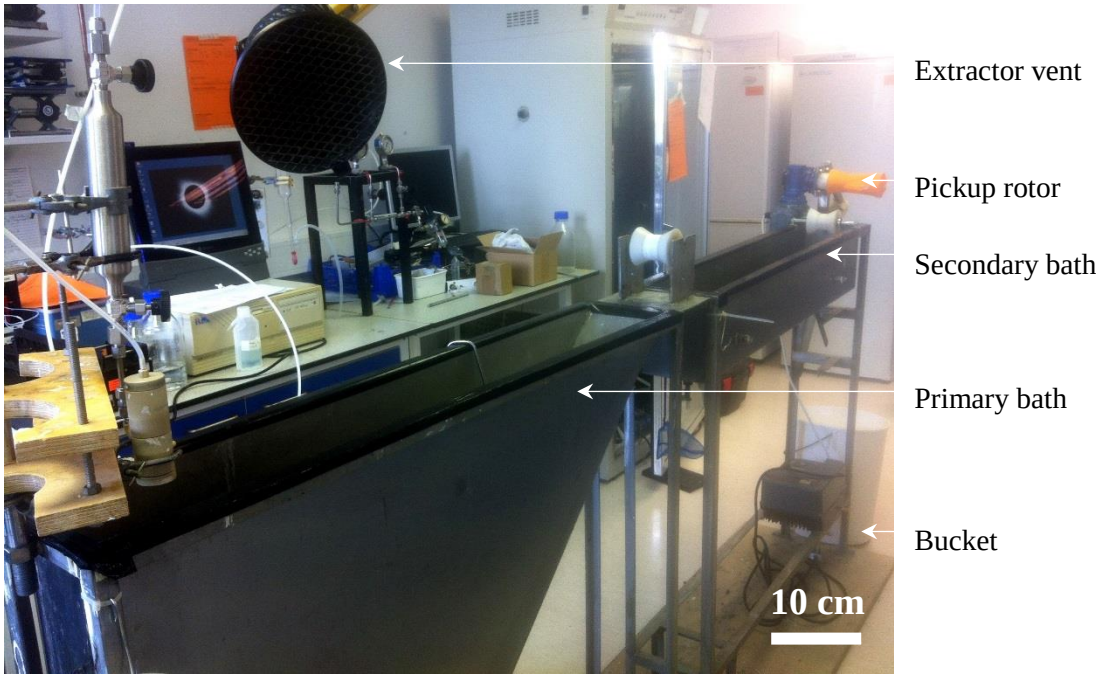

Figure 3.3 – Hollow fibre spinning rig.

3.3.2 Manufacture of NaCl Porogen

NaCl crystals (i.e. salt) with a target diameter of 5 µm were made following the method outlined by Marshall (1940). A saturated salt solution was made by dissolving 36 g of NaCl (Sigma Aldrich) into ddH_2O. 25 mL of this solution was diluted by adding another 5% of ddH_2O by volume, resulting in a volume of 26.25 mL. This was placed into a 50 mL centrifuge tube (Fisher) and frozen over dry ice for 1-2 hours. Once frozen the centrifuge tube was cracked open, and the resulting frozen salt solution was placed into 500 mL of ethanol (Sigma Aldrich) at -20°C.

The ethanol/salt solution was manually shaken vigorously until the frozen salt solution was fully melted, as indicated by the ethanol's cloudy appearance. The solution was filtered by pouring over a 0.2 µm filter paper (Sigma-Aldrich) attached to a vacuum pump (KNF Neuberger), allowing the solid salt crystals to be extracted. These were placed into a freeze dry bottle (Labconco) and placed in a vacuum desiccator (Savant Modulyo) for an hour to remove residual liquid. For manufacture of porous membranes the required quantity of salt was distributed in the solvent using a stirring flea on a magnetic stirring device (Stuart) prior to the addition of the polymer. It was theorised that scaffold porosity was affected by salt content in the dope. Salt was added as a proportion of polymer by weight as outlined in Table 3.7.

Table 3.7 – Quantities of salt required to obtain different porosities in a 25 mL polymer dope.

Proportion of Salt in Dope	Salt (g)	Polymer (g)	Solvent (g)
0%	0.0	5	20
10%	0.5	5	20
20%	1.0	5	20
40%	2.0	5	20
60%	3.0	5	20

3.3.3 Cell Passaging and Maintenance

MSC's have a poor long-term *in vitro* culturing capacity. After few passages MSCs become senescent (Kassem, 2004), reducing their differentiation potential (Chen *et al.*, 2014), and increasing the probability of malignant transformation (Rosland *et al.*, 2009). Tao *et al.* (2014) from the Worcester Polytechnic Institute seeds MSCs at passage 4 – 9 on fibrin micro-threads for their studies in treating infarcted murine models, however MSC suppliers recommend the cells are used by passage 5 (Lonza, 2011). MSCs are also very expensive, priced at £1318 at passage 1 (PromoCell, 2014) to £319 at passage 4 (ThermoFisher, 2015) for a million cells. As this work only outlines a proof of concept for an implanted hollow fibre device for the encapsulation of cells, utilising such an expensive cell for such a study would be wasteful, and thus an alternative was chosen.

MG63 human osteosarcoma cells were used instead of MSCs for all experiments in this thesis. MG63 cells grow rapidly, easily forming a monolayer (Heremans *et al.*, 1978). MG63 cells have the same risks of becoming senescent over many passages, however some authors have used MG63 cells up to passage 91 will no ill effects (Murphy *et al.*, 2001). In addition to their long life, their surface integrin subunit profile has been identified as useful for studies of initial cell attachment on various materials (Czekanska *et al.*, 2012). MG63 cells are also cheaper to purchase, with a million cells costing £329.50 (SigmaAldrich, 2013).Complete media for the growth of MG63 human osteosarcoma (Sigma Aldrich) cells was made by mixing by volume 87% Dulbecco's modified eagle medium GlutaMAX-l (DMEM) (Gibco Life Technologies), 10% heat inactivated foetal bovine serum (FBS) (Sigma), 1% penicillin/streptomycin (P/S) solution (Sigma Life Science), 1% sodium pyruvate (NaPy) solution (Sigma Life Science) and 1% non-essential amino acid (NEAA) solution (Sigma Life Science).

Passaging cells from a 75 cm^2 cell culture flask (Appleton Woods) was conducted within a laminar flow biohood (Astec Microflow) under sterile conditions. All equipment and containers were disinfected with 70% ethanol solution prior to placement in the biohood. The spent medium was aspirated from the cell culture flask via an aspirating pipette (VWR)

connected to an aspirator pump (KNF Neuberger), leaving behind the cells attached to the bottom surface.

Cells were washed with 6 mL phosphate buffered saline (PBS) (Sigma Life Science), and aspirated away. 3 mL of trypsin/EDTA solution (Sigma Life Science) was added to the flask to remove the cells from the surface, then placed in an incubator (Wolf Laboratories) at 37 °C and 5% CO_2 for 5 minutes. 3 mL of complete media was added to the flask, mixing with the 3 mL already inside, before the total 6 mL solution was transferred into a 15 mL centrifuge tube (Fisher) and centrifuged (DJB Labcare) at 1000 g for 5 minutes.

The supernatant was aspirated leaving behind a cell pellet. 6 mL of complete media was added and was gently sucked up and down the pipette to ensure the break-up of the cell pellet. 50 µL of cell solution was mixed with an equal volume of trypan blue stain (Gibco Life Technologies) to determine cell viability. 10 µL of this mixture was placed on a fast read slide which was placed under a light microscope at 10x magnification. Viable and non-viable cells were manually counted. From this the cell concentration was calculated and a volume of cell solution was determined to yield a required number of cells over a desired surface area for cell attachment. This volume was mixed with 12 mL of complete media in a new tissue culture flask, and placed back in the incubator under the same conditions.

MG63 cells were passaged in duplicate so that a back-up flask was available in case of infection. Cells were observed between passages to ascertain their health and commitment to their phenotype. MG63 cells continued to proliferate and reach confluence at a predictable and rapid rate every 72 hours for the entirety of the study. No infections arose during cell passage.

3.3.4 Cell Attachment on Flat Sheet Membranes

Flat sheets were prepared as described in Section 3.3.1. Two gaskets of 2 mm thick silicone (Goodfellow) and a custom built detachable well plate (University of Bath) were washed in vircon (Antec International), rinsed with water treated using a Midi reverse osmosis water purification system (Veolia Water) to a conductivity of 15 µS/cm (also known as ‘single distilled’ or dH_2O), and placed in a Boxer 200/40 LR autoclave (Boxer) at 121 °C and 1 barg before being brought into the biohood.

Flat sheets were soaked in 70% ethanol solution in PBS for 6 hours. Membranes were placed in the biohood, washed twice in PBS, and left to dry for a further 6 hours. The flat sheet scaffold was then placed in between two silicone gaskets and positioned into a custom well plate as shown in Figure 3.4.

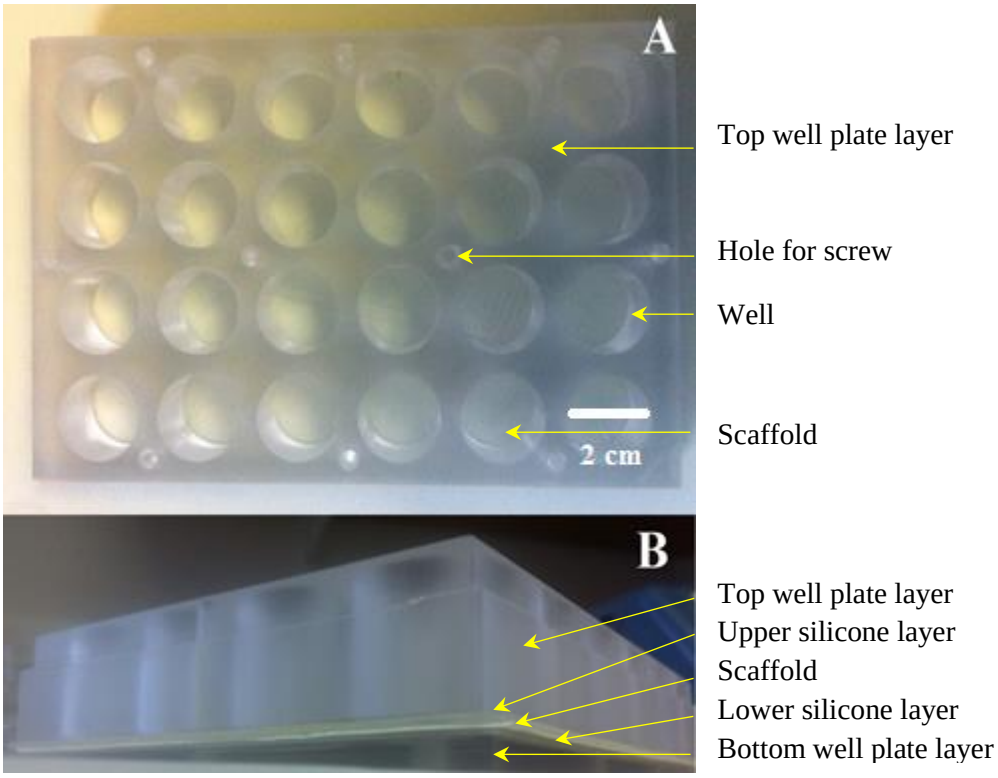

Figure 3.4 – Flat sheet scaffold in custom well plate, top down view (A) and side view (B).

The well plate featured a two part system where the flat sheet membrane could be placed between a bottom layer and a top layer with holes cut through it, allowing cells and media to be contained in a well. The well plate was held together by a series of screws. The silicone gaskets formed a liquid seal around each of the wells.

After ensuring that all screws were tight; the exposed areas of membrane were covered by complete media for 30 minutes before being aspirated away. Next, a cell suspension was added at the desired seeding density for the given area of membrane exposed in the well, fully submerging it. The well plate was covered with a cell culture plate lid (Freiner Bio One), sealed with Parafilm (VWR), and placed in an incubator at 37°C and 5% CO_2 for 6 hours.

3.3.5 External Cell Attachment onto Hollow Fibres

Silicone Bioreactor (Single Fibre)

Hollow fibres were prepared as described in Section 3.3.1 and placed into a single module bioreactor shown in Figure 3.5. This design was first innovated by researchers at Worcester Polytechnic Institute (WPI), in Boston, for cell seeding on fibrin micro-threads. Bioreactor components were autoclaved at 121°C and 1 barg prior to use. Hollow fibres were cut to a length of 3.5 cm and placed within a bioreactor consisting of 6 cm Helixmark standard silicone tubing of 1.98 mm inner diameter and 3.18 mm outer diameter (Helix Medical) with a 27 gauge syringe needle (Appleton Woods) at its inlet held in place using a slide

clamp (Qosina) that allowed for easy addition and removal of liquids from the bioreactor. A second slide clamp was placed on the bioreactor outlet.

The hollow fibre was sterilised in situ by injecting 70% ethanol into the bioreactor and storing for 12 hours in a fridge (Lec Medical) at 4°C. Ethanol was then removed, the bioreactor washed with 1 ml of DMEM three times and left for an hour to soak in DMEM. An inoculation of 100,000 cells/cm^2 in a volume of 0.1 ml was added to the bioreactor, which was then placed into a 50 mL centrifuge tube (Fisher) and onto either a static or rotating device in an incubator at 37°C and 5% CO_2 for 6 hours.

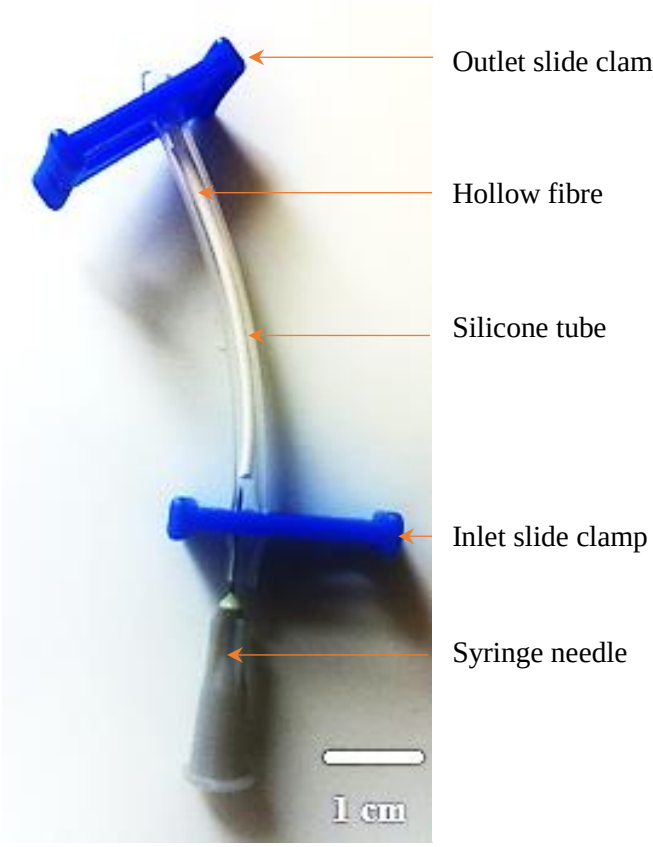

Figure 3.5 – Single fibre HFB silicone module.

Glass Bioreactor (Single Fibre or Fibre Bundle)

Hollow fibres were prepared as described in Section 3.3.1. Glass bioreactors were made by the University of Bath glass blower to desired specifications. Two different sizes of glass bioreactor were constructed, a smaller one for single fibre experiments, and a larger one to accommodate several fibres. The bioreactors were cylindrical tubes, featuring an inlet/outlet at each side of the tube and a two side ports on either end. Bioreactor dimensions for each size are shown in Table 3.8.

Table 3.8 – Dimensions of glass bioreactor modules.

Bioreactor Dimensions	Single	Multi
Tube		
Length (mm)	100	120
ID (mm)	2.5	7.5
OD (mm)	3.5	11.5
Side ports		
Length (mm)	20	25
ID (mm)	2.5	2.5
OD (mm)	3.5	5.5
Distance from end (mm)	20	35
Total Volume (mL)	0.69	5.54

Prior to all cell seeding the bioreactor was coated with Sigmacote (Sigma-Aldrich), leaving behind a hydrophobic layer inhibiting cell attachment on the glass. The bioreactor and all ancillary parts were cleaned with vircon, rinsed with ddH_2O and autoclaved at 121°C and 1 barg prior to construction in the sterile biohood. Bioreactor assembly differed slightly depending on its size.

Single Fibre Module

A fully constructed single fibre bioreactor is shown in Figure 3.6. A hollow fibre was cut to 12 cm and slotted into the bioreactor leaving 1 cm of fibre protruding out of each end. The gap between the end of the glass and the external surface of the hollow fibre were sealed using Silcoset 151 adhesive (ACC Silicones). Once dry, 70% ethanol solution was injected into the ECS of the bioreactor through a side port to sterilise its internals. The bioreactor was manually rocked side to side to ensure removal of air bubbles before capping the side ports and bioreactor ends. The bioreactor was removed from the biohood and stored in a fridge at 4°C for 12 hours. The bioreactor was then reintroduced into the biohood, the ethanol removed, the internals washed three times with DMEM, and soaked in complete media for an hour.

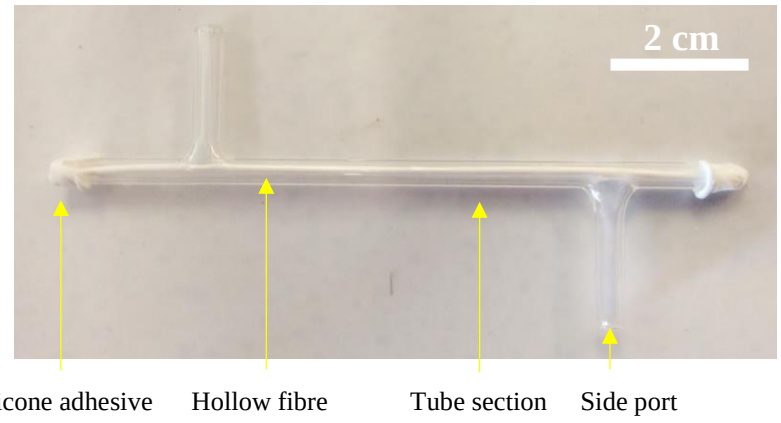

Figure 3.6 – Single fibre HFB glass module.

The media was removed and the desired number of cells in media solution was inoculated into the ECS via the side port. The number of cells in this solution was calculated in order to achieve a specific cell seeding density onto the exposed external surface of the hollow fibre. The protruding fibre was trimmed down and the exposed ends glued shut with silicone glue for external seeding. The side ports on the bioreactor were capped. Depending on the experiment the bioreactor was either a left static or attached to a rotating device in an incubator at 37°C and 5% CO_2 for a set period of time to assist in cell distribution and improve seeding efficiency.

Multi Fibre Module

Multi fibre bioreactors were prepared identically to the single fibre bioreactors with three minor differences. Hollow fibres were cut to 14 cm to account for the slightly larger bioreactor length, an annular silicone gasket of thickness 2 mm, ID 4 mm and OD 12 mm was glued onto either side of the main tube inlet/outlet to allow easy bundling of the hollow fibres within the bioreactor and fibres were individually sterilised with 70% ethanol solution prior to insertion. An assembled multi fibre bioreactor is shown in Figure 3.7.

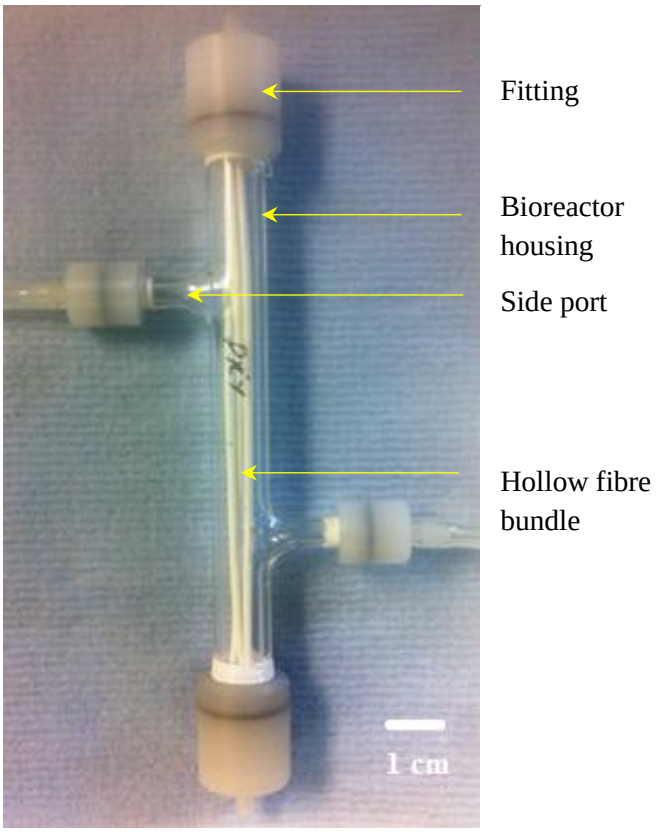

Figure 3.7 – Multi-fibre HFB glass module.

3.3.6 Internal Cell Proliferation within Hollow Fibres

Single hollow fibres were fixed into glass bioreactors, sterilised and the lumen seeded with cells. The bioreactor was attached via its side ports to a recirculating media perfusion system comprised of a multi-head peristaltic pump, a media reservoir and oxygen permeable silicone tubing. All equipment was sterilised by pumping 70% ethanol through the system, and washing with DMEM. A support for the bottles, tubing and bioreactors was made out of K'NEX (K'NEX Ltd.), a construction toy comprising of plastic rods and connectors shown in Figure 3.8. This section continues to describe the rig assembly and operation in more detail.

Figure 3.8 – A selection of K'NEX rods and connectors.

Detailed Perfusion Rig Assembly

Three hollow fibre bioreactor perfusion circuits were assembled simultaneously as described below. This allowed for the removal of a seeded bioreactor for analysis at designated time points. This method assumes that each step of the procedure is done for all three bioreactors consecutively. The K'NEX support was constructed beforehand as shown in Figure 3.9, washed with Vircon then ethanol. K'NEX could not be autoclaved.

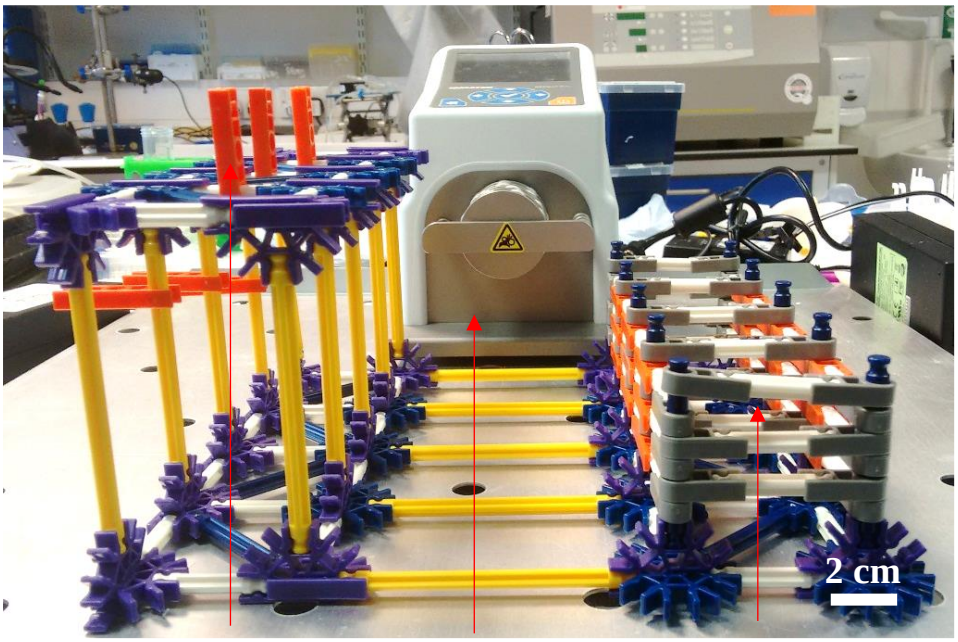

Figure 3.9 – K'NEX support structure.

All tubing, lids, fittings and glassware were washed with concentrated Savona D1 washing up liquid (Premier Products) using a syringe and soaked for 24 hours, then washed with warm tap water and dH_2O prior to assembly.

A 50 mL screw cap glass Pyrex bottle (Fisher Scientific) acted as a reservoir for the perfused liquid. Omnifit "Q" Series bottle caps (Kinesis) were used as lids. The lids had three threaded holes 1/4" in diameter in the top with plastic tubing fed to the bottom of the bottle. There was a hole at the bottom of each thread, approximately 1 mm in diameter, which allowed for inlet flow, outlet flow, and gas exchange to the bottle. Images of the reservoir system are shown in Figure 3.10.

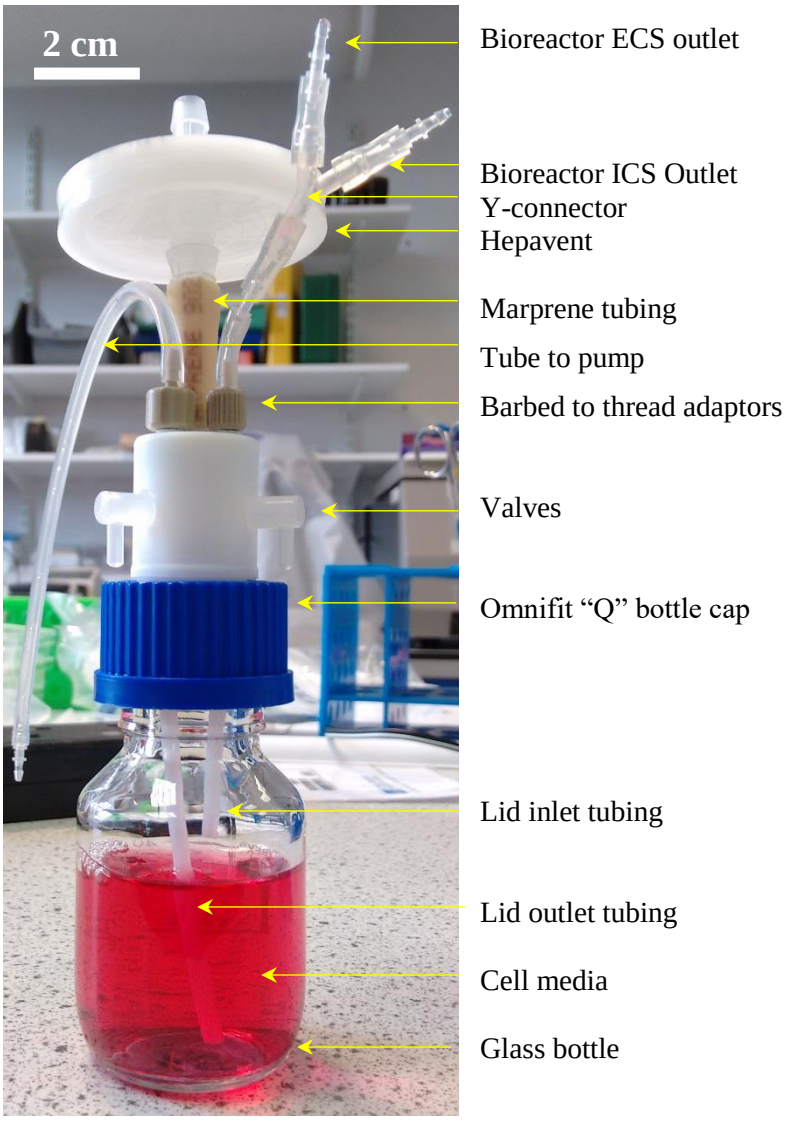

Figure 3.10 – Media reservoir with Omnifit caps.

A 1/4" flat bottom to 1/16" barbed to thread adaptor (Kinesis) was screwed into the outlet of the reservoir and 18 cm of Masterflex 0.8 mm ID platinum-cured L/S 13 silicone tubing (Cole-Parmer) was attached. This connected to 42 cm 3-Stop Pharmed 1.52 mm ID tubing (Cole-Parmer), by a 1/16" straight connector (Cole-Parmer) as shown in Figure 3.11.

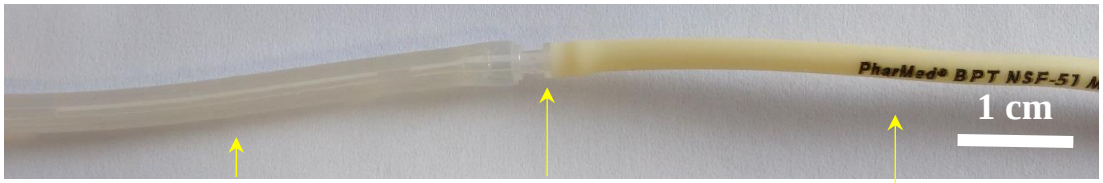

Figure 3.11 – Reservoir outlet to pump tubing.

Pump tubing was placed in a plastic brace and fitted to a REGLO peristaltic pump (Ismatech). 10 cm of L/S 13 tubing was fitted to the pump tubing outlet by a 1/16” straight connector. The other end of the L/S 13 tubing was fitted with a Masterflex barbed 1.8” ID to L/S 13/14 reducer (Cole-Parmer) to allow connection of 3 cm of Masterflex 3.1 mm ID platinum-cured L/S 16 silicone tubing (Cole-Parmer) as shown in Figure 3.12. L/S 16 tubing was selected because of its ability to fit snugly over the ends and side ports of the single fibre glass bioreactor.

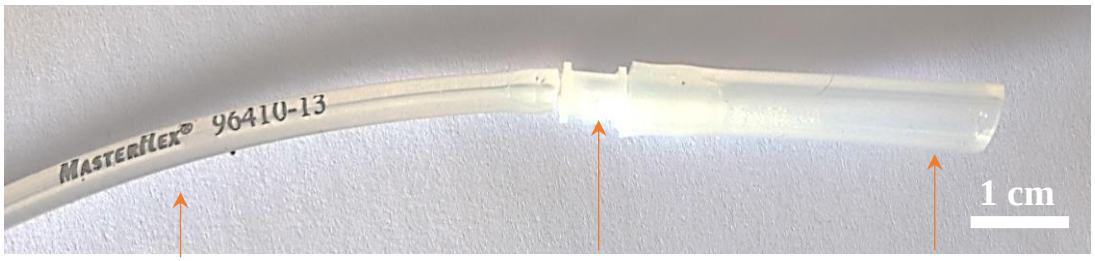

Figure 3.12 – Bioreactor ECS inlet connector.

The single fibre bioreactor was constructed by feeding a 12 cm long hollow fibre through the module and gluing in place at the ends with Silcoset adhesive. Once set, the protruding 1 cm of fibre from each end of the bioreactor was cut. The L/S 16 tubing was fitted over the one of the side ports of the single fibre glass bioreactor (the ECS inlet). The adjacent lumen inlet was capped with a male luer lock plug (Cole-Parmer) attached to 2 cm L/S 16 tubing as shown in Figure 3.13.

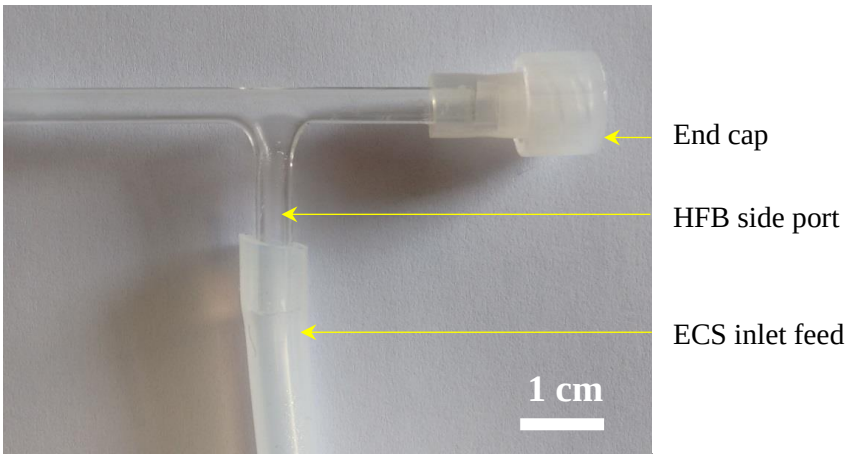

Figure 3.13 – Bioreactor ECS inlet.

Both the ECS outlet and lumen outlets were fitted with 3 cm L/S 16 tubing and joined to 15 cm L/S 13 tubing by a Masterflex barbed 1.8" ID to L/S 13/14 reducer. The outlets of both of the L/S 13 tubes were connected to 1.5 cm Masterflex 1.6 mm ID platinum-cured L/S 14 silicone tubing (Cole-Parmer) by a 1/16" straight connector. Both streams were joined at a 4 mm ID barbed Y-connector (Cole-Parmer), which in turn was attached to 1.5 cm L/S 14. Into this a 1/16" straight connector was fitted and 1.5 cm L/S 13 tubing attached. This assembly is shown in Figure 3.14 and Figure 3.15.

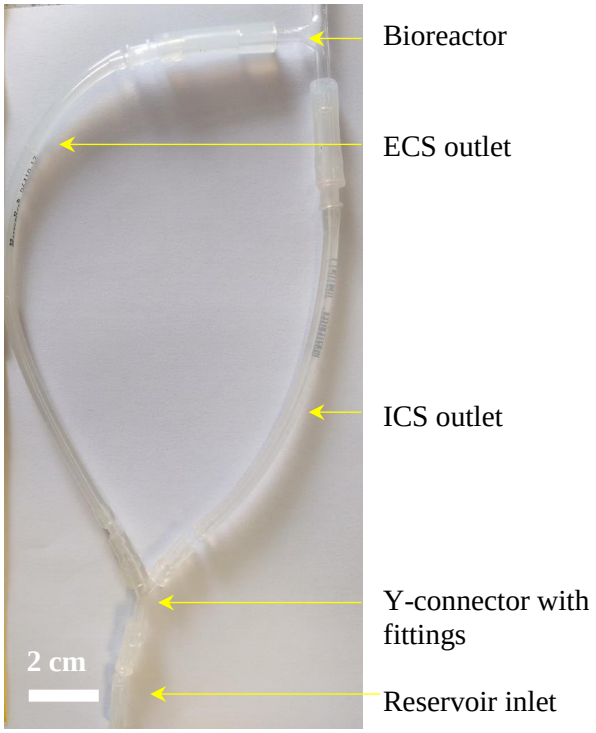

Figure 3.14 – Bioreactor outlets joined at Y-connector.

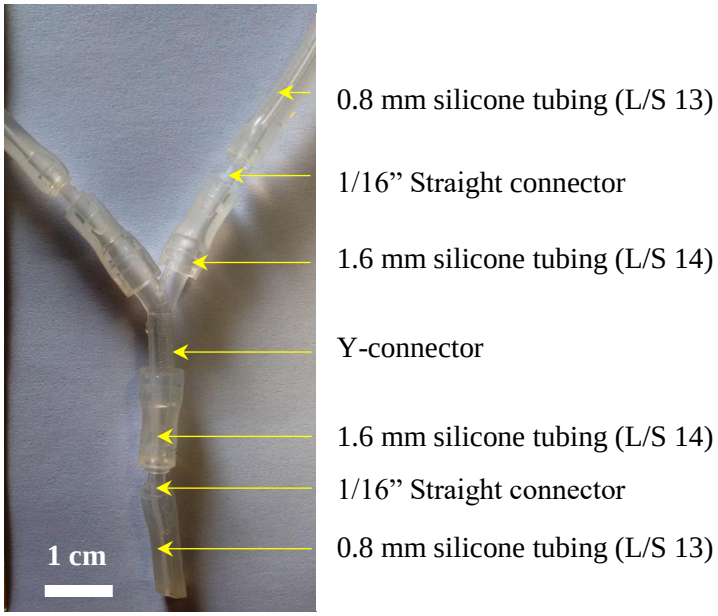

Figure 3.15 – Y-connector with attached tubes and fittings.

The bottom of the Y connector was then attached to a 1/4” flat bottom to 1/16” barbed to thread adaptor and screwed into the reservoir inlet port, completing the recycling perfusion loop. A plastic hollow bored 1/4” threaded screw is fitted into the final hole in the lid from which a Whatman Hepa-vent filtration unit (Sigma-Aldrich) was attached via 3 cm of 8 mm ID Marprene tubing (Watson-Marlow) allowing for gas exchange with the system.

Once assembled, the reservoir was filled with 20 mL 70% ethanol solution. The system was primed and left to sterilise at a flow rate of 10 µL/min for 18 hours. The system was drained of ethanol, and the bottle replaced with another containing 20 mL DMEM. The tubing was then primed, and the system washed at 30 µL/min for 6 hours. DMEM was drained and replaced with a bottle of complete cell media of volume ranging from 20 – 40 mL.

For seeding, each bioreactor was disconnected from the circuit and their end caps removed. 100,000 cells were inoculated into the lumen of the hollow fibre from the exposed ends. The ends were glued shut with Silcoset adhesive, the bioreactor flipped 180°, and then another layer of adhesive was applied. Once dry the fibre outlet was reopened and each bioreactor was re-fitted back into the circuit, and the system placed in an incubator at 37 °C and 5% CO_2. Media flow of 10 or 50 µL/min was initiated for 1, 3 or 6 days. A fully assembled bioreactor system in duplicate on the K’NEX support is shown in Figure 3.16. An alternative configuration using the same tubing, fittings and methodology was constructed for a non-recirculating variant with separate reservoirs for inlet and outlet media.

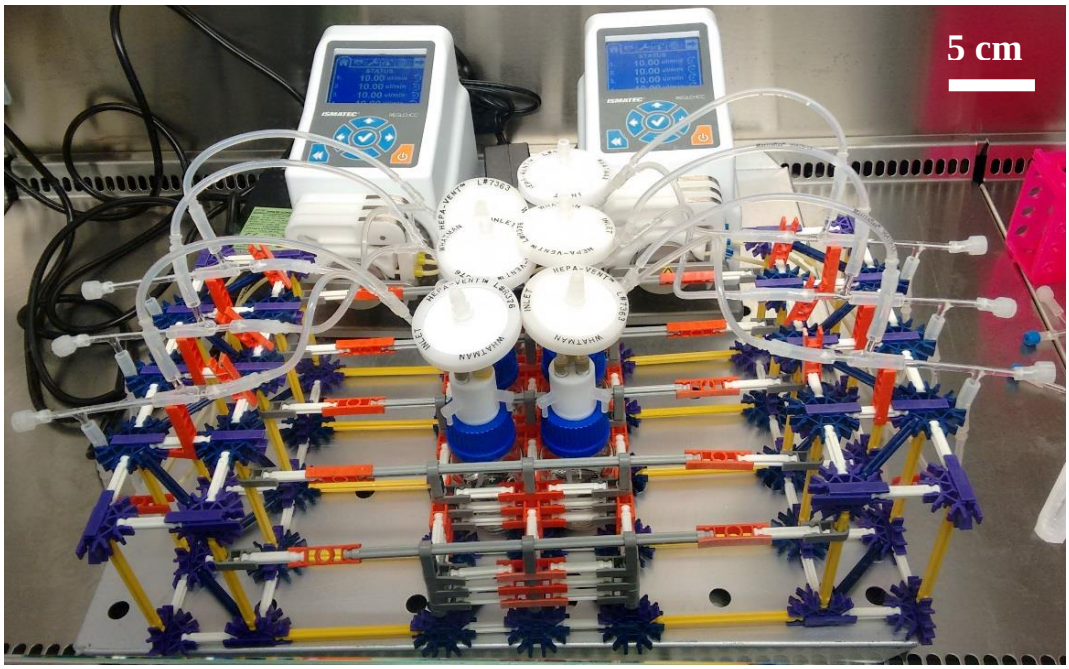

Figure 3.16 – Fully assembled bioreactor circuit (in duplicate).

At the desired time, the pump was stopped, the pump inlet tubing disconnected from the Omnifit lid and the plastic pump brace removed. The tubing and bioreactor were lifted to allow residual media to drain back into the reservoir. The reservoir, bioreactor and tubing were removed from the incubator and a media sample removed for testing. A syringe needle was used to cut the hollow fibre from the glass module, which was analysed for cell number and viability. The pump was then resumed to allow the experiment to continue for subsequent days on the remaining bioreactors.

3.4 ANALYITICAL METHODS

3.4.1 Cell Culture Analysis

Manual Cell Counting

A sample of cells in media solution was mixed in equal measure with trypan blue dye. 10 µL of this solution was pipetted into a fast read haemocytometer slide (Una Health) which contained a grid of squares visible under a light microscope at 10x magnification. Each 3 x 3 grid contained 0.1 µL, and the cells within this grid were manually counted using a handheld counter (Fisher) and scaled up to yield a cell concentration of the original sample. Cells with damaged membranes allowed the dye to penetrate into the cell cytoplasm and organelles, which were stained blue, indicating they were non-viable, and were excluded from the count unless experimentally relevant. Three to six separate samples were taken and an average was calculated. Cell concentration was calculated Equation 3.1:

$$Cell\ concentration\left[\frac{cells}{ml}\right] = \frac{Cell\ count\ \left[\frac{1}{x\ [grids]}\right]}{x\ [grids]} \times \frac{Trypan\ blue}{dilution\ factor} \times 10{,}000[mL]$$

Equation 3.1 – Calculation of cell concentration from manual counting

Picogreen Assay

Picogreen assay (Gibco Life Technologies) was used to quantify the presence of deoxyribonucleic acid (DNA) from attached cells on or within scaffolds. Samples of scaffold along with their attached cells were placed in 1x Tris & EDTA (TE) buffer (Invitrogen) and underwent two freeze-thaw cycles between -80 °C and 25 °C to lyse the cells. Picogreen reagent was diluted in sterile 1x TE buffer solution in a 1:200 ratio and 75 µL mixed in equal measure with the DNA/TE buffer solution in a well of a 96 well plate.

Samples of known concentrations of DNA were also mixed with the picogreen reagent solution in the same conditions in order to provide a calibration curve to compare the results to. Samples of known cell number also underwent the freeze-thaw cycle and were mixed with picogreen to form a standard curve of cell number verses picogreen absorbance. The well plate

was placed in a fluorospectrometer (NorthStar Scientific) at 480 nm excitation and 520 nm reading. The resulting absorbance reading was compared to the DNA standard curve (Figure 3.17), and the resulting DNA concentration was compared to the readings from the specific cell standard curve (Figure 3.18) to calculate the quantity of DNA that was present in each cell. Both standard curves were calculated from triplicate assays (n = 3) replicated on four separate days (N = 4). From this the overall number of cells attached was calculated, as well as the efficiency of attachment to the scaffold.

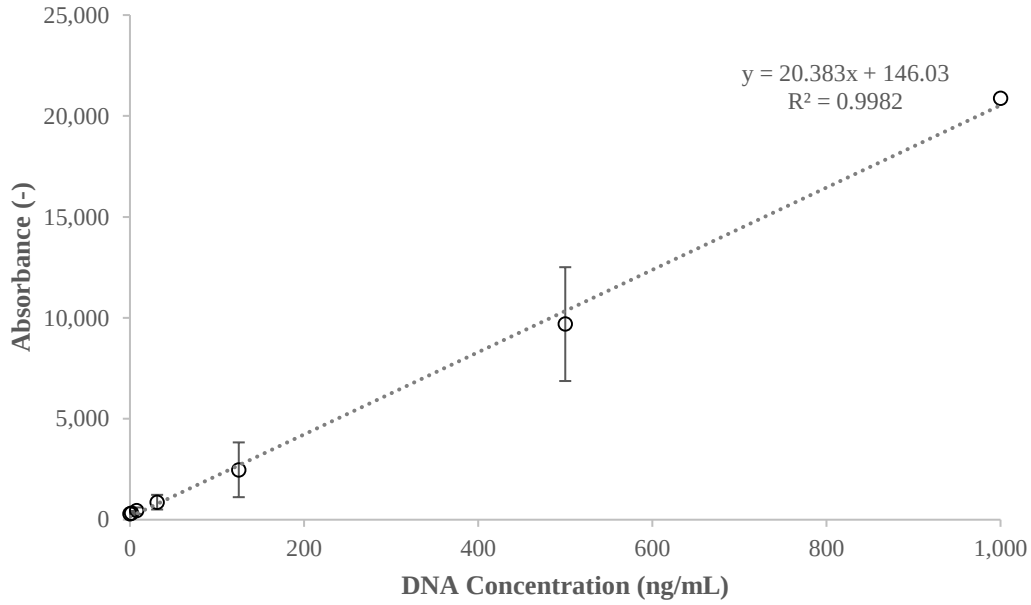

Figure 3.17 – DNA standard curve for picogreen assay (n=3, N=4, error = SD).

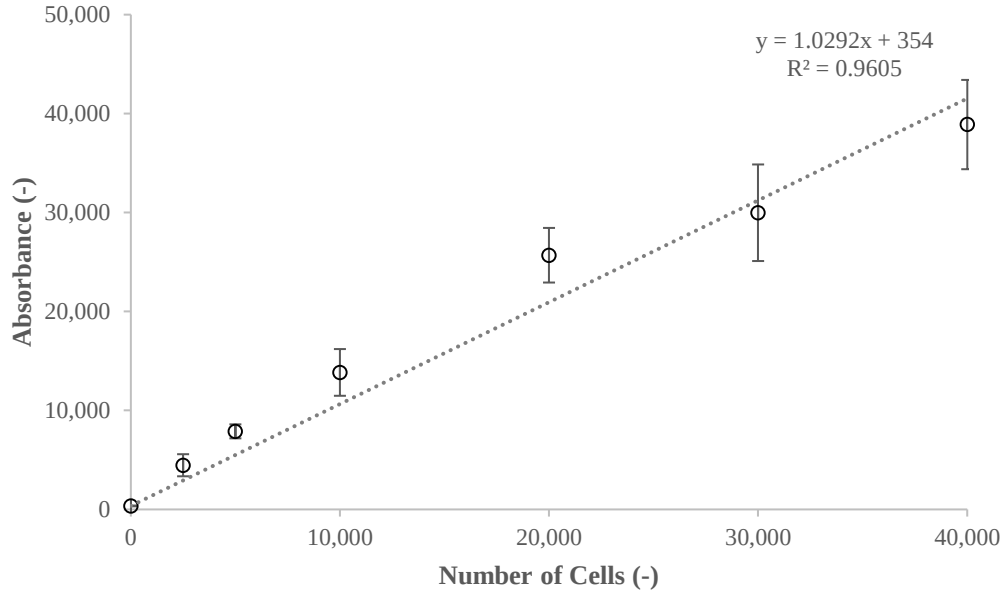

Figure 3.18 – MG63 cell line standard curve for Picogreen Assay (n=3, N=4, error = SD).

Dissolved O_2 and pH Readings

Media samples were tested for their dissolved oxygen content and pH to determine if any changes occurred as a result of cell proliferation or otherwise. When media bottles were removed from the HFB perfusion rig at the end the experiment outlined in Section 3.3.6, the valves in the "Q" Series Omnifit lids were shut. The media in the bottles was left to reach 25°C before testing. The lid was removed, the dissolved oxygen probe (Thermo-Scientific) input, and the bottle neck wrapped in Parafilm to maintain a seal. Readings are displayed on an Orion Versastar advanced electrochemistry meter (Thermo-Scientific) and were noted after stabilising over 5 minutes. This process was repeated with the pH probe (Eutech Instruments). Both probes were cleaned with ethanol and ddH_2O before and after use. Readings for oxygen and pH were used to characterise the health of the circulating media and determine if the system was infected. In-line readings of oxygen and pH within the ECS and the lumen of the HFB were not able to be taken.

3.4.2 Scaffold Analysis

SEM Imaging

Prior to being placed in a scanning electron microscope (SEM), samples were submerged in liquid nitrogen for one minute, removed, then cut using a scalpel into pieces no more than 5 mm in length for flat sheet samples, or 2 mm in height for hollow fibre cross sections. Scaffolds were mounted onto stubs using double sided conductive carbon tape (Agar Scientific), coated with gold using an Edwards Sputter Coater S150B (Edwards) and placed into a Joel JSM 648OLV SEM (Joel).

ImageJ Analysis

SEM images of porous scaffolds were analysed using ImageJ software (version 1.48). ImageJ allowed modification of raw SEM photos into binary black and white images to accentuate the contrast and differentiate pores on the surface, which ImageJ sized and counted. A macro was written to facilitate this process due to the large number of images to be analysed. Figure 3.19 shows a standard SEM image, and Figure 3.20 shows its final form after modification. An in depth tutorial can be found in Appendix B.

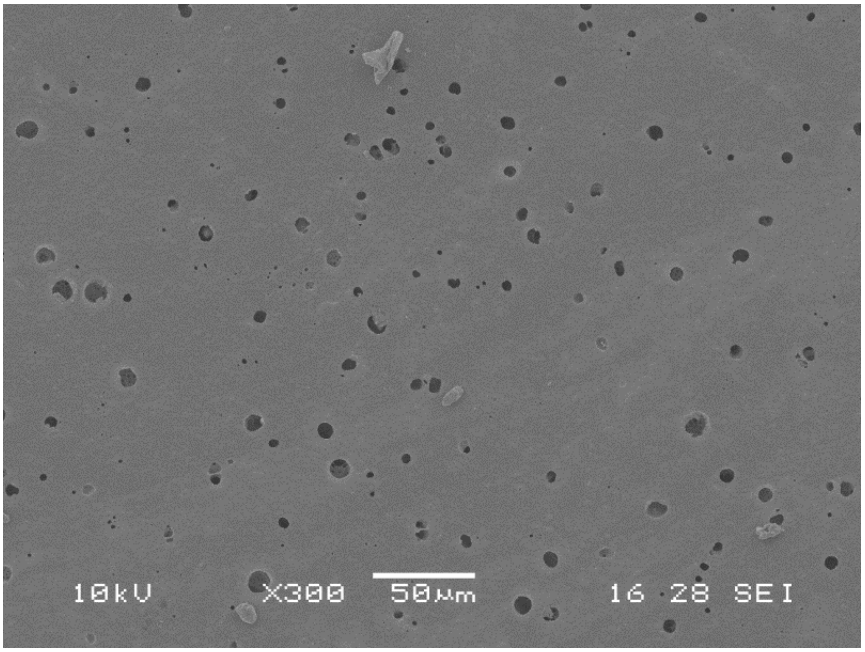

Figure 3.19 – An SEM image of porous PLGA.

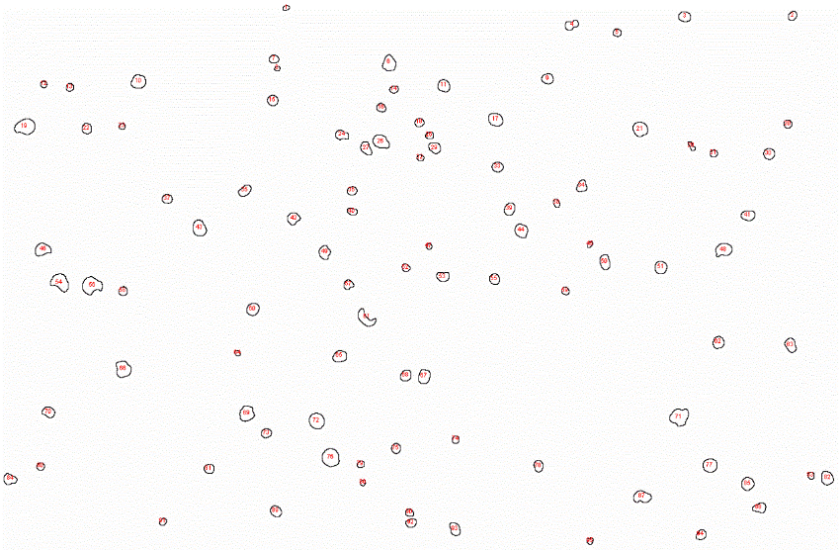

Figure 3.20 – An example of pore counting and sizing using ImageJ.

Gas Permeation

A bundle of three hollow fibres was potted into a cylindrical metal module using araldite glue (Huntsman) and supplied with a flow of N_2 at a set pressure via a sequence of metal pipes, fittings and pressure gauges (Swagelok) as shown in Figure 3.21. The bundle was glued such that N_2 passed through the central lumen at the inlet of the module, and exited radially through the fibre wall at atmospheric pressure, and not the fibre outlet (dead end mode). The flow rate of air (Q) exiting the module was measured using a bubble column (Hewlett-Packard) for 0 – 50 mL/min, an 'MOB 12000' rotameter (MPB) for 30 – 300 mL/min or a Platon NGCV rotameter (Platon) for 200 – 2000 mL/min.

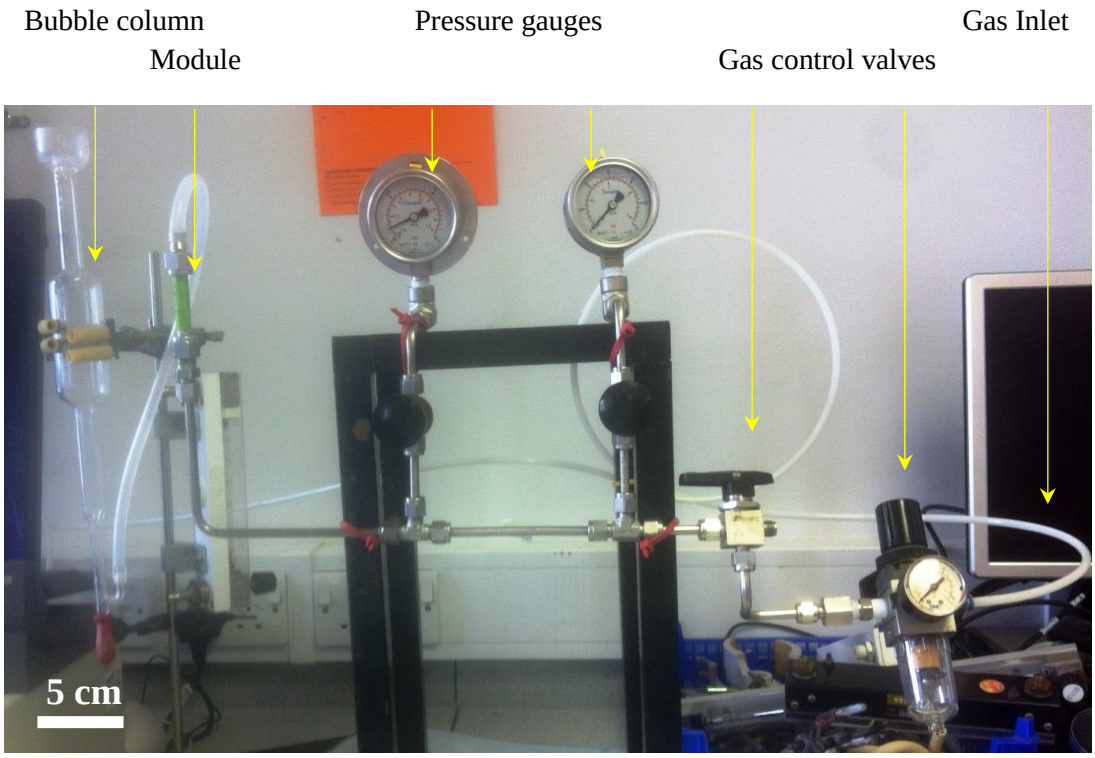

Figure 3.21 – Hollow fibre gas permeation apparatus.

This was repeated for at least five other inlet pressures ranging between 1.03 – 1.42 bar (absolute). Darcy's law (Equation 3.2) was used to calculate gas permeability κ_G of the hollow fibre, using its surface area (A), thickness, N_2 viscosity (μ) and pressure difference (ΔP) acting as the driving force.

$$Q = \left(\frac{\kappa_g A}{\mu}\right)\left(\frac{\Delta P}{x}\right)$$

Equation 3.2 – Darcy's law.

Liquid Permeation

A single hollow fibre was glued into a single glass bioreactor module as outlined in Section 3.3.5, leaving the hollow fibre lumen exposed. The bioreactor was connected to an apparatus, shown in Figure 3.22, allowing its liquid permeability to be determined. Liquid was pumped from a 1 L glass bottle (Fisher) through the hollow fibre lumen using a 205U peristaltic pump (Watson Marlow) with 1.42 mm ID PVC manifold tubing pump tubing (Watson Marlow). Liquid exiting the lumen was collected in a glass beaker on a set of weighing scales (Denver Instruments). Back pressure was applied using a needle valve (Swagelok) at the outlet. Liquid flow out of the ECS was controlled by slide clamps attached to silicone tubing connected at the bioreactor side ports. Pressure transducers (Omegadyne) were connected to the inlet and outlet of the bioreactor via a

T-piece (Cole-Parmer). The scales and pressure transducers were connected to a computer running Labview software (National Instruments), where the data was logged. Permeability was calculated using Darcy's Law (Equation 3.2).

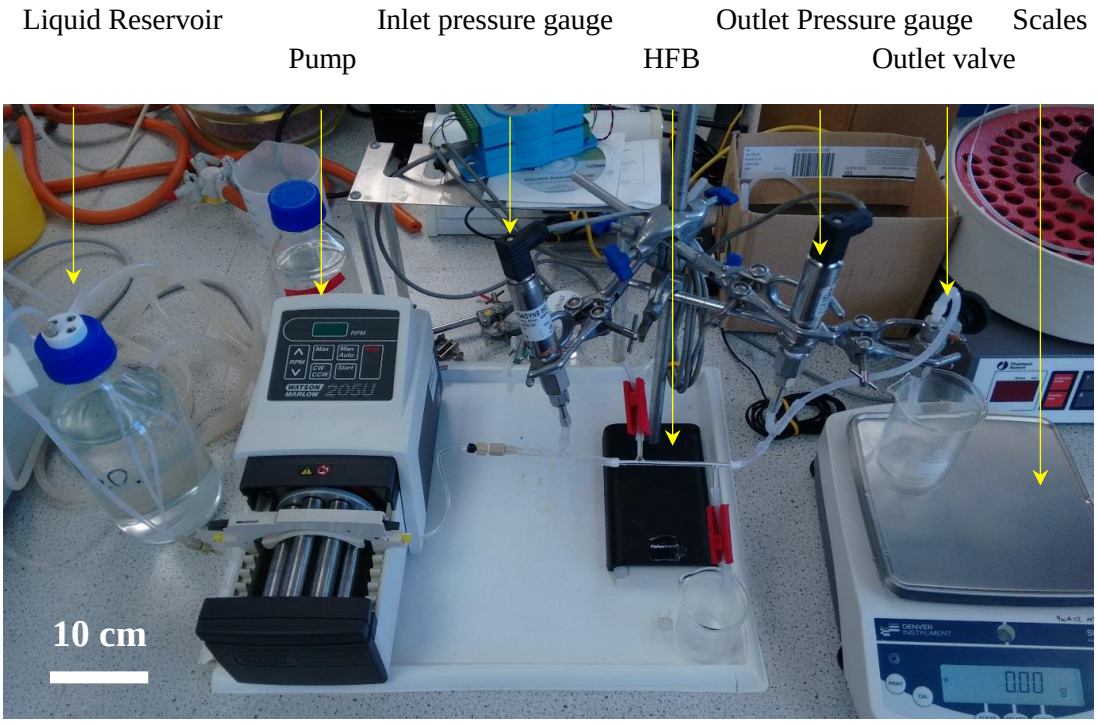

Figure 3.22 – Hollow fibre liquid permeation apparatus.

Flow rate was set to 1 ml/min and each experiment was run for 90 minutes. Prior to the experiment the pump was calibrated by pumping water though a non-porous hollow fibre bioreactor and the effluent mass measured on set of weighing scales. Mass readings were transferred to a data acquisition module and output on a computer display using LabVIEW software. A density value of the liquid used, dependant on ambient temperature, was manually written into the software to convert liquid mass to volume. The software accumulated data from the scales and pressure transducers every 0.5 seconds and output an average value dependent on the time interval set by the user. The larger the time interval, the more accurate the average measurement was. The time interval was set to 5 minutes.

The value for inlet flow rate of liquid on the pump was set in the software, which would match the calculated retentate outlet flow rate measured on the scales so long as no permeation through the membrane wall occurred. Discrepancies in retentate flow rate were attributed to liquid permeating through the membrane. This allowed calculation of retentate and permeate flow rates, as well as the volume fraction of each stream.

3.5 STATISTICAL METHODS

Captions describing experimental results in figures or tables display the number of experimental trials (*n*), replicates (*N*) and error. All error bars are as described in their respective figure captions. Error is either standard deviation (SD) from the mean due to uncertainty in repetition of experimental results, or a percentage value calculated from the propagation of uncertainty from performing calculations using several values derived from experimental, measurement or human error. Error propagation is calculated as shown in Equation 3.3 and Equation 3.4:

If: $Z = (a \pm \delta a) + (b \pm \delta b) - (c \pm \delta c) - (d \pm \delta d)$

Then: $\delta Z = \sqrt{(\delta a)^2 + (\delta b)^2 + (\delta c)^2 + (\delta d)^2}$

Equation 3.3 – Error propagation when adding or subtracting values.

If: $Z = \frac{(a \pm \delta a)(b \pm \delta b)}{(c \pm \delta c)(d \pm \delta d)}$

Then: $\delta Z = Z\sqrt{\left(\frac{\delta a}{a}\right)^2 + \left(\frac{\delta b}{b}\right)^2 + \left(\frac{\delta c}{c}\right)^2 + \left(\frac{\delta d}{d}\right)^2}$

Equation 3.4 – Error propagation when multiplying or dividing values.

A Student's t-test was used to determine significant differences between two data sets and a one way analysis of variance (ANOVA) was used for comparison between three or more independent samples using a post hoc Tukey range test. Samples were considered significantly different if there was a 95% confidence ($P < 0.05$) that this was true. Analyses were carried out using SigmaPlot (Systat) software.

CHAPTER FOUR: CELL ATTACHMENT ON EXTERNAL HOLLOW FIBRE SURFACES

4.1 INTRODUCTION

When growing cells in a bioreactor, it is important to ensure that there is a known initial quantity of cells within the bioreactor to obtain a predictable quantity of product. This is especially important when cultivating rare or expensive cell populations. In the case of the works described in this thesis, 50 million mesenchymal stem cells (MSCs) need to be grown for use as a traditionally administered cell therapy for the regeneration of human heart myocardium. As previously described in Section 2.3.1, MSCs have been utilised within biodegradable scaffolds for use in heart tissue engineering applications. Purchasing these cells can be costly, and the isolation of these cells from human patients provides yields of 812,800 ± 318,400. Because of their clinical usefulness and their cost it is paramount to ensure a high and consistent level of initial cell attachment onto the scaffold in order to minimise any wastage of these cells. The scaffolds in question are polymeric hollow fibres. Hollow fibres are manufactured as described in Section 3.3.1 and placed within a bioreactor module for external seeding as described in Section 3.3.5 and shown in Figure 3.5.

When seeding on flat sheet membranes, a known concentration of cells within a solution of growth media is inoculated onto the surface and left for a set time. During this time the cells will sink through the liquid and reach the membrane at the bottom where they will attach and be reasonably well distributed. Attempting to seed onto a hollow fibre within a bioreactor (HFB) is more complex as the cells will once again sink due to the force of gravity, but can potentially miss the scaffold completely while settling. This leads to poor utilisation of the inoculated cells and rates of cell attachment of around 20%. The hollow fibre is a cylindrical 3D (three-dimensional) scaffold located throughout the entire length of the bioreactor, leading to a more complex seeding methodology compared to with 2D (two-dimensional) flat sheet scaffolds if similar degrees of cell attachment are desired. Cells which fail to contact with the hollow fibre and fall to the bottom of the HFB have no possibility of attaching to the scaffold and are wasted if the reactor is kept in static conditions. HFBs seeded with 812,800 ± 318,400 MSCs with 20% efficiency would take 12.6 ± 5.2 days to grow to 50 million cells. If 100% efficiency could be achieved, this would reduce growth time to 9.1 ± 4.0 days. Therefore there is scope to seek alternative methods for seeding cells in HFBs. This chapter proposes a dynamic seeding regime to encourage a greater degree of cell mixing in the bioreactor and allow multiple opportunities for cells to contact the hollow fibre and potentially attach. Such an investigation has not been attempted before, making this a novel endeavour.

A number of cell attachment experiments were undertaken using MG63 human osteosarcoma cells on scaffolds of poly (lactic-co-glycolic) acid (PLGA), with a 75:25 poly(lactic acid) (PLA) to poly(glycolic acid) (PGA) ratio, in a solution with N-Methyl-2-pyrrolidone (NMP) solvent. Polymer to solvent ratio is 20:80 by weight. As a control, cell attachment was done on static flat sheet membranes placed within custom well plates as described in Section 3.3.4 to confirm the ability of cells to attach to the PLGA material over a number of different time frames. A series of static cell attachment experiments was then done on a single PLGA hollow fibre scaffold (Figure 4.1). Afterwards a series of dynamic cell attachments were conducted by attaching the HFB onto a rotating drum (Figure 4.2) at a horizontal, diagonal or vertical orientation set at of 2, 6 and 8 rotations per minute (RPM) (angular velocities of 0.25, 0.63 and 0.86 s^{-1} respectively). Finally HFBs were attached to a MACSmix rotator drive (Figure 4.3) that rotated for 1 minute at 10 RPM (1.05 s^{-1}) and paused for 4 minutes. Seeded single fibre HFB modules were placed into 50 mL centrifuge tubes to allow for easy placement onto these devices. A comparison was drawn with the static methods and the most effective combination of conditions for dynamic cell attachment was found. Afterwards experiments on bundles of hollow fibres were conducted to determine how scale up of the system affects cell attachment.

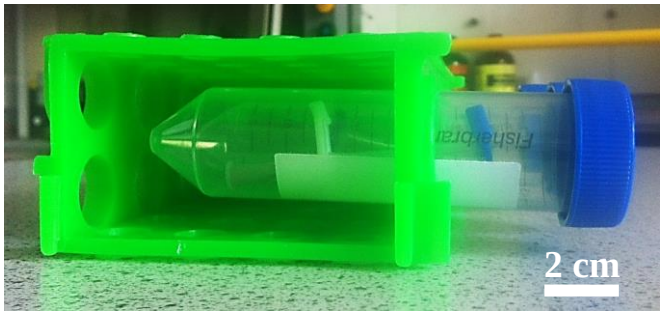

Figure 4.1 – Bioreactors in a static position.

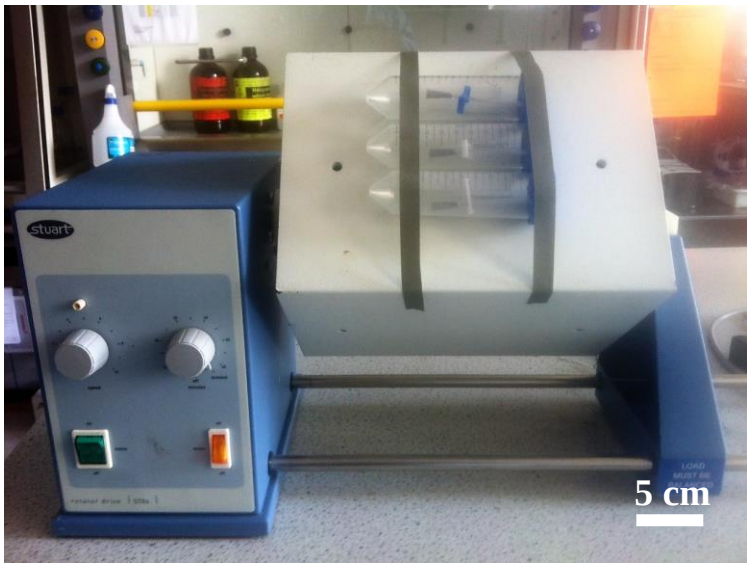

Figure 4.2 – Bioreactors attached to a Stuart STR4 rotator drive.

Figure 4.3 – Bioreactors attached to a MACSmix periodic rotating device.

It was hypothesised that a novel dynamic regime would allow a greater degree of cell attachment onto the hollow fibre scaffold due to the increased number of opportunities a cell would have to make contact with the scaffold. The aim of this chapter was to determine if a novel dynamic cell seeding regime provided a greater rate of cell attachment on hollow fibre scaffolds compared to static seeding. This aim was achieved by conducting seeding experiments on flat sheet scaffolds to determine the most efficient time for cell attachment, followed by studies on single HFB modules seeded statically and dynamically to find what parameters affected attachment, then concluding with work on dynamic seeding of a hollow fibre bundle in a bioreactor.

4.2 CELL ATTACHMENT THEORY

4.2.1 Static Seeding

Single Hollow Fibre Modules

The maximum rate of static cell attachment in the HFB system can be predicted by determining the number of cells that come into contact with the hollow fibre. As the hollow fibre does not take up the entire volume of the bioreactor and the cells are left to settle due to gravity, the cells receive one opportunity to come into contact with the hollow fibre. The collective area surrounding the hollow fibre within the bioreactor is the extra-capillary space (ECS). Assuming the inoculated cells are well mixed and settle directly downwards there will be small fraction of cells located above the scaffold that will fall directly onto it and a larger fraction that will miss the scaffold entirely if located adjacent to or beneath the module. This is illustrated in in Figure 4.4, along with the dimensions of a single fibre bioreactor. The length of the hollow fibre (L_F) in this system is 35.0 ± 0.1 mm.

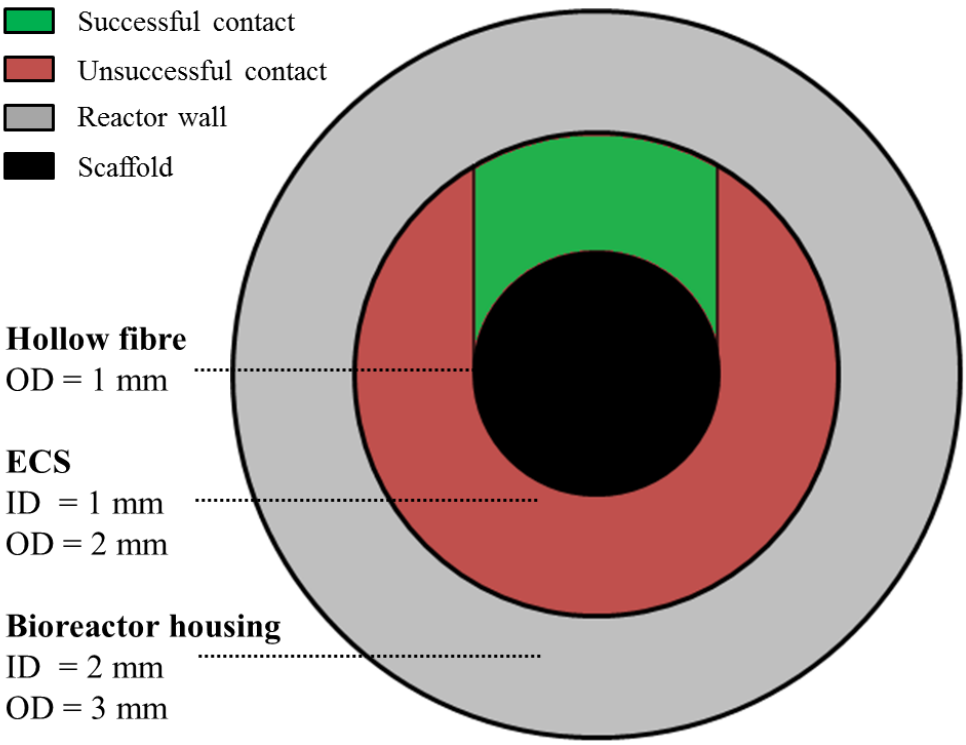

Figure 4.4 – Cross section of a single HFB module displaying the predicted cell contact area.

The volume of the green shaded region in Figure 4.4 can be calculated from shape geometry using trigonometry. While the cells are settling in three dimensions, taking the cross section of the HFB will yield an area that is proportional to the overall volume of that section. The areas in question are labelled in Figure 4.5 below:

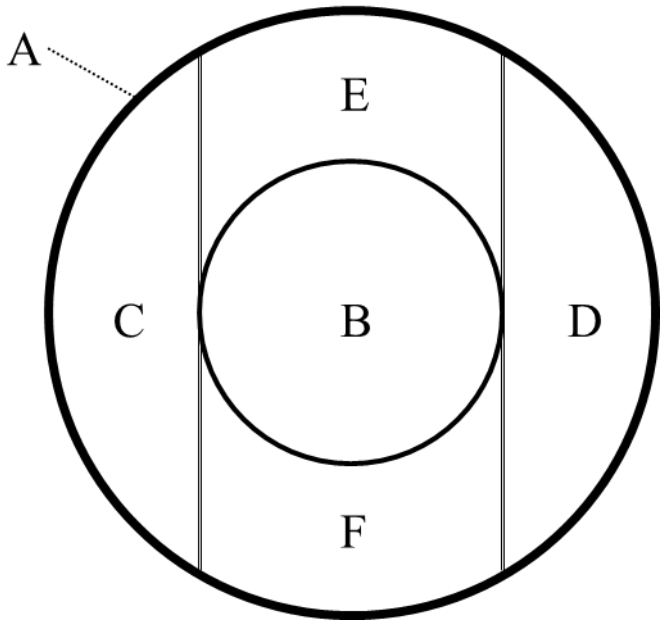

Figure 4.5 – Single HFB module geometry labelled in segments.

Area A is the cross sectional area of the inner wall of the HFB, with a diameter of 2.00 ± 0.05 mm. Area B is the cross sectional area of the hollow fibre with an outer diameter of 1.00 ± 0.05 mm. Areas C and D are chords of equal area that touch the outermost points of Area B while moving vertically downwards. Areas E and F remain, with Area E being the region of interest directly above the hollow fibre. This area is calculated in Equation 4.1, with r_{OF} representing the outer fibre radius, and r_{IB} representing the inner bioreactor wall radius.

$$Area\ A = \pi r_{IB}^2 = \pi 1^2 = \pi$$

$$Area\ B = \pi {r_{OF}}^2 = \pi 0.5^2 = 0.25\pi$$

$$Area\ C = \frac{r_{IB}^2}{2}\left(\frac{\theta\pi}{180} - \sin\theta\right)$$

$$Area\ D = \frac{r_{IB}^2}{2}\left(\frac{\theta\pi}{180} - \sin\theta\right)$$

$$Area\ E = \text{Area } A - \text{Area } B - \text{Area } C - \text{Area } D - \text{Area } F$$

$Area\ F = Area\ E$, therefore:

$$\boldsymbol{Area\ E = \frac{\pi - 0.25\pi - 2\frac{r_{IB}^2}{2}\left(\frac{\theta\pi}{180} - \sin\theta\right)}{2}}$$

Equation 4.1 – Derivation of Area E to determine theoretical cell attachment.

The angle (θ) in Equation 4.1 is the central angle of the chord (c) within the circle. Area D is a circle segment that can be calculated using the internal radius of the bioreactor (r_{IB}) and the central angle of the segment. With reference to Figure 4.6 this angle can be calculated as shown in Equation 4.2:

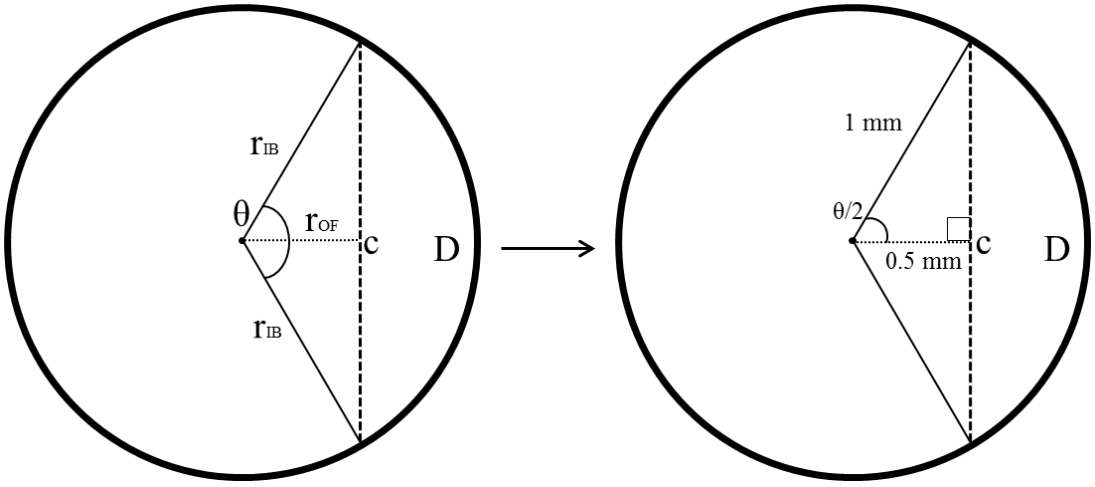

Figure 4.6 – A representation of the variables required to calculate segment area in a single HFB module.

$$cos\left(\frac{\theta}{2}\right) = \frac{Adjacent}{Hypotenuse}$$

$$\frac{\theta}{2} = \cos^{-1}\left(\frac{0.5 \pm 0.05}{1 \pm 0.05}\right) = 60°$$

$$\boldsymbol{\theta = 120° \pm 3°}$$

Equation 4.2 – Calculation of the segment angle of a chord.

By inserting the known dimensional values of the HFB system, the segment Area E can be calculated, and by multiplying the segment area by the hollow fibre length (L_F,) the volume of the segment can be found, as shown in Equation 4.3:

$$Area\ E = \frac{\pi - 0.25\pi - 2\frac{(1 \pm 0.05)^2}{2}\left(\frac{(120 \pm 3)\pi}{180} - \sin(120 \pm 3)\right)}{2}$$
$$= 0.564 \pm 0.104\ mm^2$$

$$Volume\ E = Area\ E \times L_F$$

$$Volume\ E = 0.564 \pm 0.104\ [mm^2] \times 35 \pm 0.05\ [mm]$$

$$\boldsymbol{Volume\ E = 19.7 \pm 3.6\ mm^3}$$

Equation 4.3 – Calculation of available ECS volume for cells to naturally settle onto the hollow fibre.

Volume E can then be taken as a percentage of the total available volume in the ECS:

$$Cell\ Space = (Area\ A - Area\ B) \times L_F$$

$$Cell\ Space = (\pi - 0.25\pi)[mm^2] \times 35 \pm 0.05[mm]$$
$$= 82.5 \pm 0.12\ [mm^3]$$

$$Volume\ E = \frac{19.7 \pm 3.6\ [mm^3]}{82.5 \pm 0.12\ [mm^3]} \times 100\%$$

$$\boldsymbol{Volume\ E = 24\% \pm 4\%}$$

Equation 4.4 – Calculation of available ECS percentage for cells to naturally settle onto the hollow fibre.

Assuming that: the hollow fibre is completely straight and resides in the very centre of the bioreactor, the cells in the media are well mixed throughout the entire cell space and do not interact with one another, and that cells settle due to the force of gravity directly downwards, this model indicates that a maximum 24% ± 4% of cells will have a chance to attach to the hollow fibre in this module. However this does not take into account the fact that cell attachment on the hollow fibre will become more difficult the steeper the gradient of the

available surface is. This means that cells that make fibre contact close to the chords shown in Figure 4.5 will be unlikely to attach. Therefore maximum cell attachment is likely to be smaller than 24% ± 4%

Multi Hollow Fibre Modules

Utilising the same methodology for a single hollow fibre in a bioreactor, the likelihood of a cell making contact with a bundle of hollow fibres in a larger bioreactor can be calculated.

At this point it was important to outline a new region of interest, the hollow fibre zone (HFZ). The HFZ is defined as the area in the centre of the bioreactor which may contain a hollow fibre. In the multi-fibre experiments shown later in this chapter, five hollow fibres were placed in the bioreactor through holes of radius 2.50 ± 0.05 mm at either end as described in Section 3.3.5. From this it is assumed that the cylinder which could be made from the hole of this radius along the length of the bioreactor is a volume where a hollow fibre can reside during the experiment; however it is anticipated that this method will over-estimate the area available for cell contact via gravity settling.

It was important to establish this volume because the hollow fibres were not placed into the bioreactor in the exact same position each time i.e. the bioreactors were not axisymmetric. The theoretical efficiency of any cell attachment is dependent on the cells reaching this HFZ, which is shown in the cross section in Figure 4.7:

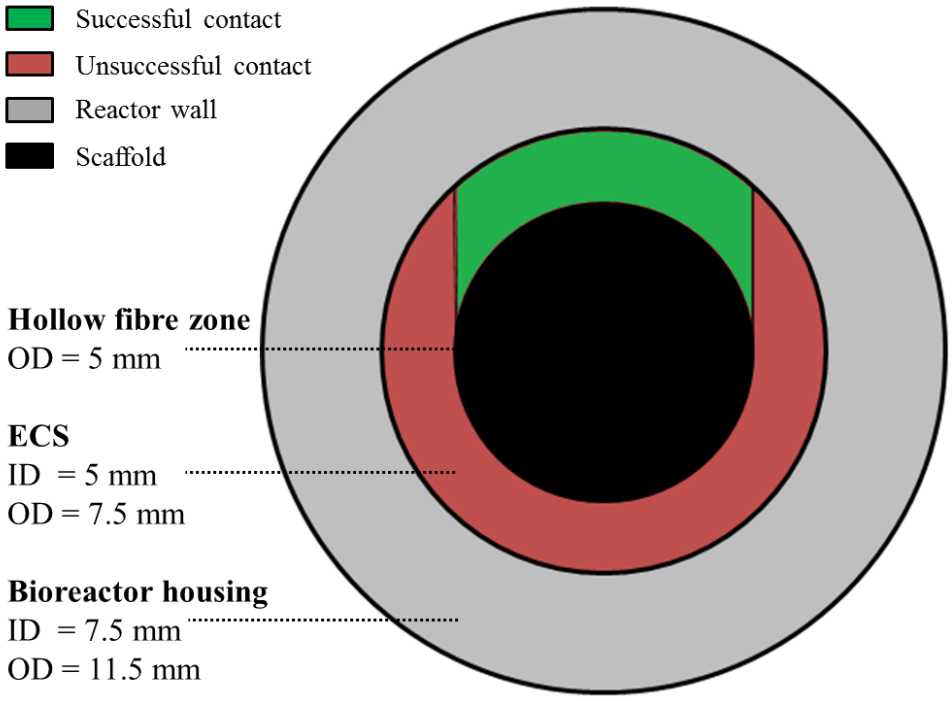

Figure 4.7 – Cross section of a multi HFB module displaying the predicted cell contact area.

Again, the area in green represents the space a cell must be located in order to have an opportunity to attach to the hollow fibre. Using the same equations for a single fibre bioreactor, the green area in Figure 4.7 equates to 30% ± 1%. of the total available volume for cells to reside after inoculation. Step by step calculation of this value is shown in Appendix C.

This value is dependent on the same assumptions as stated for the single hollow fibre bioreactor module: the hollow fibres are completely straight and reside in the very centre of the bioreactor, and the cells in the media are well mixed throughout the entire cell space and do not interact with one another. This model indicates that a maximum 30% ± 1%. of cells will have a chance to attach to a hollow fibre but cell attachment is likely to be smaller than this due to low likelihood of attachment at extreme gradients near the chords of the HFZ.

Gravity Settling of Cells

While it has been assumed that the cells are well mixed, it is also important to consider that cells may be hindered in their rate of settling due to cell-cell collisions. To determine this, an unhindered settling velocity must first be obtained. Settling velocity can be calculated by conducting a force (*F*) balance on a single cell as shown in Figure 4.8 and using cell, liquid and system properties summarised in Table 4.1.

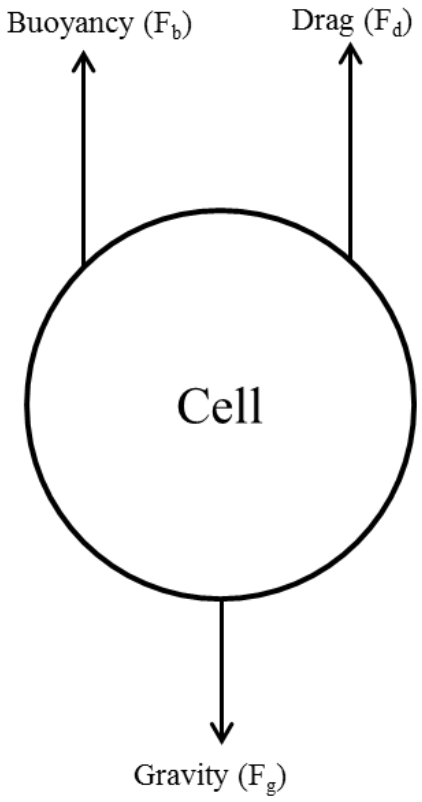

Figure 4.8 – A force balance on a single cell.

Table 4.1 – Values of various parameters in the force balances.

	Property	Value	Error	Units	Source
Cell	Radius (r_C)	1.79E-05	*5%*	m	(Pautake *et al.*, 2004)
	Density (ρ_C)	1,115	*1%*	kg/m^3	(Grover *et al.*, 2011)
	Volume (V_C)	2.38E-14	*9%*	m^3	Derived
	Mass (M_C)	2.65E-11	*9%*	kg	Derived
Media	Density (ρ_L) at 20 °C	1,000	*1%*	kg/m^3	(Invitrogen, 2015)
	Viscosity (μ_L) at 20 °C	9.80E-04	*1%*	kg/(m.s)	
System	Gravity (g)	9.81	*1%*	m/s^2	Constant

After inoculation each cell has an opportunity to settle to the bottom of the bioreactor due to gravity (F_g), but each cell is resisted by its drag through the liquid (F_d) and its intrinsic buoyancy (F_b). As the cells have very small diameters and are moving in liquid of low viscosity it has been assumed that the cell Reynolds number (Re_C) is less than 0.2, therefore the Stoke's drag force is equal to $6\pi r_C \mu_L u_C$ (Richardson *et al.*, 2002), with r_C equal to the radius of a spherical cell, μ_L being the viscosity of the cell media and u_C the cell settling velocity. This assumes that the cell in the fluid is subjected to laminar flow, that the cell is a perfectly smooth and ridged sphere, and that the cells do not collide with one another (Richardson *et al.*, 2002).

The resulting force acting on each cell is calculated by subtracting cell drag and buoyancy forces from gravitational force. Force is equal to a mass of a body multiplied by the applied gravity, and mass is equivalent to the product of the volume and density. At a uniform settling velocity resultant force is zero (Richardson *et al.*, 2002). Equation 4.5 shows how a force balance on a cell can be re-arranged to determine the cell settling velocity (u_C), using a volume of a sphere to express the volume of a cell with a known radius:

$$Resultant\ force \quad = F_g - F_b - F_d$$

$$0 \quad = V_C\ \rho_C\ g - V_C\ \rho_L\ g - 6\ \pi\ r_C\ \mu_L\ u_C$$

$$6\ \pi\ r_C\ \mu_L\ u_C = \frac{4}{3}\ \pi\ r_C^3 (\rho_C - \rho_L)\ g$$

$$u_C = \frac{2\ r_C^2}{9\ \mu_L} (\rho_C - \rho_L) g$$

Equation 4.5 – Derivation of cell settling velocity equation.

The values shown in Table 4.1 are inserted into the Equation 4.5 to yield the cell settling velocity (Equation 4.6):

$$u_C = \frac{2 \times (1.79 \times 10^{-5})^2 [m]^2}{9 \times (9.80 \times 10^{-4}) \left[\frac{kg}{m.s}\right]} \times (1115 - 1000) \left[\frac{kg}{m^3}\right] \times 9.81 \left[\frac{m}{s^2}\right]$$

$$\boldsymbol{u_C = 8.14 \times 10^{-5} \pm 0.59 \times 10^{-5}\ m/s}$$

Equation 4.6 – Calculation of cell settling velocity.

As the cell of diameter 3.58E-05 (±5%) m (d_C) is moving through a liquid of density 1,000 (± 1%) kg m^{-3} and viscosity 9.80E-04 (± 1%) kg m^{-1}s^{-1} at the above settling velocity, the particle Reynolds number of the cell (Re_c) can be calculated and shown to be less than 0.2 in Equation 4.7. This confirms the previous assumption to be true and validates the settling velocity calculation:

$$\boldsymbol{Re_C = \frac{\rho_L u_C d_C}{\mu_L}}$$

$$Re_C = \frac{1000 \left[\frac{kg}{m^3}\right] \times 8.14 \times 10^{-5} \left[\frac{m}{s}\right] \times 3.58 \times 10^{-5} [m]}{9.80 \times 10^{-4} \left[\frac{\text{kg}}{\text{m.s}}\right]}$$

$$\boldsymbol{Re_C = 0.003 \pm 3 \times 10^{-4}}$$

Equation 4.7 – Calculation of particle Reynolds number of a settling cell.

Single Hollow Fibre Modules

Given that a cell travels a known distance from the top of the bioreactor to the bottom, the maximum settling time can be calculated using Equation 4.8 knowing the settling velocity and the inner radius of the single HFB module:

$$Maximum\ Settling\ Time = \frac{Distance\ (Diameter)}{Velocity}$$

$$Maximum\ Settling\ Time = \frac{2 \times 0.001\ [m]}{8.14 \times 10^{-5} \left[\frac{m}{s}\right]}$$

$$\boldsymbol{Maximum\ Settling\ Time = 25 \pm 2\ s}$$

Equation 4.8 – Calculation of maximum settling time in a single HFB module.

It takes 25 ± 2 seconds for a cell at the very top of the single HFB module to fall 2 mm to the very bottom. As they descend any given cell may fall on top of a hollow fibre and subsequently attach. It is assumed the rest of the cells accumulate at the bottom of the reactor. Given that the unhindered settling velocity is now known, the hindered settling velocity can be determined using Equation 4.9:

$$\boldsymbol{u_H = u_C(1-f)^y}$$

Equation 4.9 – Equation for hindered settling velocity (Richardson and Zaki, 1997)..

Where u_H is the hindered settling velocity, u_C is the calculated cell settling velocity without hindering effects, y is an exponent dependent on the cell particle Reynolds number, and f is the volume fraction of the cells in suspension. For a Reynolds number less than 0.2, y has been empirically derived to be 4.65 (Richardson and Zaki, 1997). The cell volume fraction can be calculated by the division of the total volume of all the cells in the bioreactor by the volume of media within the bioreactor (Equation 4.10). For single HFB modules, 110,000 ± 18,480 cells were to be inoculated in a volume of 82.5 mm^3 media at a surface density of 100,000 ± 16,800 cells/cm^2 for external seeding on a single PLGA hollow fibre 0.5 ± 0.05 mm in outer radius, 35 ± 0.05 mm in length and surface area of 1.1 ± 0.2 cm^2:

$$f = \frac{Total\ cells\ \times Volume\ of\ one\ cell}{Volume\ of\ media\ in\ bioreactor}$$

$$f = \frac{110{,}000\ [cells] \times \frac{4}{3}\pi \times (1.79 \times 10^{-5})^3 [m^3]}{8.25\ \times 10^{-8}\ [m^3]} = 0.032\ \pm 0.007$$

Equation 4.10 – Calculation of the volume fraction of cells within the inoculant.

Once found, f, along with all other factors can be placed into the hindered cell velocity equation (Equation 4.9) to calculate a value for hindered cell velocity, shown in Equation 4.11:

$$u_H = u_C(1-f)^y$$

$$u_H = 8.14 \times 10^{-5} \left[\frac{m}{s}\right] \times (1-0.032)^{4.65}$$

$$\boldsymbol{u_H = 7.00 \times 10^{-5}\ \pm 1.60\ \times 10^{-5}\ m/s}$$

Equation 4.11 – Calculation of hindered settling velocity in a single HFB module.

This hindered settling equation is an excellent tool in describing the characteristics of sedimenting concentrated suspensions (Di Felice and Kehlenbeck, 2000). In the single hollow fibre module, hindered settling is present and reduces the settling velocity by 14%. Using this new cell settling velocity value in Equation 4.8, calculates that this increases maximum

settling time to 29 ± 7 seconds. Such a change is due to the high cell concentration in this model, and would not be as apparent at smaller cell concentrations.

Multi Hollow Fibre Modules

Following the same methodology, cell settling properties can be calculated for multi HFB modules. The physical properties of the cells and the media remain unchanged, and as such the maximum settling velocity remains at 8.14E-05 ± 0.59E-05 m/s. However, these bioreactors do have a larger inner radius of 3.75 ± 0.05 mm. The maximum settling time from the top of a multi HFB module to the bottom is recalculated using Equation 4.8 and is 92 ± 7 s for this system.

As they descend, any given cell may fall on top of a hollow fibre or within the gaps between individual fibres and subsequently attach. It is assumed the rest of the cells accumulate at the bottom of the reactor. The volume of cell inoculant must be greater to accommodate for the larger volume in the ECS of multi HFB modules, which requires a recalculation of the hindered settling velocity. 735,000 ± 69,090 cells were to be seeded in an inoculant of 4.5 mL media, at a density of 30,000 ± 2,820 cells/cm^2 for attachment on a bundle of five hollow fibres 0.65 ± 0.05 mm in outer radius, 120 ± 0.05 mm in length, and with total external surface area of 24.5 ± 1.9 cm^2. Using Equation 4.10, the volume fraction of cells in the inoculant (*f*) is calculated to be 0.004 ± 6.50E-04, and thus using Equation 4.11 the hindered settling velocity is 7.99E-05 ± 1.42E-05 m/s. This is a reduction in settling velocity of 2%, owing to the smaller concentration of cells within the whole bioreactor volume. A summary of the values calculated throughout this section is shown in Table 4.2:

Table 4.2 – List of system parameters and calculated values for single and multi HFB modules.

Parameter	Single		Multi	
	Value	Error (±)	Value	Error (±)
HFB inner radius (mm)	1.0	*0.05*	3.75	0.05
Fibre outer radius (mm)	0.5	*0.05*	0.65	0.05
Fibre length (mm)	35	*0.05*	120	0.05
Number of fibres (-)	1	-	5	-
Total external surface area (cm^2)	1.1	*0.2*	24.5	1.9
Cell number (-)	110,000	*18,480*	735,000	69,090
Inoculant Volume (mL)	0.0825	*0.0058*	4.5	0.3
Cell surface density (cells/cm^2)	100,000	*16,800*	30,000	2,820
Cell volume fraction (-)	0.032	*0.007*	0.004	6.5E-04
Unhindered settling velocity (m/s)	8.14E-05	*0.59E-05*	8.14E-05	0.59E-05
Unhindered maximum settling time (s)	25	*2*	92	7
Hindered settling velocity (m/s)	7.00E-05	*1.60E-05*	7.99E-05	1.42E-05
Hindered maximum settling time (s)	29	*7*	94	7
Percentage of cells to contact the hollow fibres	24%	*4%*	30%	1%

4.2.2 Dynamic Seeding

Cell settling velocity can be calculated in the same way as shown in the previous section, however for these experiments it is important to try and explain theoretically how centrifugal forces affect the movement of cells, and hence discover where they may travel during mixing and if they contact the hollow fibres. When attached to a rotating device gravity pulls the cells downwards to the bottom of the bioreactor (F_g), but this is counteracted by a centrifugal force (F_c) pushing the cells to the outermost point of the bioreactor, and the buoyancy force (F_b) of the media around the cell. A diagram of these forces on a particle in the rotating HFB system is shown in Figure 4.9.

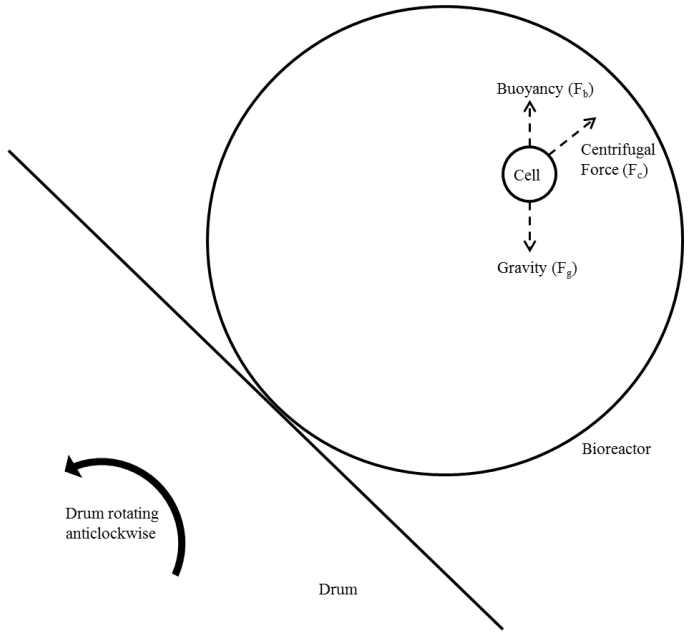

Figure 4.9 – Forces acting upon an individual cell at a specific time point (not to scale).

When a particle is moving in a liquid as the result of centrifugal action, gravitational forces are relatively small and can be neglected (Richardson *et al.*, 2002). The movement of cells due to centrifugal action is calculated by replacing gravitational acceleration (g), with centrifugal acceleration ($R\omega^2$) in the force balance, whilst assuming that the inertial acceleration terms can be neglected (Richardson *et al.*, 2002). This follows the same principle as the derivation for settling velocity in Equation 4.5 utilising values from Table 4.1:

$$u_r = \frac{2.r_C^2}{9.\mu_L}(\rho_C - \rho_L)g \quad \xrightarrow{\text{for a given time}} \quad \frac{dR}{dt} = \frac{2\,r_C^2}{9\,\mu_L}(\rho_C - \rho_L)R.\omega^2$$

Equation 4.12 – Conversion of cell settling equation to account for centrifugal forces.

u_r is equivalent to the change in radial position over time, or *dR/dt.*, and R is the radius of rotation which is the sum of the drum radius, bioreactor thickness and the distance travelled during time t. In order to standardise the speed of rotating devices and allow comparisons to

be drawn with other studies, their RPM setting is converted into the linear velocity (v) and angular velocity (ω) using Equation 4.13 and Equation 4.14 respectively. An error of 1 second is assumed when determining RPM, and measurements of distance have an error of 1 mm

$$Linear\ velocity\ (v) \quad = \quad \frac{Distance}{Time} \quad = Circumference \times RPM$$

Equation 4.13 – Linear velocity equation.

$$Angular\ velocity\ (\omega) \ = \ \frac{Linear\ velocity}{Radius}$$

Equation 4.14 – Angular velocity equation.

For the dynamic cell seeding experiments in this chapter, the Stuart STR4 rotator drum was set to one of three rotational velocities. RPM was manually tracked and converted into angular velocity using Equation 4.13 and Equation 4.14 to allow the calculation of cell settling velocity at a given angular velocity. As before with static cell settling, cell hindrance is taken into account using Equation 4.9 to calculate an accurate settling velocity. This data is shown in Table 4.3:

Table 4.3 – Calculated initial hindered settling velocity of cells in HFBs attached to a rotating drum.

Module	RPM		Linear Velocity (m/s)		Angular Velocity (s^{-1})		Initial Hindered Settling Velocity (m/s)	
	Value	*Error*	Value	*Error*	Value	*Error*	Value	*Error*
Single	2.4	*2%*	0.023	*2%*	0.25	*3%*	4.13E-08	*23%*
	6.0	*2%*	0.057	*2%*	0.62	*3%*	2.58E-07	*23%*
	8.2	*2%*	0.078	*2%*	0.86	*3%*	4.82E-07	*23%*
Multi	2.4	*2%*	0.023	*2%*	0.25	*3%*	4.96E-08	*18%*
	6.0	*2%*	0.058	*2%*	0.63	*3%*	3.10E-07	*18%*
	8.2	*2%*	0.079	*2%*	0.86	*3%*	5.78E-07	*18%*

Linear and angular velocities between bioreactor types vary slightly due to the different thicknesses of their bioreactor walls, resulting in different radii of rotation (90.5 cm and 92.0 cm respectively). Hindered settling velocities also vary between reactor types, as the concentration of cells used for both sets of experiments is different (Table 4.2).

The calculated hindered settling velocities in Table 4.3 are those which occur initially. As time goes on the cells are expected to move outwards, away from the point of rotation. This causes the value of R to increase over time, leading to an increase in cell velocity. Given this relationship, the centrifugal cell settling equation can be further modified to calculate the distance a given cell can travel over a set time at a constant angular velocity. The distance

from the central point of rotation (r_X) a cell reaches for time t is derived from Equation 4.12 and is shown in Equation 4.15:

$$\frac{dR}{dt} = \frac{2\,r_C^2}{9\,\mu_L}(\rho_C - \rho_L)R\,\omega^2$$

$$\left(\frac{9\,\mu_L}{2\,r_C^2}\right)\frac{dR}{dt} - \left((\rho_C - \rho_F)\,\omega^2\right)R = 0$$

Which is of the form:

$$a\,\frac{dR}{dt} - b\,R = 0$$

$$\frac{dR}{R} = \frac{b}{a}\,dt$$

Upon integrating between R and r_X and time 0 and time t:

$$ln\left(\frac{r_X}{R}\right) = \frac{2\,r_C^2}{9\,\mu_L}(\rho_C - \rho_L)\,\omega^2\;\;t$$

Taking the exponent and rearranging for r_X

$$\boldsymbol{r_X = R\;\;e^{\left(\frac{2\,r_C^2}{9\,\mu_L}(\rho_C - \rho_L)\,\omega^2\,t\right)}}$$

Equation 4.15 – Derivation of an equation to determine the radial position of a cell at a given time under centrifugal force.

The expected distance a cell travels under these dynamic seeding conditions for a given cell attachment time is useful in order to calculate the likelihood of cells making contact with a hollow fibre in the bioreactor. The hollow fibre zone (HFZ) is a set distance away from the wall of the bioreactor. If it is assumed that the cells which miss the fibre on their initial first static pass all accumulate at the bottom of the reactor, then it can also be assumed that these cells would all move outward from this region, travelling from one side of the bioreactor to the other under the centrifugal conditions created by the rotating drum.

For ease of analysis, it is assumed that upon starting rotation the unattached cells will move outwards from the bioreactor wall, and spread out to form a linear front of cells. This cell front will continue to move outwards towards the opposite side of the bioreactor for the duration of rotation. During this movement, a portion of this cell front will make contact the HFZ. The continuing centrifugal force from rotation would keep the contacted cells pressed onto the surface of any fibre in the HFZ and aid cell attachment. The parts of the cell front that do not contact the HFZ will continue to move outwards, eventually meeting the bioreactor wall on the opposite side. This is illustrated in Figure 4.10. Analysis of experimental dynamic cell attachment data will determine the validity of this theory.

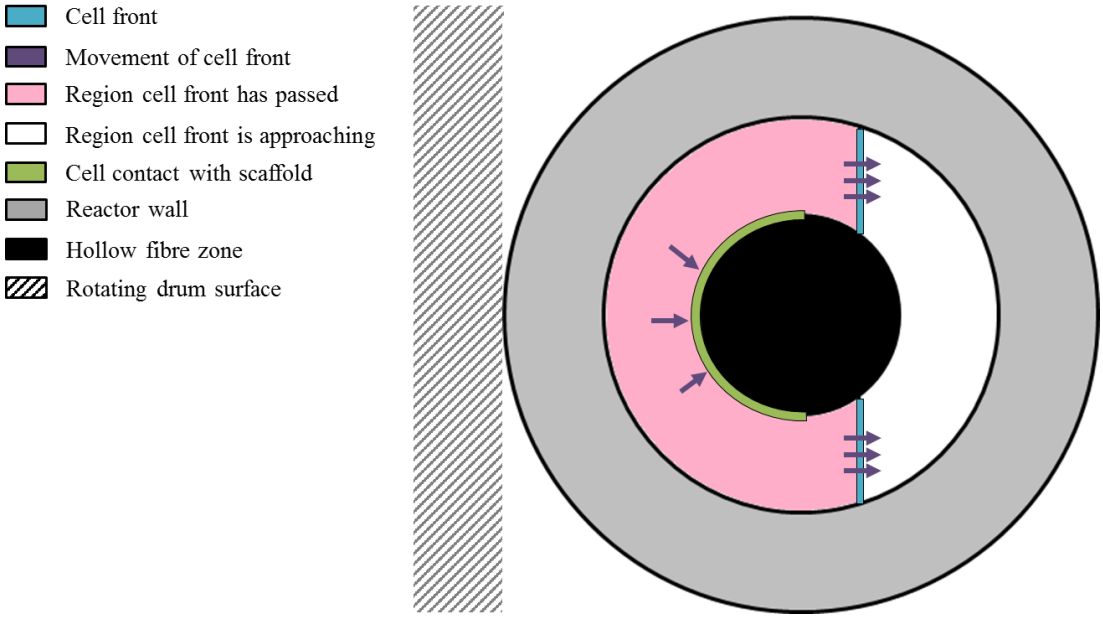

Figure 4.10 – Cross section of a single HFB module showing a moving cell front.

Assuming the linear front consisted of all non-attached cells distributed evenly, the ratio of the HFZ and inner bioreactor diameters (± 0.1 mm) could be used to determine what percentage of the cell front would contact the HFZ. This projected area for attachment would be half (50% ± 3%) of the unattached cells in a single fibre bioreactor, and two-thirds (67% ± 3%) of unattached cells in a multi-fibre bioreactor.

4.2.3 MACSmix Rotator for Single HFB Modules

Given the theoretical analysis in this chapter so far, up to 24% ± 4% of all cells will make contact with the single hollow fibre on one cell settling pass lasting 29 ± 7 seconds. The MACSmix rotator drive enabled 1 minute of rotational force at angular velocity 1.05 ± 0.03 s^{-1}, followed by 4 minutes of no rotation, i.e. 5 minutes per cycle. As the position of the bioreactor after 1 minute was approximately 180° from its starting position, this could allow multiple opportunities for cells to re-settle and make contact with the hollow fibre, whilst providing 4 minutes to allow a portion of these cells to attach. If it is assumed that 24% ± 4% % of cells will contact the hollow fibre, and a given proportion of those cells actually attach during each pass, a theoretical time for sufficient cell attachment can be calculated for any 5 minute cycle (t). The number of attached cells follows Equation 4.16 below which is plotted in Figure 4.11:

$$Attached\ Cells_{(t)} = Attached\ Cells_{(t-5)} + \left(Unattached\ Cells_{(t-5)} \times \%\ Attachment\ in\ 5\ min\right)_{Attachment \to 100\%\ as\ t \to \infty}$$

Equation 4.16 – Theoretical cell attachment on the MACSmix rotator at a given time.

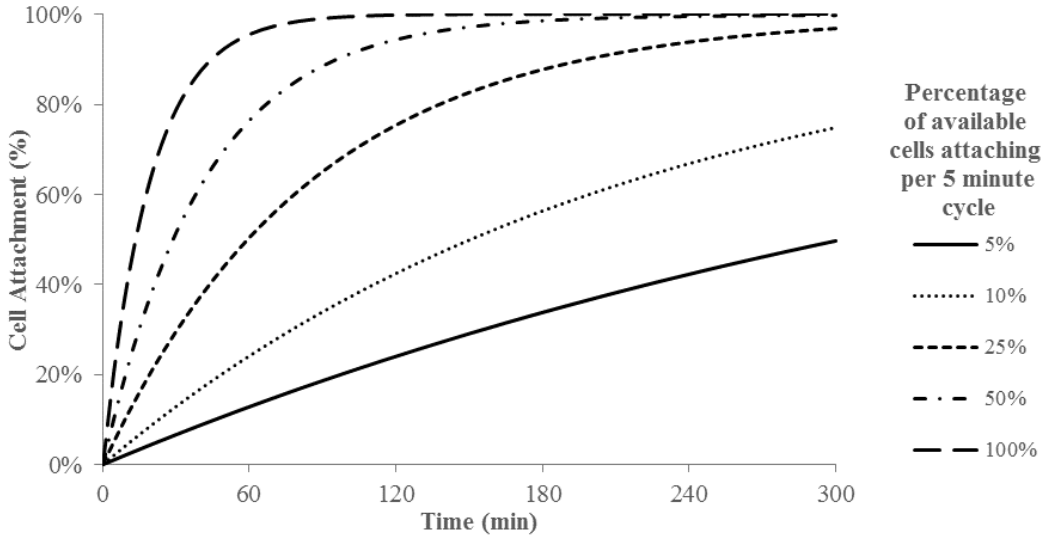

Figure 4.11 – Theoretical mean cell attachment of a hollow fibre bioreactor in a MACSmix rotator over time.

From Figure 4.11 it can be seen that the total number of cells attaching to the scaffold would increase over time as $t \rightarrow \infty$. This model assumes that cells are well distributed throughout the bioreactor after being mixed for one minute, and that cells that have attached to the hollow fibre are not removed due to agitation. Experimental data will be compared to this model to determine if the MACSmix Rotator at a 5 minute cycle time is appropriate to facilitate acceptable rates of cell attachment.

4.3 RESULTS

4.3.1 Seeding Time Selection

To determine the minimum duration necessary for cells to settle onto a scaffold and attach in sufficient quantities, an experiment was carried out on a flat sheet membrane of PLGA placed inside a custom designed detachable 96 well plate. Each column of the plate represented one of ten different time points between 5 minutes and 4 hours conducted in octuplicate (n=8). This experiment was performed once (N=1). Each well was 6.80 ± 0.05 mm in diameter, 5.00 ± 0.05 mm in height, 0.180 ± 0.004 mL in total volume and a surface area of 0.363 ± 0.008 cm^2.

Cell viability tests using trypan blue indicated that 94.5% of seeded cells were viable. Cells were seeded at 20,000 ± 2,000 cells/cm^2, requiring an inoculant of 7,400 ± 740 cells in 0.100 ± 0.002 ml cell media. 56% ± 2% of the well was filled, indicating a media depth of 2.78 ± 0.08 mm. Hindered cell settling velocity was calculated as 7.00E-05 ± 1.60E-05 m/s for this system using Equation 4.11, and maximum cell settling time was calculated to be 40 ± 10 seconds using Equation 4.8. Given the short length of settling time, and the relatively

long time taken to seed all the wells for this experiment, it is likely that all cells had settled to the bottom of each well when the timing started. The seeded scaffold was placed in an incubator at 37°C and 5% CO_2.

At each time point the corresponding column of wells were drained of residual cell media, washed with 0.1 ml phosphate buffered saline (PBS) and manually counted for cells that did not attach. Afterwards the scaffold was immersed in 0.1 ml trypsin and washed again with 0.1 ml PBS before being counted to determine the number of cells that had settled and attached during that time. The exact methodology for fixing the scaffold into the well plate, as well as cell seeding is described in Section 3.3.4.

Cell counts of both the unattached cells in media and attached cells from trypsin are shown in Table 4.4. A calculated rate of cell attachment for each time point is displayed in Figure 4.12.

Table 4.4 – Experimental cell attachment on PLGA flat sheet over time (*n*=8, *N*=1, error = SD).

Time (min)	Average Cell Count						Average Cell Attachment (%)	
	Attached		Unattached		Total			
	Av.	*SD (%)*	Av.	*SD (%)*	Av.	*SD (%)*	Av.	*SD (%)*
5	2,002	*38.5%*	8,236	*17.3%*	10,238	*42.2%*	**20%**	*11%*
10	1,060	*18.6%*	8,756	*25.4%*	9,816	*31.5%*	**11%**	*4%*
20	3,376	*30.1%*	6,706	*8.6%*	10,082	*31.3%*	**34%**	*15%*
30	4,240	*24.3%*	3,821	*22.5%*	8,061	*33.2%*	**53%**	*22%*
45	6,478	*18.9%*	2,597	*24.6%*	9,075	*31.1%*	**71%**	*26%*
60	3,769	*23.7%*	3,228	*18.9%*	6,997	*30.3%*	**54%**	*21%*
90	4,240	*28.8%*	2,189	*24.4%*	6,429	*37.7%*	**66%**	*31%*
120	5,771	*16.5%*	2,189	*22.7%*	7,960	*28.0%*	**73%**	*24%*
180	6,454	*23.9%*	1,177	*14.3%*	7,631	*27.8%*	**84%**	*31%*
240	6,596	*10.8%*	1,261	*38.1%*	7,857	*39.6%*	**84%**	*35%*

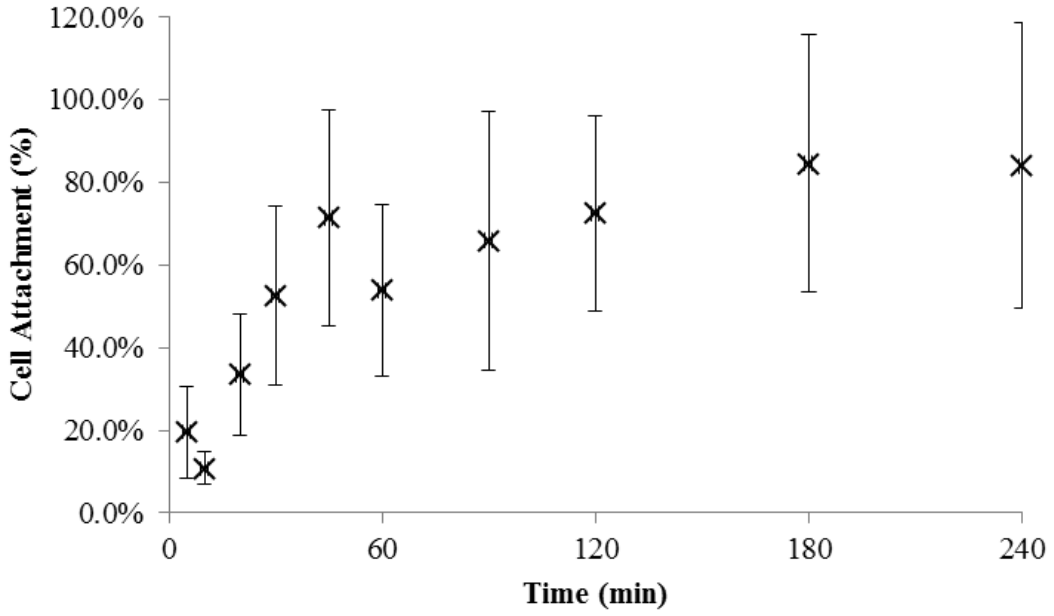

Figure 4.12 – Cell attachment on PLGA flat sheet over time (*n*=8, *N*=1, error = SD).

Figure 4.12 shows a general increase in the number of cells attached to the scaffold over time which corresponds with an associated decrease in the number of cells counted in the remaining cell medium. The data also shows wide error bars from the compound error of octuplet trypsin and media cell counts, which indicates an inherent variation in cell attachment that is not limited to the duration of cell attachment. This also led to an unequal mass balance where the number of cells seeded into each well (7,400 ± 740) did not equal the sum of the cells recovered from the residual media and the scaffold surface (Table 4.4).

4.3.2 Static Cell Attachment on Hollow Fibres

Hollow fibres were placed into a custom designed single HFB silicone module, constructed as described in Section 3.3.5 and shown in Figure 3.5. The available surface area on the fibre for cell attachment was calculated as 1.1 ± 0.2 cm^2 from the product of the fibre length (L_F) fibre diameter (d_F) the number of fibres in a bundle (N_F) and pi. 110,000 ± 18,480 MG63 cells were seeded at a density of 100,000 ± 16,800 cells/cm^2 into the bioreactor in a static environment; a much higher density than the 20,000 ± 2,000 cells/cm^2 in the previous study. This was to attempt to mitigate the impact of error of unaccounted cells. The bioreactors were placed in an incubator at 37°C and 5% CO_2. The duration of static cell attachment was set to 2 hours based upon the results found in Section 4.3.1, as this provided 73% ± 24% attachment on static flat sheets. While greater rates of static attachment were found at longer times as displayed in Figure 4.12, 2 hours was selected because it made the timing of experiments easier at the expense of only a small increase in attachment.

A single hollow fibre was selected to provide the simplest geometry for cell attachment and act as a baseline for all subsequent tests on larger bundles of hollow fibres. The efficiency of cell attachment was measured by comparing the cells removed from the scaffold surface using trypsin, and the cells initially seeded into the bioreactor. Following on from the theoretical analysis conducted in Section 4.2.1, a maximum rate of cell attachment of 24% ± 4% was expected as only that proportion of cells would have an opportunity to make contact with the fibre as they settled. Combined with the cell attachment time course data from Section 4.3.1, in 2 hours only 73% ± 24% of those cells that contact the scaffold will actually attach. This lowers the theoretical maximum static settling rate of cell attachment on PLGA hollow fibres to 18% ± 4%.

Control Experiments

Prior to the cell attachment a series of control experiments without hollow fibres present were undertaken in order to discount certain sources of cell loss. The first was conducted to determine if any cells would attach to the silicone bioreactor housing in addition to the hollow fibre scaffold. A vacant single HFB silicone module was inoculated with the same quantity of cells and left for 2 hours. After this time the bioreactor was drained, washed with PBS, and then trypsinised. A cell population equivalent to 2% ± 3% (n=9) of inoculated cells was found to remain in the bioreactor. Sigmacote could not be used to coat the bioreactor internals and prevent cell adherence because it led to the deformation of silicone bioreactor housing. The manufacturer describes this particular tubing as non-adherent, however Figure 4.13 shows evidence of cell attachment within the tubing. Cells were fixed with formalin as described in Section 3.4.1 to acquire the image.

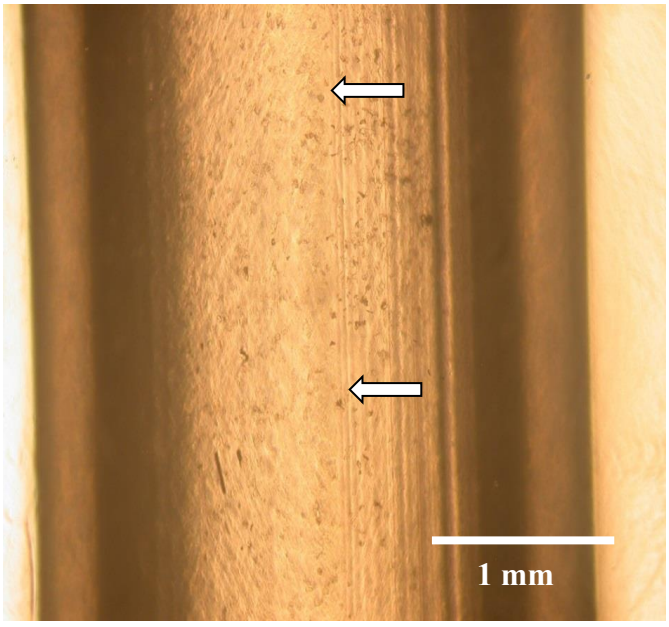

Figure 4.13 – Image of residual cells on inner walls of HFB module (x30).

Next, an experiment to calculate the number of cells lost during inoculation and cell removal was conducted. Bioreactors containing no hollow fibre were seeded and then immediately drained. Cell loss of 20% ± 14% (*n*=9) was determined. The final control test was to determine if any cells were lost due to leakage. A full 2 hour static attachment experiment was conducted, comparing the cell number before and after the experiment. The initial cell population had decreased by 20% ± 5% (*n*=3). This data is presented in Table 4.5:

Table 4.5 – Cell loss in a single HFB module after zero and two hours.

Source of Cell Loss	Cell loss		Number of Trials (*n*)
	Average	*SD*	
Bioreactor attachment	2%	*± 3%*	9
Experimental error	20%	*± 14%*	9
Bioreactor leakage	20%	*± 5%*	3

As cell losses from bioreactor leakage were within the range of error from cell losses due to experimental error, and as no leakages were visible on inspection after 2 hours, it can be concluded that no leakage occurs. The quantity of cells that attach to the silicone bioreactor inner wall were in addition to those lost from experimental error, and therefore 2% ± 3% of attached cells must be discounted from all future single fibre bioreactor studies.

From these results it was assumed that during a 2 hour experiment 20% ± 14% of cells were lost, indicating that anywhere between of 6% - 34% of the initial 110,000 cells did not have an opportunity to attach by virtue of not being seeded in the first place. It is inferred that this would decrease the initial cell number and thus have an impact on the rate of cell attachment, as displayed in Table 4.6:

Table 4.6 – Cell loss and subsequent number available for attachment.

Degree of Cell Loss		Cells Available For Attachment
Zero Cell loss	0%	110,000
Minimum Cell Loss	6%	103,400
Median Cell Loss	20%	88,000
Maximum Cell Loss	34%	72,600

This range of error increased the degree of uncertainty in all subsequent cell attachment experiments on hollow fibres. Calculated rates of cell attachment would be an average value with an associated standard deviation that would be ultimately dependent on the initial number of cells inoculated.

Static Experiments

After 58 trials the average rate of cell attachment on statically seeded single hollow fibre bioreactors was 18% ± 16%. The error includes the loss of 20% ± 14% of the initial inoculant, and also accounts for the 2% ± 3% of cells attached to the bioreactor housing. Experimental cell attachment is similar to the calculated theoretical maximum of 18% ± 4% for static seeding, and to the value of 20% found in other works.

4.3.3 Dynamic Cell Attachment in Single and Multi-Fibre Bioreactors

In order to provide multiple instances of cells coming into contact with the external hollow fibre surface, single hollow fibre silicone modules and multi hollow fibre glass modules were attached to rotating devices at various speeds and orientations to determine if a dynamic environment would improve cell attachment on the hollow fibres. A dynamic seeding regime could allow the cells that settled to the bottom of the bioreactor another opportunity to make contact with the fibre and potentially attach.

Single fibre modules were constructed and seeded as described in Section 3.3.5. Hollow fibres were 35 ± 0.05 mm long and had an outer radius of 0.5 ± 0.05 mm for a total external surface area of 1.1 ± 0.2 cm^2. For the single fibre bioreactor 110,000 ± 18,480 cells were seeded at a density of 100,000 ± 16,800 cells/cm^2. Single fibre silicone bioreactors were attached to one of two rotating devices after inoculation: a Stuart STR4 rotator drive (Figure 4.2) or a MACSmix rotator (Figure 4.3), and placed in an incubator at 37°C and 5% CO_2. In the case of the former, the rotating drum was set to rotate at one of three different rotational speeds (2, 6 or 8 RPM / 0.25, 0.63 or 0.86 s^{-1}, error = 1.7%) with the bioreactors consistently positioned horizontally to determine how changing angular velocity affected cell attachment. A second experiment was conducted with the drum set to a constant 6 RPM (0.63 s^{-1}) and the bioreactors orientated either horizontally (a), diagonally (b) or vertically (c) as shown in Figure 4.14. Finally, a MACSmix rotator device was used set to provide one minute of rotation followed by four minutes of pause to the bioreactor. Cells were allowed 2 hours to attach.

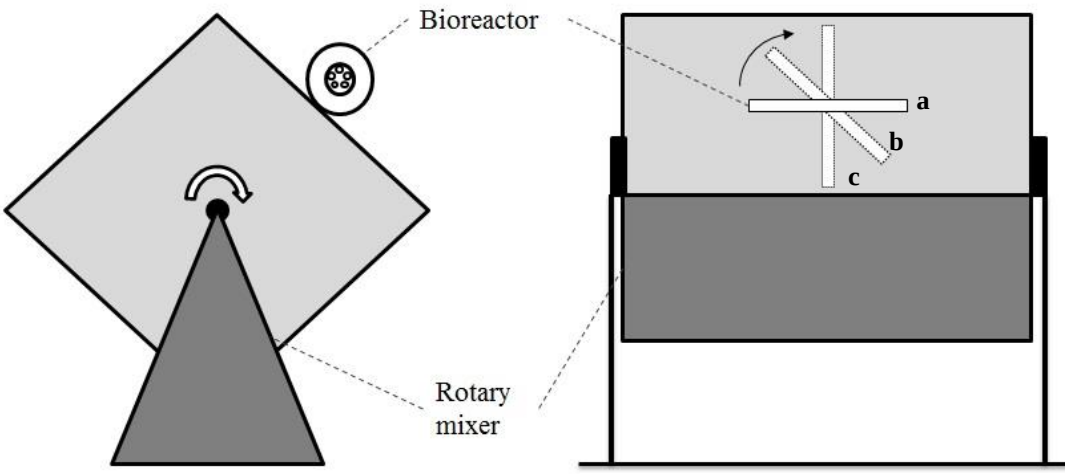

Figure 4.14 – A schematic of the rotating drum with attached bioreactor (not to scale).

Cell attachment on the single hollow fibre was quantified by performing a cell mass balance over the bioreactor using cell trypsinisation to remove attached cells, followed by manual counting. The values for cell loss calculated in Section 4.3.2 for static seeding were applied to single fibre dynamic seeding experiments. Rates of dynamic cell attachment were compared to the static rate of cell attachment calculated previously to be 18% ± 16% on average.

For multi-fibre experiments, bundles of 5 hollow fibres mounted in a large glass bioreactor were seeded and constructed as described in Section 3.3.5. Fibres were 120 ± 0.5mm long and had an outer radius of 0.65 ± 0.05 mm, providing a total external surface area of 24.5 ± 1.9 cm^2. In multi-fibre bioreactors, 735,000 ± 69,090 cells were seeded, resulting in a cell surface density of 30,000 ± 2,820 cells/cm^2. Cells were allowed 6 hours to attach. Bioreactors were attached to the Stuart STR4 rotator drive at the same angular velocities and orientations as single fibre bioreactor modules, however were not attached to the MACSmix rotator because they could not be adequately supported and frequently became dislodged. Cell attachment was quantified by calculating the difference between the manually counted initial cell inoculation and the number of unattached cells in the residual cell media after 6 hours.

The inner walls of the multi fibre glass bioreactor module was coated with Sigmacote to inhibit cell adhesion. A control experiment seeding bioreactors with no fibres fitted showed no cell attachment to the bioreactor inner surface. Cell losses of the magnitude found in the single fibre silicone bioreactors were not anticipated, as the entire volume of cell inoculant was successfully transferred into and out of the multi-fibre bioreactors. Static experiments were not conducted on multi fibre bioreactors; instead a projected value for cell attachment based off of the single fibre experiments was used. Assuming no cell loss and a proportional increase of attached cell number to reflect this, a static cell attachment of 19% ± 14% was calculated for the multi-fibre bioreactor.

Single Fibre Bioreactors

All dynamic rates of cell attachment on single fibre bioreactors for each configuration, along with standard deviation and range are shown in Table 4.7 and graphed on Figure 4.15. None of the rates of cell attachment are significantly different from one another to a 95% confidence.

Table 4.7 – Rate of cell attachment in single fibre silicone modules at different seeding conditions.

Configuration	Trials (*n*)	Cell Attachment	
		Average	*Error*
Static	58	18%	*± 16%*
Horizontal (6 RPM)	12	10%	*± 7%*
Diagonal (6 RPM)	12	12%	*± 8%*
Vertical (6 RPM)	12	9%	*± 5%*
2 RPM (horizontal)	12	13%	*± 8%*
6 RPM (horizontal)	12	10%	*± 7%*
8 RPM (horizontal)	12	9%	*± 5%*
MACSmix	9	10%	*± 4%*

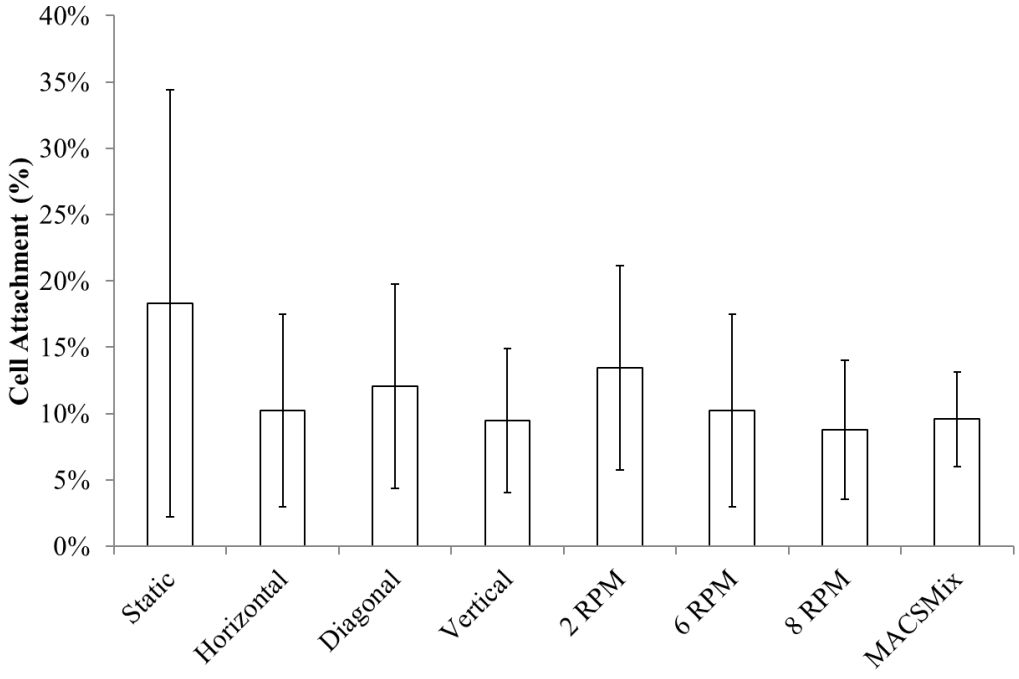

Figure 4.15 – Rate of cell attachment in single fibre silicone modules at different seeding conditions.

The theory of centrifugal settling was outlined Section 4.2.2, and described the movement of a linear front of cells moving further outwards through the bioreactor over time as a result of centrifugal action, and characterised further attachment of cells by the need to reach a designated hollow fibre zone (HFZ) in the allotted rotation time. Using Equation 4.12 and Equation 4.15 the initial hindered settling velocity and the distance a given cell can travel as a result of centrifugal action is calculated for each set rotational velocity. The time that the cell front takes to make contact with the HFZ, and the duration the cell front is pressed against the hollow fibre is also calculated. All data is shown in Table 4.8.

Table 4.8 – Data describing cell movement during dynamic seeding.

RPM		Angular Velocity (s^{-1})		Initial Hindered Settling Velocity (m/s)		Cell Front Distance Travelled (mm)		Time of Contact With HFZ (h:mm)		HFZ Contact Duration (h:mm)	
Value	***Error***	**Value**	***Error***	**Value**	***Error***	**Value**	***Error***	**Value**	***Error***	**Value**	***Error***
2	*2%*	0.25	*3%*	4.13E-08	*23%*	0.3	*23%*	2:53	*23%*	0:00	*23%*
6	*2%*	0.63	*3%*	2.58E-07	*23%*	2.2	*23%*	0:28	*23%*	1:32	*23%*
8	*2%*	0.86	*3%*	4.82E-07	*23%*	4.1	*23%*	0:15	*23%*	1:45	*23%*

Following this model at 2 RPM the linear cell front travels 0.3 mm outwards from the inner bioreactor wall in 2 hours due to centrifugal motion. As the start of HFZ begins 0.5 mm from the inner bioreactor wall (Figure 4.5), this model indicates that additional cells would not come into contact with the hollow fibre. Contact would only be initiated after 2 hr 53 minutes of rotation. At 6 RPM and 8 RPM the increased radial velocities allow the cell front to make contact with the HFZ 28 minutes and 15 minutes into the experiment, and keep cells on the surface of the HFZ for 1 hour 32 minutes and 1 hour 45 minutes respectively. Errors for the values stated here are shown in Table 4.8.

Multi Fibre Bioreactors

All rates of dynamic cell attachment on hollow fibre bundles for each configuration, along with standard deviation and range are shown in Table 4.9 and graphed on Figure 4.16. Significant differences between horizontal and both diagonal and vertical orientations to a 95% confidence are indicated (*). A value for static cell attachment assuming similar behaviour to the single fibre bioreactor system is included.

Table 4.9 – Rate of cell attachment in bundled HFBs at different seeding conditions.

Configuration	Trials (*n*)	Cell Attachment	
		Average	*Error*
Static	58	19%	*14%*
Horizontal (6 RPM)	4	39%	*12%*
Diagonal (6 RPM)	3	15%	*11%*
Vertical (6 RPM)	4	16%	*1%*
2 RPM (horizontal)	3	31%	*7%*
6 RPM (horizontal)	4	39%	*12%*
8 RPM (horizontal)	3	22%	*6%*

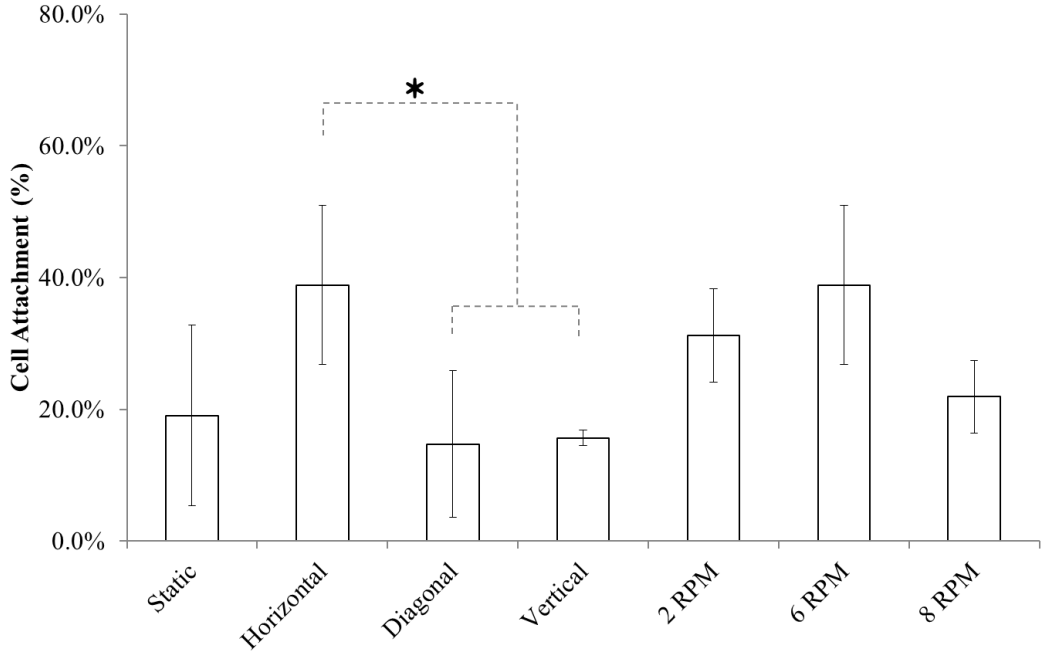

Figure 4.16 – Rate of cell attachment in bundled HFBs at different seeding conditions.

The theory of centrifugal settling was outlined Section 4.2.2, and Equation 4.12 and Equation 4.15 were used to calculate the duration of time cells were in contact with the HFZ for multi-fibre bioreactors. This is shown in Table 4.10.

Table 4.10 – Data describing cell movement during dynamic seeding.

RPM		Angular Velocity (s^{-1})		Initial Hindered Settling Velocity (m/s)		Cell Front Distance Travelled (mm)		Time of Contact With HFZ (h:mm)		HFZ Contact Duration (h:mm)	
Value	*Error*	Value	*Error*	Value	*Error*	Value	*Error*	Value	*Error*	Value	*Error*
2	*2%*	0.25	*3%*	4.96E-08	*18%*	1.1	*18%*	6:51	*18%*	0:00	*18%*
6	*2%*	0.63	*3%*	3.10E-07	*18%*	7.1	*18%*	1:06	*18%*	4:54	*18%*
8	*2%*	0.86	*3%*	5.78E-07	*18%*	13.6	*18%*	0:35	*18%*	5:25	*18%*

At 2 RPM the linear cell front travels 1.1 mm outwards from the inner bioreactor wall in 6 hours due to centrifugal motion. As the start of HFZ begins 1.25 mm from the inner bioreactor wall (Figure 4.7), this model indicates that cells would not come into contact with the hollow fibre. Contact would only be initiated after 6 hr 51 min of rotation at that velocity. At 6 RPM and 8 RPM the increased radial velocities allow the cell front to make contact with the HFZ 1 hr 6 min and 35 min into the experiment, and keep cells on the surface of the HFZ for a total of 4 hr 54 min and 5 hr 25 min respectively. Errors for the values stated here are shown in Table 4.10.

Theoretical Maximum Cell Attachment

Theoretical and experimental data can be combined to determine a theoretical maximum rate of cell attachment on single and multi-fibre bioreactors resulting from dynamic seeding. In this section, dynamic seeding of a horizontal single hollow fibre module at 6 RPM is used as an example for calculation of the theoretical maximum cell attachment. From the theory outlined in Section 4.2.1 only 24% ± 4% of inoculated cells will initially settle onto a hollow fibre prior to starting rotation. There was approximately a 5 minute gap between cell inoculation, fixing the bioreactor to the drum, and the start of rotation; which from Figure 4.12 in Section 4.3.1 for cell attachment on flat sheets would allow 20% ± 11% attachment of the cells that settled onto the surface prior to rotation. Therefore the static cell attachment in this initial 5 minutes prior to rotation can be calculated using Equation 4.17:

$$\begin{aligned} \textit{Static Phase Cell Attachment}_{\,5\,min} &= \textit{Settling Cell Contact with Hollow Fibre} \times \textit{Flat Sheet Cell Attachment}_{\,5\,min} \\ \textit{Static Phase Cell Attachment}_{\,5\,min} &= 24\% \pm 4\% \times 20\% \pm 11\% \\ \boldsymbol{\textit{Static Phase Cell Attachment}_{\,5\,min}} &= \mathbf{5\% \pm 3\%} \end{aligned}$$

Equation 4.17 – Calculation of cell attachment within initial 5 minutes prior to rotation.

It is assumed that the forces of rotation do not remove these attached cells, therefore a single hollow fibre will have 5% ± 3% of the inoculated cells already attached during the 2 hour rotational seeding phase. It is proposed in Section 4.2.2 that the remaining unattached cells move outward in a linear front due to centrifugal action, and come into contact with the hollow fibre resulting in additional cell attachment. This is dependent three main factors: the time taken for the cell front to reach the hollow fibre, the projected surface area of the hollow fibre that ensures a successful hit, and the contact time once the cell front reaches the hollow fibre.

This theoretical data is outlined for single and multi-fibre modules in Table 4.8 and Table 4.10 respectively.

In this example, upon starting rotation for 2 hours it takes 28 minutes for the cell front to make contact with the hollow fibre, allowing a total of 1 hour 32 minutes for attachment. Assuming the flat sheet data shown on Figure 4.12 in Section 4.3.1 is comparable, this results in 66% ± 31% attachment of cells that make contact with the fibre for 90 minutes. As the diameter of the single fibre is 50% ± 3% that of the inner bioreactor diameter, the projected area of the hollow fibre is such that only 50% ± 3% of the cell front will make contact with the fibre. As previously mentioned, the cell front is comprised of all unattached cells. Taking into account the 5% ± 3% that have theoretically attached already, the cell front consists of 95% ± 3% of the total cell inoculant. Given this information, the degree of theoretical cell attachment from centrifugal action can be calculated as shown in Equation 4.18:

$$\begin{matrix} Dynamic\ Phase \\ Cell\ Attachment \end{matrix} = \begin{matrix} Unattached \\ Cells \end{matrix} \times \begin{matrix} Projected \\ Fibre\ Area \end{matrix} \times \begin{matrix} Flat\ Sheet \\ Cell\ Attachment_{\ 90\ min} \end{matrix}$$

$$\begin{matrix} Dynamic\ Phase \\ Cell\ Attachment \end{matrix} = 95\% \pm 3\% \times 50.0\% \pm 3\% \times 66\% \pm 31\%$$

$$\boldsymbol{\begin{matrix} Dynamic\ Phase \\ Cell\ Attachment \end{matrix}} = \mathbf{31}\% \pm \mathbf{15}\%$$

Equation 4.18 – Calculation of cell attachment from centrifugal action.

This can be combined with the cell population on the fibre from the initial 5 minutes of static settling (Equation 4.17) to calculate total cell attachment using Equation 4.19:

$$\begin{matrix} Total\ Theoretical \\ Cell\ Attachment \end{matrix} = \begin{matrix} Static\ Phase \\ Cell\ Attachment \end{matrix} + \begin{matrix} Dynamic\ Phase \\ Cell\ Attachment \end{matrix}$$

$$\begin{matrix} Total\ Theoretical \\ Cell\ Attachment \end{matrix} = 5\% \pm 3\% + 31\% \pm 15\%$$

$$\boldsymbol{\begin{matrix} Total\ Theoretical \\ Cell\ Attachment \end{matrix}} = \mathbf{36}\% \pm \mathbf{15}\%$$

Equation 4.19 – Calculation of total theoretical cell attachment.

From these equations it can be determined that using the theories and assumptions outlined in Section 4.2, the maximum theoretical rate of cell attachment of MG63 cells in a dynamically seeded, horizontally orientated, single hollow fibre module rotated at 6 RPM is 36% ± 15%. Following this method, maximum theoretical cell attachment on horizontal single and multi-

fibre bioreactors for all three rotational settings can be calculated. This data is shown in Table 4.11.

Limitations with this calculation include allowing for the possibility that too low a rotational velocity would not provide enough centrifugal force for the cell front to make contact with the hollow fibres. This occurs on 2 RPM experiments for single and multi-fibre modules, where the only cell attachment would be from the initial cell settling before rotation was initiated. It also does not take into account if the cells that missed the fibre during the dynamic phase re-settle onto the fibre after the rotating device is stopped and the experiment ended. In that case, cell attachment could be higher than theorised. Also, no distinction could be drawn between the 6 RPM and 8 RPM settings on multi-fibre bioreactors because flat sheet cell attachment was shown to reach a maximum after 3 hours; so the additional time that cells in the 8 RPM system would have to attach during the dynamic phase did not provide any additional cell attachment. This method has not been performed for vertical or diagonal orientations because cell movement from centrifugal action is harder to predict using the equations in Section 4.2.2. Differences between theoretical and experimental cell attachment will be explained in the Discussion section of this chapter.

Table 4.11 – Parameters used to calculate theoretical dynamic cell attachment on horizontal bioreactors.

Cell Attachment	Theoretical/Experimental Parameter	Single (Horizontal)						Multi (Horizontal)					
		2 RPM		6 RPM		8 RPM		2 RPM		6 RPM		8 RPM	
		Value	***Error***	**Value**	***Error***	**Value**	***Error***	**Value**	***Error***	**Value**	***Error***	**Value**	***Error***
Static Phase	Cell contact from initial settling on hollow fibre	24%	*4%*	24%	*4%*	24%	*4%*	30%	1%	30%	*1%*	30%	1%
	Time before initiating rotation (min)	5	-	5	-	5	-	5	-	5	-	5	
	Cell attachment after this time on flat sheets	20%	*11%*	20%	*11%*	20%	*11%*	20%	*11%*	20%	*11%*	20%	*11%*
	Cell attachment on hollow fibre	**5%**	***3%***	**5%**	***3%***	**5%**	***3%***	**6%**	***3%***	**6%**	***3%***	**6%**	***3%***
Dynamic Phase	Unattached cells on bottom of bioreactor	95%	*3%*	95%	*3%*	95%	*3%*	94%	*3%*	94%	*3%*	94%	*3%*
	Total rotation time (hours)	2	-	2	-	2	-	6	-	6	-	6	-
	Projected fibre surface area relative to bioreactor	50%	*3%*	50%	*3%*	50%	*3%*	67%	*3%*	67%	*3%*	67%	*3%*
	Time cells in contact with fibre due to centrifugal action (hours)	00:00	-	01:32	-	01:45	-	00:00	-	04:54	-	05:25	-
	Cell attachment after this time on flat sheets	0%	*0%*	66%	*33%*	69%	*28%*	0%	*0%*	84%	*35%*	84%	*35%*
	Cell attachment on hollow fibre	**0%**	***0%***	**31%**	***15%***	**33%**	***13%***	**0%**	***0%***	**53%**	***22%***	**53%**	***22%***
Total	Cell Attachment From Initial Settling	5%	*3%*	5%	*3%*	5%	*3%*	6%	*3%*	6%	*3%*	6%	*3%*
	Cell Attachment From Centrifugal Action	0%	*0%*	31%	*15%*	33%	*13%*	0%	*0%*	53%	*22%*	53%	*22%*
	Total Theoretical Dynamic Cell Attachment	**5%**	*3%*	**36%**	*15%*	**38%**	*13%*	**6%**	*3%*	**59%**	*22%*	**59%**	*22%*

4.3.4 Summary of Results

A table outlining the best rates of theoretical and experimental cell attachment with on single and multi-fibre bioreactors, seeded statically and dynamically, is shown in Table 4.12:

Table 4.12 – Summary of theoretical and experimental values for static and dynamic cell attachment.

Mode	Scaffold	Data	Value	*Error*	Orientation	Setting
Static	Flat Sheet	Theoretical	100.0%	-	N/A	N/A
		Experimental	84%	*35%*	N/A	N/A
	Single Hollow Fibre	Theoretical	18%	*4%*	Horizontal	N/A
		Experimental	18%	*16%*	Horizontal	N/A
	Multi Hollow Fibre	Theoretical	19%	*14%*	Horizontal	N/A
		Experimental	Experiment not performed			
Dynamic	Single Hollow Fibre	Theoretical	38%	*13%*	Horizontal	8 RPM
		Experimental	14%	*8%*	Horizontal	2 RPM
	Multi Hollow Fibre	Theoretical	59%	*22%*	Horizontal	6 & 8 RPM
		Experimental	39%	*12%*	Horizontal	6 RPM

Table 4.12 shows that theoretical and experimental values for statically seeded, horizontal, single fibre bioreactors are similar; likely due to the simplicity of the gravity settling model. For dynamic single and multi-fibre seeding, theoretical values are greater than experimental values. This is likely due to the over-simplification of complex cell mixing behaviours in a dynamic environment, leading to an idealised theoretical value, the assumptions of which may not be fully applicable to this rotating regime. This will be further discussed in the next section.

Static flat sheets of PLGA show the greatest rates of cell attachment. This is to be expected because of their favourable geometry. However, as previously described in Section 2.3.2, hollow fibre bioreactors are proven to grow cells at a faster rate and allow the growth of a greater total number of cells than other bioreactor types (including flat sheets).

4.4 DISCUSSION

4.4.1 Static Seeding of Flat Sheet Scaffold

While MG63 cell attachment studies have been conducted on PLGA scaffolds, many of them did not characterise the initial rates of attachment (Pamula *et al.*, 2011; Park *et al.*, 2012; Cheng *et al.*, 2013). Some showed attachment efficiency after 24 hours, however it is unclear if cells had started to proliferate within that time, increasing the apparent rate of attachment. This included studies yielding ~100% attachment (Vandrovcova *et al.*, 2011), ~40% attachment (Wojak-Cwik *et al.*, 2013) and ~25% attachment (Khang *et al.*, 2002). Many others do not provide comparable data because they lack normalisation to a cell number or percentage cell attachment (Petricca *et al.*, 2006; Linh *et al.*, 2013; Son *et al.*, 2013; Kim *et al.*, 2014; Zuber *et al.*, 2014).

One study indicated 94% ± 7% attachment of MG63 cells on a porous PLGA 'tablet' scaffold after 4 hours, however this was only evaluated indirectly by measuring the number of cells remaining in the cell media (Mou *et al.*, 2011), which has been shown in Table 4.4 (Section 4.3.1) to be a poor method of determining cell attachment. Similarly, 89% ± 7% attachment of MG63 cells was found after 4 hours in a separate study, with attached cells directly counted after trypsinisation of the scaffold (Su *et al.*, 2010), which is a more reliable method than indirect measurements of remaining cells in the media . A time course study featuring attachment of 10,500 fibroblasts/cm^2 on poly (ε-caprolactone) (PCL) films confirmed using MTT assay showed cell attachment increasing between 20 minutes and 1 hour, with attachment levelling off between 1 and 2 hours (Li *et al.*, 2014). This matches the behaviour of MG63 cells attaching on PLGA flat sheets over time as shown in Figure 4.12 (Section 4.3.1).

4.4.2 Static Seeding of Single Hollow Fibre Scaffold

During control experiments of cell attachment on single fibre bioreactors it was found that 20% ± 14% (*n*=9) of cells were lost over the course of the 2 hour attachment, primarily from the cell seeding/removal steps. This systematic error arose due to the method of seeding the bioreactors. An inoculant of 0.1 mL was injected into each bioreactor via a syringe. To accelerate the seeding of multiple bioreactors per experiment, the required cell concentration was drawn up in a syringe to approximately 1 mL, and 0.1 mL of this was injected into bioreactors one after the other. Due to this method, a quantity of the 0.1 mL inoculant was not injected into the silicone tubing part of the bioreactor, instead it remained within the syringe needle. This effectively led to a number of cells that were not given an opportunity to come into contact with the hollow fibre, and the main contributing factor for the 20% ± 14% cell loss outlined in Section 4.3.2 .

Static cell attachment experiments showed an average rate of cell attachment of 18% ± 16% (*n*=58). This was consistent with the theoretical maximum cell attachment efficiency of 18% ± 4% after 2 hours calculated in Section 4.3.2. Given the number of trials, the wide standard deviation indicates that this method of cell attachment was inherently more inconsistent than postulated in theory. There was also some degree of external agitation when the bioreactor was moved from the biohood to the incubator which also may have affected the movement of the cells as they settled.

Once again, evaluating data against literature offers limited insight due to the incomparable cell quantification techniques. Single hollow fibres of PLGA spun using the same method outlined in Section 3.3.1 have been successfully seeded in well plates with human adipose stem cells under static conditions (Diban *et al.*, 2013). Studies typically focus on bundles of

hollow fibres in a bioreactor instead of single hollow fibres. No paper on cell attachment could be found that provided results as comprehensive in terms of error analysis and control experiments as those outlined in this chapter.

4.4.3 Dynamic Seeding of Single Fibre Scaffold

All dynamic methods of seeding on single fibre bioreactors yielded lower values of cell attachment compared to the static method. This indicated that mixing regimes established by the movement of the Stuart STR4 rotator drive were either insufficient to facilitate improvements in contact between cells and hollow fibre, or that the dynamic regime was sufficient to establish contact however the continuous motion of the cells made it difficult form an attachment to the hollow fibre. As previously described, the large error bars shown in Figure 4.15 arose due to cell losses during the cell inoculation and/or the media removal process.

Of the tested single fibre bioreactor orientations a diagonal positioning showed the greatest cell attachment of any dynamic method averaging at 12% ± 8%, however this was not much greater than horizontal (10% ± 7%) or vertical (10% ± 5%) attachment (Figure 4.15), so should not be taken as indicative of any trend. None of the different dynamic or static seeding configurations displayed in Figure 4.15 are statistically different from one another using a one way ANOVA and a post hoc Tukey's test. From experiments, dynamic cell attachment was greatest at lower drum angular velocity, with 13% ± 8% achieved at 2 RPM (0.25 s^{-1}) and worsening to 10% ± 7% at 6 RPM (0.63 s^{-1}) and 9% ± 5% at 8 RPM (0.86 s^{-1}). Cell attachment was worse than that achieved under static conditions (18% ± 16%), indicating that the presence of dynamic forces in this system prevented additional cell attachment over the course of 2 hours and may have actively caused the detachment of any cells initially attached between cell inoculation and rotation. The theorised centrifugal movement of settled unattached cells (Table 4.11) indicated that at 2 RPM the linear cell front would not reach the hollow fibre to facilitate another opportunity to attach. The cells that did attach were exclusively from cells which made contact with the fibre during the initial settling after inoculation, providing a maximum theoretical attachment of 5% ± 3%. It was theorised that cell-fibre contact would be facilitated at 6 RPM and 8 RPM because the cell front would move further as a result of the higher rotational velocity, leading to a maximum theoretical cell attachment of 36% ± 15% and 38% ± 13% respectively (Table 4.11); however the experimental data showed that the rate of cell attachment was not improved, and actually worsened, indicating that the greater rotational velocity prevented further cell attachment and actively removed previously attached cells.

Despite the postulated theory that the rotating and pausing regime provided by the MACSmix rotator would allow multiple opportunities for cells to encounter the hollow fibre, Figure 4.15 showed an average cell attachment of 10% ± 4%. This decrease in cell attachment may be evidence that the bioreactor was not left static for enough time to allow firm cell attachment to the hollow fibre. Static seeding on flat sheet PLGA membranes showed 20% ± 11% attachment after 5 minutes (Figure 4.12), which was greater than the attachment achieved using the MACSmix rotator that in theory would have allowed several opportunities for cells to fall onto the hollow fibre and attach. An explanation for this discrepancy could be due to the differing scaffold types, with a potential for cells to roll off the hollow fibre once contact was made lowering the effective proportion of cells that could attach from simple settling. This can be visualised referring back to Figure 4.4, assuming a narrower green region above the hollow fibre. Cells which did attach to the fibre after 5 minutes may have also been subsequently detached during the next period of rotation. If the model outlined in Figure 4.11 is applied to the experimental data, the net cell attachment per 5 minute rotation cycle is only 0.3% of available cells. This number can be increased if the hollow fibre were to take up a larger proportion of the bioreactor space to reduce the number of cells that fall past the hollow fibre on each pass. A larger pausing time would also likely allow cells to form stronger attachments to the fibre, such that fewer would be removed due to forces of rotation, however by default the MACSmix rotator could not be set to pause for a longer time.

Other publications using the same single fibre silicone bioreactor design and a MACSmix rotator at the same setting for seeding on collagen/fibrin micro-threads and have shown total attachment of 12% ± 4% cells (n=20) after seeding 100,000 human MSCs and trypsinising the bioreactor interior after 24 hours rotation (Guyette *et al.*, 2013). Attachment is greater in that study compared to this one, however control experiments similar to those described in Section 4.3.2 were not conducted. Assuming a similar degree of cell loss as described in this work, a comparable cell attachment of 15% ± 5% can be calculated, a value still larger than 10% ± 4% found in this work. This could be attributed to the longer seeding time, however differences in cell type and scaffold may account for this. Fibrin is produced naturally by the body to assist in wound healing, providing binding sites for attachment and migration of monocytes, fibroblasts and endothelial cells that PLGA lacks (Clark, 2001). No studies utilising a Stuart STR4 rotator drive, or other similar devices, for cell seeding of a single module HFB could be found.

4.4.4 Dynamic Seeding of Multi Fibre Scaffold

For multi-fibre modules the rate of attachment on horizontally orientated fibres that are dynamically seeded was shown to be superior to the static regime. The theoretical rate of cell attachment under static conditions is 19% ± 14%, whereas dynamic seeding via rotation at 2 RPM (0.25 s^{-1}), 6 RPM (0.63 s^{-1}) and 8 RPM (0.86 s^{-1}) yielded experimental cell attachments averaging 31% ± 7%, 39% ± 12% and 22% ± 6% respectively. Of the three bioreactor orientations tested at constant rotational velocity, horizontal orientation provided significantly greater cell attachment (39% ± 12%) compared to diagonal (15% ± 11%) and vertical (16% ± 1%) positioning. Angling the HFB to a vertical or diagonal orientation would have increased the gradient of the surface where the cells make contact, and increased likelihood of cells rolling off and not attaching. For a horizontal orientation an average gradient would be smaller and be more accommodating for cell attachment.

Error bars, representing standard deviation, are narrower for the seeding of multi fibre bioreactors than those for single fibre bioreactors. This is primarily due to the easier method of seeding the larger glass bioreactors. The entirety of the 4.5 mL cell inoculant/media solution was simply injected into the bioreactor via a side port, with none remaining in the syringe afterwards. The increased complexity of the single fibre silicone bioreactor, with its fixed syringe needle input port and smaller inoculant volume (0.1 mL) led to increased rates of cell loss at the expense of much smaller volumetric losses in that system.

There was no obvious correlation between drum rotational velocity and the rate of cell attachment on multi fibre bioreactors. For single fibre bioreactors was it was discussed that the increasing radial velocities would provide increasingly unfavourable shear conditions that prevented cell attachment and actively removed cells which had previously attached when initially seeded. Given the theoretical rate of static attachment on multi fibre bioreactors (19% ± 14%) was the lowest in comparison to horizontally orientated dynamically seeded bioreactors, it can be postulated that dynamic cell attachment improves rates of cell attachment in this case.

The HFZ in the multi fibre bioreactor was a greater proportion of the total bioreactor volume (44%) compared to the single fibre bioreactor (25%), and as a result had a higher projected surface area for cells to make contact with. The HFZ in the multi fibre bioreactor is comprised of a bundle of 5 hollow fibres. It is likely that a higher cell attachment rate occurred in multi fibres because cells settled between the fibres and were shielded when rotation was initiated. During rotation the settled cells at the bottom of the bioreactor moved outwards in a linear front up to the hollow fibre bundle, where again, cells infiltrated the bundle and were protected from subsequent removal.

Also, multi fibre bioreactors were rotated for 4 hours longer than single fibre bioreactors, allowing more time for cells pressed against the fibre due to centrifugal action to attach. Unfortunately, this means that attachment on single and multi-fibres are not directly comparable. However, single fibre attachment for 6 hours can be extrapolated theoretically. At 6 hours rotation the cell front would be in contact with the hollow fibre would be for 3:07h, 5:32h and 5:45h (at 2 RPM, 6 RPM and 8 RPM), and from the flat sheet cell attachment time course (Figure 4.12) any time over 3 hours provides the same degree of cell attachment (~84%). Following the methodology described in Table 4.11, theoretical cell attachment for each rotational setting with single fibres would be 45% ± 17%, which is still less than the theoretical maximum for multi-fibre bioreactors at 59% ± 22%. A similar table with values is provided in Table D.1 in Appendix D. However given the discrepancy between the theoretical and experimental data for dynamic single hollow fibres (Table 4.12), this extrapolation is likely to have a similar margin of error.

A horizontal multi fibre bioreactor rotating at 6 RPM provided the optimum conditions to facilitate the highest rate of cell attachment. It is possible that higher rotational velocities (8 RPM) may have also led to detachment of previously attached cells that had infiltrated into the space between fibres.

Bundles of hollow fibres inside a bioreactor have been used to cultivate cells of several types; however studies typically focus on the final cell quantity that can be harvested instead of initial cell seeding rates and optimisation. Rates of seeding density typically vary depending on cell type, the required final cell number, or if there is a time constraint. Studies using commercially available HFBs have been seeded for 24 hours (Nold *et al.*, 2013) or 48 hours (Roberts *et al.*, 2012) under static conditions, with cell health gauged over time by measuring concentrations of D-glucose and L-lactic acid, which were not quantified into a representative cell number. Others initiate a slow initial perfusion of cells in media through the HFB and ancillary equipment before increasing flow rate (Pinzon *et al.*, 2013; Cao *et al.*, 2014; Tapia *et al.*, 2014). Researchers using these perfused systems also do not typically quantify cell attachment, either directly through trypsinisation, or indirectly by counting unattached cells in the circulating media.

4.4.5 Comparisons, Limitations and Error Analysis

Comparing both the single and multi-fibre dynamic attachment data for each drum speed and bioreactor orientation shows a greater rate of attachment on multi fibre bioreactors in every case. Performing a student's t-test between pairs showed that horizontal, 2 RPM, 6 RPM and 8 RPM configurations are significantly greater to a 95% certainty. The reasons for this could be due to the increased relative volume that the bundle of 5 hollow fibres took up in the larger

glass bioreactor compared to the single fibre in the silicone bioreactor. Of the total volume available inside a module the hollow fibre zone takes up 25% of a single, and 44% of a multi-fibre bioreactor.

With the centrifugal settling model outlined in this chapter, the maximum rate of cell attachment would be equal to the number of cells that have the opportunity to contact the fibre when they initially settle after inoculation, plus the proportion of unattached cells in the linear cell front that make contact with the HFZ. This would be a maximum cell attachment of 38% ± 13% for single fibre modules (horizontal at 8 RPM for 2 hours) and 59% ± 22% for multi-fibre modules (horizontal at 6 or 8 RPM for 6 hours) as outlined in Table 4.12. Whilst for multi-fibre bioreactors the best experimental dynamic attachment of 39% ± 12% (horizontal at 6 RPM for 6 hours) is within the margin of error of the theoretical maximum, single fibre bioreactors show the best rate of experimental dynamic attachment to be 13% ± 8%, which below the range of the maximum theoretical attachment. From this discrepancy it can be concluded that flaws in the model must be present. The assumption of a linear cell front is an over-simplification, as cell collisions and interactions would cause cell distribution in three dimensions, perhaps in a spiral. The validity of using centrifugal particle settling equations is also questionable, given that the rotational speed is relatively low, and no published data using a similar method is available; but in and of itself this work is still useful even if parts of the theoretical analysis did not match the experimental data.

The equations used to calculate the rates of settling were derived from first principle force balances on a particle and were expressed in chemical engineering textbooks such as Coulson & Richardson's Chemical Engineering Volume 2 (Richardson *et al.*, 2002). The authors of this book placed several caveats on the application of those equations by way of assumptions. One such assumption was that the settling of a single particle was not affected by the presence of other particles in the fluid, i.e. free settling. Whilst every attempt was made to mix the cell solution into a homogeneously distributed cell suspension for inoculation, it was likely that the cells in the solution were not evenly spread away from each other and may in fact have remained in small agglomerates. This would affect the settling equation as the buoyancy force of several cells clumped together would be greater than that of a single cell. Another assumption was that the walls of the reactor did not exert an appreciable retarding effect. This was mitigated in multi-fibres by applying Sigmacote to the glass reactor walls so that no cells attached to their surface; however this was not possible in the single fibre bioreactor system. The next assumption was to consider the fluid as a continuous medium with the cells being large compared to the mean free path of the molecules that make up the fluid itself, i.e. that the movement of the molecules of the fluid did not affect the settling velocity of the cell. This was accounted for by calculating the hindered settling velocity. The final main assumption

was that the diameter of the cell was so small that its movement through the fluid can be characterised by a Reynolds number which was less than 0.2, thus falling within the remit of Stokes' law and allowing the use of a simplified drag force factor for the settling velocity calculation. Other assumptions include the fluid media as a Newtonian fluid and that the cells were perfect spheres all possessing the same radii, volume, density and mass.

With settling due to centrifugal action it was again assumed the cell was obeying stokes law in the fluid. A second derivative acceleration term in the equation of motion for the Stokes' law region was excluded because it was assumed that the cell would never acquire an equilibrium velocity in the fluid. This source also posed no restrictions on the minimum angular velocity required to be able to use the equation of motion in a centrifugal field, however it was likely that at lower angular velocities the force of gravity cannot be neglected. More investigation needs to be undertaken to ascertain if the slow movement of cells by centrifugal action postulated in this section is a valid model to explain the results shown in this chapter.

No other papers could be found which used a similar dynamic method for cell attachment as described in this report. Some computational models have been developed for rotating HFB systems, which deal with determining the speed of rotation that provides the most homogeneous mixture of cells in media, but does not model how cells may attach to hollow fibres in this system (Consolo *et al.*, 2009). In this case a HFB of length 11 cm and radius 3.6 cm is rotated about its central point tangentially for 300 seconds and determines that a homogeneous distribution of initially settled cell aggregates is achieved at 30 RPM, but does not offer a rate of cell attachment. This was converted to a linear velocity of 0.057 m/s and an angular velocity of 3.142 s^{-1}. Their linear velocity is identical to that in the dynamic rotating drum system in this study; but the angular velocity is approximately five times greater, implying that the rotational forces in the rotating drum system studied in this chapter are not enough to ensure a homogeneous mixture. However this model was only run for 300 seconds not 6 hours, and does not take into account long term cell settling due to centrifugal action.

4.5 CONCLUSIONS

From the experiments outlined in this chapter it was concluded that:

i) Cell attachment on flat sheet PLGA scaffolds increased over time from 20% ± 11% after 5 minutes to 85% ± 31% after 3 hours, after which cell attachment plateaued at a maximum value, as shown by 84% ± 35% attachment after 4 hours.

ii) Experimental results for 6 hour dynamic seeding in multi-fibre bioreactors showed that the best rate of cell attachment was 39% ± 12% at 6 RPM and at a horizontal orientation. This was double the values of 20% cell attachment found in other works.

iii) Experimental results for 2 hour dynamic seeding in single fibre bioreactors showed that all configurations provided less cell attachment than the static comparison (18% ± 16%); with the best cell attachment of 13% ± 8% at 2 RPM and at a horizontal orientation.

iv) Back calculation of cell attachment from determining the number of unattached cells in the media was shown to be an inaccurate method, as at least 20% ± 14% cells were lost during the seeding process.

This study has shown that for seeding single hollow fibres only a simple static regime is necessary, and could be further improved by simply inverting the bioreactor every 3 hours to provide the maximum rate of cell attachment over a greater surface area. During this work it became apparent that there was a high degree of error associated with large quantities of cell data. Analysing the uncertainties of the experimental method and cell counting procedures was important to put results in the correct context, which other authors tend to avoid.

For future work on cell seeding, improvements on the experimental method should be sought to mitigate error. A static control experiment should also be undertaken on the seeding of bundles of hollow fibres to check that the dynamic regime still leads to improvements. A much simpler seeding regime of manually turning bioreactors to allow cells to settle onto the fibre as many times as necessary should also be investigated to see if it matches the flat sheet data. Alternative methods of seeding should also be explored, including modifying the MACSmix rotator to allow longer static periods, and perfusion of cells through the hollow fibre bioreactor.

The improved rate of cell attachment will allow an accelerated growth of the dose of MSCs required for traditionally administered cell therapies. Initial cell attachment of 39% ± 12% of the 812,800 ± 318,400 MSCs yielded from patients would now allow 50 million MSCs to be grown in 11.2 ± 4.7 days, 1.4 days quicker than before. The novel dynamic cell attachment methodology outlined in this chapter will enable cell therapies to be administered to patients faster. In order to enable cell expansion in HFBs porous hollow fibres need to be manufactured and characterised. This is described in the next chapter.

CHAPTER FIVE: SODIUM CHLORIDE PARTICLES USED FOR MANUFACTURE OF POROUS PLGA SCAFFOLDS

5.1 INTRODUCTION

Hollow fibre bioreactors (HFBs) were chosen as the desired method for cell culture. This was due to their ability to operate in a continuous configuration, improved surface area to volume ratio, and the ability to emulate flow conditions *in vivo*. HFBs also provide the quickest rates of mesenchymal stem cell (MSC) growth compared to other bioreactor designs. A hollow fibre bioreactor can be operated in several configurations, however the most useful mode allows media to be perfused through the central lumen and slowly permeate through to the outer surface where cells have attached. This reduces the shear forces that cells are exposed to, which if too high could damage cells or lead to their detachment from the membrane surface. The previous chapter focussed on methods of improving cell attachment onto the outer surface of hollow fibres to increase the number of cells available to grow and maximise cell harvest rates.

Poly (lactic-co-glycolic acid) (75% lactide, 25% glycolide) scaffolds (PLGA) manufactured by phase inversion immersion precipitation in this study yielded non porous external surfaces as a result of formation of a thick skin layer. Beneath this layer exists access to a tortuous network of pores through which fluids would permeate through if made accessible. Standard PLGA scaffolds manufactured in this study lacked access to this sublayer, making them unsuitable for cell culture in this circumstance. Before culturing cells on PLGA hollow fibres this skin layer must be removed or penetrated.

Experiments involving changing the non-solvent, adding polyethylene glycol and partial re-dissolution of the membrane surface were all trialled to facilitate partial or complete removal of the primary skin layer, but all failed. A technique to manufacture a porogen with a desired size and a narrow size distribution from sodium chloride (NaCl) particles was found, and this material was added in an attempt to introduce pores onto PLGA membrane surfaces. This is the first time this manufacturing technique has been used to introduce pores to PLGA fibres made via immersion precipitation. This method is described in Section 3.3.2.

This chapter features the introduction of different quantities of NaCl porogen, to a PLGA/N-Methyl-2-pyrrolidone (NMP) mixture. Flat sheet and hollow fibre membranes were manufactured and imaged to determine if surface porosity formed on their surfaces. Pore number and area were analysed to determine how different quantities of NaCl altered the

external surfaces of membranes. Hollow fibre membranes made from different amounts of NaCl were analysed using gas and liquid permeation experiments to determine permeability.

5.2 PERMEATION THEORY

Permeability of hollow fibres (and other scaffold types) to fluid flow can be calculated from different equations depending on the internal structure of the membrane. Generally, the ability to permeate through a structure is inversely proportional to pore length, and proportional to pore radius (Richardson *et al.*, 2002), however several other factors are also considered. Examples of characteristic pore geometries are shown in Figure 5.1, with black and white illustrating fibre structure and void space respectively.

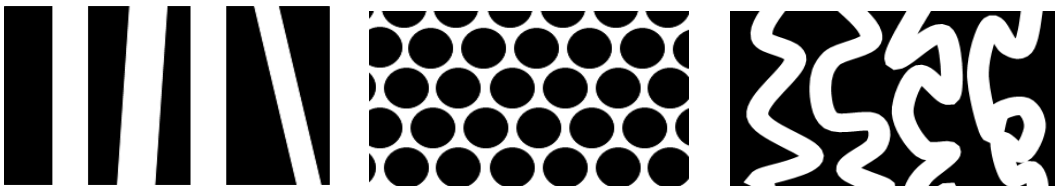

Figure 5.1 – Examples of characteristic pore geometries. (a) Parallel cylindrical pores, (b) close packed spherical structure, (c) spongy tortuous network. White regions represent open voids, black regions represent solid fibre structure.

Several equations were investigated for their applicability in modelling these structures and are outlined in Table 5.1. All equations are based on the principle equation that permeation flux (J) is equal to the product of a permeability constant (κ) and a pressure gradient driving force. Flux equations are converted into permeation flow rate (Q) using fibre geometry terms.

Table 5.1 – Equations used to characterise different porous statures in membranes.

	Darcy	**Hagen-Poiseuille**	**Carman-Kozeny**
Structure	UNDEFINED		
Flux (m/s)	$J = -\frac{\kappa}{\mu}.\frac{\Delta P}{\Delta x}$	$J = -\frac{\epsilon_s r_p^2}{8\mu\tau}.\frac{\Delta P}{\Delta x}$	$u_S = \frac{1}{K}.\frac{\varepsilon_b^3}{S^2(1-\varepsilon_b)^2\mu}.\frac{\Delta P}{\Delta x}$
Flow rate (m^3/s)	$Q = -2\pi rL\frac{\kappa}{\mu}.\frac{\Delta P}{\Delta x}$	$Q = -2\pi rL\frac{\epsilon_s r_p^2}{8\mu\tau}.\frac{\Delta P}{\Delta x}$	
Permeation (m^2)	κ	$\kappa = \frac{\epsilon_s r_p^2}{8\tau}$	$\kappa = \frac{1}{K}.\frac{\varepsilon_b^3}{S^2(1-\varepsilon_b)^2}$

Darcy's law is used as a very simple equation to calculate permeability without consideration for the geometries inside the hollow fibre. If general fibre properties such as length (L), radii (r) and thickness (x) are known, as well as fluid properties such as viscosity (μ) and

permeation rate, then permeability can be determined. Permeation is dependent on pore radius, tortuosity and surface coverage. For Darcy's law the permeation term is a 'black box' because pore geometry cannot be accurately defined.

Pores shaped as those shown in Figure 5.1a are described as a number of parallel cylindrical pores either perpendicular or oblique to the surface of the membrane. In this model all pores have equal length, pass through the whole of the membrane, and possess the same radius (r_p). Flux through this pore system can be described using the Hagen-Poiseuille equation, with ϵ_s as the surface porosity (i.e. pore coverage) and τ the tortuosity of the pore (equal to unity for cylindrical perpendicular pores). This equation assumes an incompressible and Newtonian fluid with laminar flow and constant cross-sectional area.

The permeability of a packed bed structure shown in Figure 5.1b can be calculated using the Carman-Kozney equation, assuming that fluid flow is laminar. The surface area per unit volume of particle (S), the fractional voidage of packed bed (ε_b), and the Carman constant (K) are required to calculate a permeability term using intrinsic fibre knowledge. The Carman-Kozney equation is expressed in terms of superficial velocity (u_S), as calculation of a flow rate is not particularly useful.

Figure 5.1c shows a tortuous network that may have interconnectivity and varying pore radii. There is no one equation suitable to fit geometry of this type. Both Hagen-Poiseuille and Carman-Kozney can be used (Mulder, 2003), however care should be taken in drawing conclusions based on intrinsic pore properties. Using Darcy's law to provide a value for permeability without the need to specify how the pore structure is formed, is most applicable in this case where geometry is uncertain.

5.2.1 Modelling Hollow Fibres

The phase inversion method of scaffold manufacture leads to regions with different pore geometries throughout the fibre cross-section, typically increasing in size from the water-exposed side of manufacture towards the centre of the fibre wall. This is shown in cross-section SEM images of flat sheets and hollow fibres throughout this chapter. An example image illustrating this phenomena is shown in Figure 5.2.

As both the lumen and outer walls are exposed to water during manufacture of hollow fibres, they both form a non-porous skin layer. From both walls moving inwards there are three regions of porosity with different ranges of pore diameter: 0.5 – 1 µm (primary), 2 – 5 µm (secondary), and 20 – 30 µm (tertiary) pores that join together in the centre of the fibre structure forming large macrovoids.

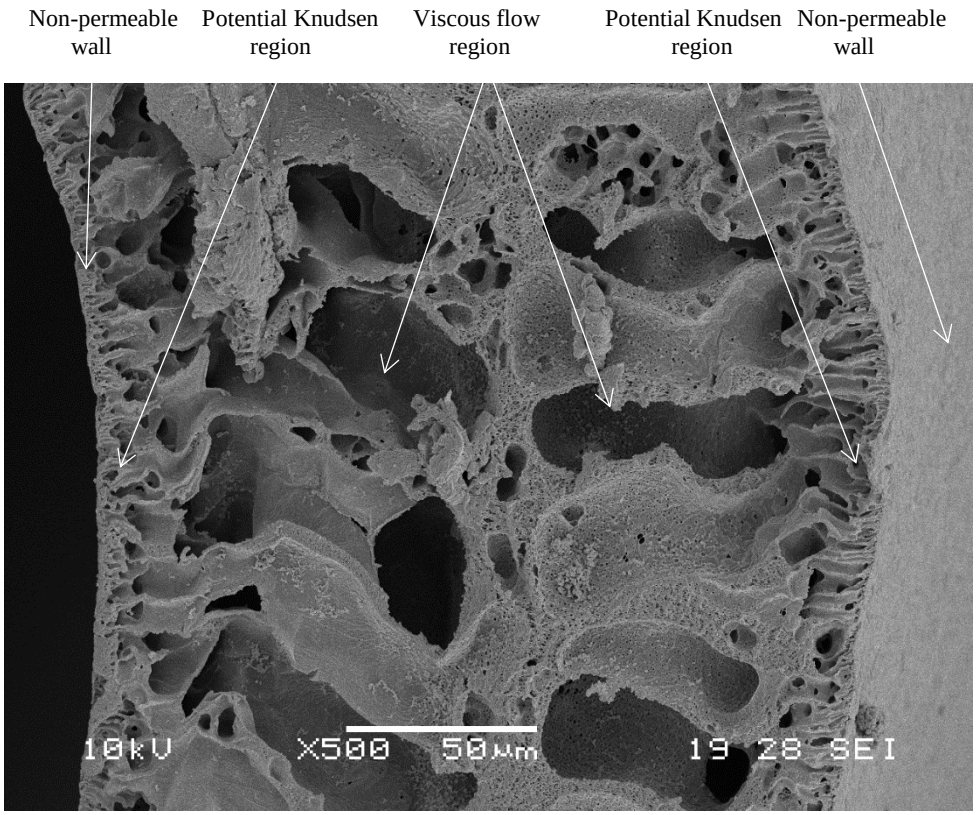

Figure 5.2 – Cross-section of hollow fibre wall with a 'non-porous' layer, narrow pores (Knudsen) and wide pores (viscous flow).

The non-porous skin layer will likely be the rate determining step as it provides the most resistance to fluid flow. If the skin layer could be made permeable, the rate limiting step would be determined by the primary pore layer, as it offers the smallest sized pores. This is visualised in Figure 5.3, showing the three porous regions in white with an equivalent pore thickness dotted through the fibre if the primary pore layer was considered to be rate limiting (not to scale).

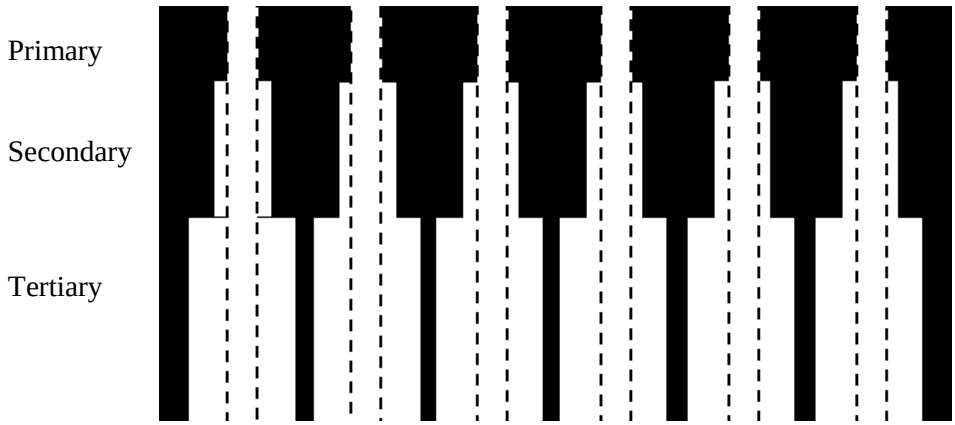

Figure 5.3 – Pore layers in hollow fibre with comparable structure if primary layer is rate limiting. Assumes removal of non-porous skin layer. For illustration only. Pores are not to scale or proportionally comparable to real pores.

Assuming the primary pore layer is the rate limiting step, and a certain amount of it is exposed via permeablising the skin layer with surface pores, the Hagen-Poiseuille equation shown in Table 5.1 could be applied to the model shown in Figure 5.3, but would yield unrealistic values for pore tortuosity. Darcy's law could be applied without using the described model with no consideration for the pore geometry to simply yield a value for permeation that would still be comparable to other works.

As the pore structure does not resemble that of a packed bed, the Carman-Kozney equation was not chosen. A permeation value calculated using Darcy's law could be applied to known packing materials to find an equivalent value, which may be useful if using the same PLGA scaffold in a packed bed bioreactor.

Consideration of Knudsen Flow

Knudsen flow arises exclusively in low pressure gas flows through membranes with pore diameters less than 0.2 µm. In these environments gas molecules possess a mean free path comparable or larger to that of the pores, increasing the likelihood of molecule-wall collisions which increases flow resistance; as opposed to viscous (Poiseuille) flow where molecule-molecule collisions dominate. The mean free path of a nitrogen molecule (λ) is calculated in Equation 5.1 with diameter 370 pm (Hirschfelder, 1955), at 1 bar gauge pressure and 298 K can be calculated using the Boltzmann constant (k_B) to determine if Knudsen flow is in effect:

$$\boldsymbol{Mean\ Free\ Path} = \frac{\boldsymbol{k_B T}}{\boldsymbol{\pi d_{N_2}^2 P\sqrt{2}}}$$

$$Mean\ Free\ Path = \frac{1.381\ \times 10^{-23}\left[\frac{m^2 kg}{s^2 K}\right] \times 298\ [K]}{(3.7 \times 10^{-10})^2[m]^2 \times \pi \times 101{,}325\left[\frac{kg}{m.s^2}\right] \times \sqrt{2}}$$

$$\boldsymbol{Mean\ Free\ Path = 0.07\ \mu m}$$

Equation 5.1 – Calculation of the mean free path of a nitrogen molecule.

As the primary layer has pores of 0.5 – 1 µm diameter, and the mean free path of nitrogen at the above conditions is 0.07 µm, it can be concluded that Knudsen flow is not applicable in this PLGA membrane.

5.2.2 Permeation

Darcy's law was used to calculate both gas permeability (κ_G) and liquid permeability (κ_L) of the hollow fibre as shown in Equation 5.2. Permeability is expressed in m^2:

$$\boldsymbol{Q = 2\pi rL\frac{\kappa}{\mu}.\frac{\Delta P}{\Delta x}}$$

Equation 5.2 – Darcy's law.

The thickness of the hollow fibre can be represented as the difference between the outer radius (r_{OF}) and inner radius (r_{IF}), or dr. Fibre surface area (A) is the available area for gas transfer and is equivalent to the surface area of a cylinder ($2\pi rL$). Equation 5.2 is rearranged to make permeability the subject in the following derivation, and integrating using outer and inner fibre radii as the limits:

$$\kappa = -\left(\frac{Q}{2\pi L}\right)\left(\frac{\mu}{\Delta P}\right)\left(\frac{dr}{r}\right)$$

$$\kappa = -\left(\frac{Q}{2\pi L}\right)\left(\frac{\mu}{\Delta P}\right)\int_{r_{IF}}^{r_{OF}}\frac{dr}{r}$$

$$\boldsymbol{\kappa = -\left(\frac{Q}{2\pi L}\right)\left(\frac{\mu}{\Delta P}\right)\ln\left(\frac{r_{OF}}{r_{IF}}\right)}$$

Equation 5.3 – General equation for permeation through a hollow fibre wall.

The driving force that causes permeation *(ΔP)* can be simplified by changing the inlet pressure and retentate pressure values into terms of atmospheric pressure (P_A) and applied gauge pressure (P_G). It is assumed that membrane properties are uniform along the length of the fibre.

Gas Permeation

For gas permeation tests the hollow fibre is operated in a dead-end mode as shown in Figure 5.4, where there no retentate flow is possible. Therefore the driving force (ΔP) is equivalent to the pressure difference between the inlet and permeate streams. The module outputs the permeating nitrogen gas to atmospheric pressure. Equation 5.4 shows how ΔP can be defined in this system:

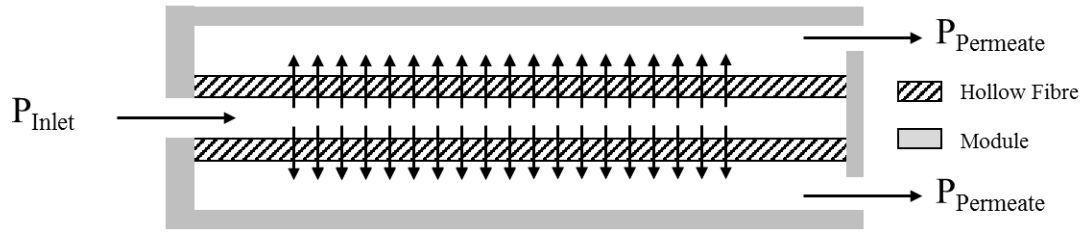

Figure 5.4 – A schematic of a single hollow fibre in dead-end mode for gas permeation.

$$\Delta P = P_{Inlet} - P_{Permeate}$$

$$\Delta P = (P_A + P_G) - P_A$$

$$\boldsymbol{\Delta P = P_G}$$

Equation 5.4 – Quantification of ΔP for gas permeation in dead-end mode.

The driving force of gas permeation is dependent on the applied gauge pressure.

Liquid Permeation

For liquid permeation tests the hollow fibre is operated in a cross-flow mode as shown in Figure 5.5, where an applied back pressure at the retentate exit enables a permeate flow across the fibre wall. Equation 5.5 shows how *ΔP* can be defined in this system:

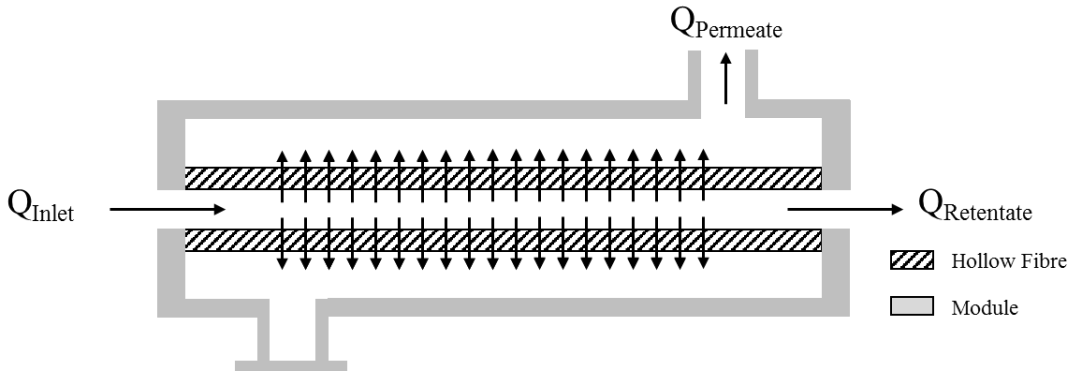

Figure 5.5 – A schematic of a single hollow fibre in cross-flow mode for liquid permeation.

$$\Delta P = P_{Inlet} - P_{Retentate}$$

$$\Delta P = (P_A + P_{G\,Inlet}) - (P_A + P_{G_{Retentate}})$$

$$\boldsymbol{\Delta P = P_{G_{Inlet}} - P_{G_{Retentate}}}$$

Equation 5.5 – Quantification of ΔP for liquid permeation in cross-flow mode.

For liquid permeation, *ΔP* is equivalent to the difference between the inlet and retentate gauge pressures.

As fibre liquid permeability depends on the change in pressure along its length it is important to isolate any other sources of pressure loss in the hollow fibre. Loss of pressure is a phenomenon that occurs in all incompressible fluids flowing through a pipe, and is caused by frictional forces between the fluid and the pipe surface. Pressure drop can be calculated using the Darcy-Weibach equation (Equation 5.6):

$$\boldsymbol{\Delta P = f_D \left(\frac{L}{D}\right)\left(\frac{\rho v^2}{2}\right)}$$

Equation 5.6 – Darcy-Weibach equation.

This is the product of the aspect ratio of the fibre length (*L*) and lumen diameter (*D*), the kinetic energy in the system and the dimensionless Darcy friction factor f_D shown in Equation 5.7:

$$f_D = \frac{64}{Re}$$

Equation 5.7 – Darcy Friction Factor.

Where *Re* is the Reynold's number of the fluid flowing through the hollow fibre lumen. Pressure lost in the fibre is also dependent on the physical roughness of the surface, however at low laminar Reynold's number this is not a factor and only starts to noticeably cause pressure loss at *Re*>4000 (Coulson and Richardson, 1999). The value for pressure loss must be taken into account to ensure that pressure losses can be exclusively attributed to permeation of liquid through the hollow fibre wall.

Other Factors

An alternative to stating how permeable a material is to fluid flow is expressing the resistance of a material to permeation. The resistance (Ω), with units m^{-1}, is membrane thickness divided by permeability and is shown in Equation 5.8:

$$\Omega = \frac{x}{\kappa}$$

Equation 5.8 – Equation expressing resistance to permeation.

Equations for permeability and resistance are only valid when flow through the pores is laminar (Mulder, 2003), therefore a Reynolds number less than 2000 is required. Reynolds number for a given pore is calculated as shown in Equation 5.9 using superficial velocity (u_S), derived from the outlet flow rate divided by the total surface area of the pores available on the inner hollow fibre surface. The average pore diameter (d_P) is also required, obtained from analysis of the porous fibre surfaces, we well as fluid density (ρ) and viscosity (μ).

$$Re = \frac{\rho u_s d_p}{\mu}$$

Equation 5.9 – Reynolds number equation.

5.3 RESULTS

5.3.1 Visual Analysis of PLGA Fibres with added NaCl Porogen

Previous attempts to manipulate PLGA have involved modifying the behaviour of polymer/solvent demixing by changing the properties of the non-solvent, or the addition of supplementary polymers to alter the polymer composition. Spinning hollow fibres using 1, 4-dioxane as a non-solvent provided localised removal of the primary skin layer, exposing the porous sublayer, however this method failed to remove or penetrate the skin along the entire polymer surface. An image of this scaffold is shown in Figure E.1 in Appendix E.

In a further attempt to add pores to the surface skin layer, a porogen was added to the polymer dope. The use of porogen in polymers used for biomedical applications is outlined in Section 2.3.6, but in short, NaCl crystals were selected due to their insolubility in NMP, their solubility in water, and the ability to be made to a desired size. NaCl crystals were manufactured as outlined in Section 3.3.2. NaCl crystal sizes were confirmed by EVOS microscopy (Figure 5.6) and an average crystal diameter of 8.8 ± 2.7 µm was measured over 121 samples. Pore dimensions of this magnitude were desired to ensure that cells would not migrate into the scaffold structure itself, while also not being damaged by high velocity media flow exiting the pores.

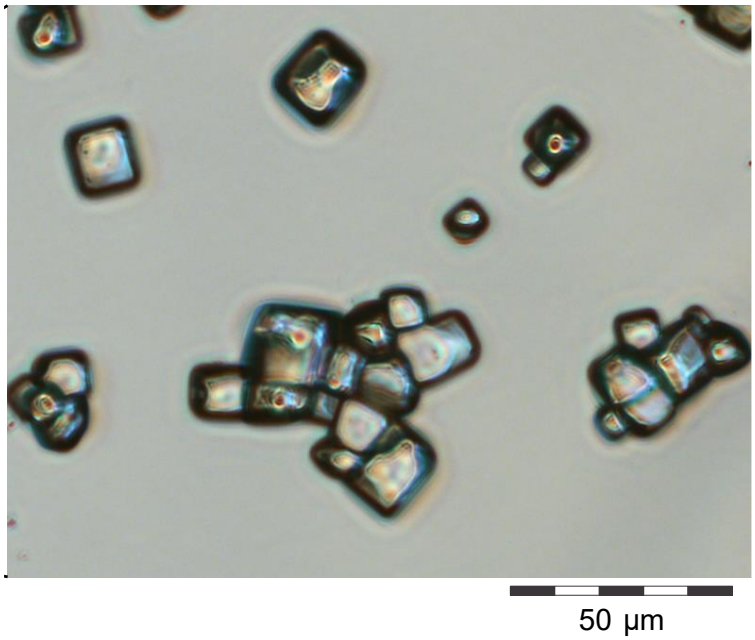

Figure 5.6 – NaCl crystals imaged using an EVOS microscope.

This results subsection outlines the addition of varied concentrations of NaCl to a PLGA/NMP mixture, and the resulting changes in structure of flat sheet and hollow fibre scaffolds. By weight percentage of PLGA in the polymer dope, 10%, 20%, 40% and 60% NaCl was added. Flat sheet and hollow fibre PLGA scaffolds were produced and pores on both external surfaces quantified by ImageJ analysis of SEM images.

SEM Images

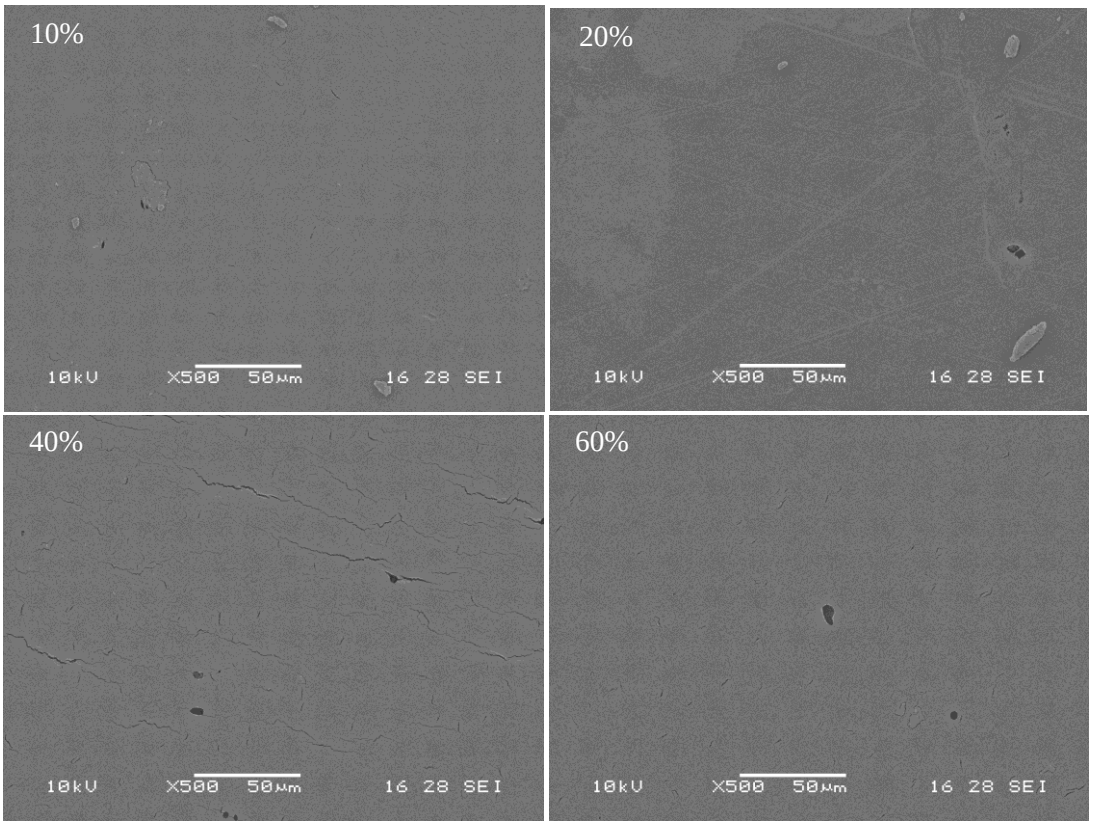

Figure 5.7 – SEM images of the top surface of PLGA flat sheets with 10%, 20%, 40% and 60% NaCl.

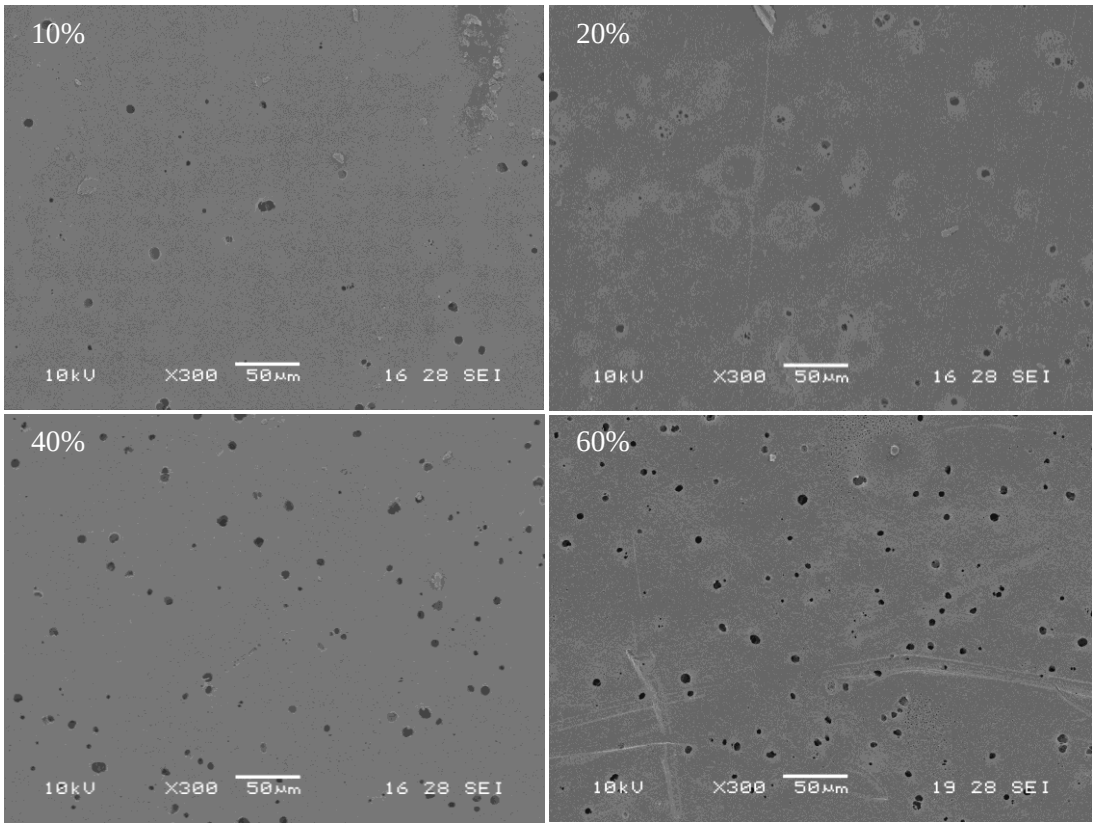

Figure 5.8 – SEM images of the bottom surface of PLGA flat sheets with 10%, 20%, 40% and 60% NaCl.

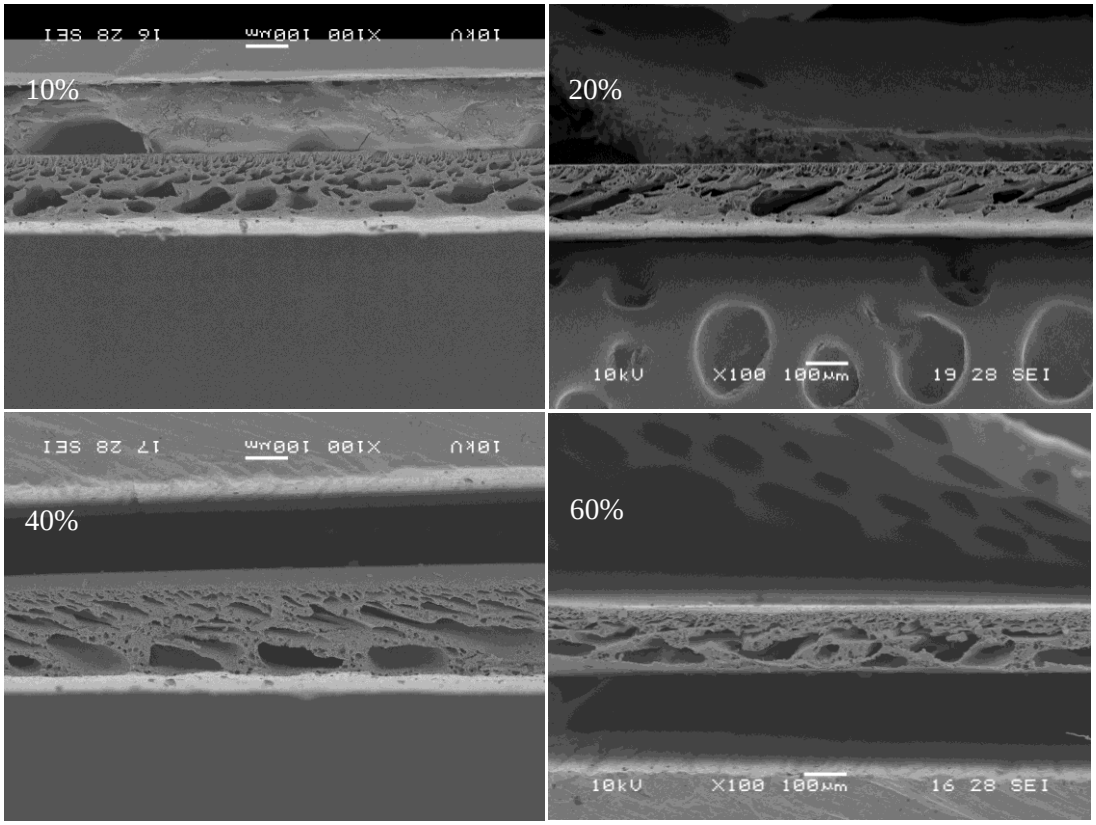

Figure 5.9 – SEM images of the cross section of PLGA flat sheets with 10%, 20%, 40% and 60% NaCl.

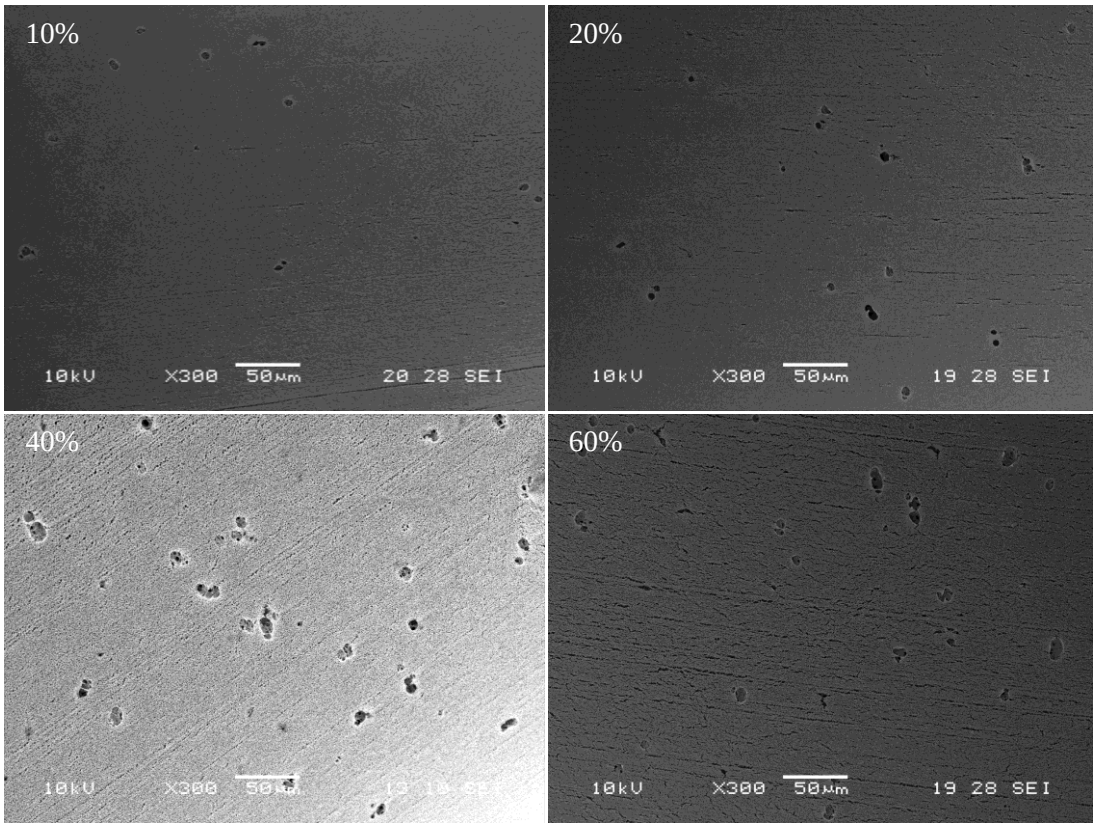

Figure 5.10 – SEM images of the inner surface of PLGA hollow fibres with 10%, 20%, 40% and 60% NaCl.

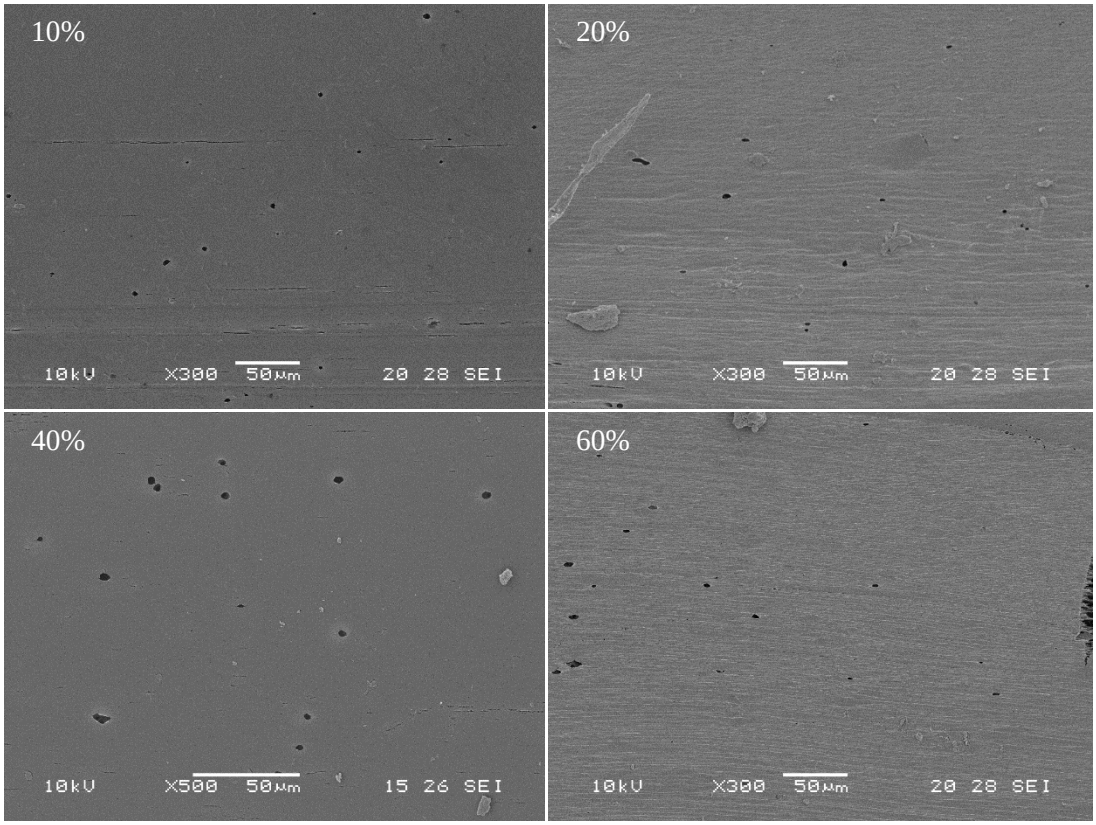

Figure 5.11 – SEM images of the outer surface of PLGA hollow fibres with 10%, 20%, 40% and 60% NaCl.

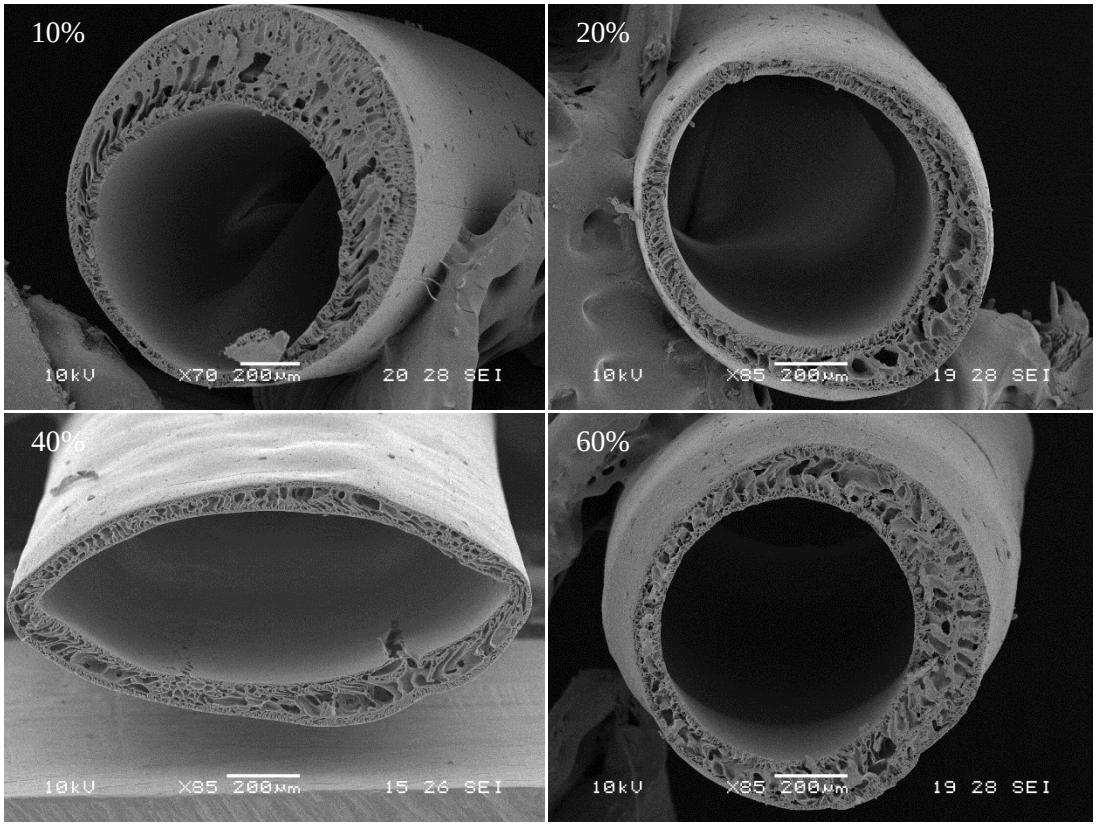

Figure 5.12 – SEM image of the cross section of PLGA hollow fibres with 10%, 20%, 40% and 60% NaCl.

5.3.2 Hollow Fibre Dimensions

Dimensions of the hollow fibres shown in Figure 5.12 are measured using the scale bars on each image. An average of four measurements for both the inner and outer diameters, and a calculated thickness value are shown in Table 5.2

Table 5.2 – Dimensions of hollow fibres.

Property (mm)	NaCl Percentage									
	0%		10%		20%		40%		60%	
	Value	*SD*	Value	*SD*	Value	*SD*	Value	*SD*	Value	*SD*
Average Outer Diameter	1.350	*1.9%*	1.250	*5.7%*	0.938	*5.7%*	1.050	*2.4%*	0.988	*1.8%*
Average Inner Diameter	1.140	*2.2%*	0.913	*5.8%*	0.738	*2.4%*	0.900	*2.8%*	0.713	*2.5%*
Average Thickness	0.105	*16.8%*	0.169	*26.2%*	0.100	*28.0%*	0.075	*23.6%*	0.138	*9.1%*

Surface Pore Analysis

Whilst the surfaces of both scaffold types can be distinguished qualitatively by observing SEM imagery, comparisons between different degrees of NaCl content for those surfaces required a quantitative analysis. SEM images were analysed using ImageJ software to count the number of pores on a given surface and to analyse the dimensions of these pores. The procedure used is outlined in Appendix B. Three random SEM images were taken for both sides of each scaffold surface for each quantity of NaCl. The total number of pores across the triplicate images were counted, their surface area quantified, and a percentage pore coverage and density on each scaffold calculated using the area of the SEM image. The top surface of flat sheets were not included as it was apparent from Figure 5.7 that they were non-porous. Data is presented in Table 5.3, with standard deviation error.

Table 5.3 – Pore data for each scaffold type, surface and NaCl content.

Surface	NaCl (%)	Pore Coverage (%)		Pore Density (Pores/mm^2)		Pore Area (μm^2)		Pore Diameter (μm)	
		Av.	*SD*	Av.	*SD*	Av.	*SD*	Av.	*SD*
Flat Sheet Bottom Surface	**10%**	0.48%	*0.08%*	221	*13*	21.8	*18.0*	5.3	*4.8*
	20%	0.34%	*0.06%*	221	*49*	15.4	*10.6*	4.4	*3.7*
	40%	1.77%	*0.26%*	749	*75*	23.6	*13.8*	5.5	*4.2*
	60%	1.44%	*0.20%*	746	*91*	19.3	*11.6*	5.0	*3.8*
Hollow Fibre Inner Surface	**10%**	0.25%	*0.10%*	120	*5*	21.1	*16.8*	5.2	*4.6*
	20%	0.34%	*0.15%*	115	*17*	29.6	*18.9*	6.1	*4.9*
	40%	0.82%	*0.36%*	260	*83*	31.5	*21.1*	6.3	*5.2*
	60%	0.68%	*0.24%*	268	*51*	25.4	*16.5*	5.7	*4.6*
Hollow Fibre Outer Surface	**10%**	0.15%	*0.01%*	101	*15*	14.6	*5.7*	4.3	*2.7*
	20%	0.13%	*0.03%*	84	*37*	15.4	*10.3*	4.4	*3.6*
	40%	0.23%	*0.06%*	270	*71*	8.4	*4.0*	3.3	*2.3*
	60%	0.17%	*0.05%*	149	*62*	11.1	*7.7*	3.8	*3.1*

A one way ANOVA with post hoc Tukey test was implemented to determine any statistical differences between the properties of the pores on scaffolds with different NaCl percentages, as well as any differences in the properties of pores found on different surface types at constant NaCl content. Direct comparison of the different surfaces for each NaCl percentage indicated that the bottom of flat sheets had the greatest pore density, followed by the inner then outer hollow fibre surfaces. Pore density on flat sheets was statistically greater than both fibre surfaces for all salt types.

Average pore density on the bottom of PLGA flat sheets is significantly similar between 10% - 20% and 40% - 60% NaCl data sets but both pairs are statistically dissimilar from each other. This illustrates a sudden increase in surface porosity between 20% and 40% NaCl doses. The same relationship is seen on the inner surface of hollow fibres, but not on the outer surface.

Average pore surface areas between all 10% NaCl surfaces were not significantly different. The pore area on inner surfaces of hollow fibres with 20% NaCl significantly larger than the other two surfaces; and for 40% NaCl and 60% NaCl all pore areas were significantly different from one another, with inner hollow fibre surface pores the largest followed by flat sheet and outer hollow fibre pores.

Average pore area differs between all NaCl percentages, but did not form any kind of correlation. As pore density between both 10% - 20% and 40% - 60% NaCl pairs were so similar, any significant difference in average pore area would affect overall pore coverage of the hollow fibre. Pore coverage on the bottom of flat sheets attained from 10% NaCl (0.48% ± 0.08%) was greater than that attained from 20% NaCl (0.34% ± 0.06%) and 40% NaCl (1.77% ± 0.26%) yielding a larger pore coverage than 60% NaCl (1.44% ± 0.20%). Average pore area on the inner surface of hollow fibres was larger with 40% NaCl, leading to a total pore coverage (0.82% ± 0.36%) greater than its 60% NaCl counterpart (0.68% ± 0.24%). The pores on the outer surface of 40% NaCl hollow fibres were significantly larger than those found on corresponding 10% and 20% fibres, leading to the largest pore coverage on that surface (0.23% ± 0.06%).

5.3.3 Gas and Liquid Permeation of Hollow Fibres

PLGA hollow fibres manufactured with 0%, 10%, 20%, 40% or 60% NaCl content were tested to indicate their permeability to nitrogen gas and ‘double distilled’ (ddH_2O) water, as outlined in Section 3.4.2, as well as their resistance and Reynolds number. These properties were compared for each fibre type at different ΔP. All experiments were repeated three times using fibres from their same respective batch. This was undertaken to determine if the porous surface indicated in SEM imagery provided penetration through the whole hollow fibre or whether

the changes were only cosmetic. Average dimensions of each hollow fibre type are shown in Table 5.2. All data was normalised to account for fibre surface area, pore properties and the number of fibres per module.

For gas permeation X-axis error from manual pressure gauge readings was 0.01 bar. Error on the Y-axis for the parameter in question was calculated from compound error as explained in Section 3.5, originating from error from the standard deviation of triplicate membrane outlet flow rate readings and measurements of membrane dimensions. Results were presented by averaging values of three repeat experiments at an applied ΔP for each fibre type. Y-axis error from the standard deviation of these average values dominate over those found from compound error.

For liquid permeation inlet and outlet pressure transducers allowed pressure measurements to be continuously measured and an average was output every 5 minutes, allowing ΔP to be calculated per time point. From comparison with the manufacturer's calibration data, the pressure transducers had an error of 0.2%, as shown on the X-axis. A 1% error was observed during permeation experiments with 0% NaCl PLGA fibres (i.e., zero permeation) which was applied as a standard degree of fluctuation of actual retentate mass measured on the scales when zero permeation was achievable. This is included in the as Y-axis error. A valve at the exit of the liquid permeation system was manipulated to impose a back pressure onto the system to increase ΔP and encourage an increased permeation. During pre-experimental testing it was discovered that the valve was not sensitive enough to allow fine control of back pressure, making experimental repeats at identical ΔP impossible. Additionally, pressure in the system never reached stable values after back pressure was applied. Pressure would slowly increase in the system until reaching the maximum allowable operating pressure of the transducers, whereupon the valve was manually re-opened to de-pressurise the system.

A range of set pressures were used for gas permeation, allowing changes in permeation to be observed at different applied ΔP. However in liquid permeation tests, due to the pressure control issues, ΔP could not be set at a repeatable stable single value. As a result all ΔP vs permeation, resistance or Reynolds number data points calculated for liquid permeation over the duration triplicate experiments (n=18, N=3) were averaged to provide a single value for all three properties.

Due to the un-centred lumen of manufactured hollow fibres shown in Figure 5.12, and the high dependence of permeability and resistance values on the thickness of the fibres, an average value for fibre thickness was calculated, as shown in Table 5.2. It was assumed that this would account for higher permeation through thinner, and lower permeation through thicker, parts of the fibre wall.

Gas Permeation

Gas permeability for hollow fibres manufactured with different weight percentages of NaCl is shown in Figure 5.13. Resistance of each fibre type, taking into account its average thickness, is displayed on Figure 5.14. Reynolds number of nitrogen gas permeating through the fibre is shown on Figure 5.15. Average values for all are summarised in Table 5.4.

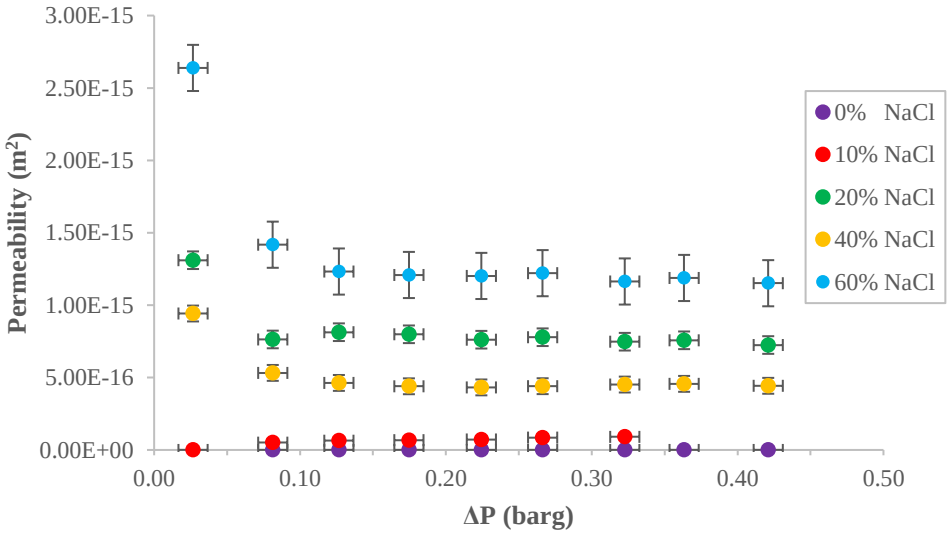

Figure 5.13 – Permeation of nitrogen through PLGA hollow fibres with different NaCl content. X error = 0.01 bar, Y error = SD (*n*=3).

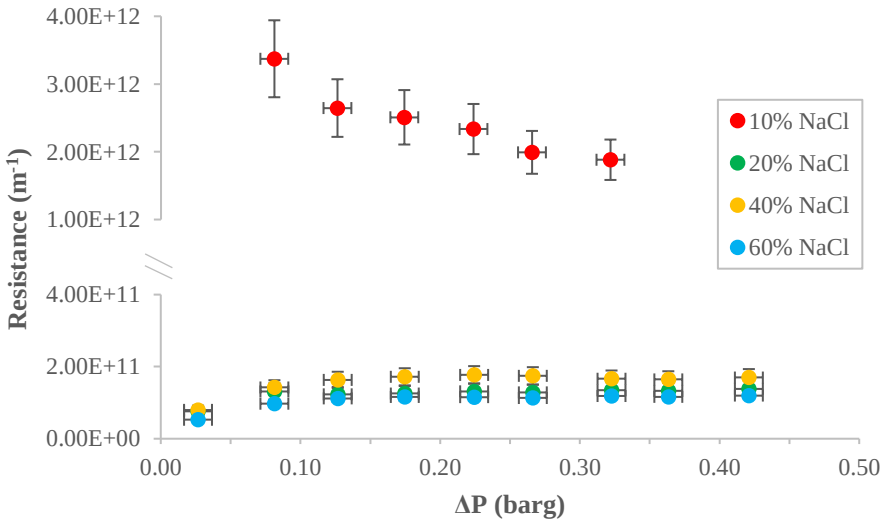

Figure 5.14 – Resistance of PLGA hollow fibres with different NaCl percentage to nitrogen permeation. X error = 0.01 bar, Y error = SD (*n*=3).

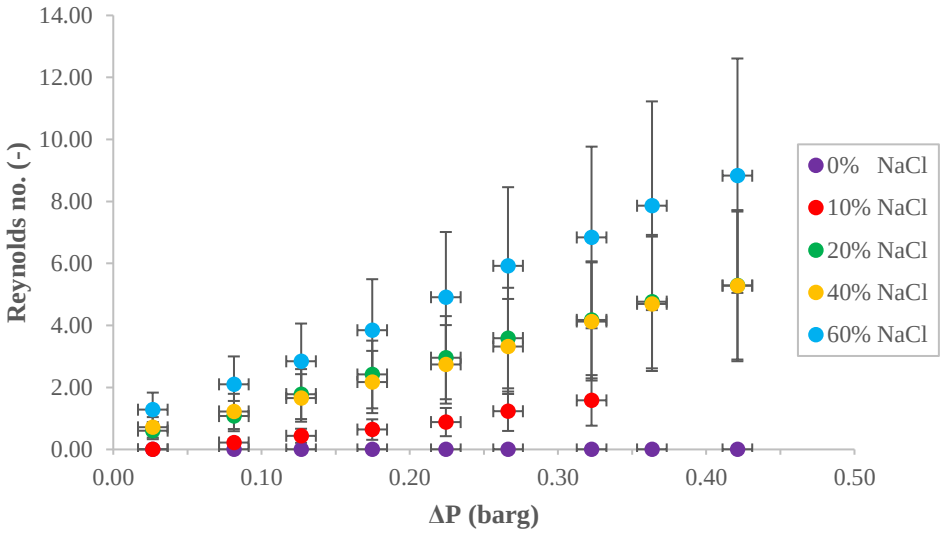

Figure 5.15 – Reynolds no. of nitrogen permeating through PLGA hollow fibre walls with different NaCl content. X error = 0.01 bar, Y error = SD (*n*=3).

Table 5.4 – Average gas permeability, resistance and flux of fibres with different NaCl content between 0.03 – 0.42 barg.

NaCl	Permeability (m^2)		Resistance (m^{-1})		Flux ($m^3m^{-2}h^{-1}bar^{-1}$)	
	Average	Error	Average	Error	Average	Error
0%	0	*N/A*	∞	*N/A*	0	*N/A*
10%	7.16E-17	*20.3%*	2.46E+12	*21.8%*	14.6	*19.7%*
20%	8.28E-16	*22.1%*	1.25E+11	*15.0%*	163.7	*24.8%*
40%	5.11E-16	*32.2%*	1.57E+11	*19.4%*	127.2	*21.5%*
60%	1.38E-15	*34.6%*	1.07E+11	*20.0%*	193.8	*19.9%*

For each fibre, permeability decreases with increasing ΔP. Permeability generally increased with NaCl content, aside from an inconsistency between 20% and 40% NaCl where 20% NaCl fibres offered greater permeability than 40% NaCl fibres. This was also reflected in the calculated values for resistance. A corresponding average nitrogen flux, normalised per unit surface area and pressure, showed a similar pattern. All permeation values were significantly different from one another. The resistance of 10% NaCl fibres was significantly greater than the other fibre types. Reynolds number increased with ΔP, and all values were low enough to assume laminar flow through the fibre. Therefore Darcy's law was applicable in these conditions.

Liquid Permeation

Liquid permeability for hollow fibres manufactured with different weight percentages of NaCl is shown in Figure 5.16. Resistance of each fibre type, taking into account its average thickness, is displayed on Figure 5.17. Reynolds number of liquid water permeating through the fibre is shown on Figure 5.18. Average values for all are summarised in Table 5.5.

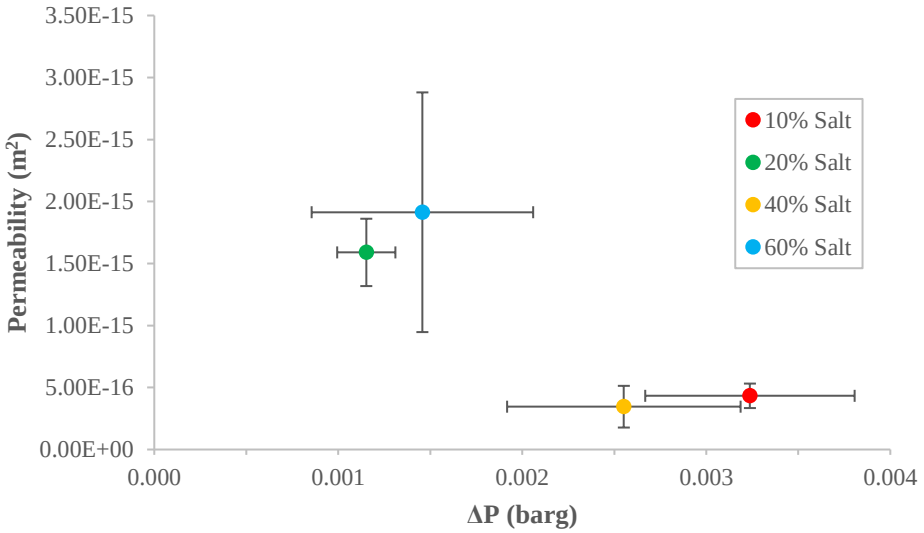

Figure 5.16 – Permeation of ddH₂O through PLGA hollow fibres with different NaCl content. X error = SD (n=54), Y error = SD (*n*=54).

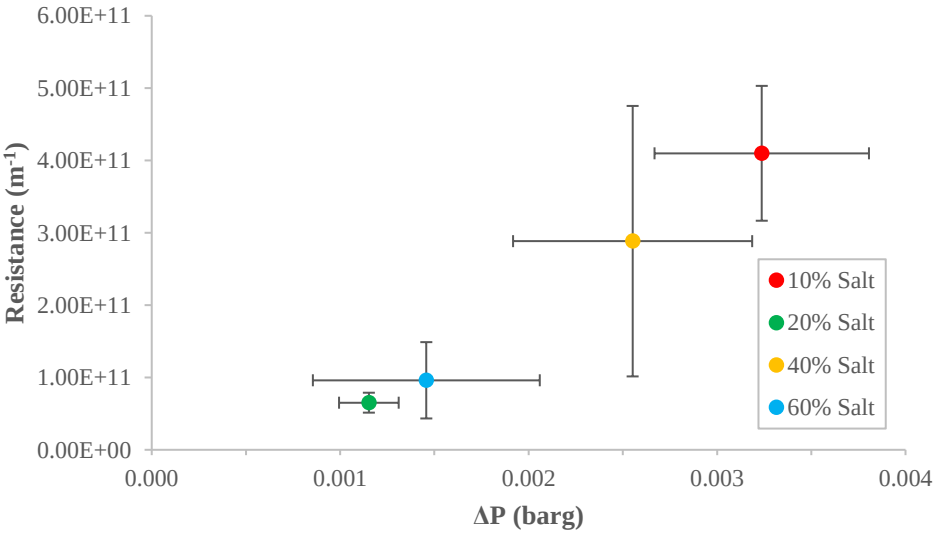

Figure 5.17 – Resistance of PLGA hollow fibres with different NaCl percentage to ddH₂O permeation. X error = SD (n=54), Y error = SD (*n*=54).

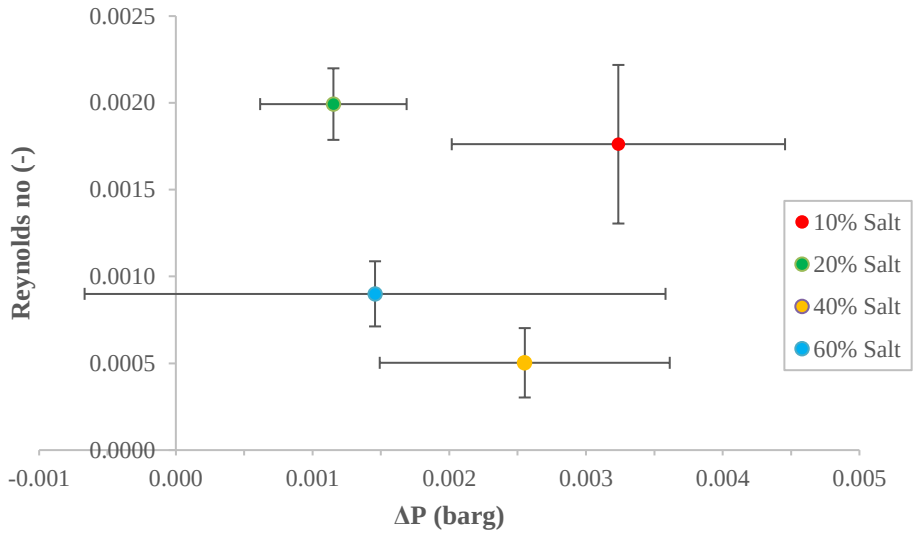

Figure 5.18 – Reynolds number of nitrogen permeating through PLGA hollow fibres with different NaCl percentage. X error = SD (n=54), Y error = SD (*n*=54).

Table 5.5 – Average liquid permeability, resistance and flux of fibres with different NaCl content between 0.001 – 0.004 barg.

NaCl	Permeability (m^2)		Resistance (m^{-1})		Flux ($m^3m^{-2}h^{-1}bar^{-1}$)	
	Average	Error	Average	Error	Average	Error
0%	0	*N/A*	∞	*N/A*	0	*N/A*
10%	4.33E-16	*22.8%*	4.10E+11	*22.7%*	1.21	*33.7%*
20%	1.59E-15	*17.1%*	6.52E+10	*21.1%*	7.23	*25.9%*
40%	3.45E-16	*48.7%*	2.88E+11	*64.8%*	2.00	*60.1%*
60%	1.91E-15	*50.5%*	9.61E+10	*54.9%*	6.63	*77.2%*

The fibre with the greatest NaCl content provided the largest permeation value. Fibres with other NaCl content yielded an inconsistent trend, with permeability decreasing in order of 60%, 20%, 10% then 40% NaCl. All average permeation values were significantly different from one another except between 10% and 40% NaCl fibres. Resistance of 20% fibres was the lowest of all types, followed by 60%, then 40% and 10% NaCl content. All average resistance values were significantly different from one another except between 20% and 60% NaCl fibres. Reynolds number was largest through 20% NaCl fibres, as was liquid flux. Liquid flow through all fibre types was laminar.

5.4 DISCUSSION

5.4.1 Membrane Morphology

SEM images in this chapter illustrated how porous surfaces could be manufactured during the phase inversion immersion precipitation process of PLGA/NMP mixtures supplemented with NaCl crystals of varying quantities. From visual inspection of these images it can be concluded that the pores on PLGA flat sheets form in limited quantities on the topside of the membrane (Figure 5.7), and primarily form on the underside (Figure 5.8). Pores form on both the inner surfaces (Figure 5.10) and outer surfaces (Figure 5.11) of PLGA hollow fibres, but are more numerous on the inner surface.

The non-porous flat sheet top surface could be attributed to the delayed demixing of PLGA and NMP in water. After immersion the PLGA remained attached to the glass support and slowly changed from a highly viscous transparent film to an opaque solid PLGA sheet (Figure 3.1). This occurred over a period of an hour. The increase in opacity was due to the PLGA/NMP demixing process continuing over time as the NMP diffused out of the film and the non-solvent (ddH_2O) penetrated downwards from the top surface to the bottom. The top of the casted polymer film was exposed to the non-solvent immediately after immersion, and took approximately two minutes to show signs of increasing opacity. During this time the NaCl on the polymer surface could be readily dissolved in the ddH_2O before demixing on the PLGA surface had fully concluded, leaving adequate time for the PLGA/NMP solution to re-fill the pores created from the vacant NaCl particles.

The NaCl in the PLGA/NMP mixture below the exposed top layer remained in solution as the PLGA/NMP solution around it demixed and a solid scaffold was formed. Once the flat sheet came away from the glass support the NaCl on the bottom surface dissolved. The flat sheet was left for approximately 3 days in ddH_2O with regular water changes to drive out any excess NMP and allow salt to leach out of the PLGA. Pores near exclusively only appeared on the bottom surface of flat sheets, indicating that the NaCl only leached out of the flat sheet downwards. This could also be attributed to the inherent buoyancy of flat sheet membranes in general, causing scaffolds to float. The top side was partially submerged, but was often exposed to air, while the underside was completely consistently submerged. The small quantity of pores that did appear on the surface would have formed in the first hour of immersion in water, as the PLGA flat sheet was still attached to the glass plate during this time while only the top side was exposed to water. However, casting flat sheets of other polymers with NaCl additive, which demixed instantly and were also prone to floating, yielded both a porous top and bottom surface (Argyle, Unpublished). In this case the surface demixing occurred at a faster rate than NaCl dissolution, allowing pores to form on the top surface.

Pores were present on both the inner and outer surfaces of hollow fibre membranes, although in reduced number compared to the underside of flat sheets. Due to the method of manufacture, both the inner and outer surfaces were exposed to non-solvent simultaneously when passed through the spinneret, allowing the demixing process to take affect from two directions and occur instantaneously. This allowed the formation of pores on their non-solvent exposed surfaces. Hollow fibres were also less thick than flat sheets, further increasing the rate at which the entire scaffold was demixed.

Formation of macrovoids in the cross sections of flat sheets (Figure 5.9) and hollow fibres (Figure 5.12) are independent from the NaCl additive (Mulder, 2003). Initially small voids were created as a by-product of the demixing process near the polymer surface. These voids increased in size due to diffusion of solvent and non-solvent, growing until polymer concentration surrounding the macrovoid was high enough to solidify. The main factors that affected macrovoid formation were the solvent/non-solvent pair chosen and the polymer concentration, which both affected the thermodynamics of demixing (Mulder, 2003). Small pores were also formed on inner surfaces throughout the cross section of flat sheets and hollow fibres as a result of NaCl leaching.

The non-proportional increase in pore number with NaCl content for each surface can be attributed to the manufacturing process. In regards to flat sheets, the method outlined in Section 3.3.1 did not form a membrane with uniform thickness. Flat sheets of thicknesses between 135 – 200 µm were formed during this study. This could be due to pouring inconsistent volumes of polymer solution onto the glass before submerging in water; however, as the polymer dope was continuously mixed on rollers prior to casting, a proportional quantity of NaCl should have been present regardless of the volume poured. All scaffolds were immersed in water for 3 days, allowing equal time for salt leaching to occur.

During setup of the hollow fibre spinning process the polymer dope was poured into the pressure vessel to be extruded through the spinneret. In the lag time between this step and the commencement of extrusion the NaCl began to settle out, leading to the initial length of fibre potentially having a greater concentration of NaCl than anticipated, decreasing gradually as the fibre was spun. Such a situation was unavoidable given the required size of the NaCl particles for cell growth applications and the excessive time required to initialise the spinning process. For future works a greater proportion of polymer mixed in with the solvent may increase its density enough to sufficiently slow the settling velocity of the NaCl; however this would increase the viscosity of the polymer, requiring a greater pressure to force it through the spinneret. Three random sections of the spun fibre for each NaCl quantity were imaged to determine if this effect caused differences in surface porosity along the length of the whole

fibre batch. Given the consistency in pore number between 10% - 20% and 40% - 60% NaCl samples on the bottom of flat sheets and inner fibre surfaces, NaCl prematurely settling is not a concern.

Neither of these methodological inconsistencies provide sufficient reason why on both scaffold types there was an obvious similarity between the two pairs of samples with differing NaCl content but near identical pore surface density. NaCl concentration seemed to affect the demixing process in such a way that an upper limit on the pore surface density was present. The four-way relationship between PLGA/NMP/water/NaCl has led to complex thermodynamic and kinetic behaviours during scaffold formation.

If one wished to model the thermodynamic and kinetic changes that arose from the demixing process in this system, all changes would have to be measured considering a moving boundary of opposing diffusion fluxes penetrating through the thickness of the film over time. The fluxes of solvent/non-solvent at a given thickness and time were dependent on the permeability of the polymer film and chemical potential (partial molar free energy), the latter of which acts as the driving force for mass transfer. Calculation of the Gibbs free enthalpy in this system requires knowledge of the number of moles and volume fraction of each component, as well as Flory-Huggins interaction parameters to determine how each component interacts with one another (Flory, 1953). Locating comparable values for the latter from literature was not possible due to the complexity of the quaternary system considered here and the sheer number of potential variables that arise between different studies (Mikos *et al.*, 1994; Fashandi and Karimi, 2014). Such variables include (but are not limited to) scaffold formation method, polymer type (including co-polymer ratios), choice of solvent and non-solvent, addition of pore-formers or other adjuncts and temperature.

Studies such as addition of PVA pore-former to hydroxyapatite scaffolds (Gallegos-Nieto *et al.*, 2015) and use of hydroxypropylcellulose pore-former on ethylcellulose coated pellets (Wang *et al.*, 2015) show increasing quantities of porogen yielding greater degrees of porosity. A study adding 20%, 40%, 60% and 80% polyethylene glycol (PEG) by weight to PLGA (85:15) to manufacture flat sheet membranes through air drying showed an increasing pore number up to 60% (Krok and Pamula, 2012). At 80% PEG surface porosity was worsened due to increasing continuity between regions of PEG in the membrane, an explanation that would not apply to the relationship outlined in Section 5.3.1. It was also observed that for each percentage PEG added the air dried side was always less porous then the surface in contact with the glass, similar to the SEM imagery shown in Section 5.3.1 however not as severe.

5.4.2 Hollow Fibre Permeability

The dimensions of each fibre type, assuming an average thickness for permeation, are shown in Table 5.4. Average dimensions are inconsistent between fibre types due to manufacturing inconsistencies between batches of fibre. The variation of thickness and the available surface area on the inner and outer fibre surfaces for permeation to occur were all normalised when calculating permeability, resistance and Reynolds number for both gas and liquid permeation.

Gas permeability of each fibre type over a ΔP of 0.03 – 0.42 barg is shown in Figure 5.13 (with the exception of 10% fibres tested to 0.32 barg), and an average permeation calculated over that range with associated error is displayed in Table 5.4. Hollow fibres with zero NaCl content yielded no value for gas permeability between the applied pressures of 0.03 – 0.42 barg; no flow rate of nitrogen gas was measured exiting radially from the fibres. Both gas and liquid permeation did occur in some fibres with zero NaCl, however these fibres were found to contain one or two larger holes of approximately 0.5 mm in diameter that were visible by eye. Imperfections in the fibre arose from transient issues in the spinning process and were excluded from the results if tested.

10% NaCl hollow fibres had an average gas permeability of 7.16E-17 m^2 (± 20.3%) and displayed a positive correlation, increasing permeability with ΔP. The porosity in this fibre was such that at the minimum applied pressure no permeation was detected. From 0.08 – 0.32 barg permeability increased by 78.9%. This pattern was consistent between replicates of each fibre for each of these fibre types. Hollow fibres with 20%, 40% and 60% NaCl content yielded an average gas permeability of 8.28E-16 m^2 (± 22.1%), 5.11E-16 m^2 (± 32.2%) and 1.38E-15 m^2 (± 34.6%), and are all shown to start at an initially higher permeation value at 0.03 barg, before suddenly dropping and then slowly decreasing between 0.08 – 0.42 barg by 5.0%, 16.7% and 18.8% respectively. This pattern was consistent between replicates of each fibre for each of these fibre types. All average gas permeabilities for each fibre type are significantly different from each other with a 95% confidence with n = 21 for 10% NaCl fibres, and n = 27 for 20%, 40% and 60% NaCl fibres.

Permeating gas flow was also measured when fibres were deformed and damaged due to prolonged exposure to higher pressures. This was characterised by a sudden spike of gas flow occurring at pressures of 0.5 – 1.0 barg. Data for these modules was retained up until the point of fibre collapse, but are only shown up to 0.42 barg to allow consistent comparisons between different fibre types.

Correcting for fibre thickness in Figure 5.14, 10% fibres possessed an average resistance of 2.46E+12 m^{-1} (± 21.8%) decreasing between 0.08 – 0.32 bar by 44.2%; and 20%, 40% and

60% fibres having an average resistance of 1.25E+11 m^{-1} (±15.0%), 1.57E+12 m^{-1} (± 19.4%), and 1.07E+11 m^{-1} (± 20.0%), all increasing by 5.5%, 19.4% and 23.2% respectively over 0.03 – 0.42 barg. Resistance of 10% fibres is significantly different from the other fibre types, which have no significant differences between each other.

Figure 5.16 displayed liquid permeability of each fibre type. For 10% NaCl fibres average permeability was 4.33E-16 m^2 (± 22.8%) at 0.003 barg (± 17.6%), 20% fibres was 1.59E-15 m^2 (± 17.1%) at 0.001 barg (± 13.7%), 40% was 3.45E-16 m^2 (± 48.7%) at 0.003 barg (±24.9 %) and 60% fibres was 1.91E-15 m^2 (± 50.5%) at 0.002 barg (±41.3%). All are significantly different from one another with a 95% confidence, except when comparing 10% and 40% fibres. N=3 and n = 54 for all samples as shown in Table 5.5.

Resistance of each fibre type to water flow is shown in Figure 5.17. 10% NaCl fibres had a resistance of 4.10E+11 m^2 (± 22.7%) at 0.003 barg (± 17.6%), 20% fibres had 6.52E+10 m^2 (± 21.1%) at 0.001 barg (± 13.7%), 40% had 2.88E+11 m^2 (± 64.8%) at 0.003 barg (± 24.9 %) and 60% fibres had 9.61E+10 m^2 (± 54.9%) at 0.002 barg (±41.3%). All are significantly different from one another with a 95% confidence, aside from comparison of 20% and 60% fibres. N = 3 and n = 54 for all samples.

A pressure loss through the bioreactor was to be expected before factoring in fibre permeability. For a fluid flowing through a pipe there is an expected loss of energy due to frictional forces between the fluid and pipe wall. This was accounted for using the Darcy-Weibach equation for pressure loss in a pipe with incompressible fluid flow, as outlined in Section 5.2. As discussed in that section, pressure losses are mainly dependant on lumen diameter. Maximum pressure loss for both gas and liquid flow was 3.97 Pa. The pressure losses for each fibre were calculated and accounted for in the graphs shown in Section 5.3.3.

Over the course of liquid permeation experiments ΔP fluctuated anywhere between approximately 0.001 – 0.004 barg, a range of 300 Pa. Large fluctuations across this range were seen between experiments, and minor fluctuations in this range occurred over a single experiment at a constant 1 ml/min inlet flow rate. Pressure fluctuation was attributed to changes in ambient temperature and pressure, and/or a minor elevation change along the bioreactor. It was these larger day to day environmental changes that led to such wide x-axis error bars in liquid permeation data (Figure 5.16 – Figure 5.18) for comparisons between each NaCl percentage for permeability, resistance and Reynolds number respectively.

Figure 5.13 and Figure 5.14 give the impression that fibre gas permeability and resistance was stabilising independent of ΔP, however a consistent increase in Reynolds number with ΔP shown in Figure 5.15 shows that this was not the case. A stabilisation effect would indicate

that gas flow through the fibre had reached a critical point where the total pore area for gas transport had become a rate-limiting factor. However, given the high compressibility of nitrogen gas, this issue would not arise until a pressure well beyond that at which the fibre could operate before failure. As discussed previously, calculation of Reynolds number was required to validate permeation data because Darcy's law's applicability was limited to laminar flow conditions, which was confirmed for all gas and liquid experiments (Figure 5.15 – Figure 5.18 respectively) with Reynolds number being less than 2000 in every circumstance. The positive Reynolds number trend with ΔP was expected for gas permeation because for each fibre the gas viscosity and density are assumed to be constant at constant temperature, superficial gas velocity is a function of applied pressure, and average pore area and pore number are constant for a given fibre type. Such a trend would also be expected for liquid permeation had readings at several values of ΔP been achievable.

Data for gas permeation generally showed increased permeation, decreased resistance and increased Reynolds number respectively as NaCl content increased. However on all three graphs the 20% and 40% plots were either out of sequence with this relationship or very close to one another. Liquid permeability also has 20% and 40% fibres out of step with the expected trend, with resistance and Reynolds number showing no correlation with NaCl content.

From the results of ImageJ analysis on fibre surfaces shown in Section 5.3.1 the surface differences between 20% and 40% fibres were the most pronounced out of all ascending comparisons. As discussed in Section 5.3.1 on the inner fibre surface the pore coverage of a 20% NaCl fibre (0.34 ± 0.15%) was significantly lower than a 40% NaCl fibre (0.82 ± 0.36%), and outer surface pore coverage for 20% NaCl (0.13 ± 0.06%) was less than 40% NaCl (0.23 ± 0.05%) although not significantly so. No data displayed in Table 5.3 indicates a reason why gas and liquid permeation of 20% and 40% fibres would be out of sequence with the general trend. From this is can be concluded that there are other intrinsic factors to the fibre that control permeability.

5.4.3 Comparisons, Limitations and Error Analysis

A property that was controlled poorly was fibre thickness. Manufacture of hollow fibres led to a non-central lumen, which yielded a non-uniform membrane thickness. Given the dependence of membrane thickness to calculate permeability and resistance, this leads to a high source of error which is not reflected in the error bars of the graphs in Section 5.3.3 as these assume an average thickness to correct for the manufacturing defect. In reality, permeation is most readily to occur through a path of least resistance, which is dependent on surface porosity, fibre tortuosity, and thickness. A sensitivity analysis investigating how recalculating permeation, resistance and Reynolds number data for the minimum and

maximum thickness of the fibres (Appendix F), showed the same patterns were shown in Section 5.3.3 for average fibre dimensions. From this it can be concluded that the membrane thickness was not a limiting factor in gas and liquid permeation in this study. The fibre cross sections in Figure 5.12 showed an increased prevalence of macrovoids in thicker regions of the fibre; and as discussed in Section 5.2.1 the rate limiting layer of a hollow fibre is its primary porous layer (assuming penetration of the non-porous skin). Therefore the existence of macropore regions in the structure of hollow fibres with greater thicknesses does not restrict fluid flow.

While it is apparent that the addition of NaCl allowed hollow fibres to gain pores which allow permeation to occur through their walls, it has not been confirmed as to what extent an open surface pore allows access to the porous centre of the fibre, which also connects with another open pore on its opposite surface. SEM imaging shows the existence of pores, and experiments have shown permeation, but this is not a proportional relationship. To some extent a degree of uncertainty during the phase inversion and NaCl leeching process is present that led to the non-proportional differences between permeation and NaCl content. In the case of 40% NaCl fibres the number of successful penetrations to the porous sublayer was fewer than that found in 20% NaCl fibres. Tortuosity must be considerably different between 20% and 40% fibres due to this.

While the primary objective was to provide porosity to the non-porous outer skin layers of the fibres, a secondary effect of additional internal porosity was also noted. This is most obviously shown in cross sections of flat sheet membranes, where pores of similar dimension to those found on the outer surfaces can be seen on the inner surfaces. These inner pores would provide additional pathways for fluid to permeate through, and reduce the tortuosity of the fibre. Despite this occurrence, the addition of more NaCl during fibre manufacture should also increase the number of these internal pores as seen on both the bottom flat sheet and inner hollow fibre surfaces. Tortuosity of a membrane cannot be determined from 2D cross-sectional imaging alone, so a value cannot be provided to compare between fibres with different NaCl content; however it can be concluded that any internal porosity gained from the additional NaCl is not significant enough to affect permeation if successful penetrations through the skin layer do not occur initially.

Given the multitude of different methods used to make hollow fibres, the variations in manufacturing for the chosen method of wet spinning, polymer dope composition, solvent/non-solvent chosen, temperature and so on, a comparison with literature that may be misleading if many differences are present between fibres in this work and others.

A batch of PLGA hollow fibre (50% DL-lactate/50% glycolide) was made from a dope containing 25% (w/w) of polymer in NMP, spun at 20 °C at a rate of 0.1 ml/min (Diban *et al.*, 2013). Spinneret needle and outer hole had diameters 0.6 mm and 1.2 mm respectively, with distilled water as the inner bore liquid at 0.30 ml/min and ethanol as the non-solvent in the coagulation bath. This led to manufacture of PLGA hollow fibres with 386 ± 34 µm ID and 495 ± 35 OD, much smaller than the fibres featured in this chapter. No porogen was added. SEM imagery showed external pores in the region of 5 – 10 µm, non-uniformly distributed in localised regions of the fibre, indicating pore formation primarily occurring due to manufacturing inconsistencies. The author noted that while a high weight percentage of PLGA is required to give the dope the required viscosity to be spun, as stated by Ellis and Chaudhuri (2007), this also contributed to the low degree of surface porosity. Liquid permeation experiments were conducted, washing in 70% ethanol solution before applying ultrapure water at several pressures in a dead-end configuration. Permeation flux through this fibre was measured at 3.7 $m^3m^{-2}h^{-1}bar^{-1}$ ± 32.4%. This indicated that the porosity gained using the method outlined in Diban *et al* (2013) yielded a greater permeation flux then fibres with 10% (1.21 $m^3m^{-2}h^{-1}bar^{-1}$ ± 33.7%) and 40% (2.00 $m^3m^{-2}h^{-1}bar^{-1}$ ± 60.1%) NaCl, however fibres with 20% (7.23 $m^3m^{-2}h^{-1}bar^{-1}$ ± 25.9%) and 60% (6.63 $m^3m^{-2}h^{-1}bar^{-1}$ ± 77.2%) NaCl showed greater permeation flux than (Diban *et al.*, 2013). Back-calculating the permeation flux from Diban *et al* (2013) to obtain values for permeability using the average pressure drop for each fibre type shows 20%, 40% and 60% fibres made in this chapter have greater values for liquid permeation then Diban *et al* (2013) (Appendix G).

Other works do feature manufacture of PLGA either with or without addition of additives to increase porosity. Some model the porosity using nitrogen gas permeation (Morgan *et al.*, 2007; Meneghello *et al.*, 2009; Ellis and Chaudhuri, 2011), but the method used was unsuitable for use in this chapter. Calculating mean pore diameter and effective porosity (analogous to resistance) using the method outlined in these works lead to wildly differing results when compared to SEM imagery of the fibre surfaces shown in Section 5.3.1 and calculations of resistance through Darcy's law on Table 5.4. Others have modelled the behaviour of fluid flow through PLGA hollow fibre bioreactors for a number of experimentally determined or assumed permeation values of the similar magnitude (2E-16 m^2) as those calculated in Section 5.3.3, (Shipley *et al.*, 2010).

Wen and Tresco (2006) performed liquid permeation on PLGA hollow fibres with added pore-forming agents, but characterised fibres in terms of their molecular weight cut off, and not their general permeability to water alone. No other works featuring the addition of different quantities of NaCl porogen to PLGA hollow fibres were found. Using PEG as a pore former for PLGA scaffolds as described by (Krok and Pamula, 2012) yielded non-porous scaffolds

when replicated for this work. Permeability of PEG/PLGA scaffolds was not measured, so no comparison could be drawn with the porous fibres described in this chapter.

5.5 CONCLUSONS

The results in this chapter indicate that addition of ~9 μm sized NaCl crystals as a porogen to PLGA/NMP solutions yields scaffolds with surface pores of ~ 5 μm that are permeable to both gas and liquid. This was the first time this method of producing NaCl had been implemented to provide porosity to the surfaces of PLGA hollow fibres manufactured via immersion precipitation. Control experiments with no NaCl were non porous. From the experiments outlined in this chapter it has been concluded:

i) Pores formed on the bottom surface of PLGA flat sheets and on both the inner and outer walls of PLGA hollow fibres as a direct result of NaCl addition.

ii) Pore densities on the bottom surface of PLGA flat sheets and the inner wall of hollow fibre membranes were statistically similar between 10% and 20% NaCl, as well as between 40% and 60% NaCl, indicating a critical NaCl concentration that is thermodynamically and/or kinetically favourable for pore formation.

iii) Pore sizes were generally different from one another on each surface at different NaCl contents, leading to a greater total area pore coverage on scaffolds with 40% NaCl compared to 60% NaCl.

iv) Fibres with 20% and 60% NaCl displayed significantly greater degrees of permeability and flux of water compared to 10% and 40% NaCl fibres.

v) The non-proportional relationship between NaCl content and fibre permeability indicates a limitation in permeation potential within the fibre structure that is not solely dependent on NaCl content.

All other factors being equal, increasing NaCl content should yield greater surface porosities on membranes once human error is eliminated in setting up the hollow fibre spinning rig. An automated spinning system would eliminate some of these issues. Liquid permeation data would be improved if several different pressures could be applied to the fibre. Replacing some components in the liquid permeation rig may improve the scope of data that can be acquired. Further care should also be taken when preparing hollow fibres for SEM imagery, as some were compressed when cut and mounted.

The next step in this work should be the application of permeable PLGA hollow fibres. Biodegradable and porous PLGA hollow fibres can allow for novel applications as cell delivery devices. The batches of porous fibres manufactured in this chapter may not be consistently porous with increasing NaCl, however that does not discount the fact that four batches of fibres with different permeabilities were manufactured.

Section 2.3.3 outlined the limitations with current methods of engineered cell delivery, and suggested that the encapsulation of cells within the lumen of hollow fibres could be a novel development to try and improve the initial rates of cell delivery into a wound site in the heart. The porous PLGA hollow fibres characterised in this chapter will be investigated for their ability to sustain a population of cells within the hollow fibre lumen. This is a vital first step to determine the feasibility of this novel approach to cell delivery. That work is outlined in Chapter 6.

[Page intentionally left blank]

CHAPTER SIX: CELL GROWTH WITHIN THE LUMEN OF A HOLLOW FIBRE

6.1 INTRODUCTION

The hollow fibre bioreactor is typically used to grow a population of cells on its external surface, facilitated by the perfusion of growth media permeating through the lumen of the hollow fibres to provide a low shear growth environment with minimal regions of stagnation that allow the removal of spent materials and cell by-products. It is their increased surface area to volume ratio, and continuous operation that make hollow fibre bioreactors a useful tool for cell growth.

If grown into high enough quantities, cell populations can be transported via a delivery device into a patient for use as a cell therapy to regenerate damaged tissue. Such treatments are on the forefront of medical science, with stem cell therapy available to assist in the treatment of (but not limited to) heart disease, diabetes and a multitude of neurodegenerative conditions. In all cases, a suitable method for cell implantation must be utilised which enables efficient cell transport to the target area, and effective interaction between the implanted cells and the host tissue.

Several different delivery methods are available, each with their advantages and disadvantages explained in detail in Section 2.3.3. In brief, delivery vectors are typically split into two categories – traditional and engineered. Traditional delivery involves direct cell administration to the target area either via a syringe, intravenously through the blood stream, or released through a catheter passed through the circulatory system; however each carry the risk of cell leakage from the site of injection, dilution of the cell dose, or complexity of administration respectively.

Engineered delivery involves cell attachment on or suspension within an implantable biodegradable scaffold, with aim to improve upon the poor rates of cell retention around treatment sites found in traditional delivery methods. Such methods include, cellular sheets, hydrogels, or micro-fibrous threads; however each have their drawbacks. In cellular sheets, attached cells are detected in significant quantities in other organs and have poor rates of migration into the damaged tissue itself. Injectable hydrogels offer much promise with many tailorable properties and improved long term retention, however can suffer from immediate expulsion from the injection site if gelation is not achieved quickly – limiting the initial dose. Cells loaded onto the surfaces of tubular threads allow cell migration throughout the scaffold,

however cells on its surface can be stripped off due to shear forces while being sewn into the wound site.

This work proposes that porous hollow fibres can offer an advantageous geometry that allows the encapsulation of cell therapies while offering improved initial retention rates of cells after delivery into the infarct site of a human heart. During the research and development of scaffolds for this application it is important to identify early how a device made in the lab can be made into a product, and also useful to recognise issues involved in product handling or feasibility of use. The first step in this process is to see if a population of cells can be successfully encapsulated within the lumen of a hollow fibre and sustained.

When treating patients suffering from an on-going heart condition the time to acquire the required concentration of cells must be short, the logistics of achieving that concentration must be relatively straightforward, and the implantation procedure to be as simple as possible for a surgeon. This can be illustrated by describing how certain scaffolds would fit into this process, and discussing their advantages and drawbacks.

If a flat sheet patch were desired then MSCs could be grown on the scaffold directly at close to 100% cell attachment efficiency, and then implanted into the patient; however this static environment would require manual media changes, provide a static growth environment which is disadvantageous for effective differentiation into cardiomyocytes if desired, and the low surface area to volume ratio of a flat sheet bioreactor system may require a larger scaffold to be implanted, increasing the complexity of the implantation procedure. Micro-fibrous threads contained in a bioreactor for external cell seeding would be similar to flat sheets as cells would grow in a static, non-continuous operation. Threads can be pre-attached to a needle and function as a surgical suture, offering a very simple method for implantation (Guyette *et al.*, 2013), but also lower cell implantation rates as cells are removed due to shearing as the suture is sown into the wound site. Cell growth within microbeads is achievable in both static and continuous flow regimes, however are typically inoculated into the wound site in a similar fashion to traditional delivery methods, leading to similar problems such as leakage and/or low cell dose concentrations. Hollow fibres allow for simple cell seeding, cultivation, differentiation and removal in a continuous flow environment, with cells seeded on the external surface to achieve these benefits. However this leads to the same issues found on all other externally seeded scaffolds where cells can detach as a result of handling and implantation.

In this chapter a potential solution is investigated. MG63 cells will be seeded within the lumen of the hollow fibre with media perfused through the extra capillary space permeating through the hollow fibre wall and feeding the cells on the inside. This would offer the same advantages

associated with a continuous flow bioreactor but would protect the cells during future transportation and implantation, increasing the number successfully reaching the wound site.

Cell number and viability, as well as D-glucose and L-lactate concentrations in the media were determined over a 6-day time course with two different ECS flow rates considered. PLGA hollow fibres with 60% NaCl by weight were used for in these experiments. Porosity and liquid permeation data for this specific hollow fibre is outlined in Section 5.3 Construction of the bioreactor and the method of cell seeding is explained in Section 3.3.6.

6.2 CELL GROWTH THEORY

6.2.1 Depletion of D-glucose

For a cell to function and reproduce new cell material (biomass), a variety of nutrients (substrates) must be consumed. These substrates are provided by the cell growth media, which contains sources of carbon, nitrogen, minerals, vitamins and energy. In the growth media used in this work, D-glucose is the main source of carbon and energy, with amino acids (primarily L-alanyl-glutamine) providing a source of nitrogen (Invitrogen, 2015).

MG63 cells are fuelled by aerobic respiration, a process which consumes substrates and oxygen to generate adenosine triphosphate (ATP), a store of chemical energy used to fuel metabolic pathways within the cell. Glucose is converted onto pyruvate with the assistance of an oxidised nicotinamide adenine dinucleotide (NADH) enzyme found within the cell and already available ATP in a process called Glycolysis. Pyruvate is oxidised using pyruvate dehydrogenase enzymes into acetyl coenzyme A (acetyl-CoA) in the presence of oxygen. Acetyl-CoA then enters the citric acid cycle (also known as the TCA or Krebs cycle), a series of enzyme driven reactions which yields a net increase of ATP as well as carbon dioxide and water as waste by-products (Bailey, 2016). In order to assist cell respiration, sodium pyruvate was supplemented into the cell media, as well as additional amino acids. This series of equations can be simplified to Equation 6.1 (Doran, 1995):

$$\boldsymbol{C_6H_{12}O_{6(aq)} + 6O_{2(g)} \rightarrow 6CO_{2(g)} + 6H_2O_{(l)} + heat}$$

Equation 6.1 – Simple aerobic respiration equation.

For each mole of oxygen consumed, the heat of reaction is approximately -460 kJ/mol, therefore for each mole of glucose consumed -2,760 kJ/mol of energy is produced (Cooney *et al.*, 1969). While this equation expresses how cells aerobically respire, it does not take into consideration additional cell biomass produced. Methods for establishing an equivalent stoichiometric equation describing this 'reaction' can be obtained by assuming the biomass as a physical quantity of C, H, O and N atoms and performing simultaneous 'goal seeking'

equations. As an adequate atomic representation of MG63 cells could not be found this method was not utilised to model ideal theoretical cell growth. This method is fully explained by Roels (1980).

6.2.2 Production of L-lactic acid

If dissolved oxygen in media is consumed at a greater rate than it can be replaced from the atmosphere in an incubator, then anaerobic respiration will take place. In limited oxygen environments glycolysis cannot take place aerobically because NADH cannot be oxidised (RSC, 2011). Under such conditions NADH is oxidised by pyruvate, forming lactic acid (which disassociates to lactate) as a by-product, which accumulates. A simplified expression for the conversion of glucose to lactic acid is shown in Equation 6.2.

$$\boldsymbol{C_6H_{12}O_{6_{(aq)}} \rightarrow 2\ C_3H_6O_{3_{(aq)}}}$$

Equation 6.2 – Simplified equation for anaerobic respiration.

Upon reintroduction of aerobic conditions lactate can then be oxidised back into pyruvate and glycolysis can continue as before; however if aerobic conditions do not resume the accumulation of lactic acid will lead to a decrease in pH, and the high concentrations of hydrogen ions will begin to negatively affect metabolic reactions and cell enzyme behaviour (Doran, 1995). Production of CO_2 during aerobic respiration and its concentration within the media also contributes to lower pH.

Lactic acid is one of the degradation products of PLGA, and its concentration from this source must be properly attributed in order to obtain accurate concentrations of lactic acid originating from cell metabolism. In this study this was achieved by performing suitable control experiments with no cells inoculated to determine the degree of PLGA degradation in the bioreactor.

6.2.3 Oxygen Dependency

Oxygen (O_2) is required as part of aerobic respiration for cells to function and proliferate. A constant atmospheric environment consisting of approximately 75% N_2, 20% O_2 and 5% CO_2 at 37°C is provided to the cell bioreactors by an incubator. As discussed in Section 2.2.3, the dissolved oxygen content of blood provided to human heart tissue is 20.4% (AnaesthesiaUK, 2005), making these incubator conditions appropriate for this experiment. The concentration of oxygen dissolved in the media is dependent on pressure, temperature and salinity, and can be calculated using Henry's law. Henry's law states that the amount of dissolved gas in liquid is proportional to its partial pressure. Henry's constant (k_H) for O_2 at standard temperature and pressure (Θ = 298 K, 1 atm) is 0.0013 mol/atm.L (Sander, 1999). The partial pressure of O_2

in the incubator is 0.20 atm and its molar mass is 32 g/mol. Therefore the amount of O_2 in water at these conditions can be calculated in Equation 6.3:

$$C_{O_2} = k_H . p_{O_2}$$

$$C_{O_2} = 0.0013 \left[\frac{mol}{atm.L}\right] \times 0.20[atm] \times 32 \left[\frac{g}{mol}\right] \times 1000 \left[\frac{mg}{g}\right]$$

$$\boldsymbol{C_{O_2} = 8.32\ mg/L}$$

Equation 6.3 – Calculation of dissolved O_2 in cell media using Henry's Law.

Salinity of the solution leads to a reduced dissolved oxygen concentration (Johnson, 2010). The cell media used for the experiments in this thesis is formulated with 6,400 mg/L NaCl as well as smaller concentrations of other salts, therefore Henry's constant must be modified to account for this. Salinity effects Henry's constant as shown in Equation 6.4:

$$\log\left(\frac{C_{O_2}\ NaCl\ solution}{C_{O_2}\ water}\right) = k_{se} . C_{NaCl}$$

Equation 6.4 – Henry's Law with consideration for salinity.

The Sechenov constant (k_{se}), is derived empirically and relates how Henry's constant changes with NaCl concentration. Jamnongwong *et al.* (2010) studied oxygen uptake in solutions of water at 25°C supplemented with NaCl at 6000 mg/L, and from that data a Sechenov constant of -2.278E-05 (-) can be determined at these conditions. Applying this value to Equation 6.4, an approximation for Henry's constant of the media with similar salinity at standard temperature and pressure can be determined in Equation 6.5:

$$\log\left(\frac{C_{O_2} media\ \left[\frac{mg}{L}\right]}{8.32\left[\frac{mg}{L}\right]}\right) = -2.278 \times 10^{-5}\ [-] \times 6000\ \left[\frac{mg}{L}\right]$$

$$\log\left(C_{O_2}\ media\right) - \log(8.32) = -0.1367$$

$$\log\left(C_{O_2}\ media\right) = 0.9201 - 0.1367$$

$$\boldsymbol{C_{O_2}\ media} = 10^{0.7834} = \boldsymbol{6.07\ mg/L}$$

Equation 6.5 – Calculation of dissolved O_2 in cell media using Henry's Law with consideration for salinity.

Oxygen is more readily soluble in liquids of a higher temperature (Sander, 1999). A measure of dissolved oxygen content at standard temperature and pressure can be modified to account for the elevated temperature in the incubator (310 K) as long as a value for the ratio of the heat

of solution of oxygen (ΔH_{sol}) to the gas constant (R_G) is known. This value is 1500 K (Sander, 1999). This is shown in Equation 6.6:

$$C_{O_2} = {C_{O_2}}^{\Theta} \times \exp\left[-\frac{\Delta H_{sol}}{R_G}\left(\frac{1}{T} - \frac{1}{T^{\Theta}}\right)\right]$$

$$C_{O_2}^{310K} = C_{O_2}^{295K} \times \exp\left[-1500\ [K]\left(\frac{1}{310\ [K]} - \frac{1}{298\ [K]}\right)\right]$$

$$\boldsymbol{C_{O_2}^{310K} = 6.07\ \left[\frac{mg}{L}\right] e^{0.1958} = 7.37\ mg/L}$$

Equation 6.6 – Calculation of dissolved O_2 in cell media using Henry's Law with consideration for salinity and temperature.

From these calculations the theoretical concentration of 7.37 mg/L O_2 is available in the media during bioreactor operations in an incubator. As the media is continuously replenished with oxygen from the incubator, it is assumed that dissolved oxygen is not rate limiting to cell growth. Dissolved oxygen concentration of the recirculating media reservoir will be measured after each time point, and used to monitor the overall health of the experiment, ensuring that no infections occur. Media infection would cause the dissolved oxygen within the bulk media to drop. In-line dissolved oxygen readings within the ECS and the lumen are not available.

6.2.4 Permeation of Media into Hollow Fibre Lumen

For cell proliferation experiments within hollow fibres it is assumed that the permeation of media from the ECS into the hollow fibre lumen occurs at the same flux as that calculated for permeation of water from within the lumen out to the ECS as investigated in Chapter 5. As pressure readings could not be taken during the cell proliferation experiments it was assumed that the pressure differential that drove permeation outwards was the same as that which would be required to cause permeation inwards. It was also assumed that the differing external pore coverage on the inner (0.68%) and outer (0.17%) surfaces of the hollow fibre were independent of this pressure differential; as the flow rate of media through a surface with a lower pore coverage would be same as that through a surface with a higher pore coverage at the same pressure difference. As shown in Table 5.5, hollow fibres with 60% salt content allowed a liquid flux (J) of 6.63 $m^3m^{-2}h^{-1}bar^{-1}$ (± 77.2%), or 0.0097 $m^3m^{-2}h^{-1}$ (±65.3%), through a surface area (A) of 2.91 cm^2 at an internal flow rate of 1 mL/min. The rate of permeation under these conditions can be calculated, as shown in Equation 6.7:

$$Q_{perm} = J \times A = 0.0097\left[\frac{m^3}{m^2 h}\right] \times 2.91\ [cm^2] = 67.74\left[\frac{mL}{day}\right]$$

Equation 6.7 – Rate of permeation through fibres at ECS flow rate of 1 mL/min.

This is a permeation fraction of 4.7% ±3.1%. By comparing the D-glucose requirements of cells growing on flat sheet PLGA, an equivalent flow of media through the ECS of a hollow fibre bioreactor can be calculated to provide a similar quantity of D-glucose to cells seeded within the lumen of the hollow fibre.

From cell growth experiments on flat sheet PLGA the average mass consumption (G) of D-glucose between Day3 and Day 6 was 0.70 mg/day. As the cell growth media had an initial D-glucose concentration (C) of 4.5 mg/mL, the volume of media required to provide the cells with this quantity of D-glucose can be calculated, as shown in Equation 6.8.

$$V_{media} = \frac{G_{glucose}}{C_{glucose}} = \frac{0.70 \left[\frac{mg}{day}\right]}{4.5 \left[\frac{mg}{mL}\right]} = 0.15 \left[\frac{mL}{day}\right] = 0.11 \left[\frac{\mu L}{min}\right]$$

Equation 6.8 – Flow rate of media permeation required for 0.70 mg/day D-glucose consumption.

As the required media permeation rate for sufficient D-glucose supply is now known, and the expected permeation fraction through the hollow fibre has been calculated, the ECS flow rate required to facilitate the required permeation can now be calculated, as shown in Equation 6.9:

$$Q_{ECS} = Q_{permeate} \times \frac{100\%}{4.7\%} = 0.15 \left[\frac{mL}{day}\right] \times \frac{100\%}{4.7\%} = 3.29 \left[\frac{mL}{day}\right] = 2.29 \left[\frac{\mu L}{min}\right]$$

Equation 6.9 – Calculation of ECS flow rate required for desired permeation.

For permeation of 0.11 µL/min, a minimum ECS flow rate of 2.29 µL/min is required to allow sufficient permeation of D-glucose into the lumen to sustain the cells. For the experiments in this Chapter ECS flow rates of 10 µL/min and 50 µL/min were set to provide permeation of 0.47 µL/min and 2.35 µL/min respectively. These values are larger than the calculated minimum ECS flow of 2.29 µL/min for permeation of 0.11 µL/min. This is to ensure that D-glucose concentration does not become a rate limiting factor for cell growth.

6.2.5 Cell Rolling/Shear

It is assumed that the vast majority of cells seeded within the lumen of the hollow fibre will successfully settle onto the internal surface. The only exception would be from cells lost during the seeding process or those that leak out of the end of the bioreactor during the initial stages of operation when media permeation is initiated. A cell's connection to a surface is governed by many factors including surface roughness, cell surface ligand concentration and surface charge. For this experiment it was assumed that the internal flow rate of permeating media would be insufficient to detach cells.

6.2.6 Bioreactor Configuration

The construction of the bioreactor with associated ancillary equipment and support structure is outlined in detail in Section 3.3.6. After cell seeding in the hollow fibre lumen the lumen inlet of the bioreactor is closed and a continuous flow rate of media at either 10 µL/min or 50 µL/min is perfused through the ECS for the duration of cell growth. Both the ECS and lumen outlets were recycled back to the media reservoir. Four bioreactors were operated in parallel, and each were removed and analysed on days 1, 3 and 6, with one bioreactor as a spare. A schematic of this configuration is shown in Figure 6.1.

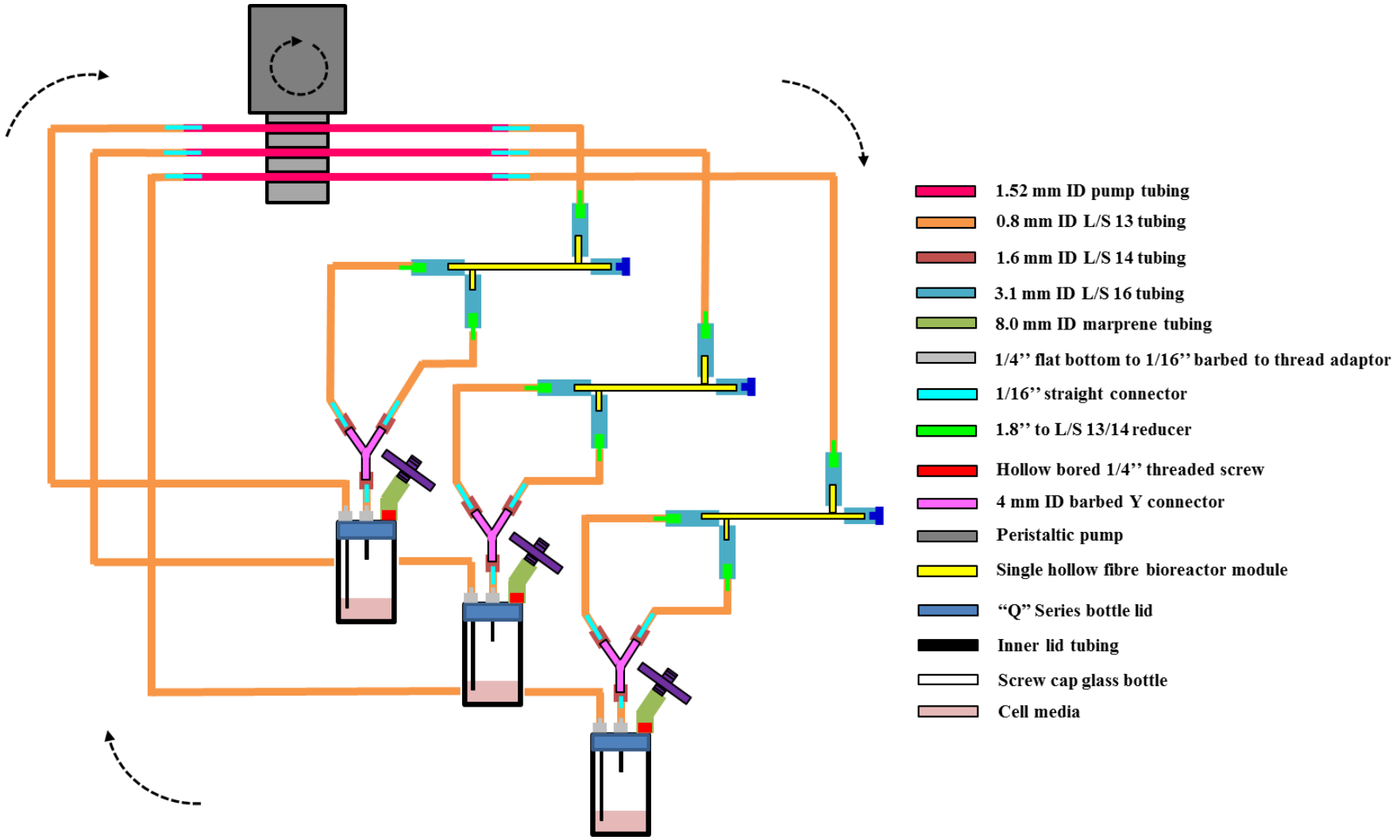

Figure 6.1 – Schematic of the hollow fibre bioreactor system for internal cell growth.

6.3 RESULTS

Control experiments for MG63 growth were performed on tissue culture plastic and on flat sheet porous PLGA in order to determine if the hollow fibre bioreactor configuration offered improved cell numbers over traditional growth methodologies. Individual wells or bioreactors were used to represent 1, 3 or 6 days growth. Viable cell count was characterised by trypsinisation of the scaffold and trypan blue staining, and total cell count quantified by performing picogreen assay. Concentration of D-glucose and L-lactic acid were obtained by performing their respective assays, taking into account a media change on Day 3 for static experiments. Dissolved oxygen and pH measurements were taken on the media reservoirs of hollow fibre bioreactor experiments on days 0, 1, 3 and 6 and used to determine if the media was infected and abort the experiment. These measurements could not be conducted on tissue culture plastic or PLGA flat sheet samples because of insufficient media volumes. The media within the lumen itself could not be analysed in-situ because in-line dissolved oxygen sensors were unavailable. Full details of these analytical methods are described in Section 3.4.1.

6.3.1 Cell Growth on Tissue Culture Plastic

Flat-bottom cell culture flasks with area 75 cm^2 were seeded at a density of 34,407 cells/cm^2 on Day 0, and mixed with 20 ml media. This provided a specific volume of 3.75 cm^2/mL cell media. Three individual flasks were seeded per experiment and each were counted for cells, checked for viability, and analysed for D-glucose and L-lactic acid concentrations on Days 1, 3 and 6. The experiment was replicated four times, with counts and assays performed in triplicate for each day of the time course. A control flask with no cells seeded was also run alongside each experiment, which was replicated five times.

Manual cell counting was performed after trypsinisation of the flask surface. Picogreen assay was performed at each step of the time course, however samples were not diluted enough which led to DNA fluorescence over the upper limit recommended by the manufacturer for reliable results. Cell media was not changed for the duration of the experiment. Initial D-glucose concentration of the media was measured as 4.50 ± 0.26 mg/mL, and initial L-lactic acid concentration was assumed to be zero, as it was not listed in the media formulation documentation (Invitrogen, 2015).

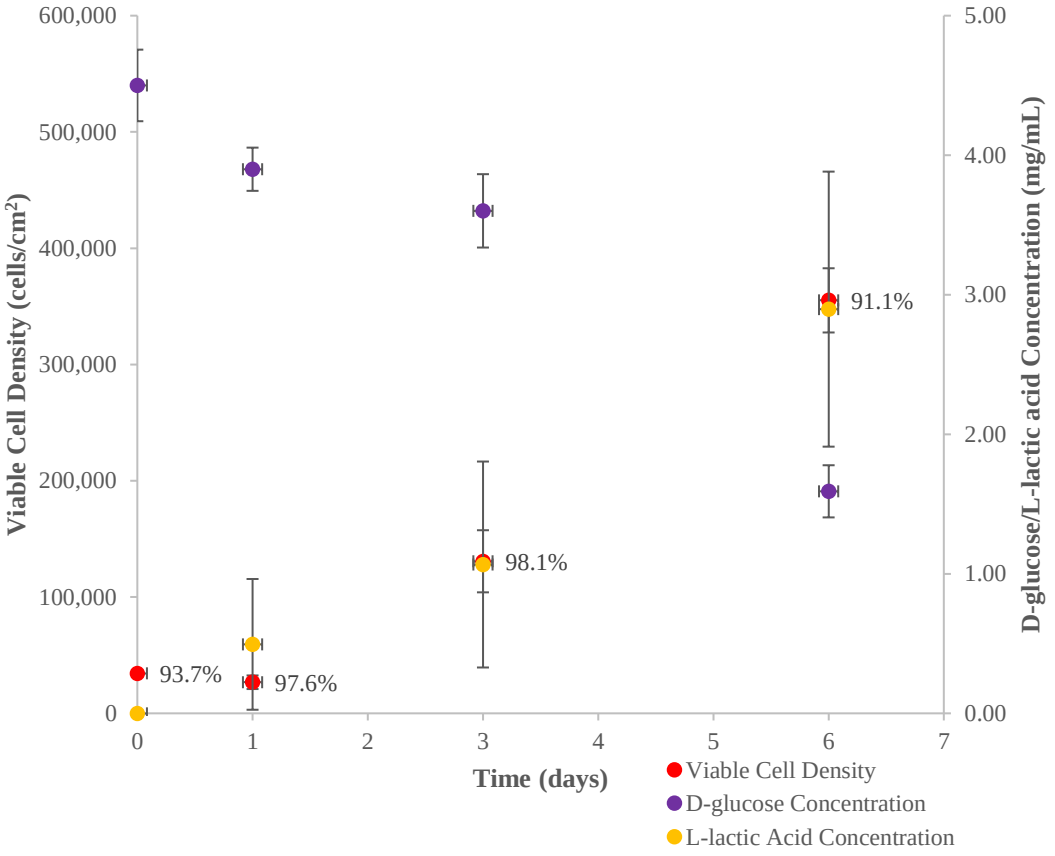

Figure 6.2 – Cell growth on tissue culture plastic. Changes in viable cell density (including viability), D-glucose and L-lactic Acid concentrations over time. X error = ± 1 hour, Y error = SD (N=4, n=3).

Table 6.1 – Average values of viable cell density, cell viability, D-glucose and L-lactic acid concentrations during cell growth on tissue culture plastic.

Day	Viable Cell Density (cells/cm²)		Cell Viability (%)		D-glucose Concentration (mg/mL)		L-lactic Acid Concentration (mg/mL)	
	Av.	*SD*	Av.	*SD*	Av.	*SD*	Av.	*SD*
0	34,407	*8,046*	93.7%	*2.7%*	4.50	*0.26*	0.00	*0.00*
1	26,746	*5,851*	97.6%	*1.5%*	3.90	*0.15*	0.48	*0.47*
3	130,773	*26,709*	98.1%	*1.1%*	3.60	*0.26*	1.05	*0.74*
6	355,164	*27,605*	91.1%	*4.9%*	1.59	*0.19*	2.84	*0.99*

The data displayed in Figure 6.2 and Table 6.1 shows an increase in viable cell density over the time course. A slight drop in cell number occurs between Day 0 and Day 1 but this was within one standard deviation of the cell count on Day 0. After Day 1 cell number shows significant increases ($P<0.05$) by Day 3 doubling every 0.873 days, and by Day 6 doubling every 2.081 days.

After seeding, cell viability remained consistent between Day 1 and Day 3, but dropped significantly ($P<0.05$) by Day 6. Reduction in viability and growth rate after Day 3 was likely due to cell over-confluence on the plastic surface, the depletion of D-glucose and increase of L-lactic acid present in the flask. This is confirmed by the decrease in media pH from 7.8 ± 0.2 to 6.9 ± 0.1. Dissolved oxygen concentration remained constant at 7.9 ±0.1 mg/L over the time course. D-glucose was in high enough concentration until Day 3 to allow for a higher growth rate, but as it was consumed it became growth limiting.

6.3.2 Cell Growth on PLGA Flat Sheet

PLGA flat sheet scaffolds were attached to a custom 24 well plate as described in Section 3.3.4. Scaffolds were seeded with 100,000 ± 16,600 viable cells on Day 0 within a media inoculant of 21.5 µL and wells filled with 1 mL media. Available attachment area within each well was 1.88 cm^2, providing a cell surface density of 53,191 ± 8,841 cells/cm^2, and a cell media specific volume of 1.88 cm^2/mL. Nine wells were seeded per scaffold, allowing for attached cells to be counted on Days 1, 3 and 6 in triplicate. An additional three wells that were not inoculated with cells acted as a control to detect any cell growth due to infection for each day of the time course. This experiment was replicated four times.

On the desired day the 1 mL media was removed from the well and retained to detect for reductions in D-glucose and increases in L-lactic acid concentrations. L-lactic acid assays were performed on wells without cells to attribute L-lactic acid resulting from breakdown of the PLGA scaffold. Scaffold surfaces were trypsinised and the cells were manually counted and checked for their viability. Wells which were used for cell growth to Day 6 had their media changed on Day 3, with calculated concentrations of D-glucose and L-lactic acid on Day 6 adjusted to reflect this. Picogreen assay for DNA quantification was not undertaken over the time course as it was not possible to remove a sample of the scaffold from the custom well plate for the freezing process.

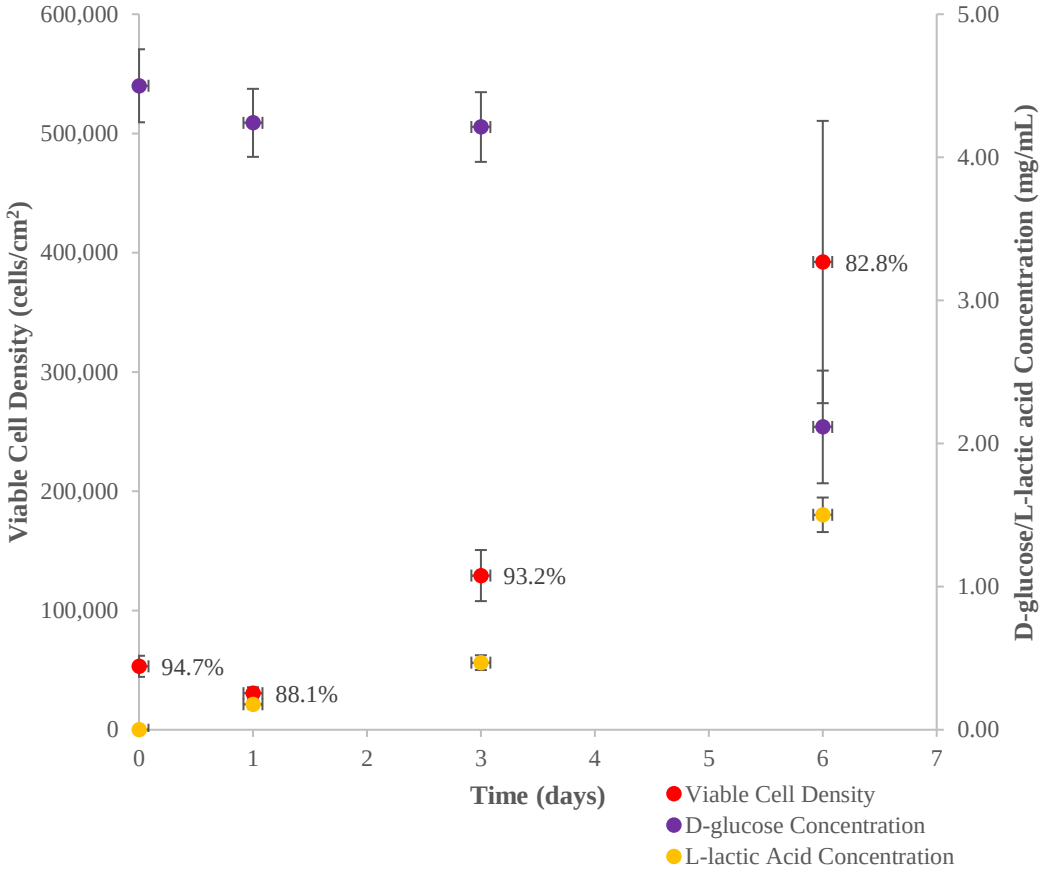

Figure 6.3 – Cell growth on PLGA flat sheets. Changes in viable cell density (including viability), D-glucose and L-lactic Acid concentrations over time. X error = ± 1 hour, Y error = SD (N=4, n=3).

Table 6.2 – Average values of viable cell density, cell viability, D-glucose and L-lactic acid concentrations during cell growth on PLGA flat sheets.

Day	Viable Cell Density (cells/cm²)		Cell Viability (%)		D-glucose Concentration (mg/mL)		L-lactic Acid Concentration (mg/mL)	
	Av.	*SD*	Av.	*SD*	Av.	*SD*	Av.	*SD*
0	53,191	*8,841*	94.7%	*1.9%*	4.50	*0.26*	0.00	*0.00*
1	30,634	*4,997*	88.1%	*5.3%*	4.24	*0.24*	0.18	*0.03*
3	129,285	*21,419*	93.2%	*4.3%*	4.21	*0.24*	0.47	*0.05*
6	392,213	*118,361*	82.8%	*5.0%*	2.12	*0.39*	1.50	*0.12*

The data shown in Figure 6.3 and Table 6.2 show an increase in viable cell density over the six-day time course experiment. The number of cells significantly increase between Day 1, 3 and 6 ($p<0.05$), however only 58% of cells of the original inoculant remained after one day, far outside the standard deviation range of Day 0. This consistent trend with a small standard deviation could be attributed to insufficient mixing of inoculant solution prior to seeding, or due to insufficient washing of the membrane surface after sterilisation with 70% ethanol, leading to death of some cells.

Cell viability significantly changed between each day ($P<0.05$): decreasing between Day 0 and Day 1, increasing between Day 1 and Day 3, before decreasing again between Day 3 and Day 6. This corresponds to the concentrations of D-glucose and L-lactic acid within each well. D-glucose concentration remains consistent from Day 1 through to Day 3 as viable cell density quadruples, doubling every 0.963 days. A significant drop ($P>0.05$) in D-glucose concentration between Day 3 and Day 6 corresponds to a reduction in the rate of cell growth, now doubling every 1.874 days, with growth rate decelerating due to the limiting concentration of D-glucose despite a media change on Day 3. L-lactic acid concentration consistently increases over the 6 days as viable cell density increases. During this experiment an average of 0.090 mg/mL L-lactic acid per day is produced from PLGA breakdown.

6.3.3 Cell Growth within Hollow Fibre Lumen

The lumen of the hollow fibre was seeded with cells, mounted into a tubular glass housing, and connected to a circuit of tubing with a continuous flow of media passing through. The full seeding and assembly process is described in Section 3.3.6. The usable length of hollow fibre was 10 cm and had an internal diameter of 0.925 mm, with a corresponding internal surface area of 2.91 cm^2 and lumen volume of 67.2 µL. The internal volume of the glass bioreactor was 0.69 mL. 100,000 cells were seeded into the hollow fibre lumen in an inoculant of 67.2 µL, providing an internal surface cell density of 34,407 cells/cm^2. Three bioreactors were seeded per experiment, each representing either 1, 3 or 6 days of growth. Experiments were replicated four times (N=4, n=1). 20 mL of media was circulated through each bioreactor through the extra capillary space between the outer hollow fibre surface and the glass housing at either 10 µL/min or 50 µL/min.

Control Experiments

Initial control experiments were undertaken to account for any differences that arose between the flat sheet and hollow fibre configurations; the first of which featured media perfusion through an empty bioreactor. This would provide a measure for any cells present in the system from insufficient sterilisation or accidental infection over the six day time course. One time course experiment was done for each of the two flow rates chosen (N=1, n=1).

Table 6.3 – Media components with no cells or fibre, 10 µL/min and 50 µL/min averaged.

Day	Picogreen Cell Concentration in Media (cells/mL)		Equivalent cell density on fibre inner surface (cells/cm^2)		D-glucose Concentration in Media (mg/mL)		L-lactic Acid Concentration in Media (mg/mL)	
	Av.	*SD*	Av.	*SD*	Av.	*SD*	Av.	*SD*
0	0	*21.4%*	0	*21.4%*	4.50	*0.26*	0.000	*0.000*
1	69	*20.0%*	16	*20.0%*	4.56	*0.30*	0.064	*0.011*
3	176	*32.5%*	42	*32.5%*	4.75	*0.33*	0.072	*0.000*
6	181	*23.6%*	43	*23.6%*	4.38	*0.30*	0.092	*0.022*

Picogreen assay on the 20 mL cell media showed a very small DNA absorbance reading, indicating some form of DNA is present in the system throughout the time course, although none could be seen during manual counting. Using a ratio of the bioreactor volume and the total volume of media in the system, an equivalent cell density that could potentially be attached to a hollow fibre and affect results of seeded experiments was shown to be no more than 43 cells/cm^2. This population did not affect the D-glucose concentration in the system, as the average reading of each day is within the standard deviation of the Day 0 D-glucose reading.

A second control experiment was performed with unseeded hollow fibres to determine the quantity of L-lactic acid over six days due to break down of PLGA. One time course experiment was done for each of the two flow rates chosen (N=1, n=1), and an average is shown in Table 6.4.

Table 6.4 – Media components with no cells, 10 µL/min and 50 µL/min averaged.

Day	Picogreen Cell Concentration in Media (cells/mL)		Equivalent cell density on fibre inner surface (cells/cm^2)		D-glucose Concentration in Media (mg/mL)		L-lactic Acid Concentration in Media (mg/mL)	
	Av.	*Error*	Av.	*Error*	Av.	*Error*	Av.	*Error*
0	0	*0*	0	*0*	4.50	*0.26*	0.000	*0.000*
1	218	*188*	52	*848*	4.20	*0.14*	0.116	*0.031*
3	180	*117*	43	*524*	4.21	*0.23*	0.132	*0.041*
6	292	*290*	69	*928*	4.25	*0.05*	0.064	*0.003*

This experiment showed a slightly larger cell concentration in the media than the previous control experiment, indicating a small population of cells remained within the hollow fibre after overnight ethanol sterilisation. D-glucose concentration decreased between Day 0 and Day 1, and was maintained through to Day 6. L-lactic acid concentration is larger than, or equal to, that found in the media only control, indicating that some degree of breakdown of PLGA occurs in this configuration. This is equivalent to an average of 0.056 mg/mL and

0.080 mg/mL L-lactic acid per day at 10 µL/min and 50 µL/min respectively, less than the 0.090 mg/mL per day on flat sheet PLGA. This remains consistent after normalising for available external scaffold surface area.

Seeded Bioreactors

The data shown in Table 6.3 and Table 6.4 was used to normalise the seeded hollow fibre experiments so that rates of cell attachment, D-glucose depletion and L-lactic acid formation could be exclusively attributed to cell growth. All three bioreactors in the time course were pumped with 20 mL media at either 10 or 50 µL/min. Each time course for both flow rates were replicated four to eight times, half were trypsinised and counted manually to characterise viable cell count, and half underwent picogreen assay to quantify total cell count. The four bioreactors that were trypsinised were also tested for D-glucose and L-lactic acid concentrations.

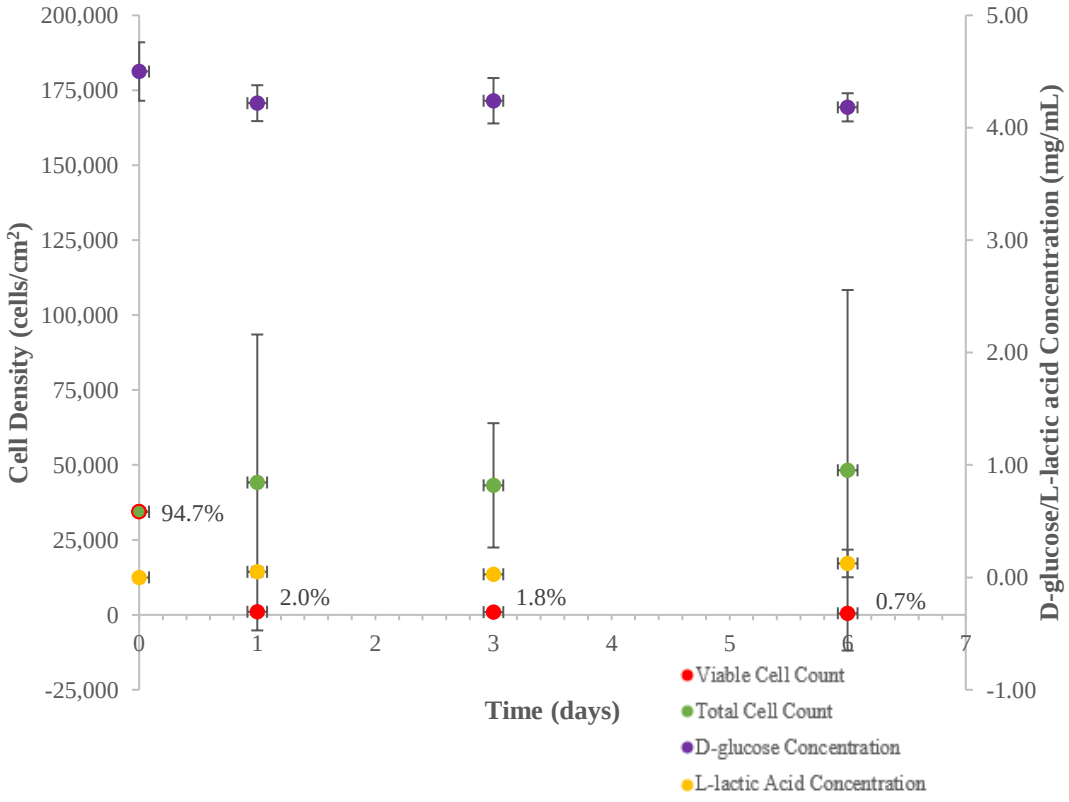

Figure 6.4 - Cell growth within PLGA hollow fibres at 10 µl/min. Changes in cell density (including viability), from manual counting and picogreen assay, D-glucose and L-lactic Acid concentrations over time. X error = ± 1 hour, Y error = SD (*N*=4, *n*=1).

Table 6.5 – Average values of cell density, cell viability, D-glucose and L-lactic acid concentrations during cell growth within PLGA hollow fibres at 10 ml/min external flow rate.

Day	Cell Density (cells/cm^2)				Cell Viability (%)		D-glucose Concentration (mg/mL)		L-lactic Acid Concentration (mg/mL)	
	Viable (Manual Count)		Total (Picogreen)							
	Av.	*SD*	Av.	*SD*	Av.	*SD*	Av.	*SD*	Av.	*SD*
0	34,407	*0*	34,364	*0*	94.7%	*0.0%*	4.50	*0.26*	0.000	*0.000*
1	869	*581*	44,171	*49,358*	2.0%	*1.3%*	4.22	*0.16*	0.050	*0.042*
3	782	*687*	43,209	*20,737*	1.8%	*1.0%*	4.24	*0.20*	0.028	*0.027*
6	320	*270*	48,235	*60,141*	0.7%	*1.5%*	4.18	*0.13*	0.124	*0.123*

Time course data for bioreactors fed with 10 µL/min media is shown in Figure 6.4 and Table 6.5. After seeding on Day 0 the average viable cell density by Day 1 dropped to 2.0% of that seeded, dropping further to 1.8% by Day 3 and 0.7% by Day 6. The total number of cells (viable and non-viable) remained constant between Day 1 and Day 6, but the percentage of viable cells decreased from 94.7% on Day 0 to 2.0% on Day 1. D-glucose concentration decreases between Day 0 and Day 1, indicating that some degree of cell respiration occurred within the initial 24 hours, however the concentration of D-glucose does not change after Day 1 due to the sudden reduction in cell viability. L-lactic acid concentration increases from zero on Day 0 to 0.05 mg/mL on Day 1, indicating that anaerobic respiration occurred quickly after seeding. This indicates that insufficient dissolved oxygen was reaching the cells in the lumen at an ECS flow rate of 10 µL/min.

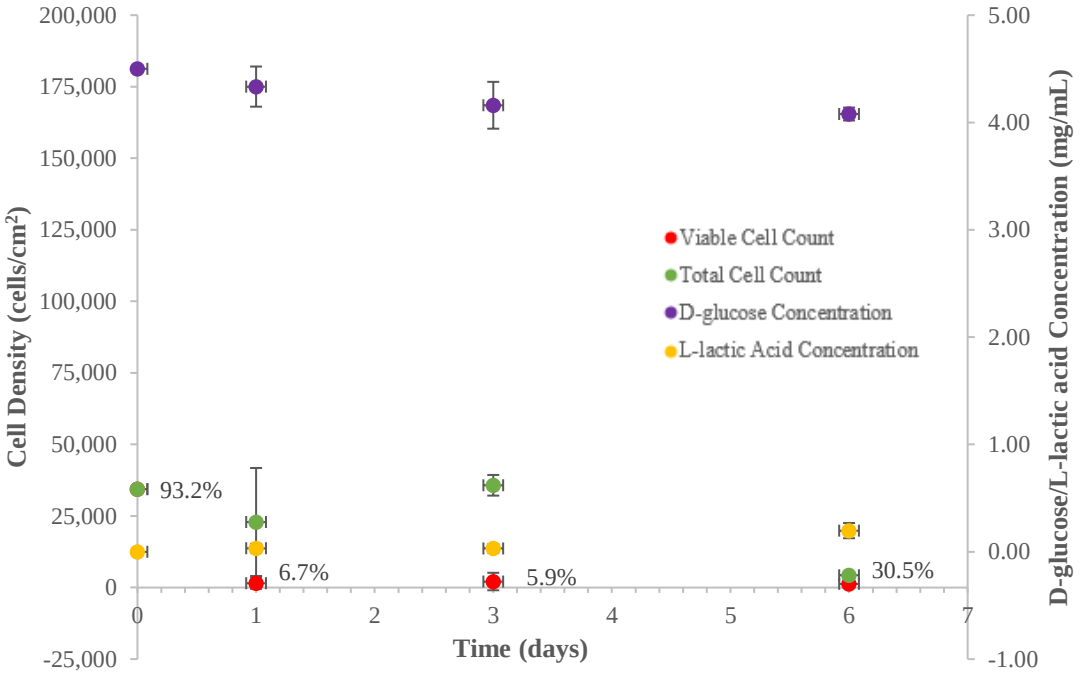

Figure 6.5 – Cell growth within PLGA hollow fibres at 50 µl/min. Changes in cell density (including viability), from manual counting and picogreen assay, D-glucose and L-lactic Acid concentrations over time. X error = ± 1 hour, Y error = SD (*N*=2, *n*=1).

Table 6.6 – Average values of cell density, cell viability, D-glucose and L-lactic acid concentrations during cell growth within PLGA hollow fibres at 50 µl/min external flow rate.

Day	Cell Density (cells/cm²)				Cell Viability (%)		D-glucose Concentration (mg/mL)		L-lactic Acid Concentration (mg/mL)	
	Viable (Manual Count)		Total (Picogreen)							
	Av.	*SD*	Av.	*SD*	Av.	*SD*	Av.	*SD*	Av.	*SD*
0	34,407	*0*	34,364	*0*	93.2%	*0.0%*	4.50	*0.26*	0.000	*0.000*
1	1,529	*1,953*	22,906	*18,863*	6.7%	*8.5%*	4.33	*0.19*	0.033	*0.041*
3	2,098	*3,051*	35,733	*3,609*	5.9%	*8.5%*	4.16	*0.22*	0.031	*0.040*
6	1,307	*265*	4,275	*517*	30.5%	*6.2%*	4.08	*0.06*	0.197	*0.071*

Time course data for bioreactors fed with 50 µL/min media is shown in Figure 6.5 and Table 6.6. Once again, the number of viable cells rapidly decreases between Day 0 and Day 1, however the number of viable cells at Day 1 is 6.7% of the seeded quantity, triple that which survived at 10 µL/min. Total number of cells remains constant (accounting for error) between Day 0 and Day 3, with a drop between Day 3 and Day 6. D-glucose consumption occurs at a faster rate between Day 0 and Day 1, as does L-lactic acid production indicating again that the initial seeded quantity of cells do respire aerobically and/or anaerobically over the initial

24 hours. The remaining viable cells up to Day 6 explain the continuing decline in D-glucose consumption, however the increase in L-lactic acid concentration at Day 6 is likely evidence of a small infection in those bioreactors. As a different bioreactor is used for each part of the time course, this would not affect the results of previous days.

6.4 DISCUSSION

6.4.1 Proliferation on Flat Surfaces

Cell seeding on static flat sheet PLGA scaffolds has shown to produce comparable viable cell densities over six days to those seeded on tissue culture plastic, as can be seen in the data shown in Figure 6.2 and Figure 6.3. Despite the larger initial seeding density used on PLGA scaffold (53,191 ± 8,841 cells/cm^2) compared to tissue culture plastic (34,407 ± 8,046 cells/cm^2), the Day 1 viable density of cells was 30,634 ± 4,997 cells/cm^2 and 26,746 ± 5,851 cells/cm^2 respectively. Aside from the initial seeding density, comparing both surfaces on each day show no significant differences between the two, implying that growth on PLGA flat sheets provides comparable cell densities to those grown on tissue culture plastic over six days. In other studies where MG63 cells were seeded on PLGA with tissue culture plastic as a control, cells on PLGA had a shorter cell doubling time (Pamula *et al.*, 2009). This has also been noted in studies of cell growth on polysulphone (Stankova *et al.*, 2014), however tissue culture growth has been shown to be better than on poly(esterurethane) (Podporska-Carroll *et al.*, 2014).

Table 6.1 and Table 6.2 indicate that both PLGA and tissue culture plastic showed shorter cell doubling times between Days 1 and 3 (0.963 and 0.873 respectively) than between Days 3 and 6 (1.874 and 1.388 respectively). This can be attributed to the increasing confluence of the cell monolayer on the surface, and likely formation of additional cell layers hindering transport of oxygen and media nutrients to the original monolayer, leading to increasing apoptotic signalling from any dying cells underneath.

This is confirmed by the depletion of D-glucose and production of L-lactic acid in both systems, however these concentrations change at a faster rate in the tissue culture flask compared to the PLGA flat sheet. Both surfaces had the same initial concentration of D-glucose in media available, but both had different volumes of media in each system. A sample of PLGA flat sheet within the custom well plate had a seeding area of 1.88 cm^2 and 1 mL media available, providing a specific area of 1.88 cm^2/mL; whereas the tissue culture plastic within a T75 flask had a seeding area of 75 cm^2 and was provided with 20 mL media, for a specific area of 3.75 cm^2/mL; with both being changed on Day 3 with an equal amount of media as previous. Tissue culture plastic had a relatively greater volume of media available throughout the time course, and therefore a larger quantity of dissolved oxygen. The growth

in the tissue culture flask resulted in larger D-glucose consumption and L-lactic acid production despite having similar cell densities over from Day 1 and Day 6 to cell growth on PLGA. Cells grown on the PLGA scaffold were exposed to less L-lactic acid than on tissue culture plastic even when accounting for the extra lactic acid formed from PLGA breakdown. This can be attributed to the increased specific volume of the media in the tissue culture flask allowing a greater quantity of L-lactic acid to reside in the media relative to the media in the well of a PLGA flat sheet.

Studies comparing the data in Figure 6.2 with other studies of MG63 cell growth on tissue culture plastic are collected in Table 6.7. To allow as near a comparison as possible the data was constrained to cell growth between days 1 and 3 for most studies. Cell doubling time was rarely directly stated in these studies, and on many occasions had to be inferred from absorption data changes between day 1 and day 3 from a variety of cell quantification methods. For the majority of studies listed an initial rate of cell attachment was not stated, with many opting for a Day 1 value as the first check on cell viability. Day 1 cell values were typically non comparable with initial seeding values in these studies because the corresponding absorption test was not performed on an initial cell sample, so were not an accurate reflection of cell attachment efficiency.

Table 6.7 – Growth of MG63 cells on tissue culture plastic in various studies.

Source	Seeding Density (cells/cm^2)	Cell Attachment Efficiency	Doubling Time (days)	Time Period	Method
This work	34,470	78% (24h)	0.873	Day 1 - 3	Manual count
Zhou *et al.* (2016)	3,125	Unknown	2.000	Day 1 - 3	WST-8 Assay
(Skindersoe *et al.*, 2015)	21,053	Unknown	1.220	Day 0 - 3	MTS Assay
Podporska-Carroll *et al.* (2014)	26,316	Unknown	1.041	Day 1 - 3	Picogreen Assay
Stankova *et al.* (2014)	2,830	43% (24h)	1.200	Day 1 - 3	Cell counter
Wang *et al.* (2011a)	10,526	80% (6 h)	2.424	Day 1 - 3	WST-1 Assay
Zhao *et al.* (2009)	Unknown	Unknown	1.300	Day 1 - 3	MTT Assay
Amaral *et al.* (2008)	10,000	Unknown	2.391	Day 1 - 3	MTT Assay
Pamula *et al.* (2009)	100,000	45% (24h)	4.314	Day 1 – 3	Cell counter
Zhao *et al.* (2006)	9,600	Unknown	1.002	Day 0 - 5	Cell counter

The cell doubling time in this work is shorter than that published in (or inferred from) other works; which can be attributed to the larger initial cell seeding density. This would allow greater initial cell contact and signalling that would accelerate the formation of a cell monolayer. Cell attachment after 24 hours was greater than the other comparable works of Stankova *et al.* (2014) and Pamula *et al.* (2009) with 43% and 45% efficiency respectively.

A comparison of the data displayed in Figure 6.3 for MG63 growth on flat sheet PLGA with that found in literature is displayed in Table 6.8. As so few other studies of seeding MG63 cells on PLGA could be found, comparison is also drawn with MG63 cells grown on other flat sheet polymeric scaffolds. The same limitations on data comparison that were discussed regarding growth on tissue culture plastic also apply here.

Table 6.8 – Growth of MG63 cells on flat sheet PLGA and other polymers in various studies.

Source	Brief Description of Scaffold Preparation	Seeding Density (cells/cm^2)	Rate of Cell Attachment	Doubling Time (Days)	Time Period (Days)	Method
This work	PLGA (75:25) flat sheet, with added NaCl for salt leaching. Dissolved in NMP solvent (20:80 wt%) and phase inverted in water non-solvent.	34,470	58% (24h)	0.963	1 – 3	Manual Count
Vandrovcova *et al.* (2011)	PLGA (85:15) flat sheet, dissolved in methylene chloride solvent (10:90 wt%) and left to evaporate in air	17,000	100% (24h)	1.181	1 – 3	Cell counter
Pamula *et al.* (2009)	PLGA (85:15), flat sheet, with added NaCl for salt leaching. Dissolved in methylene chloride (10% w/v) and left to evaporate in air	100,000	32% (24h)	3.542	1 – 7	Cell counter
Liu *et al.* (2009)	Poly(L-lactic acid) dissolved in an undisclosed solvent and phase inverted in an undisclosed non-solvent	6,494	Unknown	2.319	1 – 3	LDH Assay
Cecen *et al.* (2015)	3D Collagen scaffold coated in poly-L-lactic acid. Polymer dissolved in chloroform (4:96 wt%), and phase inverted in ethanol.	Unknown	Unknown	1.165	1 – 3	MTT Assay
Podporska-Carroll *et al.* (2014)	Poly(ester urethane) flat sheets, With added NaCl for salt leaching. Dissolved in a solution of N,N-dimethylformamide–N and N-dimethylacetamide and phase inverted in water	44,210	Unknown	1.382	1 – 3	WST-1 Assay
Stankova *et al.* (2014)	Polysulphone dissolved in dichloromethane (0.1 g/mL), poured into mould to evaporate in air	2,830	35% (24h)	1.042	1 – 3	Cell counter
Salerno *et al.* (2012)	Poly(ε-caprolactone) plates (1-2mm thick) melted and compression moulded.	12,739	Unknown	3.247	1 – 7	Almar Blue Assay
Comelles *et al.* (2010)	Commercial Poly(methyl methacrylate) sheet. Unknown method of manufacture	5,405	7% (1h) 16% (3h)	1.082	1 – 3	WST-1 Assay
Tao and Young (2006)	20% Poly(etherimide) flat sheet with porous bottom surface. Dissolved in NMP solvent (20:80 wt%), and phase inverted in a solution of 30% NMP and 70% methylene chloride. Soaked in Acetone, then water	26,316	Unknown	1.409	1 – 4	MTT Assay
Lee *et al.* (2004)	Commercial Polycarbonate sheet with 5um pores and 7.2% pore surface coverage. Unknown method of manufacture.	Unknown	Unknown	1.793	2 – 4	Manual count

Cell doubling time of MG63 cells grown on porous PLGA flat sheets with 60% NaCl by weight is shorter in this work when compared to other PLGA studies. Vandrovcova *et al.* (2011) produced PLGA flat sheets of 85:15 lactide to glycide ratio dissolved in methylene chloride by 10% weight and left to dry in air, and cultured MG63 cells had a cell doubling time of 1.181 days. Pamula *et al.* (2009) prepared PLGA scaffolds the same way, but added NaCl particles that yielded pore sizes in the range of 200 – 600 µm, two orders of magnitude larger than those formed in PLGA flat sheets described in this thesis. The PLGA sheets of various had similar to worse cell doubling times between day 1 and day 7, all of which were longer than the cell doubling time of cells grown on porous PLGA sheets in this work of 0.963 days, however by day 15 cell numbers were twice as large as that found on the non-porous PLGA, owing to the larger internal surface area now available for cell proliferation. Studies on PLA as well as other polymeric flat sheets all show a greater cell doubling time in comparison to the porous PLGA used in this study. Lee *et al.* (2004) utilised a commercially available polycarbonate sheet manufactured with 5 µm diameter pores and surface pore coverage of 7.2%, and had a cell doubling time twice that of the PLGA in this work with an average pore size of 5.0 ± 3.8 µm and coverage of 1.44% ± 0.20%. This higher pore coverage would lead to a reduced available surface area for cells to spread across and grow, which would explain the higher cell doubling time if the available surface area were filled sooner.

6.4.2 Proliferation within Hollow Fibres

The graphs displayed in Figure 6.4 and Figure 6.5 illustrate that cell growth within hollow fibres is not achievable under the tested conditions. Within 24 hours viable cell density decreased to 2.0% and 6.7% at 10 µL/min and 50 µL/min respectively. While this does indicate that, at least over this time frame, the greater ECS flow rate provided a slightly better cell survival rate, overall permeation of media from the ECS to the lumen was insufficient.

ECS flow rates were set assuming that the permeation of D-glucose was the rate limiting factor in cell respiration. It was originally assumed that sufficient dissolved oxygen would permeate through with the D-glucose in the media, as well as diffuse to the lumen from the ECS. It is clear that this assumption was in error, and that the rate of diffusion for dissolved oxygen in this system combined with permeating dissolved oxygen was insufficient. It is likely that this led to anaerobic conditions in the lumen and subsequent acidification of the media in the lumen, making the cells non-viable. In this section the diffusion of dissolved oxygen and L-lactic acid to and from the lumen will be quantified, and a mass balance of these species will be performed to quantify their deficit and accumulation in the lumen respectively. From this a new minimum ECS flow rate will be calculated to provide sufficient dissolved oxygen permeation to the lumen.

Dissolved Oxygen Mass Balance

Given that the rate of liquid permeation at an ECS flow rate of 50 µL/min is 2.35 µL/min (Q), and the concentration (C) of dissolved oxygen in the media is 7.37 mg/L, the mass flow rate (G) of dissolved oxygen at that ECS flow rate can be calculated in Equation 6.10:

$$G_{O_2} = Q_{O_2} \times C_{O_2} = 50 \left[\frac{\mu L}{\min}\right] \times 7.37 \left[\frac{mg}{L}\right] = 0.03 \left[\frac{mg}{day}\right]$$

Equation 6.10 – Mass flow rate of dissolved oxygen permeating into the lumen.

At 50 µL/min a mass flow rate of 0.03 mg/day dissolved oxygen permeates into the lumen. To further quantify the movement of oxygen in this system, diffusion of oxygen from the ECS to the lumen must be considered.

The rate of diffusion of dissolved oxygen from the ECS into the lumen, as well as the rate of diffusion of lactate from the lumen to the ECS can be characterised using a simplified 1D Fick's law model for diffusion flux (J) with knowledge of the diffusivity (D) of both species in a hollow fibre system. This is visualised in Figure 6.6.

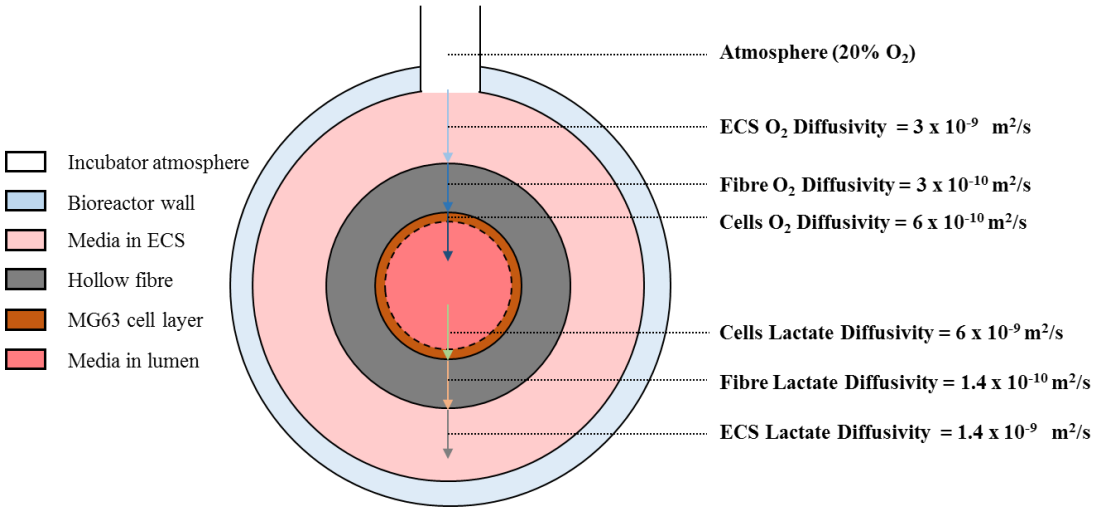

Figure 6.6 – Cross section of hollow fibre bioreactor indicating oxygen and lactate diffusivities at each point.

The values for oxygen diffusivity in the ECS of a hollow fibre were system were obtained from Ye *et al.* (2006). Diffusivity of oxygen in the bulk ECS media is 3E-09 m^2/s. Ye *et al.* (2006) also suggested that the hollow fibre itself hindered diffusion by a factor of 10, and that bone cells hindered diffusion by a factor of 5, providing diffusivity values of is 3E-10 m^2/s and 6E-10 m^2/s respectively. Holm *et al.* (1981) suggests that the diffusivity of lactate in the ECS would be 1.4E-09 m^2/s, and Eggleton *et al.* (1928) determined that the diffusivity of lactate through muscle cells is 6E-09 m^2/s. No value for diffusivity of lactate through the hollow fibre has been determined, however Shipley and Waters (2012) assumed a similar

factor of 10 hindrance as used for oxygen diffusion through the hollow fibre. All stated values for oxygen and lactate diffusivity have been used by Shipley *et al.* (2011) to model fluid and mass transport of these species within a hollow fibre bioreactor system. The modelling in this section is greatly simplified by utilising a 1D Fick's law model for diffusion flux, along with the values of diffusivity stated, and knowledge of the dimensions of the hollow fibre system.

An idealised mass flow rate of dissolved oxygen through the hollow fibre by diffusion is calculated in Equation 6.11, assuming that the media in the ECS has a dissolved oxygen concentration of 7.37 mg/L, and the dissolved oxygen in the lumen is completely exhausted at 0 mg/L. While it is likely that dissolved oxygen in the lumen is greater than zero, assuming zero provides the greatest possible concentration gradient, which results in the greatest possible diffusion flux of oxygen, which is an important limitation to quantify. The fibre is 0.138 mm thick (x) with a surface area (A) of 2.91 cm^2. The diffusivity of oxygen through the hollow fibre is selected as the rate limiting step for diffusion in this system.

$$J_{O2} = D_{O2}\frac{dC_{O2}}{dx}$$

$$J_{O_2} = 3 \times 10^{-10}\left[\frac{m^2}{s}\right] \times \frac{(7370 - 0)\left[\frac{mg}{m^3}\right]}{1.38 \times 10^{-4}[m]} = 0.016\ \left[\frac{mg}{m^2.s}\right]$$

$$G_{O_2} = \frac{J_{O_2}}{A} = \frac{0.016\left[\frac{mg}{m^2.s}\right]}{2.91\ [cm^2]} = 0.40\ \left[\frac{mg}{day}\right]$$

Equation 6.11 – Fick's law for maximum diffusion flux of dissolved oxygen through the hollow fibre wall.

This indicates that from diffusion alone, at a maximum possible concentration gradient a maximum of 0.40 mg/day oxygen permeates through the hollow fibre. This is much greater than the 0.03 mg/day that has been calculated to permeate into the lumen at an ECS flow of 50 µL/min. To complete the oxygen balance and to determine the oxygen deficit in this system, the consumption rate of oxygen by the cells needs to be calculated.

First the known mass consumption of D-glucose (0.70 mg/day) is converted into a molar consumption (N), as shown in Equation 6.12.

$$N_{glucose} = \frac{G_{glucose}}{m_{w\,glucose}} = \frac{0.70\left[\frac{mg}{day}\right]}{108.16\ \left[\frac{g}{Mol}\right]} = 0.0039\left[\frac{mMol}{day}\right]$$

Equation 6.12 – Calculation of molar daily consumption of D-glucose.

Referring to the stoichiometric reaction for aerobic cell respiration shown in Equation 6.1, 1 mole of D-glucose reacts with 6 moles of oxygen to produce the energy required to facilitate cell function. Knowing this, the molar daily consumption of oxygen can be calculated, along with the mass daily consumption, as shown in Equation 6.13.

$$N_{O_2} = 6 \times N_{glucose} = 6 \times 0.0039 \left[\frac{mMol}{day}\right] = 0.0232 \left[\frac{mMol}{day}\right]$$

$$G_{O_2} = N_{O_2} \times m_{wO_2} = 0.0232 \left[\frac{mMol}{day}\right] \times 32.00 \left[\frac{g}{Mol}\right] = 0.74 \left[\frac{mg}{day}\right]$$

Equation 6.13 – Calculation of mass daily consumption of dissolved oxygen.

Note that Equation 6.1 does not account for the requirements for production of additional biomass, only respiration of cells; however as empirical measurement of dissolved oxygen consumption could not be undertaken with flat sheet PLGA growth samples, Equation 6.1 has been used as a substitute. The mass balance of oxygen in the lumen over the initial 24 hours has now been completed, and is summarised in Table 6.9.

Table 6.9 – Mass balance on dissolved O2 in the lumen

dO2 Consumption Rate	0.74	mg/day
dO2 Diffusion Rate In	0.40	mg/day
dO2 Permeation Rate In	0.03	mg/day
dO2 Deficit	0.31	mg/day
Time until dO2 Exhausted	0.57	days

Between Day 0 and Day 1 there is a deficit of 0.31 mg/day dissolved oxygen. From this a new value for ECS flow rate can be calculated in order to provide enough oxygen to balance with the consumption rate of 0.74 mg/day. Given the concentration of dissolved oxygen in the media is 7.37 mg/L, the equivalent volume of cell media consumed over time by the cells in the lumen can be calculated, as shown in Equation 6.14.

$$Q_{O_2} = \frac{G_{O_2}}{C_{O_2}} = \frac{0.74 \left[\frac{mg}{day}\right]}{7.37 \left[\frac{mg}{L}\right]} = 100.74 \left[\frac{mL}{day}\right] = 69.96 \left[\frac{\mu L}{min}\right]$$

Equation 6.14 – Calculation of volume media consumption of dissolved oxygen.

From the liquid permeation experiments outlined in Chapter 5, the 60% NaCl PLGA hollow fibres selected for this experiment provide a permeation of 4.70% of the feed rate. Given this ratio, and the requirement for a minimum media permeation flow of 69.96 µL/min, the equivalent ECS flow rate to achieve that degree of permeation can be calculated, as shown in Equation 6.15:

$$ECS\ Flow\ Rate = \frac{100\%}{4.70\%} \times 69.69\ \left[\frac{\mu L}{min}\right] = 1487.05\ \left[\frac{\mu L}{min}\right] = 1.49\left[\frac{mL}{min}\right]$$

Equation 6.15 – Calculation of ECS flow rate for sufficient dissolved oxygen permeation.

For sufficient permeation to ensure that dissolved oxygen is not the rate limiting factor in cell growth, an ECS flow rate of 1.49 mL/min is required to ensure a permeation of 69.96 µL/min. This is much greater than the original minimum ECS flow rate when D-glucose was assumed to be rate limiting (2.29 µL/min) as well as the actual selected flow rates (10 µL/min and 50 µL/min). This is because the concentration of dissolved oxygen in the media (7.37 mg/L) is much smaller than the concentration of D-glucose (4,500 mg/L), as well as factoring in the much smaller molecular weight of molecular oxygen (32.00 g/mol) compared to D-glucose (180.16 g/mol) and how that affects molar requirements for cells.

L-lactic acid Mass Balance

So far it has been established that there is a dissolved oxygen deficiency in the bioreactors tested, however the impact of the low oxygen environment and cell death over 24 hours has not been directly linked. In order to do this the production of L-lactic acid from anaerobic respiration needs to be characterised, and how the pH within the lumen changes.

Assuming that the cells respire aerobically for so long as there is available dissolved oxygen, then respire anaerobically when the dissolved oxygen is exhausted, aerobic respiration occurs for the first 0.57 days, then anaerobic respiration for the remaining 0.43 days. As shown in Equation 6.2 in Section 6.2.2, anaerobic respiration produces 2 mol of lactic acid from 1 mol of D-glucose. Assuming that the rate of D-glucose consumption is the same during aerobic and anaerobic conditions (0.0039 mMol/day), the molar and mass rate of L-lactic acid production can be calculated as shown in Equation 6.16.

$$N_{LA} = 2 \times N_{glucose} \times 0.43 = 0.0033\left[\frac{mMol}{day}\right]$$

$$G_{LA} = N_{LA} \times m_{w_{LA}} = 0.0033\left[\frac{mMol}{day}\right] \times 90.08\left[\frac{g}{Mol}\right] = 0.30\left[\frac{mg}{day}\right]$$

Equation 6.16 – Calculation of mass daily L-lactic acid production,

The MG63 cells in the lumen produce 0.30 mg/day L-lactic acid between Day 0 and Day 1. This rate of production contained in such a small volume will likely decrease the pH, making conditions much too acidic for cell growth to continue. The maximum concentration of L-lactic acid in the lumen is calculated in Equation 6.17.

$$C_{LA} = \frac{0.30[mg]}{67.2[\mu L]} = 4.43\left[\frac{mg}{mL}\right]$$

Equation 6.17 – Calculation of concentration of L-lactic acid in the lumen.

However, L-lactic acid can diffuse away from a higher concentration in the lumen, to a region of lower concentration in the circulating media flowing in the ECS. Using the simplified 1D Fick's law model again, a mass flow rate of L-lactic acid leaving the lumen through the hollow fibre can be calculated. This assumes an L-lactic acid concentration of 4.43 mg/L within the lumen, and zero in the ECS, again to characterise the maximum possible rate of diffusion. The fibre is 0.138 mm thick with a surface area of 2.91 cm^2, and the diffusivity of L-lactic acid (D_{LA}) through the hollow fibre is 1.4E-10 m^2/s (Shipley and Waters, 2012). This calculation is shown in Equation 6.18

$$J_{LA} = D_{LA}\frac{dC_{LA}}{dx}$$

$$J_{LA} = 1.4 \times 10^{-10}\left[\frac{m^2}{s}\right] \times \frac{(4430 - 0)\left[\frac{mg}{L}\right]}{1.38 \times 10^{-4}[m]} = 0.005\ \left[\frac{mg}{m^2.s}\right]$$

$$G_{LA} = \frac{J_{LA}}{A} = \frac{0.005\left[\frac{mg}{m^2.s}\right]}{2.91\ [cm^2]} = 0.11\ \left[\frac{mg}{day}\right]$$

Equation 6.18 – Fick's law for maximum diffusion flux of L-lactic acid through the hollow fibre wall.

From this data we can determine the accumulation of L-lactic acid within the lumen over the initial day. This is summarised in Table 6.10.

Table 6.10 – Mass balance on L-lactic acid in the lumen

L-lactic Acid Production Rate	0.30	mg/day
L-lactic Acid Diffusion Rate	0.11	mg/day
L-lactic Acid Accumulation	0.19	mg/day

Now that the mass of L-lactic acid accumulating within the lumen over the first day has been calculated, the pH change of the media within the lumen can be determined. To do this a value for dissolved H^+ ions in the media solution must be calculated. This can be done through knowledge of the equilibrium reaction for L-lactic acid disassociation. L-lactic acid disassociates into a lactate ion and hydrogen ion, as shown in Equation 6.19.

$$\boldsymbol{C_3H_6O_3 \leftrightarrow C_3H_5O_3^- + H^+}$$

Equation 6.19 – Disassociation of L-lactic acid.

For this reaction, the equilibrium constant (K_a) is specified in Equation 6.20.

$$K_a = \frac{[C_3H_5O_3^-][H^+]}{[\,C_3H_6O_3]}$$

Equation 6.20 – Equilibrium constant of L-lactic acid disassociation.

This expression can be simplified by using relative molar rates of change for this reaction. This is summarised in a RICE chart, shown in Table 6.11.

Table 6.11 – A RICE chart to assist in calculating [H^+].

Reaction	$[C_3H_6O_3]$	$[C_3H_6O_3^-]$	$[H^+]$
Initial Concentration	Ca	0	0
Change	-X	+X	+ X
Equilibrium	Ca - X	X	X

The reaction components can be replaced in Equation 6.20 with the relative changes 'X'. This expression can then be reorganised into a quadratic equation allowing the concentration of H^+ in the lumen to be calculated. In this system, C_a is 0.03 mol/L, and the disassociation constant for L-lactic acid is 1.38E-04. This is shown in Equation 6.21:

$$K_a = \frac{[X][X]}{[C_a - X]}$$

$$[X]^2 + K_a[X] - K_aC_a = 0$$

$$[X] = [H^+]$$

$$[H]^2 + K_a[H] - K_aC_a = 0$$

$$[H]^2 + 1.38 \times 10^{-4}[H] - 4.21 \times 10^{-6} = 0$$

Equation 6.21 – A quadratic equation to calculate the concentration of H^+ in the lumen.

Solving Equation 6.21 yields a H^+ concentration of 1.98E-03 mol/L. This is converted into a value of pH in Equation 6.22:

$$pH = -\log_{10}[H^+] = -\log_{10}[1.98 \times 10^{-3}] = 2.7$$

Equation 6.22 – Equation to calculate pH from the concentration of hydrogen ions.

Between Day 0 and Day 1, assuming that all dissolved oxygen has been depleted and that anaerobic respiration then occurs, the pH of the media within the lumen will decrease from 7.8 to 2.7. Given that the viability of MG63 cells decreases from 100% to 75% over 24 hours when pH is decreased from 7.4 to 6.4 (Lee *et al.*, 2011), it is highly likely that the majority of the cells in this system became non-viable well before the pH would ever reach 2.7 in the

lumen. However, given that cell viability did decrease so drastically between Day 0 and Day 1, and that insufficient oxygen was permeating through to the cells in the lumen, it is likely that the production of L-lactic acid and the subsequent decrease in pH was the cause of cell death.

Improvements to the System

Increasing the ECS flow rate to a minimum of 1.49 mL/min should provide the 100,000 cells in the lumen with sufficient permeating dissolved oxygen and D-glucose in order to aerobically respire and proliferate. This would reduce the concentration of L-lactic acid in the lumen, and ensure that cells will not die due to acidification of the media. Given that oxygen is provided to the recirculating media continuously in the incubator by way of an oxygen permeable vent, the consumption of dissolved oxygen in the lumen will only be limited by the rate of media permeation, so no increase in the volume of media itself is necessary.

The increased rate of permeation will put the attached cells within the lumen under additional shear forces. Cell rolling and eventual expulsion from the lumen may occur if the adhesive forces between the cells and the membrane are not strong enough. This would be undesirable as it would adversely affect the ability of the hollow fibre to act as a device for cell delivery. Shear within the lumen would need to be calculated, and the cells subjected to tests to determine their attachment strength on PLGA. If shear forces through the lumen were a factor, the membrane itself could be altered to increase its porosity and encourage higher rates of dissolved oxygen and L-lactic acid exchange through the lumen by diffusion.

Using a smaller cell inoculant may also be beneficial in characterising the system in its current state. 100,000 cells were seeded in this system, and the values for D-glucose and dissolved oxygen consumption and L-lactic acid production were calculated based upon the demands of 100,000 cells. A future iteration of this experiment could reduce the number of seeded cells to 10,000 whilst increasing the rate of sampling to every 12 hours over 3 days. Assuming the demands of 10% of the seeded cell population was equivalent to 10% of the original dissolved oxygen demand, then dissolved oxygen consumption would be 0.07 mg/day, compared to the 0.40 mg/day that diffused in.

In conclusion, shear experiments to allow the calculation of a force balance between lumen flow rate and cell attachment strength should be conducted to determine the maximum value of ECS flow rate that can be applied. If this leads to cell removal then fibres of increased porosity should be manufactured and seeded with a lower number of cells to characterise the diffusion potential in the system and how this affects the seeded cell population.

6.5 CONCLUSIONS

The results outlined in this chapter suggest that the selected hollow fibre bioreactor configuration was insufficient to sustain a population of MG63 cells. While the experiment was ultimately unsuccessful, this was the first time MG63 cells were inoculated into the lumen of a hollow fibre to characterise its ability to grow cells, making this research a novel endeavour. This initial challenge needs to be overcome before hollow fibres can be further investigated for use as a medical device for delivery cell therapies. From the experiments outlined in this chapter it has been concluded that:

i) Flat sheets of 60% NaCl porous PLGA sustained a greater number of cells than tissue culture plastic over a 6 day time course.

ii) Cell doubling time of MG63 cells on porous flat sheet PLGA was shorter than found on other porous PLGA flat sheets, non-porous PLGA flat sheets, and on flat sheet scaffolds made from other polymers.

iii) Dissolved oxygen availability is the limiting factor that prevented cell survival after 24 hours within hollow fibres. Diffusion of dissolved oxygen into the lumen was unable to compensate for the poor rate of media permeation. Subsequent investigations into the oxygen demands of this system have shown that an ECS flow rate of 1.49 mL/min would be required for sufficient permeation of dissolved oxygen to sustain 100,000 MG63 cells.

iv) Accumulation of L-lactic acid, and its subsequent disassociation, led to an increased media acidity within the lumen (pH 2.7), which led to cell death within 24 hours.

While the aim of this chapter, to sustain a population of cells within a hollow fibre lumen, was not achieved, the limitations of this system were identified and the means to mitigate them were explored. Future work would seek to implement a greater ECS flow rate for increased permeation of dissolved oxygen, or modify the permeability of the hollow fibre itself to allow for a greater rate of dissolved oxygen diffusion into the lumen.

The limitations of traditional and engineered cell delivery mechanisms still hinder the effectiveness of clinical cell therapies, and the proposed solution outlined in this work cannot yet be discounted at this stage until further experiments are carried out.

[Page intentionally left blank]

CHAPTER SEVEN: CONCUSIONS AND FUTURE WORK

7.1 CONCLUSIONS

The literature review in Chapter 2 uncovered limitations in the current methods used to grow and deliver cell therapies to treat infarct tissue in the human heart. This thesis has investigated these limitations and has outlined solutions that could lead to accelerated and/or improved clinical outcomes for patients.

Traditionally administered cell therapies for improving cardiac function after a heart attack require a minimum of 50 million cells. Mesenchymal stem cells (MSCs) show the most promise, with those extracted from the adipose tissue surrounding the heart more likely to differentiate into cardiomyocytes. However extraction rates from this source are approximately 812,800 ± 318,400 cells, thus requiring expansion in order to be clinically useful. Hollow fibre bioreactors (HFB) were found to be the best technology for this expansion, with cells growing on the external surface of hollow fibres. Rates of cell seeding within HFB are around 20%, with the remaining cells failing to attach leading to accumulation in the bottom of the bioreactor housing. With this MSC extraction rate and cell seeding efficiency, it would take approximately 12.6 ± 5.2 days to grow 50 million cells in a HFB. Chapter 4 sought to improve upon this rate of cell attachment in order to reduce the required amount of time necessary to grow cells for traditionally administered cell therapies. This was achieved by using a novel dynamic seeding method.

Theoretical rates of cell attachment based of gravity settling onto static individual fibres indicated a maximum cell attachment of 24% ± 4%, assuming all cells that fell onto the fibre would attach. Experiments indicated that 18% ± 16% of cells attached. Both values for cell attachment are close to 20%, confirming the limitation with seeding HFBs as described in literature.

A series of experiments were carried out to determine of the act of motion would allow seeded MG63 cells more opportunities to attach to the external surface of the hollow fibre. Bioreactors were attached to a rotating drum and spun at 2, 6 or 8 RPM while orientated at different angles to determine if cell attachment would improve. A model utilising modified particle settling equations for use in a rotating environment indicated that 59% ± 22% cell attachment could be achieved in horizontally orientated bioreactors rotating at 6 RPM. Experiments under those conditions showed 39% ± 12% cell attachment, a value within the margin of error shown in the data from the theoretical model. This almost doubles the rate of cell attachment on hollow

fibres, and if applied to MSCs would allow the growth of 50 million cells in 11.2 ± 4.7 days, 1.4 days quicker than with previous rates of cell attachment of 20%.

Other experiments where bioreactors were positioned horizontally on the rotating drum (2 RPM and 8 RPM) also showed improved attachment (31% ± 7% and 22% ± 6%) over the static control, however bioreactors rotated at a constant rotational velocity at other orientations (diagonal and vertical) showed worse attachment (15% ± 11% and 16% ± 1%). The work in Chapter 4 has shown that using a novel dynamic method for seeding cells onto hollow fibres has led to improved rates of cell attachment, which reduces the amount of time necessary to produce a clinically applicable dose of MSCs.

Chapter 5 sought to manufacture porous hollow fibres for use in a HFB. Previous attempts at hollow fibre manufacture using wet-spinning phase inversion produced fibres with a thick non-porous skin layer. For use in HFBs, the fibres needed to be porous in order to allow nutrients, waste and gases to permeate through the fibre and enable cell growth. To that end, PLGA polymer was dissolved in NMP solvent and augmented with 10%, 20%, 40% and 60% sodium chloride (by weight % of PLGA). Hollow fibres and flat sheet scaffolds were manufactured and imaged to quantify surface porosity, and experiments conducted to determine how NaCl content affected the permeability of fibres.

Imaging of scaffolds revealed that addition of manufactured NaCl particles provided the internal and external surfaces of hollow fibres with pores. Addition of 10% and 20% NaCl yielded statistically similar pore densities of 120 ± 5 and 115 ± 17 pores/mm^2 and addition of 40% and 60% NaCl, yielding statistically similar pore densities of 260 ± 83 and 268 ± 51 pores/mm^2 on the inner hollow fibre surface. This indicates that the addition of larger quantities of NaCl will increase the surface pore density, however the non-linear relationship between NaCl content and subsequent surface porosity might indicate a critical NaCl concentration between 20% and 40% beyond which conditions are better suited for surface pore formation.

Similarly, liquid permeability of these fibres did not increase linearly with NaCl content, demonstrating that surface porosity was not the limiting factor for liquid permeation. This indicated that the internal tortuous network of pores within hollow fibres produced as a result of the wet-spinning phase inversion manufacturing process was rate limiting. The fibre with the greatest liquid permeability was the 60% fibres with 1.91E-15 m^2 (± 50.5%), and this batch of fibre was used for future experiments for cell growth in HFBs.

The literature review also summarised the current limitations with traditionally administered cell therapies, particularly the low rates of cell retention in the wound site that facilitated the

need for such high cell doses in the first place. Of an 'initial dose' of 50 million cells, only a 1 million cell 'functional dose' would be retained (2%), but despite this studies have shown improvements in heart function after traditionally administered treatment. It was proposed that if a similar or larger sized functional cell dose can be administered and retained at the wound site, the required expansion step to make this functional dose would be much shorter than that required to grow the typical 50 million cells for traditionally administered cell therapies, while requiring much fewer cells.

Current engineered delivery methods do utilise fewer cells, and include administering cell patches, injecting cell loaded hydrogels, or suturing cell loaded threads into a wound site; however each have their own drawbacks that limit their therapeutic potential, and still suffer from a loss of cells during implantation like traditionally administered methods. A novel device allowing the encapsulation of cells in the lumen of a porous hollow fibre was proposed as a method to protect the cells during implantation, and to allow transport of nutrients, waste and oxygen *in vivo* after implantation. Chapter 6 undertook preliminary experiments to determine if a population of cells seeded within the lumen of a hollow fibre could grow or be sustained *ex vivo.* The hollow fibres manufactured and characterised in Chapter 5 were used in this work.

MG63 cells were seeded within the lumen of 60% NaCl PLGA hollow fibres within a glass bioreactor housing. This HFB was attached to a system which pumped media through the extracapillary space of the HFB, allowing permeation and diffusion of glucose and dissolved oxygen through the fibre and into the lumen. ECS flow rates were set at 10 and 50 µL/min to ensure that glucose did not become rate limiting, and it was assumed that the incubator in which the system was placed would ensure that dissolved oxygen did not become rate limiting.

The experiments conducted in Chapter 6 showed that at the calculated required flow rates of 10 and 50 µL/min in the extracapillary space were insufficient to sustain a population of MG63 cells within the lumen of a hollow fibre. Subsequent modelling of the system revealed that limited permeation of dissolved oxygen caused the MG63 cells to anaerobically respire, which produced lactic acid that accumulated in the lumen, leading to the death of cells from the increased acidic conditions (pH 2.7). Suggested improvements to the system include increasing the ECS flow rate to a minimum of 1.49 mL/min to enable sufficient permeation of dissolved oxygen to sustain 100,000 MG63 cells, or manufacture a fibre with greater permeability to facilitate additional dissolved oxygen transfer by diffusion.

While this particular *ex vivo* experiment did not successfully sustain cells over 6 days, the limitations of this system were identified and the means to mitigate them in future works

was investigated. Work on cell encapsulation within hollow fibres should continue to be explored, as this novel route for cell delivery cannot yet be dismissed.

7.2 FUTURE WORK

The work contained within this thesis stands on its own merits, however there is scope to achieve additional improvements in external cell attachment on hollow fibres, and to further investigate encapsulated cell growth within a hollow fibre for eventual use as a cell delivery device. This section will discuss further avenues to the research outlined in this work.

Cell Attachment on Hollow Fibre External Surfaces (Chapter 4)

Cell attachment was improved from 18% ± 16% to 39% ± 12%, which would reduce the time to grow 50 million MSCs from 12.6 ± 5.2 days to 11.2 ± 4.7 days, however if cell attachment were further improved this would further reduce the growth time. If all inoculated cells attached in the HFB, it would only take 9.1 ± 4.0 days. This this shows that MSC growth time could be reduced by an additional 2.1 days. While it is unlikely that 100% attachment could be achieved, this study has shown that there is scope to investigate dynamic seeding as a viable alternative to standard static seeding, and to that end further dynamic regimes should be trialled to seek further improvements.

One particular regime that should be investigated further is cell seeding using the periodic mixing offered by the MACSmix rotator drive. While in Chapter 4 it showed the near worst rate of cell attachment (10% ± 4%), cells were only allowed 4 minutes to attach between each minute of rotation. Studies on flat sheets has shown rates of attachment increase from 20% ± 11% after 5 minutes to 84% ± 31% after 3 hours, therefore a longer waiting time in between periods of rotation might offer improved cell attachment in the first instance, while offering additional opportunities for cells that miss the hollow fibre to attach after rotation.

The theoretical model for dynamic attachment could also be improved. In this work it was assumed that a moving linear cell front resulting from centrifugal force allowing cells to make contact with the hollow fibre(s) at the centre of a bioreactor. Other models for cell movement could be more appropriate, for example modelling attachment as a result of random cell/fibre collisions, or modelling cell movement in a spiral instead of a linear front.

Sodium Chloride Particles Used for Manufacture of Porous PLGA Scaffolds (Chapter 5)

While every effort was made to maintain constant fibre spinning conditions between different quantities, hollow fibres with different NaCl concentrations formed hollow fibres of differing internal and external diameters. Wet-spinning is an intricate manufacturing method, requiring a specific polymer flow rate and internal water bore flow rate. Spinning was successful within a range of these flow rates, however not necessarily at the same flow rates between spinning batches. While salt content can affect viscosity of polymer solutions, which in turn affects the required flow rate of polymer, no trend between salt content, spinning flow rates, or resultant fibre dimensions was observed.

It was also extremely difficult to successfully wet-spin hollow fibres. Given the high failure rate of the equipment, only a single batch of each NaCl/PLGA/NMP fibre mixture could be produced. Therefore, abnormalities displayed in the data could be caused by batch to batch variation and not necessarily by variations from NaCl content alone. Alternative methods for hollow fibre production, such as melt-spinning, should be investigated to determine if it would provide more consistent fibre production.

As the fibres were to be used to encapsulate cells, with cell media passively permeating through, additional liquid permeation experiments using cell growth media would be useful to characterise any fouling may affect the permeability of the fibres and how this would impact the encapsulated cells. If fouling effects were observed, then fibres with a higher molecular weight cut off would be required, or the bioreactor configuration would require alteration to treat fouled membranes by back flushing.

Study of liquid permeation at an applied back pressure was attempted but the available equipment did not allow for fine enough variations in pressure to provide a consistent permeate stream from the hollow fibre walls. If the apparatus could be reconstructed to allow for this permeation could be controlled, allowing a greater degree of operational flexibility when the fibre is used in the bioreactor.

The results in Chapter 5 showed statistically similar pore densities in certain fibre surfaces between 10% - 20% and 40% - 60% NaCl content. Characterisation of NaCl content between 20% - 40% should be investigated to determine the nature of this sudden increase in pore density.

Increasing NaCl content does not correlate with increased gas or liquid permeability of hollow fibres. As surface porosity is not the rate limiting step to permeation as first postulated, studies on how NaCl content affects the internal porous network should be carried out to see if the addition of porogen improves the interconnectivity of the macrovoids within the hollow fibre structure.

Cell Growth within the Lumen of a Hollow Fibre (Chapter 6)

The encapsulated population of 100,000 MG63 cells became non-viable 24 hours after seeding. It was determined that insufficient dissolved oxygen was permeating from the extracapillary space at the set flow rates of 10 and 50 µL/min, resulting in aerobic respiration of cells, and formation of lactic acid which acidified the media within the lumen. To ensure sufficient dissolved oxygen permeation for aerobic respiration of cells, the ECS flow rate should be increased to a minimum of 1.49 mL/min.

However, care should be taken at this ECS flow rate, as the subsequent flow rate of permeated media within the lumen could lead to increased shear stresses that could damage the cells or remove them from the internal lumen wall. Studies should be conducted to quantify the shear forces within the lumen, and to determine the strength of the bonds between the cells and the hollow fibre surface in order to provide a maximum flow rate the cells can resist. If shear is too great at an ECS flow rate of 1.49 mL/min then the porosity of the hollow fibre should be increased by adding more NaCl particles during fibre manufacture in order to further facilitate dissolved oxygen transfer by diffusion.

If subsequent experiments are successful in sustaining a population of 100,000 cells, further work should aim to sustain larger cell populations of MSCs up to the functional dose offered by traditional methods of 1 million cells, and then beyond. From here studies should further detail how a successful medical device can be manufactured, with particular focus on the practicalities of removing the hollow fibre from the bioreactor housing without the loss of cells, the logistics of retaining those cells as the fibre is transported, and ensuring a suitable biodegradation profile of the hollow fibre to meet the required clinical outcome.

REFERENCES

Abdel-Latif, A., Bolli, R., Tleyjeh, I.M., Montori, V.M., Perin, E.C., Hornung, C.A., Zuba-Surma, E.K., Al-Mallah, M. & Dawn, B., 2007. Adult bone marrow-derived cells for cardiac repair - A systematic review and meta-analysis. *Arch. Intern. Med.*, 167(10), pp. 989-997.

Acott, S.M., 2014. Co-mixtures of non-solvents for PLGA demixing and porous surface formation. [Unpublished].

Adair, T.H.M., J.P.;, 2010. *Angiogenesis.* San Rafael, USA: Morgan & Claypool Life Sciences.

AHA, 2016. *Understanding Blood Pressure Readings* [Online]. American Heart Association. Available from: http://www.heart.org/HEARTORG/Conditions/HighBloodPressure/KnowYourNumbers/Understanding-Blood-Pressure-Readings_UCM_301764_Article.jsp [Accessed 06 December 2016].

Ahmadi, A., Toeg, H.D., DaSilva, J.N., Kordos, M., Thorn, S.L., Renaud, J.M., Beanlands, R.B., deKemp, R., Suuronen, E.J. & Ruel, M., 2010. A COLLAGEN MATRIX FOR ENDOTHELIAL PROGENITOR CELL THERAPY IMPROVES CARDIAC FUNCTION IN A MOUSE MYOCARDIAL INFARCTION MODEL. *Can. J. Cardiol.*, 26, pp. 85D-85D.

Akar, A.R., Durdu, S., Arat, M., Kilickap, M., Kucuk, N.O., Arslan, O., Kuzu, I. & Ozyurda, U., 2009. Five-year follow-up after transepicardial implantation of autologous bone marrow mononuclear cells to ungraftable coronary territories for patients with ischaemic cardiomyopathy. *European Journal of Cardio-Thoracic Surgery*, 36(4), pp. 633-643.

Amaral, M., Dias, A.G., Gomes, P.S., Lopes, M.A., Silva, R.F., Santos, J.D. & Fernandes, M.H., 2008. Nanocrystalline diamond: In vitro biocompatibility assessment by MG63 and human bone marrow cells cultures. *J. Biomed. Mater. Res. Part A*, 87A(1), pp. 91-99.

AnaesthesiaUK, 2005. *Oxygen content of blood* [Online]. Fellowship of the British Royal College of Anaesthetists. Available from: http://www.frca.co.uk/article.aspx?articleid=100344 [Accessed 06 December 2016].

Argyle, I.S., M.; Luetchford, K.; Ellis, M.J.;, Unpublished. *Micro-crystal sodium chloride as a porogen for polystyrene asymmetric membrane synthesis.*

Ascione, R., 2013. *RE: Discussion on MSC differentiation into cardiomyocytes in host myocardium tissue.*

Azimi, B., Nourpanah, P., Rabiee, M. & Arbab, S., 2014. Poly (lactide -co- glycolide) Fiber: An Overview. *Journal of Engineered Fibers and Fabrics*, 9(1), pp. 47-66.

Baheiraei, N., Yeganeh, H., Ai, J., Gharibi, R., Ebrahimi-Barough, S., Azami, M., Vahdat, S. & Baharvand, H., 2015. Preparation of a porous conductive scaffold from aniline pentamer-modified polyurethane/PCL blend for cardiac tissue engineering. *J. Biomed. Mater. Res. Part A*, 103(10), pp. 3179-3187.

Bailey, R., 2016. *Cellular Respiration* [Online]. Available from: http://biology.about.com/od/cellularprocesses/a/cellrespiration.htm [Accessed 05 September 2016].

Banerjee, I., Fuseler, J.W., Price, R.L., Borg, T.K. & Baudino, T.A., 2007. Determination of cell types and numbers during cardiac development in the neonatal and adult rat and mouse. *Am. J. Physiol.-Heart Circul. Physiol.*, 293(3), pp. H1883-H1891.

Barbash, I.M., Chouraqui, P., Baron, J., Feinberg, M.S., Etzion, S., Tessone, A., Miller, L., Guetta, E., Zipori, D., Kedes, L.H., Kloner, R.A. & Leor, J., 2003. Systemic delivery of bone marrow-derived mesenchymal stem cells to the infarcted myocardium - Feasibility, cell migration, and body distribution. *Circulation*, 108(7), pp. 863-868.

Bayes-Genis, A., Galvez-Monton, C., Prat-Vidal, C. & Soler-Botija, C., 2013. Cardiac adipose tissue: A new frontier for cardiac regeneration? *Int. J. Cardiol.*, 167(1), pp. 22-25.

Beard, D.A., 2006. Modeling of oxygen transport and cellular energetics explains observations on in vivo cardiac energy metabolism. *PLoS Comput. Biol.*, 2(9), pp. 1093-1106.

Behfar, A., Yamada, S., Crespo-Diaz, R., Nesbitt, J.J., Rowe, L.A., Perez-Terzic, C., Gaussin, V., Homsy, C., Bartunek, J. & Terzic, A., 2010. Guided Cardiopoiesis Enhances Therapeutic Benefit of Bone Marrow Human Mesenchymal Stem Cells in Chronic Myocardial Infarction. *J. Am. Coll. Cardiol.*, 56(9), pp. 721-734.

Benzeval, I., Ellis, M.J. & Turner, I.G., 2012. Stem cell expansion in a fluidised bed bioreactor for accelerated osseointegration of bone substitute material. *J. Tissue Eng. Regen. Med.*, 6, pp. 346-346.

Bergmann, O., Bhardwaj, R.D., Bernard, S., Zdunek, S., Barnabe-Heider, F., Walsh, S., Zupicich, J., Alkass, K., Buchholz, B.A., Druid, H., Jovinge, S. & Frisen, J., 2009. Evidence for Cardiomyocyte Renewal in Humans. *Science*, 324(5923), pp. 98-102.

BHF, 2014. *Cardiovascular Disease Statistics 2014* [Online]. British Heart Foundation. Available from: https://www.bhf.org.uk/-/media/files/publications/research/bhf_cvd-statistics-2014_web_2.pdf [Accessed 02 September 2016].

BHF, 2015. *Cardiovascular Disease Statistics 2015* [Online]. British Heart Foundation. Available from: https://www.bhf.org.uk/-/media/files/publications/research/bhf-cvd-statistics-2015-final.pdf [Accessed 02 September 2016].

Bini, T.B., Gao, S.J., Tan, T.C., Wang, S., Lim, A., Hai, L.B. & Ramakrishna, S., 2004. Electrospun poly(L-lactide-co-glycolide) biodegradable polymer nanofibre tubes for peripheral nerve regeneration. *Nanotechnology*, 15(11), pp. 1459-1464.

Blausen, 2014. *Medical gallery of Blausen Medical 2014* [Online]. Wikiversity Journal of Medicine 1 (2). Available from: https://en.wikiversity.org/wiki/Wikiversity_Journal_of_Medicine/Medical_gallery_of_Blausen_Medical_2014 [Accessed 02 September 2016].

Bolli, R., Chugh, A.R., D'Amario, D., Loughran, J.H., Stoddard, M.F., Ikram, S., Beache, G.M., Wagner, S.G., Leri, A., Hosoda, T., Sanada, F., Elmore, J.B., Goichberg, P., Cappetta, D., Solankhi, N.K., Fahsah, I., Rokosh, D.G., Slaughter, M.S., Kajstura, J. & Anversa, P., 2011. Cardiac stem cells in patients with ischaemic cardiomyopathy (SCIPIO): initial results of a randomised phase 1 trial. *Lancet*, 378(9806), pp. 1847-1857.

Bonaros, N., Rauf, R., Wolf, D., Margreiter, E., Tzankov, A., Schlechta, B., Kocher, A., Ott, H., Schachner, T. & Hering, S., 2006. Combined transplantation of skeletal myoblasts and angiopoietic progenitor cells reduces infarct size and apoptosis and improves cardiac function in chronic ischemic heart failure. *The Journal of thoracic and cardiovascular surgery*, 132(6), pp. 1321-1328. e2.

Boo, L., Selvaratnam, L., Tai, C.C., Ahmad, T.S. & Kamarul, T., 2011. Expansion and preservation of multipotentiality of rabbit bone-marrow derived mesenchymal stem cells in dextran-based microcarrier spin culture. *J. Mater. Sci.-Mater. Med.*, 22(5), pp. 1343-1356.

Brugmans, M., Driessen-Mol, A., Rubbens, M.P., Cox, M.A.J. & Baaijens, F.P.T., 2015. Poly-epsilon-caprolactone scaffold and reduced in vitro cell culture: beneficial effect on compaction and improved valvular tissue formation. *J. Tissue Eng. Regen. Med.*, 9(12), pp. E289-E301.

Calvillo, L., Latini, R., Kajstura, J., Leri, A., Anversa, P., Ghezzi, P., Salio, M., Cerami, A. & Brines, M., 2003. Recombinant human erythropoietin protects the myocardium from ischemia-reperfusion injury and promotes beneficial remodeling. *Proceedings of the National Academy of Sciences of the United States of America*, 100(8), pp. 4802-4806.

Cao, X., Kwek, K.Y.C., Chan, J.K.Y., Chen, Q.F. & Lim, M., 2014. The hollow fiber bioreactor as a stroma-supported, serum-free ex vivo expansion platform for human umbilical cord blood cells. *Biotechnol. J.*, 9(7), pp. 980-989.

Carola, R., Harley, J.P. & Noback, C.R., 1992. *Human Anatomy*. 3rd ed. New York, USA: McGraw-Hill.

Carpentier, A. & Chachques, J.C., 1985. MYOCARDIAL SUBSTITUTION WITH A STIMULATED SKELETAL-MUSCLE - 1ST SUCCESSFUL CLINICAL CASE. *Lancet*, 1(8440), pp. 1267-1267.

Casado, J.G., Blazquez, R., Jorge, I., Alvarez, V., Gomez-Mauricio, G., Ortega-Munoz, M., Vazquez, J. & Sanchez-Margallo, F.M., 2014. Mesenchymal stem cell-coated sutures enhance collagen depositions in sutured tissues. *Wound Repair and Regeneration,* 22(2), pp. 256-264.

Caspi, O. & Gepstein, L., 2006. Stem cells for myocardial repair. *Eur. Heart J. Suppl.,* 8(E), pp. E43-E54.

Catanzano, O., Acierno, S., Russo, P., Cervasio, M., De Caro, M.D., Bolognese, A., Sammartino, G., Califano, L., Marenzi, G., Calignano, A., Acierno, D. & Quaglia, F., 2014. Melt-spun bioactive sutures containing nanohybrids for local delivery of anti-inflammatory drugs. *Mater. Sci. Eng. C-Mater. Biol. Appl.,* 43, pp. 300-309.

Cebr, 2014. *Cost of cardiovascular disease to hit €122.6 billion by 2020 in six major European economies* [Online]. Centre for Economics and Business Research. Available from: https://www.cebr.com/wp-content/uploads/2015/08/Short-Report-18.08.14.pdf [Accessed 02 September 2016].

Cecen, B., Kozaci, D., Yuksel, M., Erdemli, D., Bagriyanik, A. & Havitcioglu, H., 2015. Biocompatibility of MG-63 cells on collagen, poly-L-lactic acid, hydroxyapatite scaffolds with different parameters. *Journal of Applied Biomaterials & Functional Materials,* 13(1), pp. 10-16.

Ceci-Ginistrelli, E., Pontremoli, C., Pugliese, D., Barbero, N., Boetti, N.G., Barolo, C., Visentin, S. & Milanese, D., 2017. Drug release kinetics from biodegradable UV-transparent hollow calcium-phosphate glass fibers. *Mater. Lett.,* 191, pp. 116-118.

Chen, G.C., Yue, A.H., Ruan, Z.B., Yin, Y.G., Wang, R.Z., Ren, Y. & Zhu, L., 2014. Monitoring the biology stability of human umbilical cord-derived mesenchymal stem cells during long-term culture in serum-free medium. *Cell and Tissue Banking,* 15(4), pp. 513-521.

Chen, Q.Z., Harding, S.E., Ali, N.N., Lyon, A.R. & Boccaccini, A.R., 2008. Biomaterials in cardiac tissue engineering: Ten years of research survey. *Mater. Sci. Eng. R-Rep.,* 59(1-6), pp. 1-37.

Chen, X., Xu, H., Wan, C., McCaigue, M. & Li, G., 2006. Bioreactor expansion of human adult bone marrow-derived mesenchymal stem cells. *Stem Cells,* 24(9), pp. 2052-2059.

Chen, Y., Wang, J.P., Shen, B., Chan, C.W.Y., Wang, C.Y., Zhao, Y.H., Chan, H.N., Tian, Q., Chen, Y.F., Yao, C.L., Hsing, I.M., Li, R.A. & Wu, H.K., 2015. Engineering a Freestanding Biomimetic Cardiac Patch Using Biodegradable Poly(lactic-co-glycolic acid) (PLGA) and Human Embryonic Stem Cell-derived Ventricular Cardiomyocytes (hESC-VCMs). *Macromolecular Bioscience,* 15(3), pp. 426-436.

Cheng, D.L., Cao, X.D., Gao, H.C. & Wang, Y.J., 2013. Superficially porous poly(lactic-co-glycolic acid)/calcium carbonate microsphere developed by spontaneous pore-forming method for bone repair. *RSC Adv.*, 3(19), pp. 6871-6878.

Chilukuri, D., McMaster, O., Bergman, K., Colangelo, P., Snow, K. & Toerner, J.G., 2015. The Hollow Fiber System Model in the Nonclinical Evaluation of Antituberculosis Drug Regimens. *Clin. Infect. Dis.*, 61, pp. S32-S33.

Chin, B.B., Nakamoto, Y., Bulte, J.W.M., Pittenger, M.F., Wahl, R. & Kraitchman, D.L., 2003. In-111 oxine labelled mesenchymal stem cell SPECT after intravenous administration in myocardial infarction. *Nuclear Medicine Communications*, 24(11), pp. 1149-1154.

Choi, Y.S., Matsuda, K., Dusting, G.J., Morrison, W.A. & Dilley, R.J., 2010. Engineering cardiac tissue in vivo from human adipose-derived stem cells. *Biomaterials*, 31(8), pp. 2236-2242.

Chugh, A.R., Beache, G.M., Loughran, J.H., Mewton, N., Elmore, J.B., Kajstura, J., Pappas, P., Tatooles, A., Stoddard, M.F., Lima, J.A.C., Slaughter, M.S., Anversa, P. & Bolli, R., 2012. Administration of Cardiac Stem Cells in Patients With Ischemic Cardiomyopathy: The SCIPIO Trial Surgical Aspects and Interim Analysis of Myocardial Function and Viability by Magnetic Resonance. *Circulation*, 126(11), pp. S54-S64.

Clark, R.A.F., 2001. Fibrin and wound healing. *Fibrinogen*, 936, pp. 355-367.

Cohn, L.H., 2003. Fifty Years of Open-Heart Surgery. *Circulation*, 107(17), pp. 2168-2170.

Comelles, J., Estevez, M., Martinez, E. & Samitier, J., 2010. The role of surface energy of technical polymers in serum protein adsorption and MG-63 cells adhesion. *Nanomedicine-Nanotechnology Biology and Medicine*, 6(1), pp. 44-51.

Consolo, F., Fiore, G.B., Truscello, S., Caronna, M., Morbiducci, U., Montevecchi, F.M. & Redaelli, A., 2009. A Computational Model for the Optimization of Transport Phenomena in a Rotating Hollow-Fiber Bioreactor for Artificial Liver. *Tissue Eng. Part C-Methods*, 15(1), pp. 41-55.

Cooney, C.L., Wang, D.I.C. & Mateles, R.I., 1969. MEASUREMENT OF HEAT EVOLUTION AND CORRELATION WITH OXYGEN CONSUMPTION DURING MICROBIAL GROWTH. *Biotechnol. Bioeng.*, 11(3), pp. 269-&.

Costanzo, L.S., 2007. *Physiology*. Lippincott Williams & Wilkins.

Coulson, J.M. & Richardson, J.F., 1999. *Coulson & Richardson's Chemical Engineering: Fluid flow, heat transfer and mass transfer. Solutions. Volume 1*. 6th ed.: Butterworth-Heinemann.

Covidien, 2016. *DEXON S SUTURE* [Online]. Available from: www.covidien.com/imageServer.aspx?contentID=14356.../pdf [Accessed 05 September 2016].

Crotts, G. & Park, T.G., 1998. Protein delivery from poly(lactic-co-glycolic acid) biodegradable microspheres: release kinetics and stability issues. *Journal of microencapsulation,* 15(6), pp. 699-713.

Cui, L.G., Zhang, N., Cui, W.W., Zhang, P.B. & Chen, X.S., 2015. A Novel Nano/Micro-Fibrous Scaffold by Melt-Spinning Method for Bone Tissue Engineering. *Journal of Bionic Engineering,* 12(1), pp. 117-128.

Culme-Seymour, E., 2012. Cell Therapy and Regenerative Medicine Glossary. *Regenerative Medicine,* 7(3s), pp. S1-S124.

Cutnell, J.D.J., Cutnell, K.W.J.D. & Johnson, K.W., 1995. *Physics.* (0471597732).

Czekanska, E.M., Stoddart, M.J., Richards, R.G. & Hayes, J.S., 2012. IN SEARCH OF AN OSTEOBLAST CELL MODEL FOR IN VITRO RESEARCH. *European Cells & Materials,* 24, pp. 1-17.

Dailey, L.A., Jekel, N., Fink, L., Gessler, T., Schmehl, T., Wittmar, M., Kissel, T. & Seeger, W., 2006. Investigation of the proinflammatory potential of biodegradable nanoparticle drug delivery systems in the lung. *Toxicology and applied pharmacology,* 215(1), pp. 100-8.

David, B., Bonnefont-Rousselot, D., Oudina, K., Degat, M.C., Deschepper, M., Viateau, V., Bensidhoum, M., Oddou, C. & Petite, H., 2011. A Perfusion Bioreactor for Engineering Bone Constructs: An In Vitro and In Vivo Study. *Tissue Eng. Part C-Methods,* 17(5), pp. 505-516.

De Napoli, I.E., Scaglione, S., Giannoni, P., Quarto, R. & Catapano, G., 2011. Mesenchymal stem cell culture in convection-enhanced hollow fibre membrane bioreactors for bone tissue engineering. *J. Membr. Sci.,* 379(1-2), pp. 341-352.

Di Felice, R. & Kehlenbeck, R., 2000. Sedimentation velocity of solids in finite size vessels. *Chem. Eng. Technol.,* 23(12), pp. 1123-1126.

Diaz-Herraez, P., Garbayo, E., Simon-Yarza, T., Formiga, F.R., Prosper, F. & Blanco-Prieto, M.J., 2013. Adipose-derived stem cells combined with Neuregulin-1 delivery systems for heart tissue engineering. *European journal of pharmaceutics and biopharmaceutics : official journal of Arbeitsgemeinschaft fur Pharmazeutische Verfahrenstechnik e.V,* 85(1), pp. 143-50.

Diaz, M.E., Graham, H.K., O'Neill, S.C., Trafford, A.W. & Eisner, D.A., 2005. The control of sarcoplasmic reticulum Ca content in cardiac muscle. *Cell Calcium,* 38(3-4), pp. 391-396.

Dib, N., Michler, R.E., Pagani, F.D., Wright, S., Kereiakes, D.J., Lengerich, R., Binkley, P., Buchele, D., Anand, I., Swingen, C., Di Carli, M.F., Thomas, J.D., Jaber, W.A., Opie, S.R., Campbell, A., McCarthy, P., Yeager, M., Dilsizian, V., Griffith, B.P., Korn, R., Kreuger, S.K., Ghazoul, M., MacLellan, W.R., Fonarow, G., Eisen, H.J., Dinsmore, J. & Diethrich, E., 2005. Safety and feasibility of autologous myoblast transplantation in patients with ischemic cardiomyopathy - Four-year follow-up. *Circulation,* 112(12), pp. 1748-1755.

Diban, N., Haimi, S., Bolhuis-Versteeg, L., Teixeira, S., Miettinen, S., Poot, A., Grijpma, D. & Stamatialis, D., 2013. Hollow fibers of poly(lactide-co-glycolide) and poly(epsilon-caprolactone) blends for vascular tissue engineering applications. *Acta Biomater.,* 9(5), pp. 6450-6458.

Domenech, M., Polo-Corrales, L., Ramirez-Vick, J.E. & Freytes, D.O., 2016. Tissue Engineering Strategies for Myocardial Regeneration: Acellular Versus Cellular Scaffolds? *Tissue Engineering Part B-Reviews,* 22(6), pp. 438-458.

Doran, P.M., 1995. *Bioprocess Engineering Principles.* 1st ed.: Academic Press, The Netherlands.

Edmondson, R., Broglie, J.J., Adcock, A.F. & Yang, L., 2014. Three-dimensional cell culture systems and their applications in drug discovery and cell-based biosensors. *Assay and drug development technologies,* 12(4), pp. 207-218.

Eggermann, J., Kliche, S., Jarmy, G., Hoffmann, K., Mayr-Beyrle, U., Debatin, K.M., Waltenberger, J. & Beltinger, C., 2003. Endothelial progenitor cell culture and differentiation in vitro: a methodological comparison using human umbilical cord blood. *Cardiovasc. Res.,* 58(2), pp. 478-486.

Eggleton, G.P., Eggleton, P. & Hill, A., 1928. The coefficient of diffusion of lactic acid through muscle. *Proceedings of the Royal Society of London. Series B, Containing Papers of a Biological Character,* 103(727), pp. 620-628.

Ellis, M., Jarman-Smith, M. & Chaudhuri, J.B., 2005. Bioreactor Systems for Tissue Engineering: A Four-Dimensional Challenge. In: J. Chaudhuri & M. Al-Rubeai, eds. *Bioreactors for Tissue Engineering.* Springer Netherlands, pp. 1-18.

Ellis, M.J. & Chaudhuri, J.B., 2007. Poly(lactic-co-glycolic acid) hollow fibre membranes for use as a tissue engineering scaffold. *Biotechnol. Bioeng.,* 96(1), pp. 177-187.

Ellis, M.J. & Chaudhuri, J.B., 2008. Human bone derived cell culture on PLGA flat sheet membranes of different lactide : glycolide ratio. *Biotechnol. Bioeng.,* 101(2), pp. 369-377.

Ellis, M.J. & Chaudhuri, J.B., 2011. The relationship between poly(lactide-co-glycolide) monomer ratio, molecular weight and hollow fibre membrane scaffold morphology. *Asia-Pac. J. Chem. Eng.,* 6(6), pp. 832-839.

Elseberg, C.L., Leber, J., Salzig, D., Wallrapp, C., Kassem, M., Kraume, M. & Czermak, P., 2012. Microcarrier-based expansion process for hMSCs with high vitality and undifferentiated characteristics. *Int. J. Artif. Organs*, 35(2), pp. 93-107.

Ethicon, 2014. *Coated VICRYL® (polyglactin 910) Suture* [Online]. Available from: http://www.ethicon.com/healthcare-professionals/products/wound-closure/absorbable-sutures/coated-vicryl-polyglactin-910-suture#!overview [Accessed 05 Sept 2016].

Falanga, V., 2005. Wound healing and its impairment in the diabetic foot. *Lancet*, 366(9498), pp. 1736-43.

Fambri, L., Pegoretti, A., Fenner, R., Incardona, S.D. & Migliaresi, C., 1997. Biodegradable fibres of poly(L-lactic acid) produced by melt spinning. *Polymer*, 38(1), pp. 79-85.

Farahmand, P., Lai, T.Y., Weisel, R.D., Fazel, S., Yau, T., Menasche, P. & Li, R.-K., 2008. Skeletal myoblasts preserve remote matrix architecture and global function when implanted early or late after coronary ligation into infarcted or remote myocardium. *Circulation*, 118(14 suppl 1), pp. S130-S137.

Fashandi, H. & Karimi, M., 2014. Evidence for the Impression of Phase Behavior of Nonsolvent/Solvent/Polymer Ternary System on Morphology of Polyethersulfone Electrospun Nanofibers. *Fibers and Polymers*, 15(7), pp. 1375-1386.

Ferrari, C., Balandras, F., Guedon, E., Olmos, E., Chevalot, I. & Marc, A., 2012. Limiting Cell Aggregation During Mesenchymal Stem Cell Expansion on Microcarriers. *Biotechnol. Prog.*, 28(3), pp. 780-787.

Ferrari, C., Olmos, E., Balandras, F., Tran, N., Chevalot, I., Guedon, E. & Marc, A., 2014. Investigation of Growth Conditions for the Expansion of Porcine Mesenchymal Stem Cells on Microcarriers in Stirred Cultures. *Appl. Biochem. Biotechnol.*, 172(2), pp. 1004-1017.

FiberCell, 2014. *HOLLOW FIBER BIOREACTORS AND RELATED PRODUCTS* [Online]. Available from: http://www.fibercellsystems.com/documents/FiberCellSystemsBrochure.pdf [Accessed 07 March 2014].

Flory, P.J., 1953. *Principles of Polymer Chemistry*. Cornell University Press.

Forte, G., Franzese, O., Pagliari, S., Pagliari, F., Di Francesco, A.M., Cossa, P., Laudisi, A., Fiaccavento, R., Minieri, M., Bonmassar, E. & Di Nardo, P., 2009. Interfacing Sca-1(pos) Mesenchymal Stem Cells with Biocompatible Scaffolds with Different Chemical Composition and Geometry. *Journal of Biomedicine and Biotechnology*.

Francis, M.P., Sachs, P.C., Elmore, L.W. & Holt, S.E., 2010. Isolating adipose-derived mesenchymal stem cells from lipoaspirate blood and saline fraction. *Organogenesis*, 6(1), pp. 11-14.

Freeman, B.T., Kouris, N.A. & Ogle, B.M., 2015. Tracking Fusion of Human Mesenchymal Stem Cells After Transplantation to the Heart. *Stem Cells Translational Medicine,* 4(6), pp. 685-694.

Frith, J.E., Thomson, B. & Genever, P.G., 2010. Dynamic Three-Dimensional Culture Methods Enhance Mesenchymal Stem Cell Properties and Increase Therapeutic Potential. *Tissue Eng. Part C-Methods,* 16(4), pp. 735-749.

Fujimoto, K.L., Ma, Z.W., Nelson, D.M., Hashizume, R., Guan, J.J., Tobita, K. & Wagner, W.R., 2009. Synthesis, characterization and therapeutic efficacy of a biodegradable, thermoresponsive hydrogel designed for application in chronic infarcted myocardium. *Biomaterials,* 30(26), pp. 4357-4368.

Gallegos-Nieto, E., Medellin-Castillo, H.I. & de Lange, D.F., 2015. A complete structural performance analysis and modelling of hydroxyapatite scaffolds with variable porosity. *Computer Methods in Biomechanics and Biomedical Engineering,* 18(11), pp. 1225-1237.

Garg, T., Singh, O., Arora, S. & Murthy, R.S.R., 2012. Scaffold: A Novel Carrier for Cell and Drug Delivery. *Critical Reviews in Therapeutic Drug Carrier Systems,* 29(1), pp. 1-63.

GE-Healthcare, 2015. *ReadyToProcess WAVE 25 Rocker* [Online]. Available from: http://www.gelifesciences.com/webapp/wcs/stores/servlet/catalog/en/GELifeSciences-uk/products/AlternativeProductStructure_23093/28986744 [Accessed 05 September 2016].

Georgiev-Hristov, T., Garcia-Arranz, M., Garcia-Gomez, I., Garcia-Cabezas, M.A., Trebol, J., Vega-Clemente, L., Diaz-Agero, P. & Garcia-Olmo, D., 2012. Sutures enriched with adipose-derived stem cells decrease the local acute inflammation after tracheal anastomosis in a murine model. *European Journal of Cardio-Thoracic Surgery,* 42(3), pp. E40-E47.

Godara, P., McFarland, C.D. & Nordon, R.E., 2008. Design of bioreactors for mesenchymal stem cell tissue engineering. *J. Chem. Technol. Biotechnol.,* 83(4), pp. 408-420.

Gretzer, C., Gisselfalt, K., Liljensten, E., Ryden, L. & Thomsen, P., 2003. Adhesion, apoptosis and cytokine release of human mononuclear cells cultured on degradable poly(urethane urea), polystyrene and titanium in vitro. *Biomaterials,* 24(17), pp. 2843-2852.

Grover, W.H., Bryan, A.K., Diez-Silva, M., Suresh, S., Higgins, J.M. & Manalis, S.R., 2011. Measuring single-cell density. *Proceedings of the National Academy of Sciences,* 108(27), pp. 10992-10996.

Guyette, J.P., Fakharzadeh, M., Burford, E.J., Tao, Z.W., Pins, G.D., Rolle, M.W. & Gaudette, G.R., 2013. A novel suture-based method for efficient transplantation of stem cells. *J. Biomed. Mater. Res. Part A,* 101(3), pp. 809-818.

Gyongyosi, M., Blanco, J., Marian, T., Tron, L., Petnehazy, O., Petrasi, Z., Hemetsberger, R., Rodriguez, J., Font, G., Pavo, I.J., Kertesz, I., Balkay, L., Pavo, N., Posa, A., Emri, M., Galuska, L., Kraitchman, D.L., Wojta, J., Huber, K. & Glogar, D., 2008. Serial Noninvasive In Vivo Positron Emission Tomographic Tracking of Percutaneously Intramyocardially Injected Autologous Porcine Mesenchymal Stem Cells Modified for Transgene Reporter Gene Expression. *Circulation-Cardiovascular Imaging,* 1(2), pp. 94-103.

Hagege, A.A., Marolleau, J.P., Vilquin, J.T., Alheritiere, A., Peyrard, S., Duboc, D., Abergel, E., Messas, E., Mousseaux, E., Schwartz, K., Desnos, M. & Menasche, P., 2006. Skeletal myoblast transplantation in ischemic heart failure - Long-term follow-up of the first phase I cohort of patients. *Circulation,* 114, pp. I108-I113.

Hami, L.S., Green, C., Leshinsky, N., Markham, E., Miller, K. & Craig, S., 2004. GMP production and testing of Xcellerated T Cells (TM) for the treatment of patients with CLL. *Cytotherapy,* 6(6), pp. 554-562.

Hare, J.M., Traverse, J.H., Henry, T.D., Dib, N., Strumpf, R.K., Schulman, S.P., Gerstenblith, G., DeMaria, A.N., Denktas, A.E., Gammon, R.S., Hermiller, J.B., Reisman, M.A., Schaer, G.L. & Sherman, W., 2009. A Randomized, Double-Blind, Placebo-Controlled, Dose-Escalation Study of Intravenous Adult Human Mesenchymal Stem Cells (Prochymal) After Acute Myocardial Infarction. *Journal of the American College of Cardiology,* 54(24), pp. 2277-2286.

Hasan, A., Waters, R., Roula, B., Dana, R., Yara, S., Alexandre, T. & Paul, A., 2016. Engineered Biomaterials to Enhance Stem Cell-Based Cardiac Tissue Engineering and Therapy. *Macromol Biosci,* 16(7), pp. 958-77.

Hasche, E.T., Fernandes, C., Benfreedman, S. & Jeremy, R.W., 1995. RELATION BETWEEN ISCHEMIA TIME, INFARCT SIZE, AND LEFT-VENTRICULAR FUNCTION IN HUMANS. *Circulation,* 92(4), pp. 710-719.

He, Z.L., Sun, Y., Cao, J. & Duan, Y.R., 2016. Degradation behavior and biosafety studies of the mPEG-PLGA-PLL copolymer. *Physical Chemistry Chemical Physics,* 18(17), pp. 11986-11999.

Hegemann, D., Brunner, H. & Oehr, C., 2003. Plasma treatment of polymers for surface and adhesion improvement. *Nuclear Instruments & Methods in Physics Research Section B-Beam Interactions with Materials and Atoms,* 208, pp. 281-286.

Heremans, H., Billiau, A., Cassiman, J.-J., Mulier, J. & De Somer, P., 1978. In vitro cultivation of human tumor tissues II. Morphological and virological characterization of three cell lines. *Oncology,* 35(6), pp. 246-252.

Hill, M.A., 2016. *Cardiovascular System - Heart Histology* [Online]. UNSW Embryology. Available from: https://embryology.med.unsw.edu.au/embryology/index.php/Cardiovascular_System_-_Heart_Histology [Accessed 02 September 2016].

Hirschfelder, J.O.C., C. F.; Bird, R. B.;, 1955. *Molecular theory of gases and liquids.* 1st ed.: Wiley, New York.

Hofmann, M., Wollert, K.C., Meyer, G.P., Menke, A., Arseniev, L., Hertenstein, B., Ganser, A., Knapp, W.H. & Drexler, H., 2005. Monitoring of bone marrow cell homing into the infarcted human myocardium. *Circulation,* 111(17), pp. 2198-2202.

Holm, S., Maroudas, A., Urban, J.P.G., Selstam, G. & Nachemson, A., 1981. NUTRITION OF THE INTERVERTEBRAL-DISK - SOLUTE TRANSPORT AND METABOLISM. *Connect. Tissue Res.,* 8(2), pp. 101-119.

Hou, D.M., Youssef, E.A.S., Brinton, T.J., Zhang, P., Rogers, P., Price, E.T., Yeung, A.C., Johnstone, B.H., Yock, P.G. & March, K.L., 2005. Radiolabeled cell distribution after intramyocardial, intracoronary, and interstitial retrograde coronary venous delivery - Implications for current clinical trials. *Circulation,* 112(9), pp. I150-I156.

Hsieh, P.C.H., Davis, M.E., Lisowski, L.K. & Lee, R.T., 2006. Endothelial-cardiomyocyte interactions in cardiac development and repair. *Annual Review of Physiology.* Palo Alto: Annual Reviews, pp. 51-66.

Huang, X., Wang, W.P., Zheng, Z., Fan, W.L., Mao, C., Shi, J.L. & Li, L., 2016. Surface monofunctionalized polymethyl pentene hollow fiber membranes by plasma treatment and hemocompatibility modification for membrane oxygenators. *Applied Surface Science,* 362, pp. 355-363.

Ilic, D. & Polak, J.M., 2011. Stem cells in regenerative medicine: introduction. *Br. Med. Bull.,* 98(1), pp. 117-126.

Ilyas, A., Islam, M., Asghar, W., Menon, J.U., Wadajkar, A.S., Nguyen, K.T. & Iqbal, S.M., 2013. Salt-Leaching Synthesis of Porous PLGA Nanoparticles. *Ieee Transactions on Nanotechnology,* 12(6), pp. 1082-1088.

Inthanon, K., Daranarong, D., Techaikool, P., Punyodom, W., Khaniyao, V., Bernstein, A.M. & Wongkham, W., 2016. Biocompatibility Assessment of PLCL-Sericin Copolymer Membranes Using Wharton's Jelly Mesenchymal Stem Cells. *Stem Cells International*, p. 16.

Invitrogen, 2015. *Technical Resources - 10566 - DMEM, high glucose, GlutaMAX(TM)* [Online]. Available from: https://www.thermofisher.com/uk/en/home/technical-resources/media-formulation.45.html [Accessed 05 September 2016].

Ishikane, S., Hosoda, H., Yamahara, K., Akitake, Y., Kyoungsook, J., Mishima, K., Iwasaki, K., Fujiwara, M., Miyazato, M., Kangawa, K. & Ikeda, T., 2013. Allogeneic Transplantation of Fetal Membrane-Derived Mesenchymal Stem Cell Sheets Increases Neovascularization and Improves Cardiac Function after Myocardial Infarction in Rats. *Transplantation,* 96(8), pp. 697-706.

Iskandrian, A.S. & Segal, B.L., 1979. STRUCTURE AND FUNCTION OF THE CORONARY-ARTERIES - HOW ARE THEY RELATED. *Catheterization and Cardiovascular Diagnosis,* 5(2), pp. 101-105.

Iwaguro, H. & Asahara, T., 2005. Endothelial Progenitor Cell Culture and Gene Transfer. In: Z. Sun, ed. *Molecular Cardiology.* Humana Press, pp. 239-247.

Jafri, M.S., Dudycha, S.J. & O'Rourke, B., 2001. Cardiac energy metabolism: Models of cellular respiration. *Annual Review of Biomedical Engineering,* 3, pp. 57-81.

Jamnongwong, M., Loubiere, K., Dietrich, N. & Hebrard, G., 2010. Experimental study of oxygen diffusion coefficients in clean water containing salt, glucose or surfactant: Consequences on the liquid-side mass transfer coefficients. *Chemical Engineering Journal,* 165(3), pp. 758-768.

Johnson, M.T., 2010. A numerical scheme to calculate temperature and salinity dependent air-water transfer velocities for any gas. *Ocean Science,* 6(4), pp. 913-932.

Jujo, K., Ii, M. & Losordo, D.W., 2008. Endothelial progenitor cells in neovascularization of infarcted myocardium. *J. Mol. Cell. Cardiol.,* 45(4), pp. 530-544.

Kadi, F., Schjerling, P., Andersen, L.L., Charifi, N., Madsen, J.L., Christensen, L.R. & Andersen, J.L., 2004. The effects of heavy resistance training and detraining on satellite cells in human skeletal muscles. *J. Physiol.-London,* 558(3), pp. 1005-1012.

Kaiser, N.J. & Coulombe, K.L.K., 2015. Physiologically inspired cardiac scaffolds for tailored in vivo function and heart regeneration. *Biomed. Mater.,* 10(3), p. 15.

Kaiser, S.C., Kraume, M., Eibl, D. & Eibl, R., 2015. Single-Use Bioreactors for Animal and Human Cells. In: M. AlRubeai, ed. *Animal Cell Culture.* Cham: Springer Int Publishing Ag, pp. 445-500.

Kang, M.S., Kim, J.H., Singh, R.K., Jang, J.H. & Kim, H.W., 2015. Therapeutic-designed electrospun bone scaffolds: Mesoporous bioactive nanocarriers in hollow fiber composites to sequentially deliver dual growth factors. *Acta Biomater.,* 16, pp. 103-116.

Kanno, S. & Saffitz, J.E., 2001. The role of myocardial gap junctions in electrical conduction and arrhythmogenesis. *Cardiovasc. Pathol.,* 10(4), pp. 169-177.

Kassem, M., 2004. Mesenchymal stem cells: Biological characteristics and potential clinical applications. *Cloning and Stem Cells,* 6(4), pp. 369-374.

Kawamoto, A., Ii, M. & Asahara, T., 2011. *Vascular Regeneration: Endothelial Progenitor Cell Therapy for Ischemic Diseases.* Dordrecht: Springer.

Kellar, R.S., Landeen, L.K., Shepherd, B.R., Naughton, G.K., Ratcliffe, A. & Williams, S.K., 2001. Scaffold-based three-dimensional human fibroblast culture provides a structural matrix that supports angiogenesis in infarcted heart tissue. *Circulation,* 104(17), pp. 2063-2068.

Khang, G., Choee, J.H., Rhee, J.M. & Lee, H.B., 2002. Interaction of different types of cells on physicochemically treated poly(L-lactide-co-glycolide) surfaces. *J. Appl. Polym. Sci.,* 85(6), pp. 1253-1262.

Kim, E.-H. & Heo, C.Y., 2014. Current applications of adipose-derived stem cells and their future perspectives. *World Journal of Stem Cells,* 6(1), pp. 65-68.

Kim, J.H., Park, I.S., Park, Y., Jung, Y., Kim, S.H. & Kim, S.H., 2013. Therapeutic angiogenesis of three-dimensionally cultured adipose-derived stem cells in rat infarcted hearts. *Cytotherapy,* 15(5), pp. 542-556.

Kim, S.H. & Jung, Y., 2015. Bi-layered PLCL/(PLGA/beta-TCP) composite scaffold for osteochondral tissue engineering. *Journal of Bioactive and Compatible Polymers,* 30(2), pp. 178-187.

Kim, T.H., Yun, Y.P., Park, Y.E., Lee, S.H., Yong, W., Kundu, J., Jung, J.W., Shim, J.H., Cho, D.W., Kim, S.E. & Song, H.R., 2014. In vitro and in vivo evaluation of bone formation using solid freeform fabrication-based bone morphogenic protein-2 releasing PCL/PLGA scaffolds. *Biomed. Mater.,* 9(2).

Kim, Y.J., Kim, H.K., Cho, H.H., Bae, Y.C., Suh, K.T. & Jung, J.S., 2007. Direct comparison of human mesenchymal stem cells derived from adipose tissues and bone marrow in mediating neovascularization in response to vascular ischemia. *Cell. Physiol. Biochem.,* 20(6), pp. 867-876.

Klabunde, R.E., 2014. *Oxygen Transport and Diffusion* [Online]. Cardiovascular Physiology Concepts. Available from: http://www.cvphysiology.com/Microcirculation/M002 [Accessed 06 December 2016].

Koh, G.Y., Klug, M.G., Soonpaa, M.H. & Field, L.J., 1993. DIFFERENTIATION AND LONG-TERM SURVIVAL OF C2C12 MYOBLAST GRAFTS IN HEART. *J. Clin. Invest.,* 92(3), pp. 1548-1554.

Kornowski, R., Hong, M.K., Gepstein, L., Goldstein, S., Ellahham, S., Ben-Haim, S.A. & Leon, M.B., 1998. Preliminary animal and clinical experiences using an electromechanical endocardial mapping procedure to distinguish infarcted from healthy myocardium. *Circulation,* 98(11), pp. 1116-1124.

Krok, M. & Pamula, E., 2012. Poly(L-lactide-co-glycolide) microporous membranes for medical applications produced with the use of polyethylene glycol as a pore former. *J. Appl. Polym. Sci.,* 125, pp. E187-E199.

Kuo, Y.C. & Leou, S.N., 2006. Effects of composition, solvent, and salt particles on the physicochemical properties of polyglycolide/poly(lactide-co-glycolide) scaffolds. *Biotechnol. Prog.*, 22(6), pp. 1664-1670.

Kutschka, I., Chen, I.Y., Kofidis, T., Arai, T., von Degenfeld, G., Sheikh, A.Y., Hendry, S.L., Pearl, J., Hoyt, G., Sista, R., Yang, P.C., Blau, H.M., Gambhir, S.S. & Robbins, R.C., 2006. Collagen matrices enhance survival of transplanted cardiomyoblasts and contribute to functional improvement of ischemic rat hearts. *Circulation*, 114, pp. I167-I173.

Kwak, S., Haider, A., Gupta, K.C., Kim, S. & Kang, I.K., 2016. Micro/Nano Multilayered Scaffolds of PLGA and Collagen by Alternately Electrospinning for Bone Tissue Engineering. *Nanoscale Research Letters*, 11, pp. 1-16.

Lakshmanan, R., Krishnan, U. & Sethuraman, S., 2012. Living cardiac patch: the elixir for cardiac regeneration. *Expert opinion on biological therapy*, 12(12), pp. 1623-40.

Lambrechts, T., Papantoniou, I., Rice, B., Schrooten, J., Luyten, F.P. & Aerts, J.M., 2016. Large-scale progenitor cell expansion for multiple donors in a monitored hollow fibre bioreactor. *Cytotherapy*, 18(9), pp. 1219-1233.

Lancaster, J., Juneman, E., Hagerty, T., Do, R., Hicks, M., Meltzer, K., Standley, P., Gaballa, M., Kellar, R., Goldman, S. & Thai, H., 2010. Viable Fibroblast Matrix Patch Induces Angiogenesis and Increases Myocardial Blood Flow in Heart Failure After Myocardial Infarction. *Tissue Eng. Part A*, 16(10), pp. 3065-3073.

Le Blanc, K., 2003. Immunomodulatory effects of fetal and adult mesenchymal stem cells. *Cytotherapy*, 5(6), pp. 485-489.

Lee, G.H., Hwang, J.D., Choi, J.Y., Park, H.J., Cho, J.Y., Kim, K.W., Chae, H.J. & Kim, H.R., 2011. An acidic pH environment increases cell death and pro-inflammatory cytokine release in osteoblasts: The involvement of BAX Inhibitor-1. *Int. J. Biochem. Cell Biol.*, 43(9), pp. 1305-1317.

Lee, K.Y. & Mooney, D.J., 2001. Hydrogels for tissue engineering. *Chem. Rev.*, 101(7), pp. 1869-1879.

Lee, S.J., Choi, J.S., Park, K.S., Khang, G., Lee, Y.M. & Lee, H.B., 2004. Response of MG63 osteoblast-like cells onto polycarbonate membrane surfaces with different micropore sizes. *Biomaterials*, 25(19), pp. 4699-4707.

Lee, Y.S., Joo, W.S., Kim, H.S. & Kim, S.W., 2016. Human Mesenchymal Stem Cell Delivery System Modulates Ischemic Cardiac Remodeling With an Increase of Coronary Artery Blood Flow. *Molecular Therapy*, 24(4), pp. 805-811.

Leger, J.J., Berson, G., Delcayre, C., Klotz, C., Schwartz, K., Leger, J., Stephens, M. & Swynghedauw, B., 1975. HEART CONTRACTILE PROTEINS. *Biochimie,* 57(11-1), pp. 1249-1273.

Lemieux, H. & Hoppel, C.L., 2009. Mitochondria in the human heart. *Journal of Bioenergetics and Biomembranes,* 41(2), pp. 99-106.

Li, D.W., Wu, T., He, N.F., Wang, J., Chen, W.M., He, L.P., Huang, C., Ei-Hamshary, H.A., Al-Deyab, S.S., Ke, Q.F. & Mo, X.M., 2014. Three-dimensional polycaprolactone scaffold via needleless electrospinning promotes cell proliferation and infiltration. *Colloid Surf. B-Biointerfaces,* 121, pp. 432-443.

Li, M.S., Zhao, Z.P., Li, N. & Zhang, Y., 2013a. Controllable modification of polymer membranes by long-distance and dynamic low-temperature plasma flow: Treatment of PE hollow fiber membranes in a module scale. *J. Membr. Sci.,* 427, pp. 431-442.

Li, W., Yao, S.Y., Ma, K.M. & Chen, P., 2013b. Effect of plasma modification on the mechanical properties of carbon fiber/phenolphthalein polyaryletherketone composites. *Polymer Composites,* 34(3), pp. 368-375.

Li, X.Q., Song, K.D. & Liu, T.Q., 2016. *Growth and Metabolism of Bone Marrow Mesenchymal Stem Cells within Collagen Scaffolds in a Novel Bioreactor.* Singapore: World Scientific Publ Co Pte Ltd.

Li, Z.Q. & Guan, J.J., 2011. Hydrogels for Cardiac Tissue Engineering. *Polymers,* 3(2), pp. 740-761.

Liang, H.X., Li, X.D., Shimer, A.L., Balian, G. & Shen, F.H., 2014. A novel strategy of spine defect repair with a degradable bioactive scaffold preloaded with adipose-derived stromal cells. *Spine Journal,* 14(3), pp. 445-454.

Libonati, J.R., Colby, A.M., Caldwell, T.M., Kasparian, R. & Glassberg, H.L., 1999. Systolic and diastolic cardiac function time intervals and exercise capacity in women. *Med. Sci. Sports Exerc.*, 31(2), pp. 258-263.

Lin, Y.C., Leu, S., Sun, C.K., Yen, C.H., Kao, Y.H., Chang, L.T., Tsai, T.H., Chua, S., Fu, M., Ko, S.F., Wu, C.J., Lee, F.Y. & Yip, H.K., 2010. Early combined treatment with sildenafil and adipose-derived mesenchymal stem cells preserves heart function in rat dilated cardiomyopathy. *J. Transl. Med.,* 8.

Linh, N.T.B., Min, Y.K. & Lee, B.T., 2013. Fabrication and in vitro evaluations with osteoblast-like MG-63 cells of porous hyaluronic acid-gelatin blend scaffold for bone tissue engineering applications. *J. Mater. Sci.,* 48(12), pp. 4233-4242.

Litalien, G.J., Kidson, I.G., Megerman, J. & Abbott, W.M., 1979. INVIVO MEASUREMENT OF BLOOD-VESSEL WALL THICKNESS. *American Journal of Physiology*, 237(2), pp. H265-H268.

Liu, Z.M., Lee, S.Y., Sarun, S., Peschel, D. & Groth, T., 2009. Immobilization of poly (ethylene imine) on poly (l-lactide) promotes MG63 cell proliferation and function. *J. Mater. Sci.-Mater. Med.*, 20(11), pp. 2317-2326.

Lonza, 2011. *Poietics human mesenchymal stem cells instructions for use* [Online]. Available from: http://bio.lonza.com/uploads/tx_mwaxmarketingmaterial/Lonza_ManualsProductInstructions_Poietics_Human_Mesenchymal_Stem_Cells.pdf [Accessed 07 September 2016].

Maceira, A.M., Prasad, S.K., Khan, M. & Pennell, D.J., 2006. Normalized left ventricular systolic and diastolic function by steady state free precession cardiovascular magnetic resonance. *J. Cardiov. Magn. Reson.*, 8(3), pp. 417-426.

Makadia, H.K. & Siegel, S.J., 2011. Poly Lactic-co-Glycolic Acid (PLGA) as Biodegradable Controlled Drug Delivery Carrier. *Polymers*, 3(3), pp. 1377-1397.

Makkar, R.R., Smith, R.R., Cheng, K., Malliaras, K., Thomson, L.E.J., Berman, D., Czer, L.S.C., Marban, L., Mendizabal, A., Johnston, P.V., Russell, S.D., Schuleri, K.H., Lardo, A.C., Gerstenblith, G. & Marban, E., 2012. Intracoronary cardiosphere-derived cells for heart regeneration after myocardial infarction (CADUCEUS): a prospective, randomised phase 1 trial. *Lancet*, 379(9819), pp. 895-904.

Marshall, F.-H., 1940. A Method for Obtaining Powders of Uniform Sodium Chloride Crystals in Various Size Ranges, and the Effect of Size upon the Intensity of X-Ray Reflection. *Physical Review*, 58(7), pp. 642-650.

Mason, C. & Dunnill, P., 2007. A brief definition of regenerative medicine. *Regenerative Medicine*, 3(1), pp. 1-5.

Mazzaschi, T.M., D.;, 2015. *Embryonic Stem Cell Research* [Online]. Association of American Medical Colleges. Available from: https://www.aamc.org/advocacy/research/74440/embryonicstemcellresearch.html [Accessed 02 September 2016].

Medorex, 2014. *Fixed-bed bioreactors and fermentors* [Online]. Available from: http://www.medorex.com/flycms/Fixed-bed-fermentors/0731465357.html [Accessed 05 September 2016].

Medtronic, 2016. *Polysorb™ 2mm Soft Tissue Reattachment System* [Online]. Available from: http://www.medtronic.com/covidien/products/sports-surgery/polysorb-2mm-soft-tissue-reattachment-system [Accessed 05 September 2016].

Meissner, P., Schroder, B., Herfurth, C. & Biselli, M., 1999. Development of a fixed bed bioreactor for the expansion of human hematopoietic progenitor cells. *Cytotechnology,* 30(1-3), pp. 227-234.

Menasche, P., 2005. Skeletal myoblast for cell therapy. *Coronary Artery Dis.,* 16(2), pp. 105-110.

Menasché, P., Alfieri, O., Janssens, S., McKenna, W., Reichenspurner, H., Trinquart, L., Vilquin, J.-T., Marolleau, J.-P., Seymour, B. & Larghero, J., 2008. The myoblast autologous grafting in ischemic cardiomyopathy (MAGIC) trial first randomized Placebo-controlled study of myoblast transplantation. *Circulation,* 117(9), pp. 1189-1200.

Menasche, P., Hagege, A.A., Vilquin, J.T., Desnos, M., Abergel, E., Pouzet, B., Bel, A., Sarateanu, S., Scorsin, M., Schwartz, K., Bruneval, P., Benbunan, M., Marolleau, J.P. & Duboc, D., 2003. Autologous skeletal myoblast transplantation for severe postinfarction left ventricular dysfunction. *J. Am. Coll. Cardiol.,* 41(7), pp. 1078-1083.

Meneghello, G., Parker, D.J., Ainsworth, B.J., Perera, S.P., Chaudhuri, J.B., Ellis, M.J. & De Bank, P.A., 2009. Fabrication and characterization of poly(lactic-co-glycolic acid)/polyvinyl alcohol blended hollow fibre membranes for tissue engineering applications. *J. Membr. Sci.,* 344(1-2), pp. 55-61.

Mertaniemi, H., Escobedo-Lucea, C., Sanz-Garcia, A., Gandia, C., Makitie, A., Partanen, J., Ikkala, O. & Yliperttula, M., 2016. Human stem cell decorated nanocellulose threads for biomedical applications. *Biomaterials,* 82, pp. 208-220.

Meuwly, F., Ruffieux, P.A., Kadouri, A. & von Stockar, U., 2007. Packed-bed bioreactors for mammalian cell culture: Bioprocess and biomedical applications. *Biotechnol. Adv.,* 25(1), pp. 45-56.

Miettinen, J.A., Ylitalo, K., Hedberg, P., Jokelainen, J., Kervinen, K., Niemela, M., Saily, M., Koistinen, P., Savolainen, E.R., Ukkonen, H., Pietila, M., Airaksinen, K.E.J., Knuuti, J., Vuolteenaho, O., Makikallio, T.H. & Huikuri, H.V., 2010. Determinants of functional recovery after myocardial infarction of patients treated with bone marrow-derived stem cells after thrombolytic therapy. *Heart,* 96(5), pp. 362-367.

Mikos, A.G., Thorsen, A.J., Czerwonka, L.A., Bao, Y., Langer, R., Winslow, D.N. & Vacanti, J.P., 1994. PREPARATION AND CHARACTERIZATION OF POLY(L-LACTIC ACID) FOAMS. *Polymer,* 35(5), pp. 1068-1077.

Miller, R.A., Brady, J.M. & Cutright, D.E., 1977. DEGRADATION RATES OF ORAL RESORBABLE IMPLANTS (POLYLACTATES AND POLYGLYCOLATES) - RATE MODIFICATION WITH CHANGES IN PLA-PGA COPOLYMER RATIOS. *J. Biomed. Mater. Res.,* 11(5), pp. 711-719.

Mizukami, A., Orellana, M.D., Caruso, S.R., Prata, K.D., Covas, D.T. & Swiech, K., 2013. Efficient expansion of mesenchymal stromal cells in a disposable fixed bed culture system. *Biotechnol. Prog.*, 29(2), pp. 568-572.

Morgan, S.M., Tilley, S., Perera, S., Ellis, M.J., Kanczler, J., Chaudhuri, J.B. & Oreffo, R.O.C., 2007. Expansion of human bone marrow stromal cells on poly-(DL-lactide-co-glycolide) (P(DL)LGA) hollow fibres designed for use in skeletal tissue engineering. *Biomaterials,* 28(35), pp. 5332-5343.

Moschouris, K., Firoozi, N. & Kang, Y.Q., 2016. The application of cell sheet engineering in the vascularization of tissue regeneration. *Regenerative Medicine,* 11(6), pp. 559-570.

Mou, Z.L., Zhao, L.J., Zhang, Q.A., Zhang, J. & Zhang, Z.Q., 2011. Preparation of porous PLGA/HA/collagen scaffolds with supercritical CO2 and application in osteoblast cell culture. *J. Supercrit. Fluids,* 58(3), pp. 398-406.

Mozid, A.M., Arnous, S., Sammut, E.C. & Mathur, A., 2011. Stem cell therapy for heart diseases. *British Medical Bulletin,* 98(1), pp. 143-159.

Mulder, J., 2003. *Basic Principles of Membrane Technology.* 2nd ed. Dordrecht, The Neatherlands: Kluwer Academic Publishers.

Muller-Ehmsen, J., Whittaker, P., Kloner, R.A., Dow, J.S., Sakoda, T., Long, T.I., Laird, P.W. & Kedes, L., 2002. Survival and development of neonatal rat cardiomyocytes transplanted into adult myocardium. *J. Mol. Cell. Cardiol.,* 34(2), pp. 107-116.

Mummery, C.L. & Lee, R.T., 2013. Is heart regeneration on the right track? *Nat. Med.,* 19(4), pp. 412-413.

Munarin, F., Petrini, P., Bozzini, S. & Tanzi, M.C., 2012. New perspectives in cell delivery systems for tissue regeneration: natural-derived injectable hydrogels. *Journal of Applied Biomaterials & Functional Materials,* 10(2), pp. 67-81.

Murphy, M.G., Mailhot, J., Borke, J., Wataha, J., Sharawy, M. & Smith, A., 2001. The effects of rhBMP-2 on human osteosarcoma cells and human gingival fibroblasts in vitro. *Journal of Oral Implantology,* 27(1), pp. 16-24.

Murry, C.E., Soonpaa, M.H., Reinecke, H., Nakajima, H., Nakajima, H.O., Rubart, M., Pasumarthi, K.B.S., Virag, J.I., Bartelmez, S.H., Poppa, V., Bradford, G., Dowell, J.D., Williams, D.A. & Field, L.J., 2004. Haematopoietic stem cells do not transdifferentiate into cardiac myocytes in myocardial infarcts. *Nature,* 428(6983), pp. 664-668.

Mygind, T., Stiehler, M., Baatrup, A., Li, H., Zoua, X., Flyvbjerg, A., Kassem, M. & Bunger, C., 2007. Mesenchymal stem cell ingrowth and differentiation on coralline hydroxyapatite scaffolds. *Biomaterials,* 28(6), pp. 1036-1047.

Naderi, H., Matin, M.M. & Bahrami, A.R., 2011. Review paper: Critical Issues in Tissue Engineering: Biomaterials, Cell Sources, Angiogenesis, and Drug Delivery Systems. *Journal of Biomaterials Applications*, 26(4), pp. 383-417.

Narita, T., Shintani, Y., Ikebe, C., Kaneko, M., Campbell, N.G., Coppen, S.R., Uppal, R., Sawa, Y., Yashiro, K. & Suzuki, K., 2013. The Use of Scaffold-free Cell Sheet Technique to Refine Mesenchymal Stromal Cell-based Therapy for Heart Failure. *Molecular Therapy*, 21(4), pp. 860-867.

NCBI, 2009. *Myocardium* [Online]. National Center for Biotechnology Information. Available from: http://www.ncbi.nlm.nih.gov/mesh/68009206 [Accessed 02 September 2016].

NCBI, 2011. *Muscles* [Online]. National Center for Biotechnology Information. Available from: http://www.ncbi.nlm.nih.gov/mesh/68009132 [Accessed 02 September 2016].

Ndrepepa, G., Mehilli, J., Martinoff, S., Schwaiger, M., Schomig, A. & Kastrati, A., 2007. Evolution of left ventricular ejection fraction and its relationship to infarct size after acute myocardial infarction. *J. Am. Coll. Cardiol.*, 50(2), pp. 149-156.

NHS-England, 2013. *NHS allocations for 2013/14* [Online]. Online. Available from: https://www.england.nhs.uk/allocations-2013-14/ [Accessed 02 September 2016].

Nichols, M.T., N; Luengo-Fernandez, R; Leal, J; Grey, A; Scarborough, P; Rayner, M;, 2012. European Cardiovascular Disease Statistics 2012. *European Society of Cardiology*.

Niebruegge, S., Bauwens, C.L., Peerani, R., Thavandiran, N., Masse, S., Sevaptisidis, E., Nanthakumar, K., Woodhouse, K., Husain, M., Kumacheva, E. & Zandstra, P.W., 2009. Generation of Human Embryonic Stem Cell-Derived Mesoderm and Cardiac Cells Using Size-Specified Aggregates in an Oxygen-Controlled Bioreactor. *Biotechnol. Bioeng.*, 102(2), pp. 493-507.

Nijland, F., Kamp, O., Verhorst, P.M.J., de Voogt, W.G. & Visser, C.A., 2002. Early acute prediction of improvement in ejection fraction after myocardial infarction using low dose dobutamine echocardiography. *Heart*, 88(6), pp. 592-596.

Nogueira, F.B.D., Silva, S.A., Haddad, A.F., Peixoto, C.M., de Carvalho, R.M., Tuche, F.A.A., Soares, V.E., Sousa, A.L.S., Rabischoffsky, A., Mesquita, C.T., Borojevic, R. & Dohmann, H.F.R., 2009. Systolic Function of Patients with Myocardial Infarction Undergoing Autologous Bone Marrow Transplantation. *Arquivos Brasileiros De Cardiologia*, 93(4), pp. 374-379.

Nold, P., Brendel, C., Neubauer, A., Bein, G. & Hackstein, H., 2013. Good manufacturing practice-compliant animal-free expansion of human bone marrow derived mesenchymal stroma cells in a closed hollow-fiber-based bioreactor. *Biochem. Biophys. Res. Commun.*, 430(1), pp. 325-330.

Osiecki, M.J., Michl, T.D., Babur, B.K., Kabiri, M., Atkinson, K., Lott, W.B., Griesser, H.J. & Doran, M.R., 2015. Packed Bed Bioreactor for the Isolation and Expansion of Placental-Derived Mesenchymal Stromal Cells. *PLoS One,* 10(12), p. 18.

Pai, R.K., 2016. *Heart Failure: Compensation by the Heart and Body* [Online]. University of Michigan. Available from: http://www.uofmhealth.org/health-library/aa86963 [Accessed 02 December 2016].

Pamula, E., Filova, E., Bacakova, L., Lisa, V. & Adamczyk, D., 2009. Resorbable polymeric scaffolds for bone tissue engineering: The influence of their microstructure on the growth of human osteoblast-like MG 63 cells. *J. Biomed. Mater. Res. Part A,* 89A(2), pp. 432-443.

Pamula, E., Kokoszka, J., Cholewa-Kowalska, K., Laczka, M., Kantor, L., Niedzwiedzki, L., Reilly, G.C., Filipowska, J., Madej, W., Kolodziejczyk, M., Tylko, G. & Osyczka, A.M., 2011. Degradation, Bioactivity, and Osteogenic Potential of Composites Made of PLGA and Two Different Sol-Gel Bioactive Glasses. *Ann. Biomed. Eng.,* 39(8), pp. 2114-2129.

Park, J.S., Choi, J.B., Jo, S.Y., Lim, Y.M., Gwon, H.J., Khil, M.S. & Nho, Y.C., 2012. Characterization and structure analysis of PLGA/collagen nanofibrous membranes by electrospinning. *J. Appl. Polym. Sci.,* 125, pp. E595-E603.

Pascual-Gil, S., Simon-Yarza, T., Garbayo, E., Prosper, F. & Blanco-Prieto, M.J., 2015. Tracking the in vivo release of bioactive NRG from PLGA and PEG-PLGA microparticles in infarcted hearts. *J. Control. Release,* 220, pp. 388-396.

Pautake, C., SCHIEKER, M., TISCHER, T., KOLK, A., NETH, P., MUTSCHLER, W. & MILZ, S., 2004. Characterization of osteosarcoma cell lines MG-63, Saos-2 and U-2 OS in comparison to human osteoblasts. *Anticancer research,* 24(6), pp. 3743-3748.

Petricca, S.E., Marra, K.G. & Kumta, P.N., 2006. Chemical synthesis of poly(lactic-co-glycolic acid)/hydroxyapatite composites for orthopaedic applications. *Acta Biomater.,* 2(3), pp. 277-286.

Pinzon, N.M., Cook, A.G. & Ju, L.K., 2013. Continuous Rhamnolipid Production Using Denitrifying Pseudomonas aeruginosa Cells in Hollow-Fiber Bioreactor. *Biotechnol. Prog.,* 29(2), pp. 352-358.

Pivsa-Art, W., Pivsa-Art, S., Fujii, K., Nomura, K., Ishimoto, K., Aso, Y., Yamane, H. & Ohara, H., 2015. Compression molding and melt-spinning of the blends of poly(lactic acid) and poly(butylene succinate-co-adipate). *J. Appl. Polym. Sci.,* 132(16), p. 9.

Podporska-Carroll, J., Ip, J.W.Y. & Gogolewski, S., 2014. Biodegradable poly(ester urethane) urea scaffolds for tissue engineering: Interaction with osteoblast-like MG-63 cells. *Acta Biomater.,* 10(6), pp. 2781-2791.

Postema, A.R., Luiten, A.H., Oostra, H. & Pennings, A.J., 1990. HIGH-STRENGTH POLY(L-LACTIDE) FIBERS BY A DRY-SPINNING HOT-DRAWING PROCESS .2. INFLUENCE OF THE EXTRUSION SPEED AND WINDING SPEED ON THE DRY-SPINNING PROCESS. *J. Appl. Polym. Sci.,* 39(6), pp. 1275-1288.

Prabhakaran, M.P., Venugopal, J., Kai, D. & Ramakrishna, S., 2011. Biomimetic material strategies for cardiac tissue engineering. *Mater. Sci. Eng. C-Mater. Biol. Appl.,* 31(3), pp. 503-513.

PromoCell, 2014. *Human Mesenchymal Stem Cells from Adipose Tissue (hMSC-AT)* [Online]. Available from: http://www.promocell.com/index.php?id=540&tx_dqextshop_pi1%5Bselected_country%5D=GBR [Accessed 07 September 2016].

Qiu, L.Y. & Zhu, K.J., 2001. Design of a core-shelled polymer cylinder for potential programmable drug delivery. *International Journal of Pharmaceutics,* 219(1-2), pp. 151-160.

Qu, Z.H. & Ding, J.D., 2013. Physical modification of the interior surfaces of PLGA porous scaffolds using sugar fibers as template. *J. Biomater. Sci.-Polym. Ed.,* 24(4), pp. 447-459.

Quyyumi, A.A., Waller, E.K., Murrow, J., Esteves, F., Galt, J., Oshinski, J., Lerakis, S., Sher, S., Vaughan, D., Perin, E., Willerson, J., Kereiakes, D., Gersh, B.J., Gregory, D., Werner, A., Moss, T., Chan, W.S., Preti, R. & Pecora, A.L., 2011. CD34(+) cell infusion after ST elevation myocardial infarction is associated with improved perfusion and is dose dependent. *American Heart Journal,* 161(1).

Radisic, M. & Christman, K.L., 2013. Materials Science and Tissue Engineering: Repairing the Heart. *Mayo Clinic Proceedings,* 88(8), pp. 884-898.

Rafiq, Q.A., Brosnan, K.M., Coopman, K., Nienow, A.W. & Hewitt, C.J., 2013. Culture of human mesenchymal stem cells on microcarriers in a 5 l stirred-tank bioreactor. *Biotechnol. Lett.,* 35(8), pp. 1233-1245.

Ramanathan, T. & Skinner, H., 2005. Coronary blood flow. *Continuing Education in Anaesthesia, Critical Care & Pain,* 5(2), pp. 61-64.

Ranjbar-Mohammadi, M., Zamani, M., Prabhakaran, M.P., Bahrami, S.H. & Ramakrishna, S., 2016. Electrospinning of PLGA/gum tragacanth nanofibers containing tetracycline hydrochloride for periodontal regeneration. *Mater. Sci. Eng. C-Mater. Biol. Appl.,* 58, pp. 521-531.

Rauh, J., Milan, F., Gunther, K.P. & Stiehler, M., 2011. Bioreactor Systems for Bone Tissue Engineering. *Tissue Engineering Part B-Reviews,* 17(4), pp. 263-280.

Reckhenrich, A.K., Kirsch, B.M., Wahl, E.A., Schenck, T.L., Rezaeian, F., Harder, Y., Foehr, P., Machens, H.G. & Egana, J.T., 2014. Surgical Sutures Filled with Adipose-Derived Stem Cells Promote Wound Healing. *PLoS One,* 9(3), p. 10.

Reinecke, H. & Murry, C.E., 2000. Transmural replacement of myocardium after skeletal myoblast grafting into the heart: Too much of a good thing? *Cardiovasc. Pathol.,* 9(6), pp. 337-344.

Reinecke, H., Zhang, M., Bartosek, T. & Murry, C.E., 1999. Survival, integration, and differentiation of cardiomyocyte grafts - A study in normal and injured rat hearts. *Circulation,* 100(2), pp. 193-202.

Richardson, J.F., Harker, J.H. & Backhurst, J.R., 2002. *Chemical Engineering.* 5th ed. Oxford, UK: Elsevier Science.

Richardson, J.F. & Zaki, W.N., 1997. Sedimentation and fluidisation: part 1. *Chem. Eng. Res. Des.,* 75, pp. S82-S99.

Roberts, I., Baila, S., Rice, R.B., Janssens, M.E., Nguyen, K., Moens, N., Ruban, L., Hernandez, D., Coffey, P. & Mason, C., 2012. Scale-up of human embryonic stem cell culture using a hollow fibre bioreactor. *Biotechnol. Lett.,* 34(12), pp. 2307-2315.

Rodrigues, C.A.V., Fernandes, T.G., Diogo, M.M., da Silva, C.L. & Cabral, J.M.S., 2011. Stem cell cultivation in bioreactors. *Biotechnol. Adv.,* 29(6), pp. 815-829.

Roels, J.A., 1980. APPLICATION OF MACROSCOPIC PRINCIPLES TO MICROBIAL-METABOLISM. *Biotechnol. Bioeng.,* 22(12), pp. 2457-2514.

Rojewski, M.T., Fekete, N., Baila, S., Nguyen, K., Furst, D., Antwiler, D., Dausend, J., Kreja, L., Ignatius, A., Sensebe, L. & Schrezenmeier, H., 2013. GMP-Compliant Isolation and Expansion of Bone Marrow-Derived MSCs in the Closed, Automated Device Quantum Cell Expansion System. *Cell Transplant.,* 22(11), pp. 1981-2000.

Roncalli, J., Mouquet, F., Piot, C., Trochu, J.N., Le Corvoisier, P., Neuder, Y., Le Tourneau, T., Agostini, D., Gaxotte, V., Sportouch, C., Galinier, M., Crochet, D., Teiger, E., Richard, M.J., Polge, A.S., Beregi, J.P., Manrique, A., Carrie, D., Susen, S., Klein, B., Parini, A., Lamirault, G., Croisille, P., Rouard, H., Bourin, P., Nguyen, J.M., Delasalle, B., Vanzetto, G., Van Belle, E. & Lemarchand, P., 2011. Intracoronary autologous mononucleated bone marrow cell infusion for acute myocardial infarction: results of the randomized multicenter BONAMI trial. *European Heart Journal,* 32(14), pp. 1748-1757.

Rosland, G.V., Svendsen, A., Torsvik, A., Sobala, E., McCormack, E., Immervoll, H., Mysliwietz, J., Tonn, J.C., Goldbrunner, R., Lonning, P.E., Bjerkvig, R. & Schichor, C., 2009. Long-term Cultures of Bone Marrow-Derived Human Mesenchymal Stem Cells Frequently Undergo Spontaneous Malignant Transformation (This article contains errors due to a cross contamination of the cell lines we used. To correct this issue we published a letter in Cancer Res. 2010 Aug 1,70(15),6393-6). *Cancer Research,* 69(13), pp. 5331-5339.

Rota, M., Padin-Iruegas, M.E., Misao, Y., De Angelis, A., Maestroni, S., Ferreira-Martins, J., Fiumana, E., Rastaldo, R., Arcarese, M.L. & Mitchell, T.S., 2008. Local activation or implantation of cardiac progenitor cells rescues scarred infarcted myocardium improving cardiac function. *Circulation research,* 103(1), pp. 107-116.

RSC, 2011. *Respiration* [Online]. Royal Society of Chemistry. Available from: http://www.rsc.org/Education/Teachers/Resources/cfb/respiration.htm [Accessed 05 September 2016].

Rubart, M., Soonpaa, M.H., Nakajima, H. & Field, L.J., 2004. Spontaneous and evoked intracellular calcium transients in donor-derived myocytes following intracardiac myoblast transplantation. *J. Clin. Invest.,* 114(6), pp. 775-783.

Rufaihah, A.J. & Seliktar, D., 2016. Hydrogels for therapeutic cardiovascular angiogenesis. *Adv. Drug Deliv. Rev.,* 96, pp. 31-39.

Rungarunlert, S., Klincumhom, N., Bock, I., Nemes, C., Techakumphu, M., Pirity, M.K. & Dinnyes, A., 2011. Enhanced cardiac differentiation of mouse embryonic stem cells by use of the slow-turning, lateral vessel (STLV) bioreactor. *Biotechnol. Lett.,* 33(8), pp. 1565-1573.

Rutledge, K., Cheng, Q.S., Pryzhkova, M., Harris, G.M. & Jabbarzadeh, E., 2014. Enhanced Differentiation of Human Embryonic Stem Cells on Extracellular Matrix-Containing Osteomimetic Scaffolds for Bone Tissue Engineering. *Tissue Eng. Part C-Methods,* 20(11), pp. 865-874.

Salem, R., Denault, A.Y., Couture, P., Belisle, S., Fortier, A., Guertin, M.C., Carrier, M. & Martineau, R., 2006. Left ventricular end-diastolic pressure is a predictor of mortality in cardiac surgery independently of left ventricular ejection fraction. *Br. J. Anaesth.,* 97(3), pp. 292-297.

Salerno, A., Zeppetelli, S., Oliviero, M., Battista, E., Di Maio, E., Iannace, S. & Netti, P.A., 2012. Microstructure, degradation and in vitro MG63 cells interactions of a new poly(epsilon-caprolactone), zein, and hydroxyapatite composite for bone tissue engineering. *Journal of Bioactive and Compatible Polymers,* 27(3), pp. 210-226.

Sander, R., 1999. *Compilation of Henry's Law Constants for Inorganic and Organic Species of Potential Importance in Environmental Chemistry* [Online]. Max-Planck Institute of Chemistry. Available from: http://www.henrys-law.org/henry-3.0.pdf [Accessed 05 September 2016].

Sanganalmath, S.K. & Bolli, R., 2013. Cell therapy for heart failure a comprehensive overview of experimental and clinical studies, current challenges, and future directions. *Circulation research,* 113(6), pp. 810-834.

Schaffer, D., Bronzino, J.D. & Peterson, D.R., 2012. *Stem Cell Engineering: Principles and Practices.* CRC Press.

Schenke-Layland, K., Strem, B.M., Jordan, M.C., DeEmedio, M.T., Hedrick, M.H., Roos, K.P., Fraser, J.K. & MacLellan, W.R., 2009. Adipose Tissue-Derived Cells Improve Cardiac Function Following Myocardial Infarction. *J. Surg. Res.*, 153(2), pp. 217-223.

Schmuck, E.G., Mulligan, J.D., Ertel, R.L., Kouris, N.A., Ogle, B.M., Raval, A.N. & Saupe, K.W., 2014. Cardiac Fibroblast-Derived 3D Extracellular Matrix Seeded with Mesenchymal Stem Cells as a Novel Device to Transfer Cells to the Ischemic Myocardium. *Cardiovascular Engineering and Technology*, 5(1), pp. 119-131.

Schots, R., De Keulenaer, G., Schoors, D., Caveliers, V., Dujardin, M., Verheye, S., Van Camp, G., Franken, P.R., Roland, J., Van Riet, I. & Everaert, H., 2007. Evidence that intracoronary-injected CD133(+) peripheral blood progenitor cells home to the myocardium in chronic postinfarction heart failure. *Experimental Hematology*, 35(12), pp. 1884-1890.

Schuleri, K.H., Feigenbaum, G.S., Centola, M., Weiss, E.S., Zimmet, J.M., Turney, J., Kellner, J., Zviman, M.M., Hatzistergos, K.E. & Detrick, B., 2009. Autologous mesenchymal stem cells produce reverse remodelling in chronic ischaemic cardiomyopathy. *European heart journal*, p. ehp265.

Scorsin, M., Hagege, A., Vilquin, J.T., Fiszman, M., Marotte, F., Samuel, J.L., Rappaport, L., Schwartz, K. & Menasche, P., 2000. Comparison of the effects of fetal cardiomyocyte and skeletal myoblast transplantation on postinfarction left ventricular function. *J. Thorac. Cardiovasc. Surg.*, 119(6), pp. 1169-1175.

Searcey, D.S., C;, 2014. *Inside the Private Umbilical Cord Blood Banking Business* [Online]. Wall Street Journal. Available from: http://www.wsj.com/articles/SB10001424052702303887804579501500366071342 [Accessed 02 September 2016].

Seeley, R.R., Tate, P. & Stephens, T.D., 2000. *Anatomy and Physiology.* New York, USA: McGraw-Hill Companies.

Sheng, C.C., Zhou, L. & Hao, J.J., 2013. Current Stem Cell Delivery Methods for Myocardial Repair. *Biomed Research International*.

Shier, D., Butler, J. & Lewis, R., 1996. *Hole's Human Anatomy.* McGraw-Hill.

Shim, W., Mehta, A., Wong, P., Chua, T. & Koh, T.H., 2013. Critical path in cardiac stem cell therapy: an update on cell delivery. *Cytotherapy*, 15(4), pp. 399-415.

Shipley, R.J., Davidson, A.J., Chan, K., Chaudhuri, J.B., Waters, S.L. & Ellis, M.J., 2011. A Strategy to Determine Operating Parameters in Tissue Engineering Hollow Fiber Bioreactors. *Biotechnol. Bioeng.*, 108(6), pp. 1450-1461.

Shipley, R.J. & Waters, S.L., 2012. Fluid and mass transport modelling to drive the design of cell-packed hollow fibre bioreactors for tissue engineering applications. *Math. Med. Biol.*, 29(4), pp. 329-359.

Shipley, R.J., Waters, S.L. & Ellis, M.J., 2010. Definition and Validation of Operating Equations for Poly(Vinyl Alcohol)-Poly(Lactide-Co-Glycolide) Microfiltration Membrane-Scaffold Bioreactors. *Biotechnol. Bioeng.*, 107(2), pp. 382-392.

Shuman, J.A., Zurcher, J.R., Sapp, A.A., Burdick, J.A., Gorman, R.C., Gorman, J.H., Goldsmith, E.C. & Spinale, F.G., 2013. Localized targeting of biomaterials following myocardial infarction: A foundation to build on. *Trends in Cardiovascular Medicine*, 23(8), pp. 301-311.

Sidney, L.E., Heathman, T.R.J., Britchford, E.R., Abed, A., Rahman, C.V. & Buttery, L.D.K., 2015. Investigation of Localized Delivery of Diclofenac Sodium from Poly(D,L-Lactic Acid-co-Glycolic Acid)/Poly(Ethylene Glycol) Scaffolds Using an In Vitro Osteoblast Inflammation Model. *Tissue Eng. Part A*, 21(1-2), pp. 362-373.

Siepe, M., Giraud, M.N., Liljensten, E., Nydegger, U., Menasche, P., Carrel, T. & Tevaearai, H.T., 2007. Construction of skeletal myoblast-based polyurethane scaffolds for myocardial repair. *Artificial Organs*, 31(6), pp. 425-433.

SigmaAldrich, 2013. *MG-63 Cell Line human* [Online]. Available from: http://www.sigmaaldrich.com/catalog/product/sigma/86051601?lang=en&region=GB [Accessed 07 September 2016].

Sikavitsas, V.I., Bancroft, G.N. & Mikos, A.G., 2002. Formation of three-dimensional cell/polymer constructs for bone tissue engineering in a spinner flask and a rotating wall vessel bioreactor. *J. Biomed. Mater. Res.*, 62(1), pp. 136-148.

Siminiak, T., Fiszer, D., Jerzykowska, O., Grygielska, B., Rozwadowska, N., Kalmucki, P. & Kurpisz, M., 2005. Percutaneous trans-coronary-venous transplantation of autologous skeletal myoblasts in the treatment of post-infarction myocardial contractility impairment: the POZNAN trials. *European Heart Journal*, 26(12), pp. 1188-1195.

Simon-Yarza, T., Formiga, F.R., Tamayo, E., Pelacho, B., Prosper, F. & Blanco-Prieto, M.J., 2013. PEGylated-PLGA microparticles containing VEGF for long term drug delivery. *International Journal of Pharmaceutics*, 440(1), pp. 13-18.

Sjoblom, J., Muhrbeck, J., Witt, N., Alam, M. & Frykman-Kull, V., 2014. Evolution of Left Ventricular Ejection Fraction After Acute Myocardial Infarction Implications for Implantable Cardioverter-Defibrillator Eligibility. *Circulation*, 130(9), pp. 743-748.

Skindersoe, M.E., Krogfelt, K.A., Blom, A., Jiang, G.W., Prestwich, G.D. & Mansell, J.P., 2015. Dual Action of Lysophosphatidate-Functionalised Titanium: Interactions with Human

(MG63) Osteoblasts and Methicillin Resistant Staphylococcus aureus. *PLoS One,* 10(11), p. 17.

Smadja, D.M., Cornet, A., Emmerich, J., Aiach, M. & Gaussem, P., 2007. Endothelial progenitor cells: Characterization, in vitro expansion, and prospects for autologous cell therapy. *Cell Biol. Toxicol.,* 23(4), pp. 223-239.

SMI, 2010. *Surgicryl ® PGA Polyglycolic acid* [Online]. Available from: http://www.sutures.be/sutures/01_foil_packs/01_absorbable/polyglycolic.html [Accessed 05 September 2016].

Somerville, R.P.T., Devillier, L., Parkhurst, M.R., Rosenberg, S.A. & Dudley, M.E., 2012. Clinical scale rapid expansion of lymphocytes for adoptive cell transfer therapy in the WAVE (R) bioreactor. *J. Transl. Med.,* 10, p. 11.

Son, S.R., Linh, N.T.B., Yang, H.M. & Lee, B.T., 2013. In vitro and in vivo evaluation of electrospun PCL/PMMA fibrous scaffolds for bone regeneration. *Sci. Technol. Adv. Mater.,* 14(1).

Song, K.D., Liu, Y., Wang, H., Liu, T.Q., Fang, M.Y., Shi, F.X., Macedo, H.M., Ma, X.H. & Cui, Z.F., 2011. Ex Vivo Expansion of Human Umbilical Cord Blood Hematopoietic Stem/Progenitor Cells with Support of Microencapsulated Rabbit Mesenchymal Stem Cells in a Rotating Bioreactor. *Tissue Eng. Regen. Med.,* 8(3), pp. 334-345.

Soonpaa, M.H., Koh, G.Y., Klug, M.G. & Field, L.J., 1994. FORMATION OF NASCENT INTERCALATED DISKS BETWEEN GRAFTED FETAL CARDIOMYOCYTES AND HOST MYOCARDIUM. *Science,* 264(5155), pp. 98-101.

Spectrum-Labs, 2012. *CELLMAX® Hollow Fiber Cell Culture System* [Online]. Available from: https://webshop.fishersci.com/webfiles/uk/web-docs/CELLMAX.PDF [Accessed 07 March 2014].

Stankova, L., Fraczek-Szczypta, A., Blazewicz, M., Filova, E., Blazewicz, S., Lisa, V. & Bacakova, L., 2014. Human osteoblast-like MG 63 cells on polysulfone modified with carbon nanotubes or carbon nanohorns. *Carbon,* 67, pp. 578-591.

Storm, M.P., Sorrell, I., Shipley, R., Regan, S., Luetchford, K.A., Sathish, J., Webb, S. & Ellis, M.J., 2016. Hollow Fiber Bioreactors for In Vivo-like Mammalian Tissue Culture. *J. Vis. Exp.,* (111), p. 12.

Stubbe, B.G., De Smedt, S.C. & Demeester, J., 2004. "Programmed polymeric devices" for pulsed drug delivery. *Pharm. Res.,* 21(10), pp. 1732-1740.

Su, J.C., Wang, Z.W., Yan, Y.G., Wu, Y.F., Cao, L.H., Ma, Y.H., Yu, B.Q. & Li, M., 2010. Nanoporous Calcium Silicate and PLGA Biocomposite for Bone Repair. *J. Nanomater.*

Synthecon, 2015. *AUTOCLAVABLE SLOW TURNING LATERAL VESSELS (STLVS)* [Online]. Available from: http://synthecon.com/pages/synthecon_autoclavable_slow_turning_lateral_vessels_28.asp [Accessed 05 September 2016].

Tandon, N. & Joachim, M., Super Cells: Building with Biology. In: London: TED Conferences, 2014.

Tang, X.-L., Rokosh, G., Sanganalmath, S.K., Yuan, F., Sato, H., Mu, J., Dai, S., Li, C., Chen, N. & Peng, Y., 2010. Intracoronary administration of cardiac progenitor cells alleviates left ventricular dysfunction in rats with a 30-day-old infarction. *Circulation*, 121(2), pp. 293-305.

Tao, C.T. & Young, T.H., 2006. Polyetherimide membrane formation by the cononsolvent system and its biocompatibility of MG63 cell line. *J. Membr. Sci.*, 269(1-2), pp. 66-74.

Tao, Z.-W., Favreau, J.T., Guyette, J.P., Hansen, K.J., Lessard, J., Burford, E., Pins, G.D. & Gaudette, G.R., 2014. Delivering stem cells to the healthy heart on biological sutures: effects on regional mechanical function. *J. Tissue Eng. Regen. Med.*, pp. n/a-n/a.

Tapia, F., Vogel, T., Genzel, Y., Behrendt, I., Hirschel, M., Gangemi, J.D. & Reichl, U., 2014. Production of high-titer human influenza A virus with adherent and suspension MDCK cells cultured in a single-use hollow fiber bioreactor. *Vaccine*, 32(8), pp. 1003-1011.

Techne, 2012. *Cell Culture System - Biological Stirrers and Culture Vessels* [Online]. Available from: http://www.techne.com/adminimages/Cell_culture_Vesssels.pdf [Accessed 07 September 2016].

Terumo-BCT, 2012. *Quantum® Cell Expansion System* [Online]. Available from: https://www.terumobct.com/location/emea/products-and-services/Pages/Quantum-Cell-Expansion-System.aspx [Accessed 05 September 2016].

Thai, H.M., Juneman, E., Lancaster, J., Hagerty, T., Do, R., Castellano, L., Kellar, R., Williams, S., Sethi, G., Schmelz, M., Gaballa, M. & Goldman, S., 2009. Implantation of a Three-Dimensional Fibroblast Matrix Improves Left Ventricular Function and Blood Flow After Acute Myocardial Infarction. *Cell Transplant.*, 18(3), pp. 283-295.

ThermoFisher, 2015. *StemPro® Human Adipose-Derived Stem Cells* [Online]. Available from: https://www.thermofisher.com/order/catalog/product/R7788115?ICID=search-product [Accessed 07 September 2016].

Thomson, J.A., Itskovitz-Eldor, J., Shapiro, S.S., Waknitz, M.A., Swiergiel, J.J., Marshall, V.S. & Jones, J.M., 1998. Embryonic stem cell lines derived from human blastocysts. *Science*, 282(5391), pp. 1145-1147.

Timmins, N.E., Kiel, M., Gunther, M., Heazlewood, C., Doran, M.R., Brooke, G. & Atkinson, K., 2012. Closed system isolation and scalable expansion of human placental mesenchymal stem cells. *Biotechnol. Bioeng.,* 109(7), pp. 1817-1826.

Timmins, N.E., Palfreyman, E., Marturana, F., Dietmair, S., Luikenga, S., Lopez, G., Fung, Y.L., Minchinton, R. & Nielsen, L.K., 2009. Clinical Scale Ex Vivo Manufacture of Neutrophils From Hematopoietic Progenitor Cells. *Biotechnol. Bioeng.,* 104(4), pp. 832-840.

Tomanek, R.J. & Runyan, R.B., 2012. *Formation of the Heart and its Regulation.* Birkhäuser Boston.

Tous, E., Ifkovits, J.L., Koomalsingh, K.J., Shuto, T., Soeda, T., Kondo, N., Gorman, J.H., Gorman, R.C. & Burdick, J.A., 2011. Influence of Injectable Hyaluronic Acid Hydrogel Degradation Behavior on Infarction-Induced Ventricular Remodeling. *Biomacromolecules,* 12(11), pp. 4127-4135.

Tran, R.T., Naseri, E., Kolasnikov, A., Bai, X.C. & Yang, J., 2011. A new generation of sodium chloride porogen for tissue engineering. *Biotechnol. Appl. Biochem.,* 58(5), pp. 335-344.

Tsai, A.C., Liu, Y.J. & Ma, T., 2016. Expansion of human mesenchymal stem cells in fibrous bed bioreactor. *Biochemical Engineering Journal,* 108, pp. 51-57.

Urbich, C. & Dimmeler, S., 2004. Endothelial progenitor cells - Characterization and role in vascular biology. *Circulation Research,* 95(4), pp. 343-353.

Van Beekvelt, M.C., Colier, W.N., Wevers, R.A. & Van Engelen, B.G., 2001. Performance of near-infrared spectroscopy in measuring local O(2) consumption and blood flow in skeletal muscle. *Journal of applied physiology (Bethesda, Md. : 1985),* 90(2), pp. 511-9.

van der Bogt, K.E.A., Schrepfer, S., Yu, J., Sheikh, A.Y., Hoyt, G., Govaert, J.A., Velotta, J.B., Contag, C.H., Robbins, R.C. & Wu, J.C., 2009. Comparison of Transplantation of Adipose Tissue- and Bone Marrow-Derived Mesenchymal Stem Cells in the Infarcted Heart. *Transplantation,* 87(5), pp. 642-652.

Vandrovcova, M., Douglas, T., Hauk, D., Grossner-Schreiber, B., Wiltfang, J., Bacakova, L. & Warnke, P.H., 2011. Influence of Collagen and Chondroitin Sulfate (CS) Coatings on Poly-(Lactide-co-Glycolide) (PLGA) on MG 63 Osteoblast-Like Cells. *Physiol. Res.,* 60(5), pp. 797-813.

Volpe, B.B., Duarte, A.D.S., Ribeiro, T.B., Stocchero, I., Kharmandayan, P., Saad, S.T.O., Bustorff-Silva, J.M. & Luzo, A.C.M., 2014. Mesenchymal stromal cells from adipose tissue attached to suture material enhance the closure of enterocutaneous fistulas in a rat model. *Cytotherapy,* 16(12), pp. 1709-1719.

Walker, C.A. & Spinale, F.G., 1999. THE STRUCTURE AND FUNCTION OF THE CARDIAC MYOCYTE: A REVIEW OF FUNDAMENTAL CONCEPTS. *J Thorac Cardiovasc Surg,* 118(2), pp. 375-382.

Wang, B., Cai, Q., Zhang, S., Yang, X.P. & Deng, X.L., 2011a. The effect of poly (L-lactic acid) nanofiber orientation on osteogenic responses of human osteoblast-like MG63 cells. *Journal of the Mechanical Behavior of Biomedical Materials,* 4(4), pp. 600-609.

Wang, L., Shi, J., Liu, L., Secret, E. & Chen, Y., 2011b. Fabrication of polymer fiber scaffolds by centrifugal spinning for cell culture studies. *Microelectronic Engineering,* 88(8), pp. 1718-1721.

Wang, M.C., Ma, L., Li, D. & Gao, C.Y., 2013. Polycaprolactone scaffolds or anisotropic particles: The initial solution temperature dependence in a gelatin particle-leaching method. *Polymer,* 54(1), pp. 277-283.

Wang, T.W., Wu, H.C., Wang, H.Y., Lin, F.H. & Sun, J.S., 2009. Regulation of adult human mesenchymal stem cells into osteogenic and chondrogenic lineages by different bioreactor systems. *J. Biomed. Mater. Res. Part A,* 88A(4), pp. 935-946.

Wang, Y.L., Dai, J.J., Chang, X.Y., Yang, M.Y., Shen, R.F., Shan, L., Qian, Y. & Gao, C.S., 2015. Model Drug as Pore Former for Controlled Release of Water-Soluble Metoprolol Succinate from Ethylcellulose-Coated Pellets Without Lag Phase: Opportunities and Challenges. *Aaps Pharmscitech,* 16(1), pp. 35-44.

Warnock, J.N., Bratch, K. & Al-Rubeai, M., 2005. Packed Bed Bioreactors. In: J. Chaudhuri & M. Al-Rubeai, eds. *Bioreactors for Tissue Engineering: Principles, Design and Operation.* Dordrecht: Springer Netherlands, pp. 87-113.

Weber, C., Freimark, D., Portner, R., Pino-Grace, P., Pohl, S., Wallrapp, C., Geigle, P. & Czermak, P., 2010. Expansion of human mesenchymal stem cells in a fixed-bed bioreactor system based on non-porous glass carrier - Part A: Inoculation, cultivation, and cell harvest procedures. *Int. J. Artif. Organs,* 33(8), pp. 512-525.

Wei, Z.M., Zhang, Q.C., Peng, M.L., Wang, X.J., Long, S.R. & Yang, J., 2014. Preparation and drug delivery study of electrospun hollow PES ultrafine fibers with a multilayer wall. *Colloid and Polymer Science,* 292(6), pp. 1339-1345.

Wen, X.J. & Tresco, P.A., 2006. Fabrication and characterization of permeable degradable poly(DL-lactide-co-glycolide) (PLGA) hollow fiber phase inversion membranes for use as nerve tract guidance channels. *Biomaterials,* 27(20), pp. 3800-3809.

Werner, L., Deutsch, V., Barshack, I., Miller, H., Keren, G. & George, J., 2005. Transfer of endothelial progenitor cells improves myocardial performance in rats with dilated cardiomyopathy induced following experimental myocarditis. *J. Mol. Cell. Cardiol.,* 39(4), pp. 691-697.

Widmaier, E.P., Raff, H. & Strang, K.T., 2006. *Vander's Human Physiology: The Mechanisms of Body Function.* 10th ed. New York, USA: McGraw-Hill Higher Education.

Wiedeman, M.P., 1963. DIMENSIONS OF BLOOD VESSELS FROM DISTRIBUTING ARTERY TO COLLECTING VEIN. *Circulation Research,* 12(4), pp. 375-&.

Williams, A.R., Hatzistergos, K.E., Addicott, B., McCall, F., Carvalho, D., Suncion, V., Morales, A.R., Da Silva, J., Sussman, M.A., Heldman, A.W. & Hare, J.M., 2013. Enhanced Effect of Combining Human Cardiac Stem Cells and Bone Marrow Mesenchymal Stem Cells to Reduce Infarct Size and to Restore Cardiac Function After Myocardial Infarction. *Circulation,* 127(2), pp. 213-223.

Wojak-Cwik, I.M., Hintze, V., Schnabelrauch, M., Moeller, S., Dobrzynski, P., Pamula, E. & Scharnweber, D., 2013. Poly(L-lactide-co-glycolide) scaffolds coated with collagen and glycosaminoglycans: Impact on proliferation and osteogenic differentiation of human mesenchymal stem cells. *J. Biomed. Mater. Res. Part A,* 101(11), pp. 3109-3122.

Wu, J., Zeng, F.Q., Huang, X.P., Chung, J.C.Y., Konecny, F., Weisel, R.D. & Li, R.K., 2011. Infarct stabilization and cardiac repair with a VEGF-conjugated, injectable hydrogel. *Biomaterials,* 32(2), pp. 579-586.

Wu, J., Zhang, X.-h., Li, X.-l. & Yang, L., 2016. Adipose tissue volume differences around the heart between subjects without coronary atherosclerosis and coronary heart disease patients. *Acta cardiologica,* 71(3), p. 291.

Wu, K.H., Han, Z.C., Mo, X.M. & Zhou, B., 2012. Cell delivery in cardiac regenerative therapy. *Ageing Research Reviews,* 11(1), pp. 32-40.

Wung, N., Acott, S.M., Tosh, D. & Ellis, M.J., 2014. Hollow fibre membrane bioreactors for tissue engineering applications. *Biotechnol. Lett.,* 36(12), pp. 2357-2366.

Xie, S.J., Zhu, Q., Wang, B., Gu, H.J., Liu, W., Cui, L., Cen, L.A. & Cao, Y.L., 2010. Incorporation of tripolyphosphate nanoparticles into fibrous poly(lactide-co-glycolide) scaffolds for tissue engineering. *Biomaterials,* 31(19), pp. 5100-5109.

Xin, M., Olson, E.N. & Bassel-Duby, R., 2013. Mending broken hearts: cardiac development as a basis for adult heart regeneration and repair. *Nature Reviews Molecular Cell Biology,* 14(8), pp. 529-541.

Xin, X., Liu, Q.Q., Chen, C.X., Guan, Y.X. & Yao, S.J., 2016. Fabrication of bimodal porous PLGA scaffolds by supercritical CO2 foaming/particle leaching technique. *J. Appl. Polym. Sci.,* 33(27), p. 9.

Xu, C.Y., Inai, R., Kotaki, M. & Ramakrishna, S., 2004. Aligned biodegradable nanotibrous structure: a potential scaffold for blood vessel engineering. *Biomaterials,* 25(5), pp. 877-886.

Xu, Z.Y., Li, J.Y., Zhou, H., Jiang, X.D., Yang, C., Wang, F., Pan, Y.Y., Li, N.N., Li, X.Y., Shi, L.N. & Shi, X.M., 2016. Morphological and swelling behavior of cellulose nanofiber (CNF)/poly(vinyl alcohol) (PVA) hydrogels: poly(ethylene glycol) (PEG) as porogen. *RSC Adv.,* 6(49), pp. 43626-43633.

Yang, D.Z., Wang, W., Li, L.P., Peng, Y.L., Chen, P., Huang, H.Y., Guo, Y.L., Xia, X.W., Wang, Y.Y., Wang, H.Y., Wang, W.E. & Zeng, C.Y., 2013a. The Relative Contribution of Paracine Effect versus Direct Differentiation on Adipose-Derived Stem Cell Transplantation Mediated Cardiac Repair. *PLoS One,* 8(3).

Yang, Y., Li, J.Z., Pan, X.P., Zhou, P.C., Yu, X.P., Cao, H.C., Wang, Y.J. & Li, L.J., 2013b. Co-culture with mesenchymal stem cells enhances metabolic functions of liver cells in bioartificial liver system. *Biotechnol. Bioeng.,* 110(3), pp. 958-968.

Yao, J., Korotkova, T., Riboh, J., Chong, A., Chan, J. & Smith, R.L., 2008. Bioactive Sutures for Tendon Repair: Assessment of a Method of Delivering Pluripotential Embryonic Cells. *Journal of Hand Surgery-American Volume,* 33A(9), pp. 1558-1564.

Yao, J., Korotkova, T. & Smith, R.L., 2011. Viability and Proliferation of Pluripotential Cells Delivered to Tendon Repair Sites Using Bioactive Sutures-An In Vitro Study. *Journal of Hand Surgery-American Volume,* 36A(2), pp. 252-258.

Yao, J., Woon, C.Y.L., Behn, A., Korotkova, T., Park, D.Y., Gajendran, V. & Smith, R.L., 2012. The Effect of Suture Coated With Mesenchymal Stem Cells and Bioactive Substrate on Tendon Repair Strength in a Rat Model. *Journal of Hand Surgery-American Volume,* 37A(8), pp. 1639-1645.

Ye, H., Das, D.B., Triffitt, J.T. & Cui, Z., 2006. Modelling nutrient transport in hollow fibre membrane bioreactors for growing three-dimensional bone tissue. *J. Membr. Sci.,* 272(1–2), pp. 169-178.

Yeatts, A.B., Choquette, D.T. & Fisher, J.P., 2013. Bioreactors to influence stem cell fate: Augmentation of mesenchymal stem cell signaling pathways via dynamic culture systems. *Biochim. Biophys. Acta-Gen. Subj.,* 1830(2), pp. 2470-2480.

You, Y., Lee, S.J., Min, B.M. & Park, W.H., 2006. Effect of solution properties on nanofibrous structure of electrospun poly(lactic-co-glycolic acid). *J. Appl. Polym. Sci.,* 99(3), pp. 1214-1221.

Yu, J.S., Du, K.T., Fang, Q.Z., Gu, Y.P., Mihardja, S.S., Sievers, R.E., Wu, J.C. & Lee, R.J., 2010. The use of human mesenchymal stem cells encapsulated in RGD modified alginate microspheres in the repair of myocardial infarction in the rat. *Biomaterials,* 31(27), pp. 7012-7020.

Yuan, Y.F., Kallos, M.S., Hunter, C. & Sen, A., 2014. Improved expansion of human bone marrow-derived mesenchymal stem cells in microcarrier-based suspension culture. *J. Tissue Eng. Regen. Med.,* 8(3), pp. 210-225.

Zafar, H., Sharif, F. & Leahy, M.J., 2014. Measurement of the blood flow rate and velocity in coronary artery stenosis using intracoronary frequency domain optical coherence tomography: Validation against fractional flow reserve. *IJC Heart & Vasculature,* 5, pp. 68-71.

Zhang, J., Yan, D.X., Lei, J., Xu, J.Z., Hsiao, B.S. & Li, Z.M., 2013. Ultraporous poly(lactic acid) scaffolds with improved mechanical performance using high-pressure molding and salt leaching. *J. Appl. Polym. Sci.,* 130(5), pp. 3509-3520.

Zhang, M., Methot, D., Poppa, V., Fujio, Y., Walsh, K. & Murry, C.E., 2001. Cardiomyocyte grafting for cardiac repair: Graft cell death and anti-death strategies. *J. Mol. Cell. Cardiol.,* 33(5), pp. 907-921.

Zhang, Z.Y., Teoh, S.H., Teo, E.Y., Chong, M.S.K., Shin, C.W., Tien, F.T., Choolani, M.A. & Chan, J.K.Y., 2010. A comparison of bioreactors for culture of fetal mesenchymal stem cells for bone tissue engineering. *Biomaterials,* 31(33), pp. 8684-8695.

Zhao, G., Zinger, O., Schwartz, Z., Wieland, M., Landolt, D. & Boyan, B.D., 2006. Osteoblast-like cells are sensitive to submicron-scale surface structure. *Clinical Oral Implants Research,* 17(3), pp. 258-264.

Zhao, M., Yang, X.F., Huang, J.M., Zhou, Y.L., Tan, J.B. & Wang, L.T., 2009. Effects of receptor activator of NF-kappa B ligand gene silencing on the human osteoblast-like MG63 cells. *Biologia,* 64(1), pp. 208-214.

Zhou, W., Zhu, Y., Chen, S., Xu, R.J. & Wang, K.Z., 2016. Fibroblast growth factor receptor 1 promotes MG63 cell proliferation and is associated with increased expression of cyclin-dependent kinase 1 in osteosarcoma. *Molecular Medicine Reports,* 13(1), pp. 713-719.

Zhu, S.J., Xie, J.G., Branford-White, C., Zhu, L.M. & Donghua, U., 2007. *Preparation and application of drug delivery using hollow fiber technology.* Shanghai: Donghua Univ Press.

Zhu, X., 2015. The Cardiac Skeleton and the Aortic Root. In: X. Zhu, ed. *Surgical Atlas of Cardiac Anatomy.* Dordrecht: Springer Netherlands, pp. 101-118.

Zuber, A., Borowczyk, J., Zimolag, E., Krok, M., Madeja, Z., Pamula, E. & Drukala, J., 2014. Poly(L-lactide-co-glycolide) thin films can act as autologous cell carriers for skin tissue engineering. *Cell. Mol. Biol. Lett.,* 19(2), pp. 297-314.

APPENDIX A: DETAILED HOLLOW FIRBE SPINNING PROCEEDURE

Spinning hollow fibres is a multi-step process, but can all be done in the space of one day depending on how much you need to spin and how lucky you are. Please use look at the attached schematic when setting up. Prior to spinning, make sure that the RO water tank is completely full. If not, please follow the SOP for filling it. Put on PPE NOW! (Lab coat, goggles, gloves)

Filling the Spinning Rig

- Check that all outlet tubing is free from tears and is tightly constricted with clamps.
- Find the large blue and white buckets in 4.02
- Go down to the plant room on level 1 (through the Mays hydrogen lab) and retrieve the red trolley. Take it upstairs in the lift.
- Place the buckets on the trolley and take through to 4.05. Ideally with someone to help with doors. You can wedge open 4.02, but not 4.05.
- Fill both buckets while they are on the trolley. Be very careful when moving the trolley at heavy load.
- Wheel the trolley into 4.02 and back into the space between the rig and the work surfaces.
- Use your foot to push the hydraulic lever and raise the trolley to its maximum height.
- Gently tip the first bucket to fill up the rig. Rest the bucket against the lip of the metal trough and use it to assist in pouring. Repeat with the second bucket.
- Release the hydraulics by turning the handle on the trolley. Use it to control the decent of the trolley.
- Repeat until the whole rig is filled. It should take 6-8 buckets to fill. Half way through filling the metal walls of the rig will bounce outwards and make a sound. Do not be alarmed!
- Leave a bucket of water beside the rig as a source of RO water for later.
- Return the trolley to the plant room.

Assembling the spinneret

The spinneret is made from three parts, the top part (with the inlet at the top and the needle sat at the bottom), the chamber part (with the polymer inlet in its side), and the extra bit that screws into the bottom of the chamber part. There is no reason for these two parts to be separated, so screw the extra part onto the chamber part before starting. All components and equipment should be in the top drawer nearest the spinning rig on the centre island.

Testing the Needle for Water Leaks

- Check that the needle part of the spinneret is clean, free from any residual white polymer chunks, and is dry.
- Select the needle. Check the needle is clear by forcing a narrow metal thread down the bore of the needle.
- The top part of the spinneret has a moving part for no real reason. It is a threaded section that can freely move up and down, and can actually be removed if enough force is applied. Move it to the very top of the top part and wrap a double layer of PTFE tape around the exposed smooth cylindrical section directly beneath it.
- Gently twist and force this part back down over the PTFE, twisting with the direction of the tape (as you should do always) until it has reached the very bottom.
- Wrap a couple of layers of PTFE tape around the threads of this same part.
- Fill up a large container with RO water and place the inlet tube to the peristaltic pump inside; taping he tube to the container if necessary (it tends to flick out).
- The pump should be set to the correct tube setting by default. Check the two digit number at the end of the serial number on the tubing and check it matches with the number that is lit up on the pump itself. This means that the flow rates displayed should be accurate.
- Screw the pump outlet tubing onto the top of the needle part of the spinneret.
- Initiate the pump, causing liquid to enter the tubing at the desired flow rate. Turn off the pump when water is around 10 cm away from reaching the top part of the spinneret (this is called priming the pump).
- Wrap the base of the needle with a few wraps of PTFE tape.
- Gently force the PTFE end of the needle into the outlet of the needle part. Use a wide pair of tweezers if you wish. Make sure you twist with the movement of the thread.
- When you are confident the needle is tight, place the chamber part of the spinneret over the top part, ensuring the needle has found the hole in the bottom of the chamber part, and tighten.

- The needle needs to poke out of the bottom of the spinneret by 1-2 mm. If it is barely showing from the bottom of the spinneret then re-seat the needle in the top part and check again.
- Unscrew the chamber part of the spinneret, hold the top part needle side down, and initiate a flow rate of around 12 ml/min from the pump.
- Check the connection between the needle and the top part of the spinneret for leaks. A very obvious drop will appear to form if a leak is present. Allow water to flow for 2 minutes.
- When you are sure there are no leaks, reverse the flow of the pump to remove all liquid from inside the needle and the first 10 cm of the tubing that is entering the top part of the spinneret.
- Screw the chamber part back onto the top part and rest the spinneret on its side. This is to protect the needle. Don't leave the needle in the top part of the spinneret if you are just going to leave it and do something else. The spinneret WILL put weight on the needle and potentially bend it.

Setting up the Pressure Vessel

- Locate the pressure vessel (PV), two valves, the gas inlet line, the PV-spinneret connection line and the two connectors used to attach the valves to those lines.
- Check that they are all clean; with no solidified polymer lumps stuck in the tubes or lining any threads etc, and also dry.
- The valves will be labelled; one will be to control the PV inlet and the other for the PV outlet. The valves have arrows showing the direction of flow through them.
- The first objective is to test the equipment attached to the bottom of the PV for leaks before polymer is poured in.
- Wrap PTFE around the thread of the bottom of the PV outlet valve, screw in the connector, and then repeat with the top of the PV outlet valve and screw into the bottom of the PV, tightening with spanners.
- Screw the outlet tubing into the bottom of the valve connector. No need for PTFE.
- Do the same with the equipment to be placed at the top of the PV, but do not excessively tighten as this will soon be removed.
- Fix the PV into the arms above the spinning rig.
- Attach the gas line from the wall to the PV inlet.
- Ensure that the PV inlet valve, PV outlet valve and the Wall valve are all closed
- Go to the gas canister in the storage cupboard.

- There are two pressure gauges; P1 (on the left) shows the pressure exiting the gas canister in bar gauge, and P2 (on the right) shows the pressure of gas (the quantity) in the gas canister itself.
- Open the tank outlet valve by one turn with the allen key already attached.
- Turn the regulator valve clockwise to pressurise the copper line between the gas canister and the wall valve. Turn until a pressure of 2 bar gauge.
- Return back to the PV and open the Wall valve and the PV inlet valve. Everywhere between the gas canister up to and including the PV will be at 2 bar gauge, as confirmed by P3 on the gas line.
- Use a dilute mixture of soap and water in a squirty bottle and spray the joints between the PV outlet valve and the PV. If you see bubble expand in a certain joint, that joint must be tightened.
- Either way, the PV must now be depressurised. Close the Wall valve and slowly open the PV outlet valve to remove pressurised air between these two points. P3 should read zero. Tighten the joints if leaks were found.
- Close the PV outlet valve; remove the gas line from the PV inlet valve, then remove the PV inlet valve from the PV.
- Pour the polymer into the top of the PV, being careful to not hit the threads. If you do, give them a wipe. The polymer will eat away at the PTFE otherwise.
- Wrap new PTFE around the PV inlet valve and reattach to the top of the PV.
- Reattach the gas line and tighten everything one more time with spanners.
- Close the PV inlet valve and open the wall valve to pressurise everything up to the PV inlet valve. Check that joint for leaks
- Fully open the PV inlet valve and test the joint between it and the PV for leaks.
- If leaks are found, close the wall valve and carefully loosen the joint between the gas line and the PV inlet valve. A small hiss will mean that pressure is being released. The pressure being read in P3 will decrease to zero.
- If totally leak free leave pressurised and you are good to go!

Actually Spinning

- If you are at this point all this should be true:
    - Polymer is in the PV.
    - Needle is attached to spinneret and is leak free.
    - Pressure from the gas tank is set to 2 bar gauge.
    - The spinning rig is full of RO water.
    - PV outlet valve is closed, all other valves are open.
    - The motor is plugged in.
    - A bucket of RO water has been placed below the bucket to collect fibres.
    - The water pump is primed and has access to enough water to pump continuously.
- Attach the spinneret to the arm above the water. Raise the arm to its highest point.
- Attach the polymer inlet line to the spinneret. It is short and inflexible; do not drop it into the water. If you do, dry it off and pull out the subsequent solid bit of polymer from the end.
- Turn the peristaltic pump on initiate water flow through the spinneret at 12 ml/min.
- The flow will be a continuous stream that will fall straight downwards into the water bath. If it is angled wipe the outlet with a paper towel. If it persists the spinneret may not be fully cleaned internally or the needle not centred. Dismantle the spinneret and check.
- Reduce the flow to the lowest you can get it while maintaining a constant flow from the spinneret that doesn't 'widen' the stream or cause drops of water to form (7-9 ml/min).
- Open the PV outlet valve halfway and watch as the polymer flows through the tubing. There will be a delay before polymer leaves the spinneret as the chamber fills with polymer.
- The polymer will start to coagulate as it flows out of the spinneret and contacts the flowing water. Use a pair of tweezers to guide a string of polymer into the water. This may take a little while. If the polymer is not forming as desired, try changing the water flow rate or increasing the gas pressure (to increase the polymer flow rate).
- Once you are happy with the extruded polymer, loosen the arm holding the spinneret and lower the spinneret into the water bath by about 5 mm so that the needle is below the water.
- Allow the fibre to fall to the bottom of the tank and use the hooking arm attached to the spinning rig to take the fibre upwards, over the central roller and into the second

bath. Allow a degree of slack in the fibre ‘string’ when doing this and do not pull the fibre taught.

- Place the roller side of the hooking arm into the deepest part of the rig and ensure that the fibre is trapped underneath it. This will guide the polymer downwards and prevent it from spiralling as it leaves the spinneret.
- Guide the fibre through the second bath and underneath the second roller.
- Switch on the pickup motor on the lowest speed setting. Hook the fibre underneath and then over the roller and guide it down into the fibre collection bucket.
- Check the condition of the polymer as it comes out. If the lumen is too large reduce the water flow rate. If you want the outer diameter of the polymer to be larger increase the polymer flow rate. Modifying these values can only do so much. A lot of it is dependent on the properties of the polymer itself.
- The flow rate of fibre leaving the spinneret must be equal to that of the speed of the pickup motor to avoid the fibre spiralling (motor too slow) or being stretched and held taught (motor too fast). Continuously check to make sure that neither of things are happening.
- Check that the fibre is correctly being aimed into the collection bucket and is being picked up by the motor correctly. Sometimes the fibres can get knotted on the pickup rotor.
- If the fibre on the motor keeps on ‘slipping’ try to find something to wrap around it that will provide grip to the fibre (paper towels maybe). Make sure that whatever is wrapped around the motor maintains the smooth cylindrical surface of the roller on the motor. If there are sharp edges then the fibre could bend at sharp angles instead of maintaining a good shape.
- Keep checking all of these things until enough fibre is obtained or the polymer has run out. When all polymer is used up a very obvious bubbling sound can be heard from the spinneret.

Shut Down Procedure

This can vary depending on whether or not the spinning process has been ended early with polymer still in the PV. Polymer can remain in the PV for another spinning session as long as the PV inlet and outlet valves are closed.

No Polymer to Recover

- Close PV outlet valve.
- Switch off water flow pump.
- Allow all fibre to be taken through the water bath and deposited in the collection bucket.
- Close wall valve.
- Detach water line from the spinneret.
- Detach the polymer inlet line from the spinneret.
- Hold a glass flask under the line and slightly open the PV outlet valve to depressurise the PV and the gas line up to the wall valve. Watch P3 decrease to zero. The glass flask is to collect any residual polymer as it is shot out of the PV.
- Unscrew the gas line from the PV inlet valve and remove the PV with valves from the support arms. Place to one side.
- Go back to the gas canister and turn the regulator valve anti-clockwise to shut it. P1 will still display the pressure set during the spinning process because the copper line between the regulator valve and the wall valve is still pressurised. Close the tank outlet valve with the allen key attached.
- Slightly open the wall valve whilst holding onto the gas line tightly. A hissing will be heard as the pressurised air rushes out of the gas line. The line is depressurised when no air is flowing. Check that P3 and P1 now read zero bar gauge

Polymer to Recover

- Close PV outlet valve.
- Switch off water flow pump.
- Allow all fibre to be taken through the water bath and deposited in the collection bucket.
- Close PV inlet valve.
- Detach water line from the spinneret.
- Detach the polymer inlet line from the spinneret.

- Hold a glass flask under the line and slightly open the PV outlet valve to depressurise the PV and the gas line up to the wall valve. Watch P3 decrease to zero. The glass flask is to collect any residual polymer as it is shot out of the PV.
- Close the regulator valve on the gas canister. P1 and P3 will still display the pressure set during the spinning process because the copper line between the regulator valve and the PV inlet valve is still pressurised.
- Gently loosen the connection between the gas line and the PV inlet valve until a hiss of air escaping can be heard. P3 and P1 will fall to zero as the line is depressurised. Tighten the connection when done
- Go back to the gas canister and open the regulator valve to a pressure of 0.5 bar gauge. This lower pressure is required to ease the remaining polymer from the PV into the glass container.
- Open the PV inlet valve fully and open the PV outlet valve slightly, with the glass container under the line exiting the PV.
- The polymer should flow at a moderate flow rate. Close off the PV outlet valve as soon as you can see that no more polymer is leaving the PV into the outlet line. Try and retrieve as much polymer from the line as possible, however if you don't shut it off in time air will be forced into the glass container, leading to air bubbles forming in the polymer.
- Place a lid on the glass container, label it, and place it to one side.
- Close the regulator valve and the tank outlet valve and open the PV outlet valve to depressurise the whole system. Check that P1 and P3 read zero bar gauge.

Washing up

When washing up do not leave things in to soak for prolonged periods of time (overnight). This will cause the polymer to expand more and make it very difficult to remove.

- Prepare a wash bowl with water in it and place it in the sink
- Remove the valves and connectors from the pressure vessel. Submerge all but the PV inlet valve and that connector in the wash bowl (the PV inlet valve has not been exposed to polymer).
- Remove the spinneret from the holding arm, dismantle and be ready to catch any excess polymer still in the spinneret.
- Remove the needle with tweezers at its base and place to one side.
- Run the main spinneret components under a gentle water flow to coagulate the polymer and remove with tweezers. Repeat another time and place in the wash bowl

- Very gently wash the needle, removing all PTFE tape. Remove coagulated polymer with a paper towel in a gloved hand. Clean the bore of the needle with a thin metal thread and leave out on paper towels to dry.
- Remove any coagulated polymer from the submerged spinneret using tweezers, making sure to also remove all PTFE tape, and checking in all the crevices and inlet/outlet ports. Pay special attention to cleaning the threads. Use a large metal needle to clean the polymer outlet hole at the bottom of the spinneret. Leave out on paper towels to dry
- Clean the PV outlet valve connector in the same way.
- The coagulated polymer on the inside of the polymer inlet tubing can be easily removed by flowing compressed air from the hood through it. Submerge again and repeat.
- It will be hard to remove coagulated polymer from the PV outlet valve. Open the valve fully and alternate between scraping away the polymer and applying a compressed air flow. Fully close the valve then scrape the valve needle. Hold the valve internals into the light for a better look.
- Remove the PV from the wash bowl and wash the internals with water from the tap at a high flow rate, being sure to hit the inner walls with the jet stream. If the skin has peeled off as a result you will see a blockage in the pressure vessel. Use tweezers to remove or apply a compressed air flow to shoot it out. Repeat and leave to dry.
- When all components have dried, place back in the drawer.

Draining Water Rig

- Place a bucket under the second trough and loosen the clamp to drain it. Only half fill the bucket because it will have to be drained in the sink and it can get very heavy.
- Put the long tube that exits the bottom of the first trough into the sink. Ensure it is fully secured before loosening the two clamps along its length. This flow will stop at about 75% empty.
- Move the tubing into a bucket and drain and empty into the sink. The tank will now be about 95% empty. Be prepared to stop flow to empty the bucket a few times.
- Move the tubing into a short sided wash bowl to get the final bit of water out.
- Empty the water tank on the pump inlet and drain all water from the pump tubing.
- Mop up any spillages and clear any work surfaces

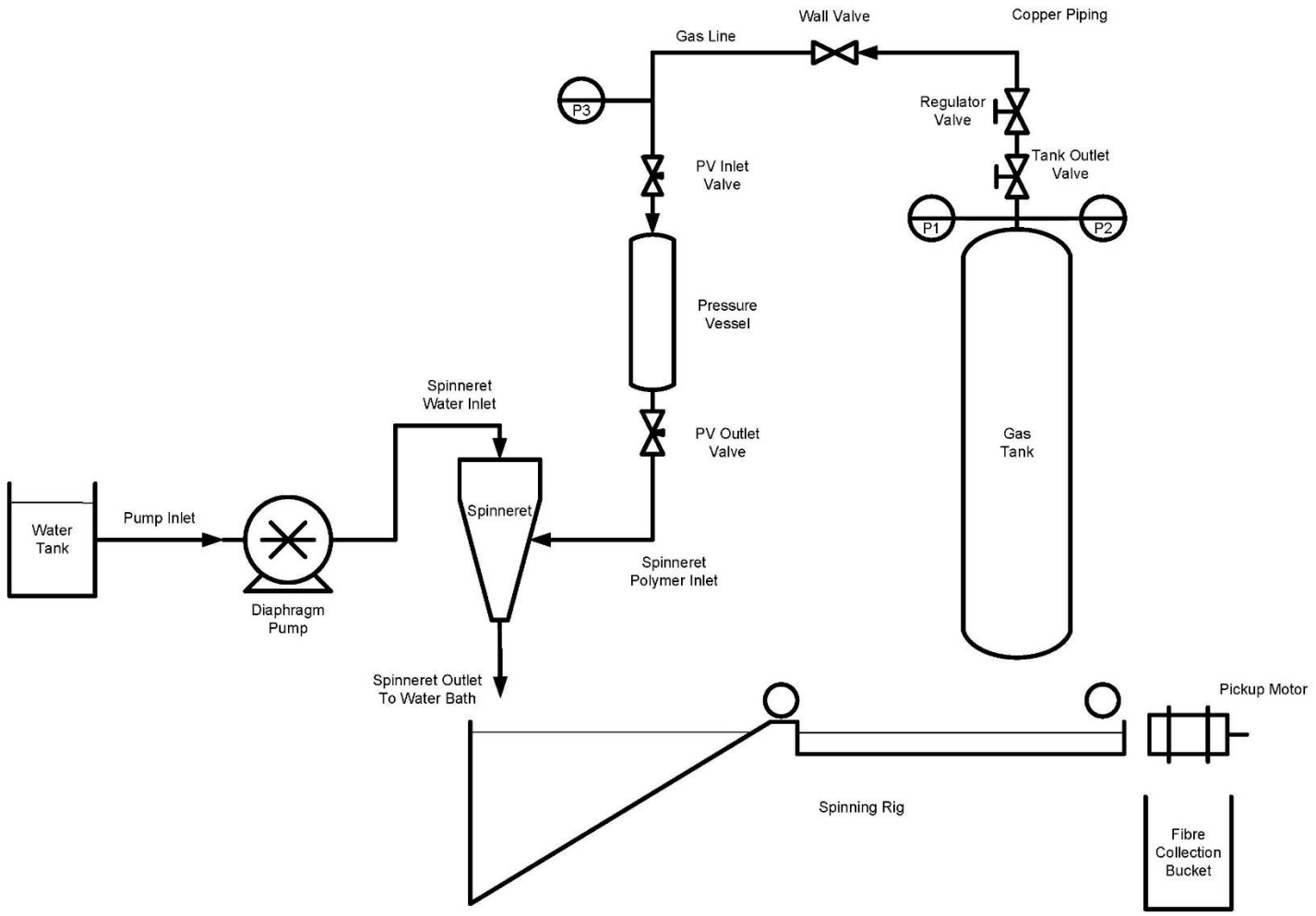

Figure A.1 - Schematic of Spinning Rig

APPENDIX B: DETAILED PROCEEDURE FOR ANALYSIS OF SEM IMAGES USNG IMAGE J SOFTWARE

SEM images of porous scaffolds were analysed using ImageJ software (version 1.48). ImageJ allowed modification of raw SEM photos into binary black and white images to differentiate pores on the surface, which ImageJ sized and counted. A macro was written to facilitate this process due to the large number of images to be analysed. An example of SEM image modification of Figure B.1 is outlined in this section

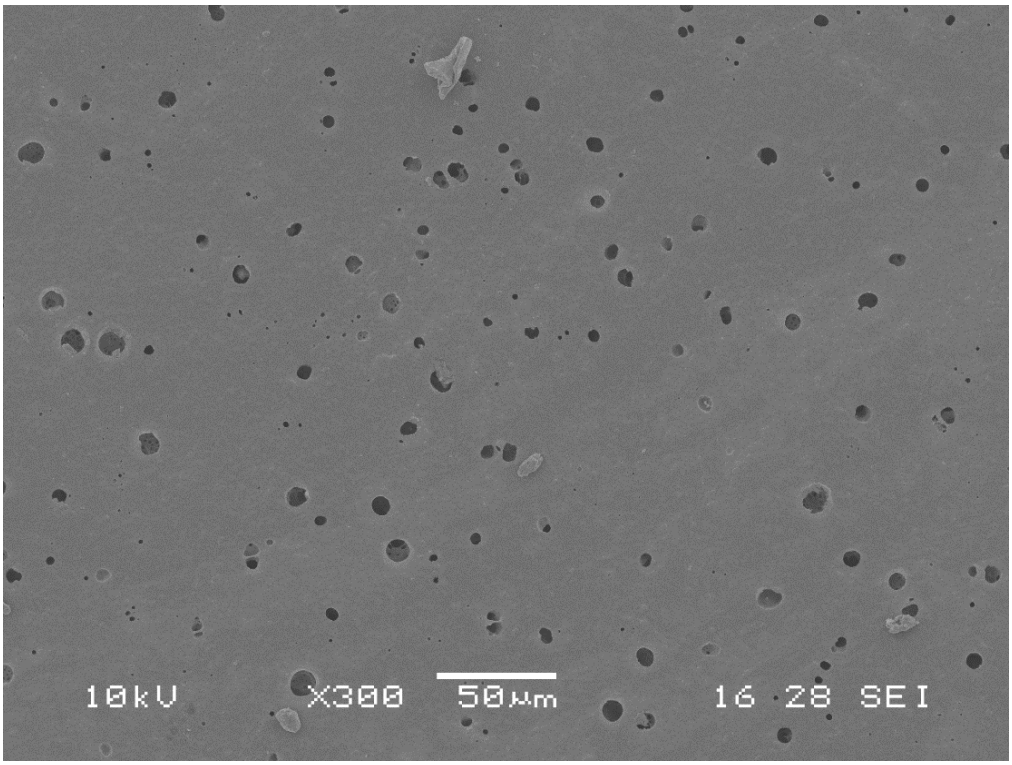

Figure B.1 – SEM image of a flat sheet PLGA scaffold

Firstly the scale bar on the raw SEM image was used as a reference to attribute SI length units to the image instead of pixels, the default ImageJ unit. A line of known pixel length was placed over the scale bar length, and assigned the same length. Figure B.2 shows a yellow line of 150 pixel length being made equivalent to 50 µm, the same length shown on the SEM image.

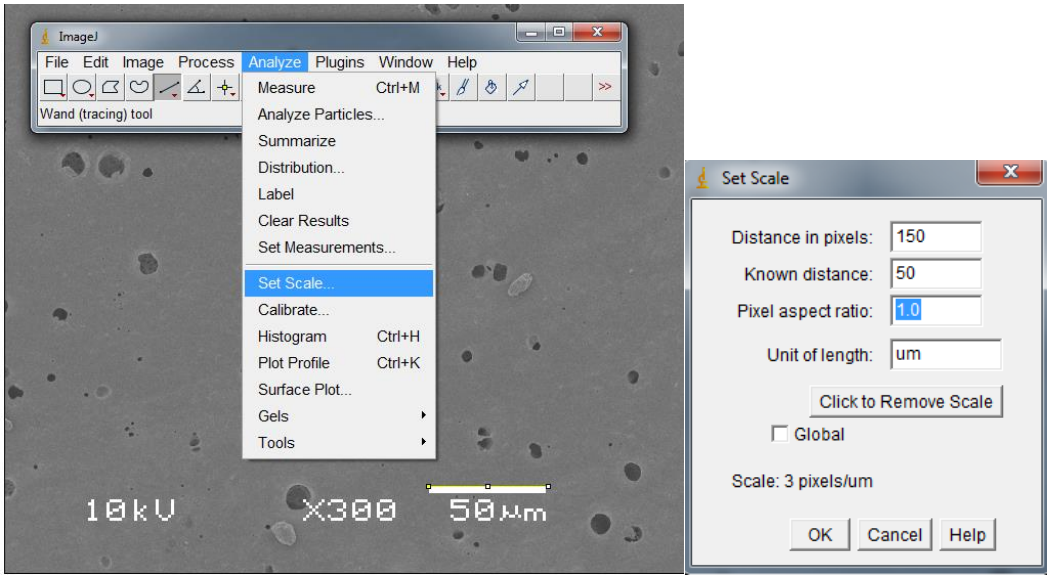

Figure B.2 – Menu for setting a comparable scale

Next, the image was cropped to remove the overlaid text at the bottom (Figure B.3).

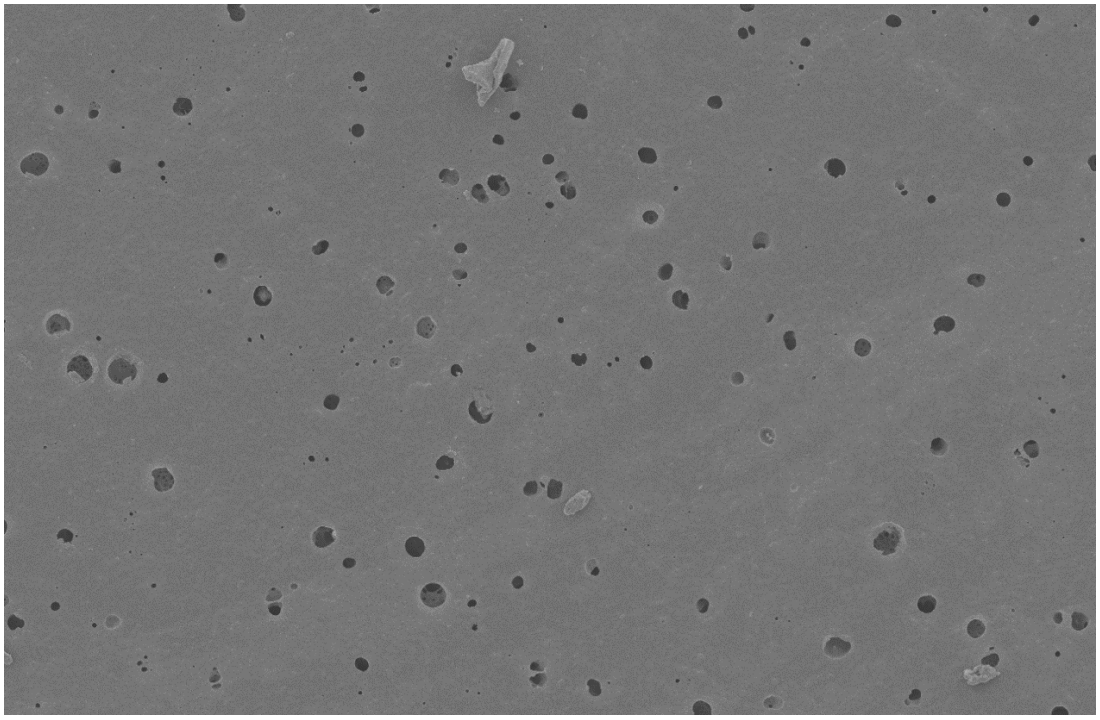

Figure B.3 – Cropped SEM image

A bandpass filter was applied to the cropped image, as shown in Figure B.4.

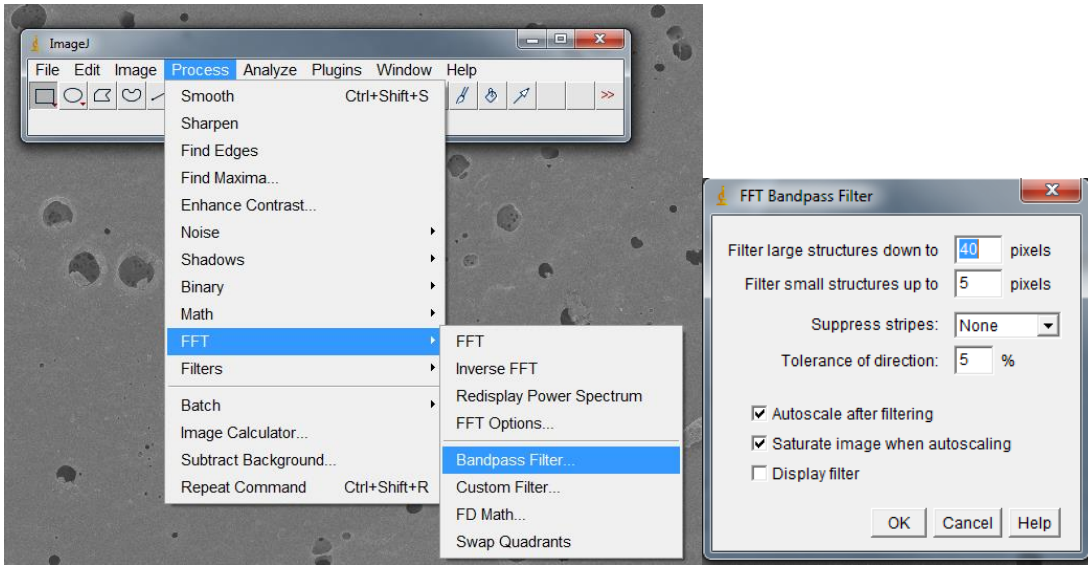

Figure B.4 – Menu to apply a bandpass filter

Large structures, such as pores or any other points of contrast, were filtered down to 40 pixels. This smoothed out the obvious variations in the brightness of the image, i.e. increased the prominence of the larger dark pores compared to the lighter surface surrounding them. Smaller structures were filtered up to 5 pixels, increasing the prominence of the lighter surface surrounding the smaller pores. This acted as a shading correction to increase the degree of contrast between pore areas and non-pore areas, resulting in Figure B.5.

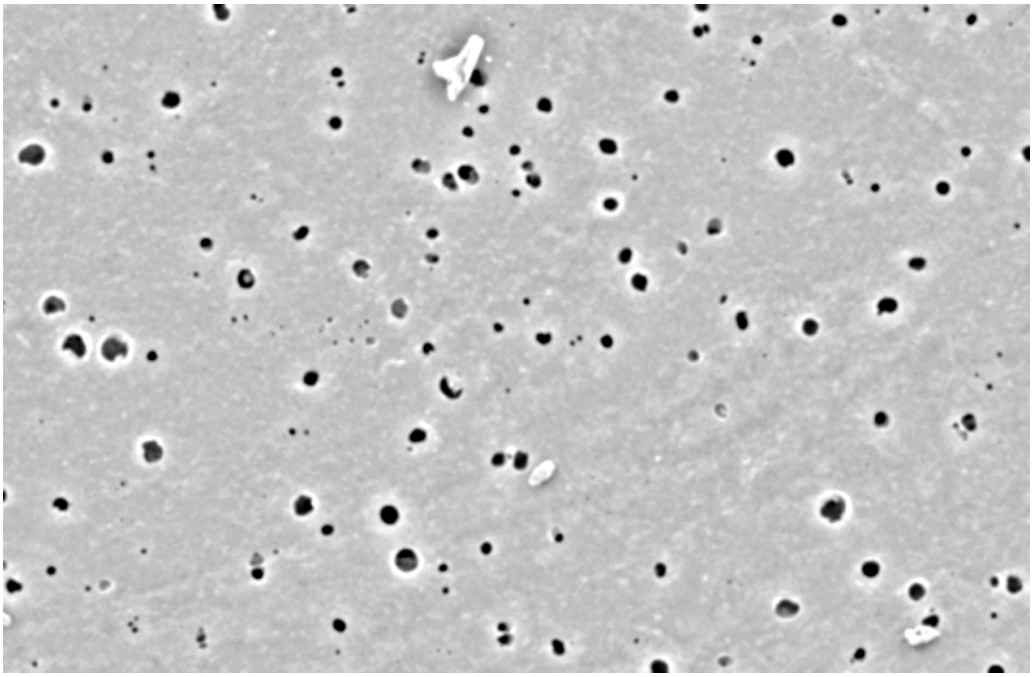

Figure B.5 – Image with a bandpass filter applied

The colour threshold of this image was modified in order to obtain a binary image for particle analysis (Figure B.6).

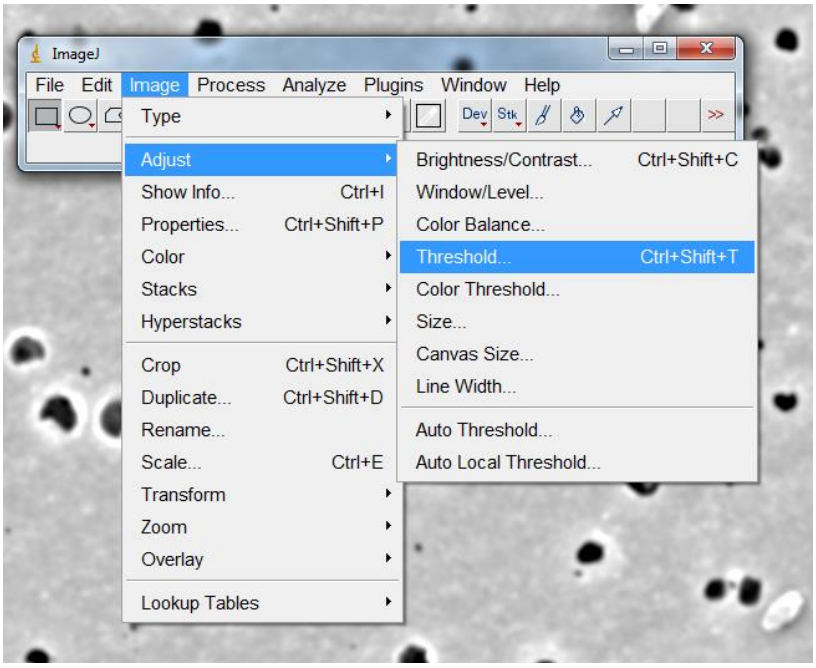

Figure B.6 – Menu to modify image colour threshold

Altering threshold settings allowed grayscale images to be modified to highlight areas of interest from the background. In the first instance an 'Over/Under' display mode was selected and the sliders changed until the entirety of pores were highlighted in blue (Figure B.7). This is then applied to the image.

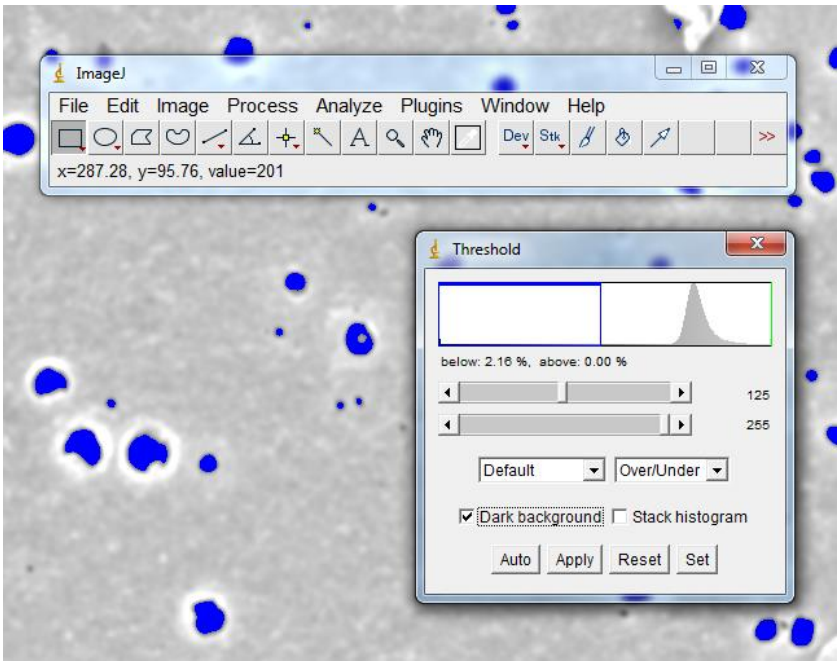

Figure B.7 – Menu showing colour threshold sliders

Display mode is changed to black and white, and applied again without changing the sliders, producing Figure B.8.

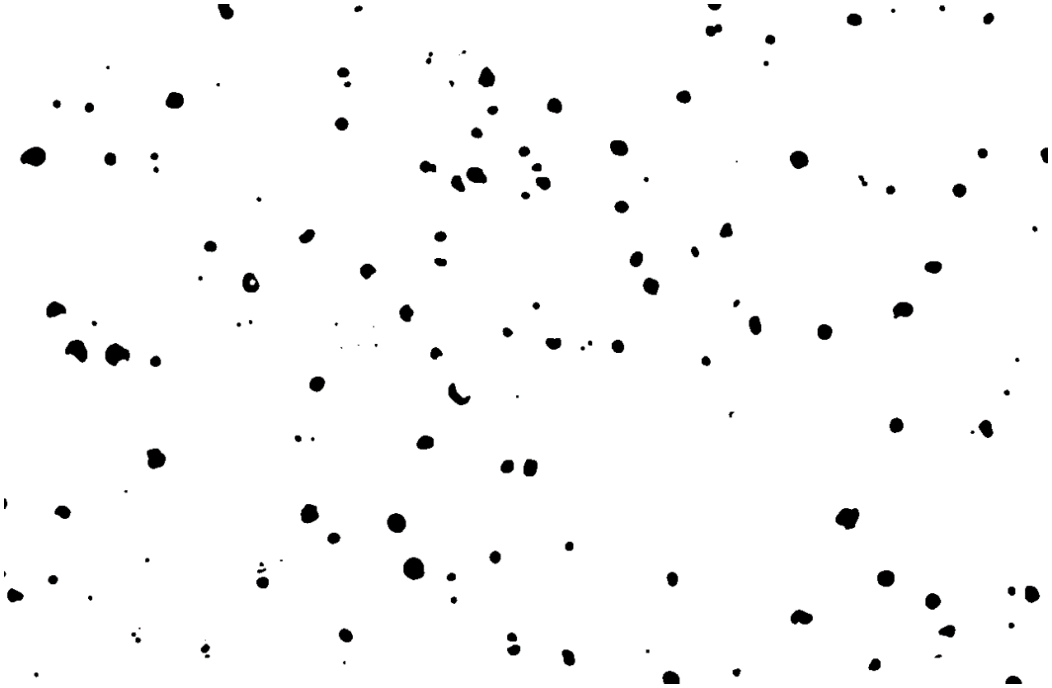

Figure B.8 – Binary image showing surface pores in black

From this the black 'particles' can be analysed for their geometric properties (Figure B.9). The outlines of the particles are selected, as well as the desired ranges of particle size and circularity.

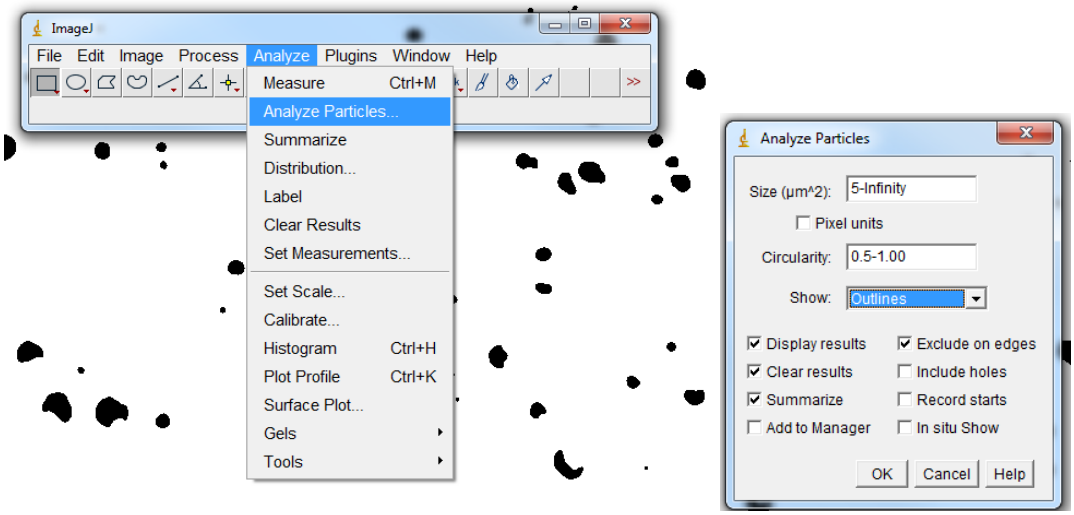

Figure B.9 – Menu to outline the pores and select desired parameters

A final image is output (Figure B.10) with each pore allocated a number.

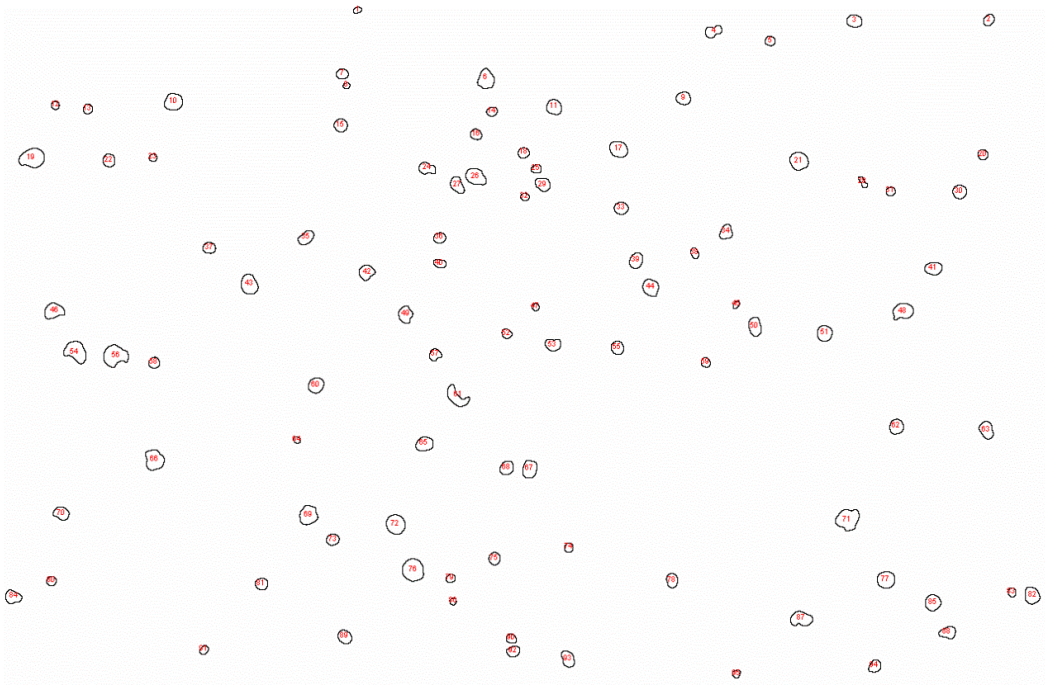

Figure B.10 – Image of pores circled and numbered

A set of data for each particle is also output. The desired properties that are tabulated can be selected from a large list of geometric attributes (Figure B.11).

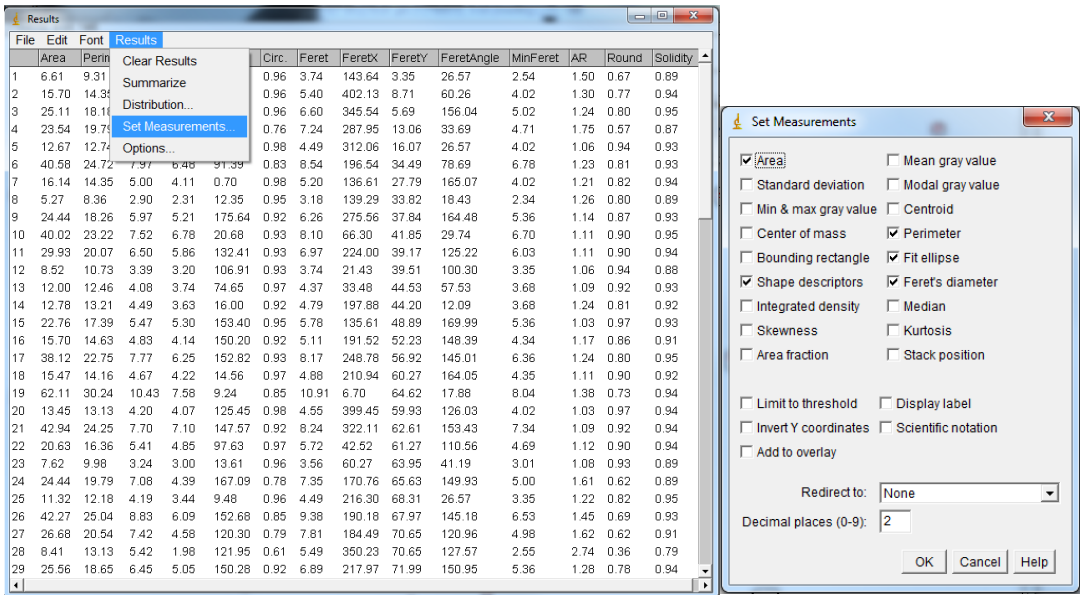

Figure B.11 – Selection of desired geometry properties to be exported

The macro code of this procedure for this particular image is included in Figure B.12.

```
run("Set Scale...", "distance=0 known=0 pixel=1 unit=pixel");
//setTool("line");
makeLine(553, 846, 702, 846);
run("Set Scale...", "distance=149.33 known=50 pixel=1
unit=um");
//setTool("rectangle");
makeRectangle(0, 0, 1278, 833);
run("Crop");
saveAs("Tiff", "\\\\myfiles\\sma25\\dos\\PhD\\Thesis\\5.
Results Chapter 2 - PLGA Porosity\\Image J\\Image Export\\1.
Cropped.tif");
run("Bandpass Filter...", "filter_large=40 filter_small=5
suppress=None tolerance=5 autoscale saturate");
saveAs("Tiff", "\\\\myfiles\\sma25\\dos\\PhD\\Thesis\\5.
Results Chapter 2 - PLGA Porosity\\Image J\\Image Export\\2.
Bandpass.tif");
setAutoThreshold("Default dark");
//run("Threshold...");
setThreshold(125, 255);
setOption("BlackBackground", false);
run("Convert to Mask");
setAutoThreshold("Default");
setAutoThreshold("Default dark");
setThreshold(0, 128);
run("Convert to Mask");
saveAs("Tiff", "\\\\myfiles\\sma25\\dos\\PhD\\Thesis\\5.
Results Chapter 2 - PLGA Porosity\\Image J\\Image Export\\3.
Threhsold.tif");
run("Analyze Particles...", "size=5-Infinity circularity=0.50-
1.00 show=Outlines display exclude clear summarize");
saveAs("Tiff", "\\\\myfiles\\sma25\\dos\\PhD\\Thesis\\5.
Results Chapter 2 - PLGA Porosity\\Image J\\Image Export\\4.
Pores.tif");
saveAs("Results", "\\\\myfiles\\sma25\\dos\\PhD\\Thesis\\5.
Results Chapter 2 - PLGA Porosity\\Image J\\Image
Export\\Results.xls");
run("Close");
run("Close");
```

Figure B.12 – Macro code to obtain surface porosity data from an SEM image

APPENDIX C: CALCULATION OF CELL SETTLING CONTACT AREA FOR MULTI FIBRE MODULES

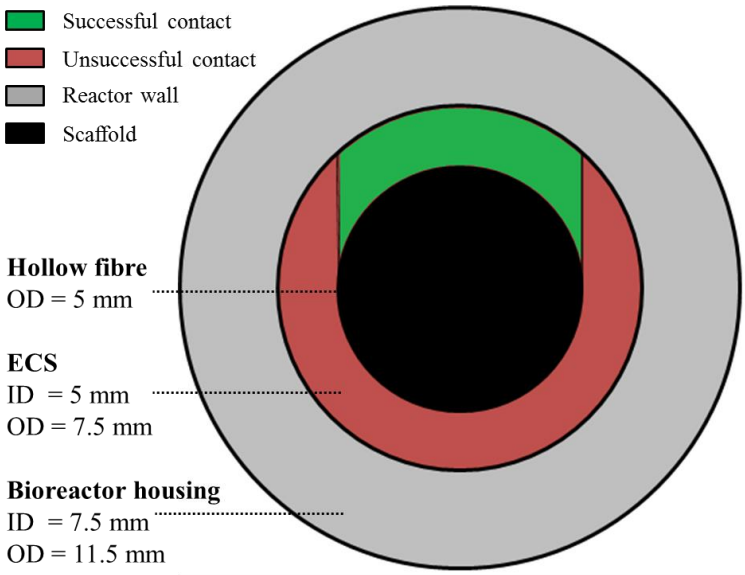

Figure C.1 – Cross section of a multi HFB module displaying the predicted cell contact area

The volume of the green shaded region in Figure C.1 can be calculated from shape geometry using trigonometry. While the cells are settling in three dimensions, taking the cross section of the HFB will yield an area that is proportional to the overall volume of that section. The areas in question are labelled in Figure C.2 below:

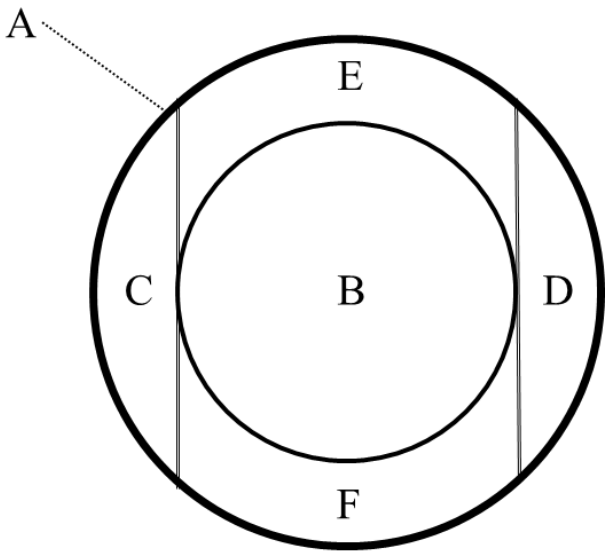

Figure C.2 – Single HFB module geometry labelled in segments

Area A is the cross sectional area of the inner wall of the HFB, with a diameter of 7.50 ± 0.05 mm. Area B is the cross sectional area of the hollow fibre with an outer diameter of 5.00 ± 0.05 mm. Areas C and D are chords of equal area that touch the outermost points of Area B while moving vertically downwards. Areas E and F remain, with Area E being the region of interest directly above the hollow fibre. This area is calculated in Equation C.1, with r_{OF} representing the outer fibre radius, and r_{IB} representing the inner bioreactor wall radius.

$$Area\ A = \pi r_{IB}^2 = \pi 3.75^2 = 14.06\pi$$

$$Area\ B = \pi r_{OF}^2 = \pi 2.5^2 = 6.25\pi$$

$$Area\ C = \frac{r_{IB}^2}{2}\left(\frac{\theta\pi}{180} - \sin\theta\right)$$

$$Area\ D = \frac{r_{IB}^2}{2}\left(\frac{\theta\pi}{180} - \sin\theta\right)$$

$$Area\ E = \text{Area}\ A - \text{Area}\ B - \text{Area}\ C - \text{Area}\ D - \text{Area}\ F$$

$$Area\ F = Area\ E\ \therefore$$

$$\boldsymbol{Area\ E = \frac{14.06\pi - 6.25\pi - 2\frac{r_{IB}^2}{2}\left(\frac{\theta\pi}{180} - \sin\theta\right)}{2}}$$

Equation C.1 – Calculation of Area E to determine theoretical cell attachment

The angle (θ) in Equation C.1 is the central angle of the chord (c) within the circle. Area D is a circle segment that can be calculated using the internal radius of the bioreactor (r_{IB}) and the central angle of the segment. With reference to Figure C.3, this angle can be calculated as shown in Equation C.2:

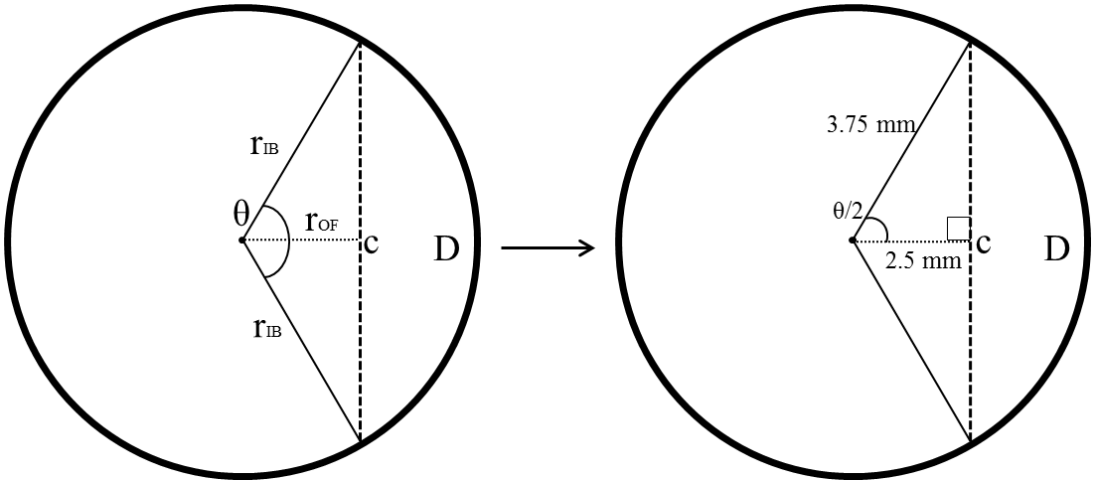

Figure C.3 – A representation of the variables required to calculate segment area in a single HFB module

$$cos\left(\frac{\theta}{2}\right) = \frac{Adjacent}{Hypotenuse}$$

$$\frac{\theta}{2} = \cos^{-1}\left(\frac{2.5 \pm 0.05}{3.75 \pm 0.05}\right) = 48.2°$$

$$\boldsymbol{\theta = 96.4° \pm 0.7°}$$

Equation C.2 – Calculation of the segment angle of a chord

By inserting the known dimensional values of the HFB system, the segment Area E can be calculated, and by multiplying the segment area by the hollow fibre length (L_{hf}) the volume of the segment can be found, as shown in Equation C.3:

$$Area\ E = \frac{14.06\pi - 6.25\pi - 2\frac{(3.75 \pm 0.05)^2}{2}\left(\frac{(96.4 \pm 0.7)\pi}{180} - \sin(96.4 \pm 0.7)\right)}{2}$$

$$= 7.43 \pm 0.22\ mm^2$$

$$Volume\ E = Area\ E \times L_{hf}$$

$$Volume\ E = 7.43 \pm 0.22\ [mm^2] \times 120 \pm 0.05\ [mm]$$

$$\boldsymbol{Volume\ E = 891 \pm 27\ [mm^3]}$$

Equation C.3 – Calculation of available ECS volume for cells to naturally settle onto the hollow fibre

Volume E can then be taken as a percentage of the total available volume in the ECS:

$$Cell\ Space = (Area\ A - Area\ B) \times L$$

$$Cell\ Space = (14.06\pi - 6.25\pi)[mm^2] \times 120 \pm 0.05[mm]$$
$$= 2944 \pm 1\ [mm^3]$$

$$Volume\ E = \frac{891 \pm 27[mm^3]}{2944 \pm 1\ [mm^3]} \times 100\%$$

$$\boldsymbol{Volume\ E = 30\% \pm 1\%}$$

Equation C.4 – Calculation of available ECS percentage for cells to naturally settle onto the hollow fibre

Assuming that: the hollow fibre is completely straight and resides in the very centre of the bioreactor, the cells in the media are well mixed throughout the entire cell space and do not interact with one another, and that cells settle due to the force of gravity directly downwards, this model indicates that a maximum 30% ± 1% of cells will have a chance to attach to the hollow fibre in this module. However this does not take into account the fact that cell attachment on the hollow fibre will become more difficult the steeper the gradient of the

available surface is. This means that cells that make fibre contact close to the chords shown in Figure C.2 will be unlikely to attach. Therefore maximum cell attachment is likely to be smaller than 30% ± 1%.

APPENDIX D: SUPPLEMENTARY DATA TABLES

Table D.1 – Extrapolation of theoretical attachment on single fibre modules over 6 hours

Cell Attachment	Theoretical/Experimental Parameter	Single Fibre Bioreactor 6h Extrapolation					
		2 RPM		6 RPM		8 RPM	
		Value	***Error***	**Value**	***Error***	**Value**	***Error***
Static Phase	Cell contact from initial settling on hollow fibre	23.9%	*4.4%*	23.9%	*4.4%*	23.9%	*4.4%*
	Time before initiating rotation (min)	5	-	5	-	5	-
	Cell attachment after this time on flat sheets	19.6%	*11.2%*	19.6%	*11.2%*	19.6%	*11.2%*
	Cell attachment on hollow fibre	**4.7%**	***2.7%***	**4.7%**	***2.7%***	**4.7%**	***2.7%***
Dynamic Phase	Unattached cells on bottom of bioreactor	95.3%	*2.7%*	95.3%	*2.7%*	95.3%	*2.7%*
	Total rotation time (hours)	6	-	6	-	6	-
	Projected fibre surface area relative to bioreactor	50.0%	-	50.0%	-	50.0%	-
	Time cells in contact with fibre due to centrifugal action (hours)	03:07	-	05:32	-	05:45	-
	Cell attachment after this time on flat sheets	83.9%	*34.5%*	83.9%	*34.5%*	83.9%	*34.5%*
	Cell attachment on hollow fibre	**40.0%**	***16.5%***	**40.0%**	***16.5%***	**40.0%**	***16.5%***
Total	Cell Attachment From Initial Settling	4.7%	*2.7%*	4.7%	*2.7%*	4.7%	*2.7%*
	Cell Attachment From Centrifugal Action	40.0%	*16.5%*	40.0%	*16.5%*	40.0%	*16.5%*
	Total Theoretical Dynamic Cell Attachment	**44.7%**	*16.7%*	**44.7%**	*16.7%*	**44.7%**	*16.7%*

APPENDIX E: SUPPLEMENTARY SEM IMAGES

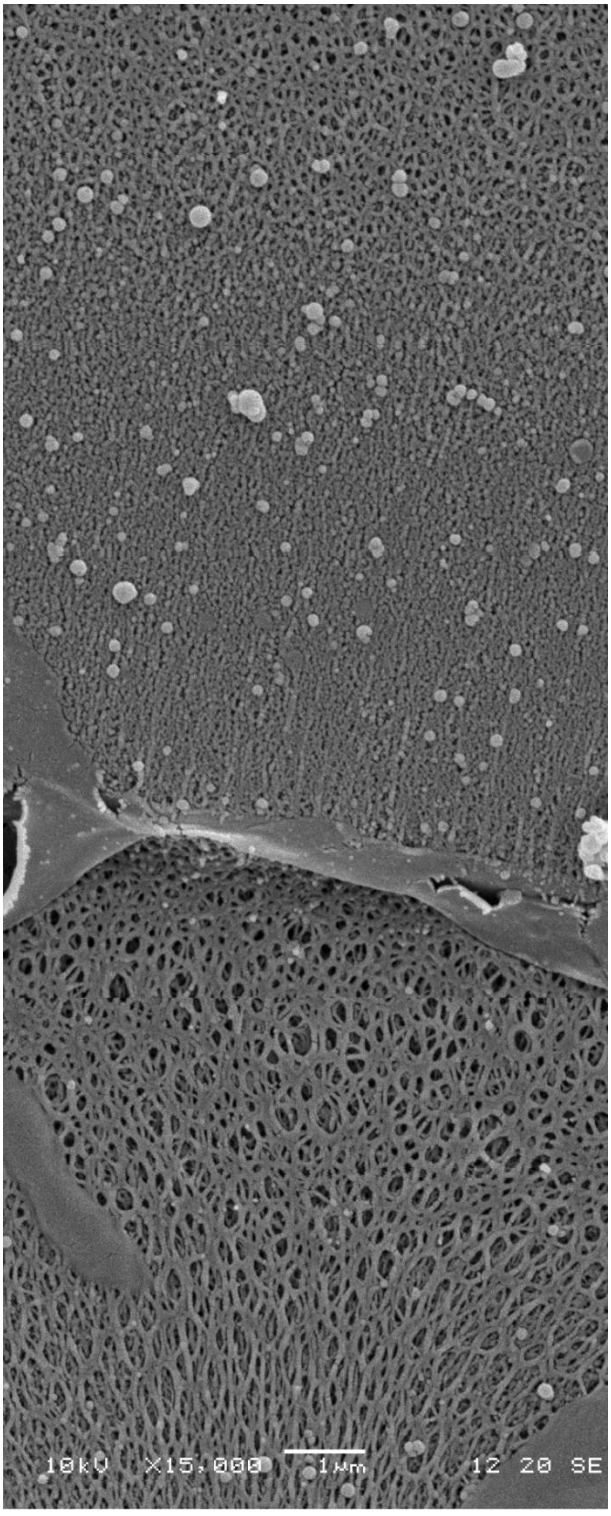

Figure E.1 – SEM image of the outer surface of PLGA hollow fibre spun with dioxane as the non-solvent

APPENDIX F: PERMEATION SENSITIVITY ANALYSIS

Minimum Fibre Thickness

Table F.1 – Minimum fibre dimensions

Property (µm)	NaCl Percentage									
	0%		10%		20%		40%		60%	
	Value	*Error*	Value	*Error*	Value	*Error*	Value	*Error*	Value	*Error*
Outer Diameter	1350	*1.9%*	1250	*5.7%*	937.5	*5.7%*	1050	*2.4%*	987.5	*1.8%*
Inner Diameter	1140	*2.2%*	912.5	*5.8%*	737.5	*2.4%*	900	*2.8%*	712.5	*2.5%*
Thickness	105	*16.8%*	169	*26.2%*	100	*28.0%*	75	*23.6%*	138	*9.1%*

Gas Permeation

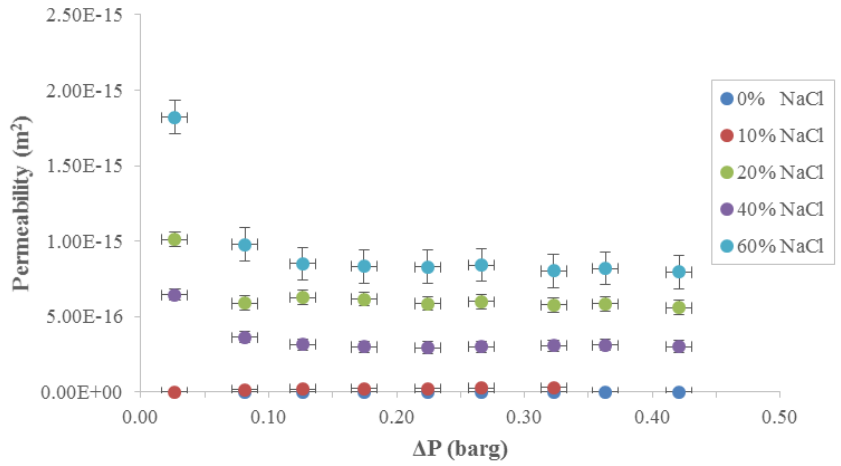

Figure F.1 – Permeation of nitrogen through PLGA hollow fibres with different NaCl content. X error = 0.01 bar, Y error = SD (n=3).

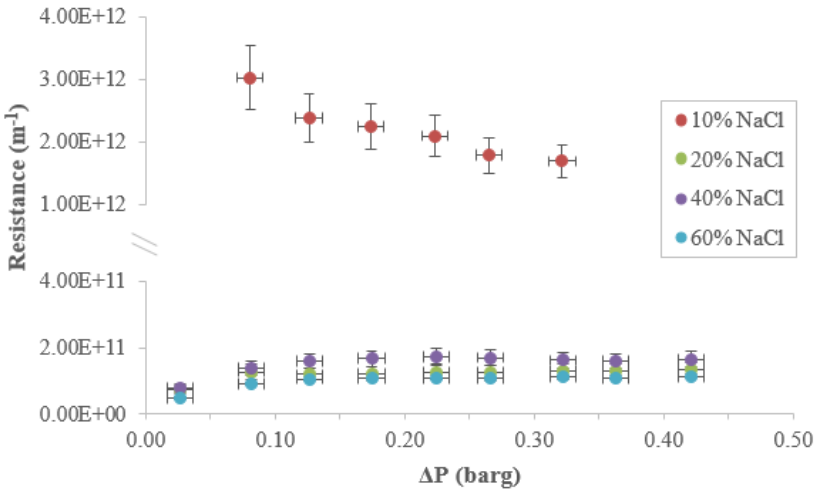

Figure F.2– Resistance of PLGA hollow fibres with different NaCl percentage to nitrogen permeation. X error = 0.01 bar, Y error = SD (n=3).

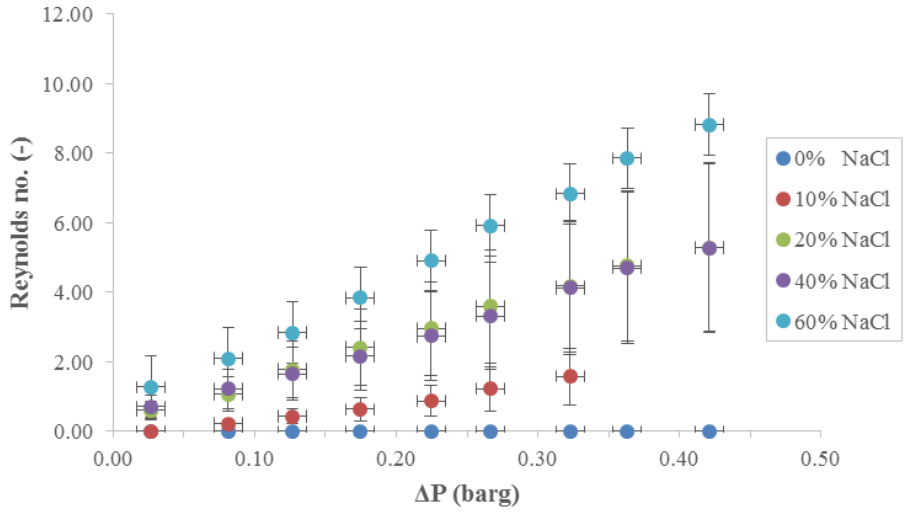

Figure F.3 – Reynolds no. of nitrogen permeating through PLGA hollow fibre walls with different NaCl content. X error = 0.01 bar, Y error = SD (n=3)

Table F.2 – Average gas permeability, resistance and flux of fibres with different NaCl content between 0.03 – 0.42 barg

NaCl	Permeability (m^2)		Resistance (m^{-1})		Flux ($m^3m^{-2}h^{-1}bar^{-1}$)	
	Average	Error	Average	Error	Average	Error
0%	0	*N/A*	∞	*N/A*	0	*N/A*
10%	2.37E-17	*42.1%*	2.20E+12	*21.8%*	14.6	*19.7%*
20%	6.39E-16	*22.1%*	1.21E+11	*15.0%*	163.7	*24.8%*
40%	3.49E-16	*32.2%*	1.53E+11	*19.4%*	127.2	*21.5%*
60%	9.52E-16	*34.6%*	1.01E+11	*20.0%*	193.8	*19.9%*

Liquid Permeation

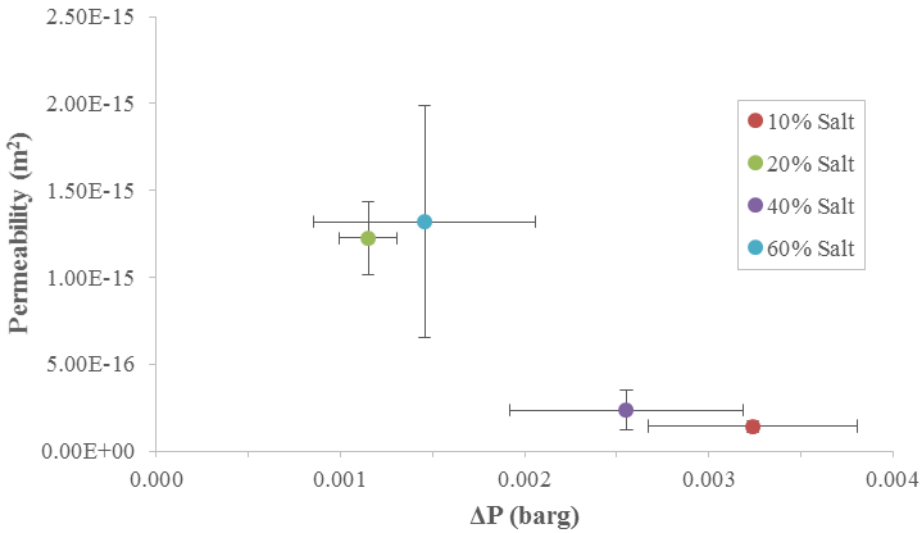

Figure F.4 – Permeation of ddH_2O through PLGA hollow fibres with different NaCl content. X error = SD (n=54), Y error = SD (n=54).

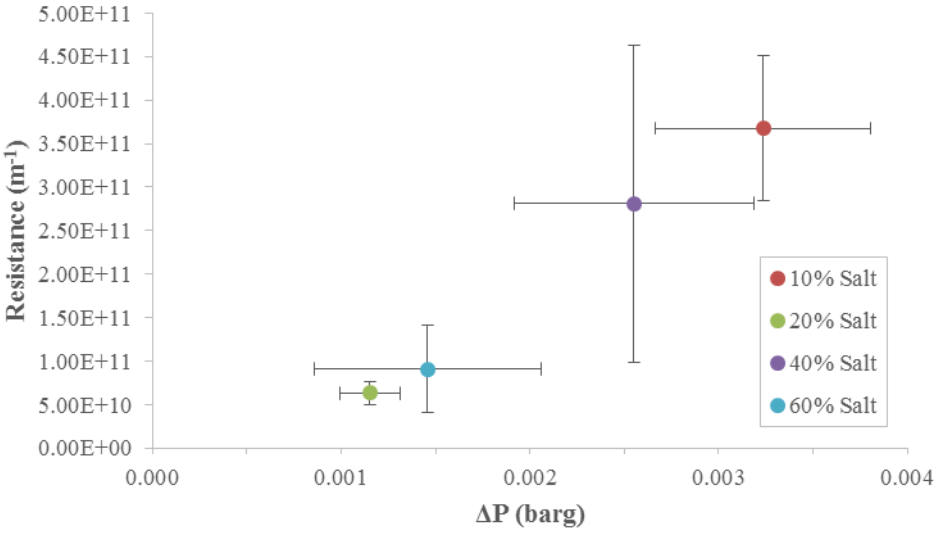

Figure F.5 – Resistance of PLGA hollow fibres with different NaCl percentage to ddH_2O permeation. X error = SD (n=54), Y error = SD (n=54).

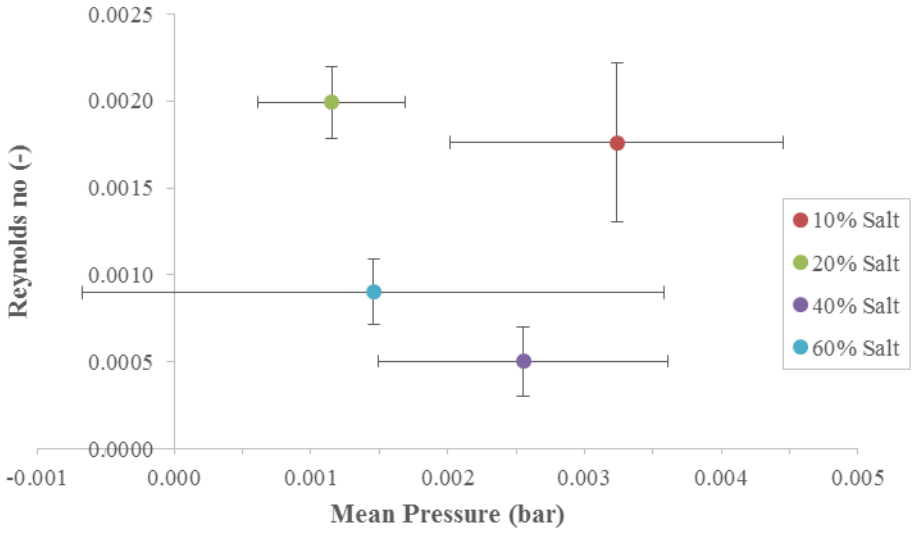

Figure F.6 – Reynolds number of nitrogen permeating through PLGA hollow fibres with different NaCl percentage. X error = SD (n=54), Y error = SD (n=54).

Table F.3 – Average liquid permeability, resistance and flux of fibres with different NaCl content between 0.001 – 0.004 bar

NaCl	Permeability (m^2)		Resistance (m^{-1})		Flux ($m^3m^{-2}h^{-1}bar^{-1}$)	
	Average	Error	Average	Error	Average	Error
0%	0	*N/A*	∞	*N/A*	0	*N/A*
10%	4.33E-16	*22.8%*	4.10E+11	*22.7%*	1.21	*33.7%*
20%	1.59E-15	*17.1%*	6.52E+10	*21.1%*	7.23	*25.9%*
40%	3.45E-16	*48.7%*	2.88E+11	*64.8%*	2.00	*60.1%*
60%	1.91E-15	*50.5%*	9.61E+10	*54.9%*	6.63	*77.2%*

Maximum Fibre Thickness

Table F.4 – Maximum fibre dimensions

Property (µm)	NaCl Percentage									
	0%		10%		20%		40%		60%	
	Value	*Error*	Value	*Error*	Value	*Error*	Value	*Error*	Value	*Error*
Outer Diameter	1350	*1.9%*	1612.5	*5.7%*	1187.5	*5.7%*	1220	*2.4%*	1212.5	*1.8%*
Inner Diameter	1140	*2.2%*	912.5	*5.8%*	737.5	*2.4%*	900	*2.8%*	712.5	*2.5%*
Thickness	105	*16.8%*	350	*26.2%*	225	*28.0%*	160	*23.6%*	250	*9.1%*

Gas Permeation

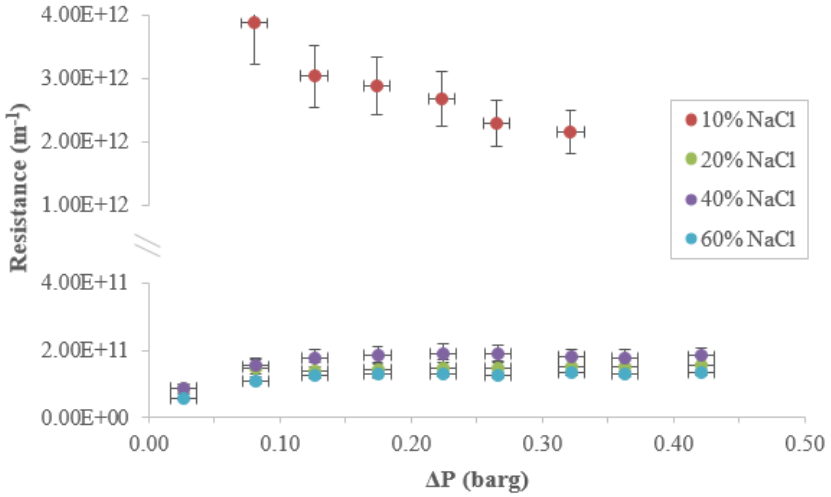

Figure F.7 – Permeation of nitrogen through PLGA hollow fibres with different NaCl content. X error = 0.01 bar, Y error = SD (n=3).

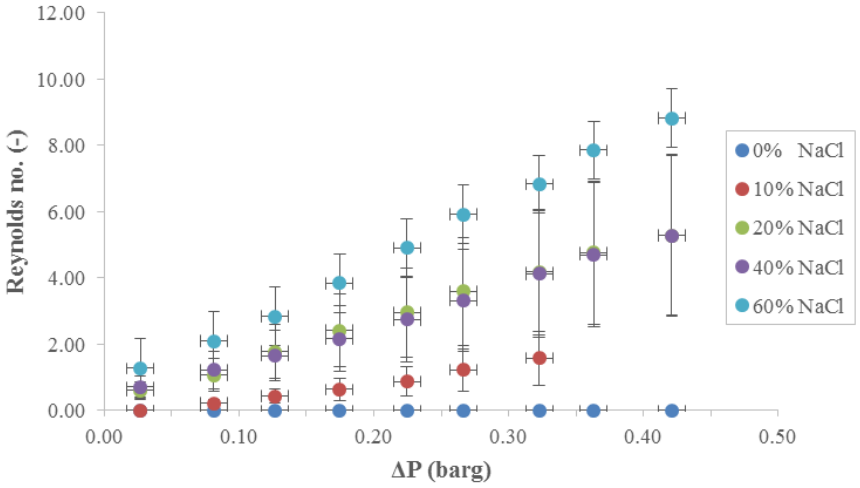

Figure F.8 – Resistance of PLGA hollow fibres with different NaCl percentage to nitrogen permeation. X error = 0.01 bar, Y error = SD (n=3).

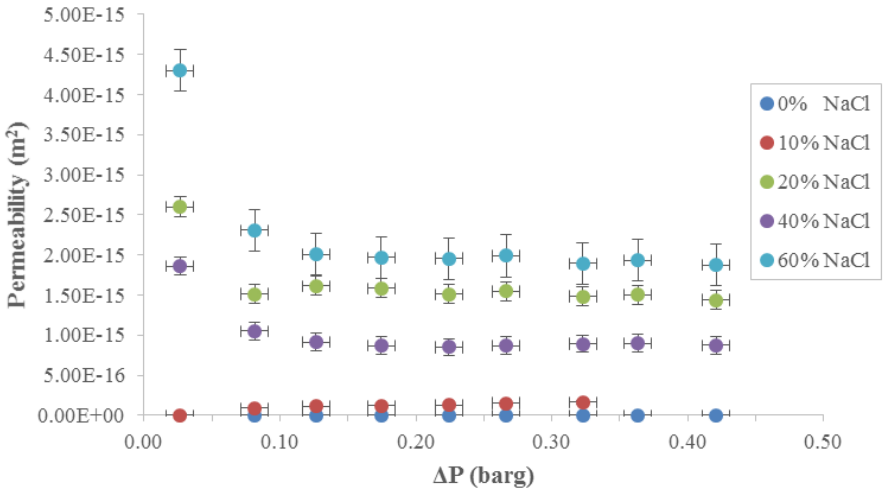

Figure F.9 – Reynolds no. of nitrogen permeating through PLGA hollow fibre walls with different NaCl content. X error = 0.01 bar, Y error = SD (n=3)

Table F.5 – Average gas permeability, resistance and flux of fibres with different NaCl content between 0.03 – 0.42 barg

NaCl	Permeability (m^2)		Resistance (m^{-1})		Flux ($m^3m^{-2}h^{-1}bar^{-1}$)	
	Average	Error	Average	Error	Average	Error
0%	0	*N/A*	∞	*N/A*	0	*N/A*
10%	1.30E-16	*42.1%*	2.82E+12	*21.8%*	14.6	*19.7%*
20%	1.64E-15	*22.1%*	1.41E+11	*15.0%*	163.7	*24.8%*
40%	1.01E-15	*32.2%*	1.69E+11	*19.4%*	127.2	*21.5%*
60%	2.25E-15	*34.6%*	1.19E+11	*20.0%*	193.8	*19.9%*

Liquid Permeation

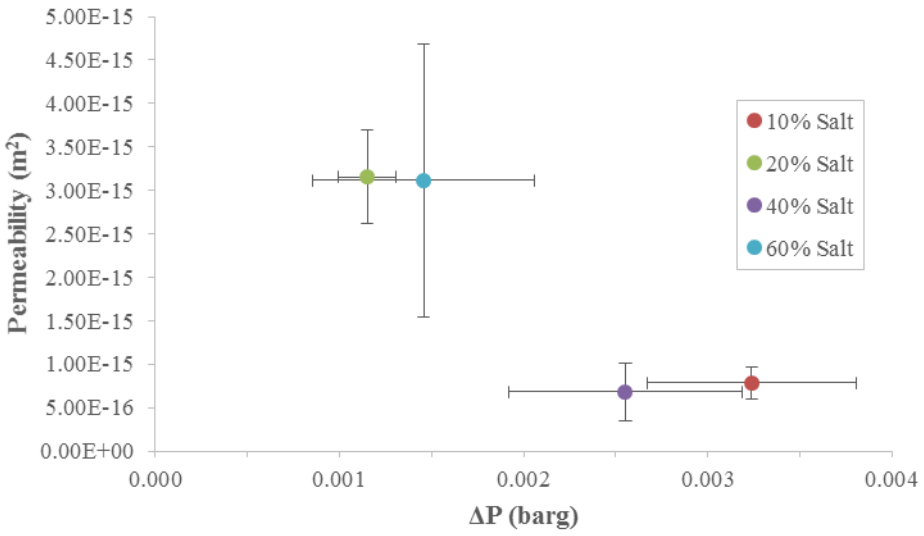

Figure F.10 – Permeation of ddH_2O through PLGA hollow fibres with different NaCl content. X error = SD (n=54), Y error = SD (n=54).

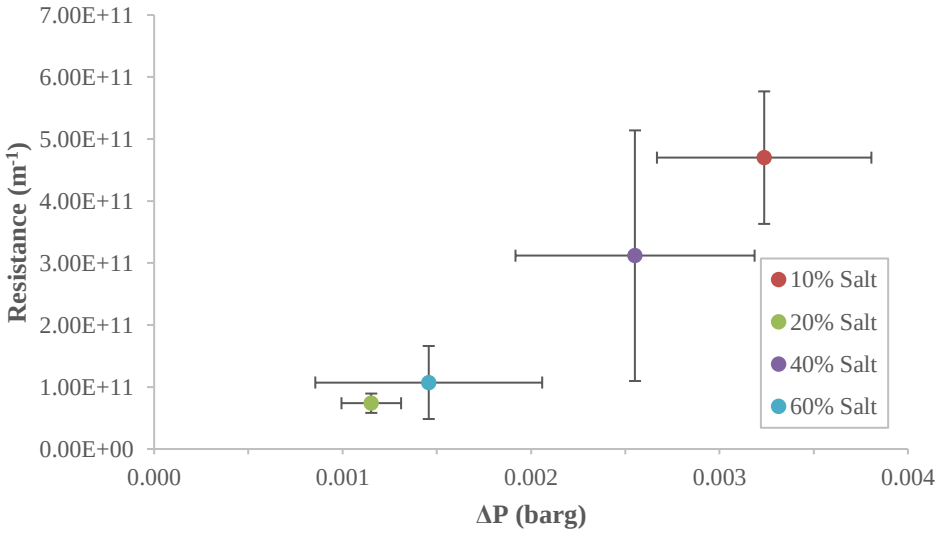

Figure F.11 – Resistance of PLGA hollow fibres with different NaCl percentage to ddH_2O permeation. X error = SD (n=54), Y error = SD (n=54).

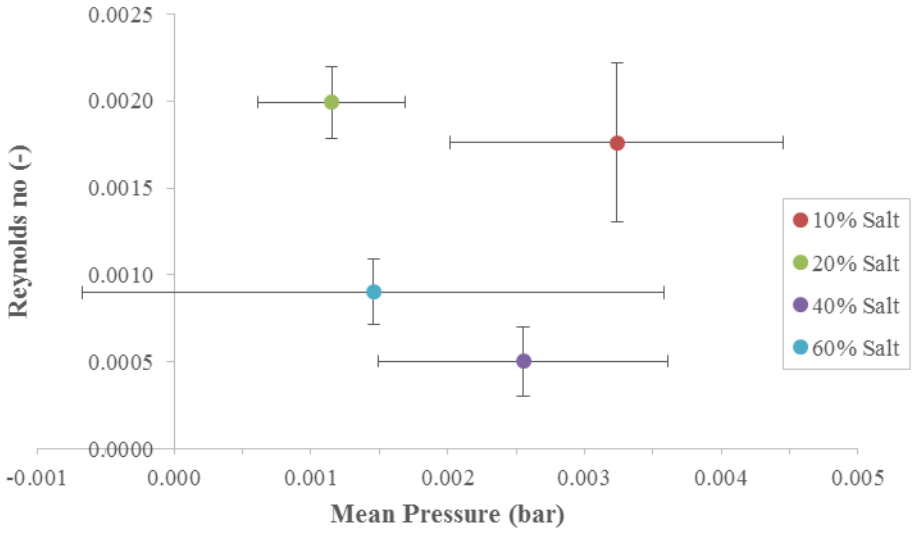

Figure F.12 – Reynolds number of nitrogen permeating through PLGA hollow fibres with different NaCl percentage. X error = SD (n=54), Y error = SD (n=54).

Table F.6 – Average liquid permeability, resistance and flux of fibres with different NaCl content between 0.001 – 0.004 bar

NaCl	Permeability (m^2)		Resistance (m^{-1})		Flux ($m^3m^{-2}h^{-1}bar^{-1}$)	
	Average	Error	Average	Error	Average	Error
0%	0	*N/A*	∞	*N/A*	0	*N/A*
10%	7.83E-16	*22.8%*	4.70E+11	*22.7%*	1.21	*33.7%*
20%	3.16E-15	*17.1%*	7.38E+10	*21.1%*	7.23	*25.9%*
40%	6.82E-16	*48.7%*	3.12E+11	*64.8%*	2.00	*60.1%*
60%	3.12E-15	*50.5%*	1.07E+11	*54.9%*	6.63	*77.2%*

APPENDIX G: PERMEATION LITERATURE COMPARISON

This section takes a value of flux through a hollow fibre found in Diban *et al* (2013), and uses it to determine an equivalent value for permeability using the dimensions of hollow fibres made in this thesis.

From Diban et al, 2013:

Parameter	Units	Value	SD	% error
Permeation flux	$m^3/m^2.h.bar$	3.7	1.2	32.4%
Inner diameter	m	3.86E-04	3.40E-05	8.8%
Outer diameter	m	4.95E-04	3.50E-05	7.1%
Thickness	m	5.50E-5	3.00E-06	5.5%
Length	m	7.00E-02		

From My Work

Salt		Value	SD	% error
10%	**ΔP** (barg)	0.0032	0.0006	17.6%
20%	**ΔP** (barg)	0.0012	0.0002	13.7%
40%	**ΔP** (barg)	0.0026	0.0006	24.9%
60%	**ΔP** (barg)	0.0015	0.0006	41.3%

Table G.1 – Values for permeability and resistance for hollow fibres described in Diban, *et al* (2013)

Average Pressure Drop (Pa)	For fibre with Salt Content:	Permeation Flux ($m^3/m^2.h.bar$)		Flux ($m^3/m^2.s$)		Flow Rate (m^3/s)		Permeability (m^2)		Resistance (m^{-1})	
		Value	*Error*	Value	*Error*	Value	*Error*	Value	*Error*	Value	*Error*
324	10%	3.7	*32.4%*	3.33E-06	*36.9%*	2.82E-10	*37.9%*	4.19E-16	*43.3%*	1.31E+11	*43.6%*
115	20%	3.7	*32.4%*	1.18E-06	*35.2%*	1.01E-10	*36.3%*	4.19E-16	*40.4%*	1.31E+11	*40.8%*
255	40%	3.7	*32.4%*	2.62E-06	*40.9%*	2.23E-10	*41.8%*	4.19E-16	*49.9%*	1.31E+11	*50.2%*
146	60%	3.7	*32.4%*	1.50E-06	*52.5%*	1.27E-10	*53.3%*	4.19E-16	*68.3%*	1.31E+11	*68.6%*

APPENDIX H: LIST OF PUBLICATIONS AND CONTRIBUTIONS

Acott, S.M., Hansen, K.J., Ellis, M.J., Gaudette, G.R., 2017. Cell seeding process efficiency for cylindrical scaffolds. *Awaiting submission*.

Wung, N., Acott, S.M., Tosh, D. & Ellis, M.J., 2014. Hollow fibre membrane bioreactors for tissue engineering applications. *Biotechnol. Lett.,* 36(12), pp. 2357-2366.

Acott, S.M., ICHEME Biochemical Engineering Special Interest Group Student Exchange Award 2013. *Biochemical Engineering Special Interest Group Newsletter,* Issue 114, pp 5-6. Available at: http://www.icheme.org/~/media/Documents/Subject%20Groups/Biochemical_engineering/Newsletters/BESIG-News-114-Aug-14-web-version.pdf

Acott S.M., Ascione R., Ellis, M.J., 2013. Cell seeding in hollow fibre bioreactors. *In*: *Tissue and Cell Engineering Society Annual Conference (TCES)*, 2013-07-23 - 2013-07-25.